UNIVERSITY OF SOUTHAMPTON

FACULTY OF ENGINEERING AND THE ENVIRONMENT

Mechanical Engineering Department

Microstructural Stability and Flow Properties of an Al-Mg-Sc alloy Processed at Different Temperatures using Severe Plastic Deformation

by

Pedro Henrique Rodrigues Pereira

Thesis for the degree of Doctor of Philosophy

April 2018

UNIVERSITY OF SOUTHAMPTON

ABSTRACT

FACULTY OF ENGINEERING AND THE ENVIRONMENT

Thesis for the degree of Doctor of Philosophy

MICROSTRUCTURAL STABILITY AND FLOW PROPERTIES OF AN Al-Mg-Sc ALLOY PROCESSED AT DIFFERENT TEMPERATURES USING SEVERE PLASTIC DEFORMATION

Pedro Henrique Rodrigues Pereira

Experiments were systematically conducted to evaluate the thermal stability and flow properties of an Al-3Mg-0.2Sc alloy both without and with processing at different temperatures using equal-channel angular pressing (ECAP) and high-pressure torsion (HPT).

The average grain size of the solution treated material was ~300 μm and this was reduced to ~250 nm after 8 passes of ECAP at room temperature (RT). Tests were conducted in both the coarse and ultrafine-grained (UFG) Al alloy to determine the mechanical properties and deformation mechanisms over seven orders of magnitude of strain rate from $\sim 10^{-4}$ to $\sim 10^{3}$ s^{-1} at 298, 523 and 673 K. The results confirm that there is no apparent breakdown in the Hall-Petch relationship in Al-Mg-Sc alloys with average grain sizes down to ~0.1 μm. Profuse shear banding and grain refinement were observed in the coarse-grained metal during dynamic testing at 4×10^{3} s^{-1} but in the ECAP-processed alloy there was minor grain coarsening. Dynamic strain ageing occurred in both the coarse and UFG Al-Mg-Sc alloy tested at RT for strain rates below $\sim 10^{-1}$ s^{-1} with a transition in flow mechanism from dislocation climb in the coarse-grained material to superplasticity in the ECAP-processed alloy at 673 K with strain rates from $\sim 10^{-4}$ to $\sim 10^{-2}$ s^{-1}.

After processing through severe plastic deformation (SPD) procedures, samples of the Al alloy were annealed for 1 h at temperatures up to 773 K or mechanical tested at high temperatures using strain rates from 3.3×10^{-4} to 1 s^{-1}. The microstructural evolution was investigated using advanced techniques such as transmission electron microscopy (TEM), electron backscattered diffraction (EBSD) and X-ray diffraction (XRD). The mechanical properties were assessed through microhardness measurements and tensile testing using miniature specimens having the same dimensions.

ECAP processing at 300 K led to higher hardness values and finer grain structures than ECAP at 600 K (~0.60 μm). The alloy processed by ECAP at 600 K exhibited lower driving pressures for grain boundary migration and therefore an improved thermal stability compared with the metal processed at RT. As a result, it displayed larger grain sizes than the alloy processed by ECAP at RT after annealing at $T \geq 623$ K. After annealing at 723 and 773 K, the metal processed by ECAP at 300 K displayed a bimodal distribution of grains, whereas samples processed by ECAP at 600 K exhibited uniform microstructures. High superplastic elongations were attained in miniature specimens of the ECAP-processed material when tested at ~523-773 K. However, they were notably lower than after tensile testing using regular ECAP samples. For tests performed at $T \geq 673$ K, the alloy processed at 600 K displayed superior superplasticity and it achieved a maximum elongation of ~1490 % after testing at 723 K. Conversely, low temperature superplasticity was obtained at faster deformation rates in samples processed by ECAP at 300 K.

HPT processing promotes further hardening and grain refinement in the Al alloy by comparison with ECAP. The HPT-processed samples displayed an average boundary spacing of ~0.15 μm and hardness values of > 180 Hv. The metal processed by HPT at 450 K also exhibited a lower dislocation density of $\sim 7 \times 10^{12}$ m^{-2} and a more uniform microstructure. The microstructural stability was enhanced by conducting HPT processing at 450 K. Although abnormal coarsening was observed in the HPT discs after annealing at 623 and 673 K, the metal processed at 450 K exhibited slower coarsening kinetics and it had grain sizes below 2 μm after annealing at 673 K. After HPT at RT, the Al alloy displayed excellent superplasticity at low homologous temperatures and it achieved a maximum elongation of ~850 % for tests performed at 523 K. However, the overall elongations decreased at $T \geq 623$ K and superplasticity was only attained at 673 K using a strain rate of 4.5×10^{-3} s^{-1}.

The Al-3Mg-0.2Sc alloy processed through 10 turns of HPT at 450 K displayed superior superplastic ductilities among all SPD processing conditions. Elongations of > 1100 % were achieved after testing at 673 K using strain rates from 3.3×10^{-4} to 1.0×10^{-1} s^{-1}. A record elongation of ~1880 % for HPT-processed metals was attained at 1.5×10^{-2} s^{-1} at 673 K. High strain rate superplasticity was also obtained for an extended range of strain rates at temperatures down to 473 K. Analysis of the data confirms a stress exponent of $n = 2$ for samples of the SPD-processed alloy having elongations of ≥ 400 %. This indicates that superplastic flow by grain boundary sliding is accommodated by dislocation climb in Al-Mg-Sc alloys. The calculated activation energies for superplasticity lie within the range of ~99-125 kJ mol^{-1} for all processing temperatures and they are higher than the activation energy for grain boundary diffusion in pure Al (~86 kJ mol^{-1}).

Table of Contents

List of Tables

List of Figures

List of Figures

Academic Thesis: Declaration of Authorship

I, Pedro Henrique Rodrigues Pereira, declare that this thesis and the work presented in it are my own and has been generated by me as the result of my own original research.

Microstructural Stability and Flow Properties of an Al-Mg-Sc alloy Processed at Different Temperatures using Severe Plastic Deformation

I confirm that:

1. This work was done wholly or mainly while in candidature for a research degree at the University of Southampton;
2. Where any part of this thesis has previously been submitted for a degree or any other qualification at this University or any other institution, this has been clearly stated;
3. Where I have consulted the published work of others, this is always clearly attributed;
4. Where I have quoted from the work of others, the source is always given. With the exception of such quotations, this thesis is entirely my own work;
5. I have acknowledged all main sources of help;
6. Where the thesis is based on work done by myself jointly with others, I have made clear exactly what was done by others and what I have contributed myself;
7. Parts of this work have been published as:
    - P.H.R. Pereira, Y. Huang, T.G. Langdon, Examining the mechanical properties and superplastic behaviour in an Al-Mg-Sc alloy after processing by HPT, Letters on Materials 5 (2015) 294-300.
    - P.H.R. Pereira, Y. Huang, T.G. Langdon, Influence of Initial Heat Treatment on the Microhardness Evolution of an Al-Mg-Sc Alloy Processed by High-Pressure Torsion, Materials Science Forum 879 (2016) 1471-1476.
    - P.H.R. Pereira, Y.C. Wang, Y. Huang, T.G. Langdon, Influence of grain size on the flow properties of an Al-Mg-Sc alloy over seven orders of magnitude of strain rate, Materials Science and Engineering A 685 (2017) 367-376.
    - P.H.R. Pereira, Y. Huang, T.G. Langdon, Examining the Thermal Stability of an Al-Mg-Sc alloy processed by High-Pressure Torsion, Materials Research (2017), in press.

- P.H.R. Pereira, Y. Huang, T.G. Langdon, Examining the microhardness evolution and thermal stability of an Al-Mg-Sc alloy processed by high-pressure torsion at a high temperature, Journal of Materials Research and Technology 6 (2017) 348-354.
- P.H.R. Pereira, Y. Huang, T.G. Langdon, Thermal stability and superplastic behaviour of an Al-Mg-Sc alloy processed by ECAP and HPT at different temperatures, IOP Conference Series: Materials Science and Engineering 194 (2017) 012013.
- P.H.R. Pereira, Y. Huang, M. Kawasaki, T.G. Langdon, An examination of the superplastic characteristics of Al-Mg-Sc alloys after processing, Journal of Materials Research 31 (2017) 4541-4553.

Acknowledgements

I would like to express my sincere gratitude to Prof. Terence G. Langdon for his enthusiasm, motivation and continuous guidance during my PhD journey at the University of Southampton. I am also grateful for his comments and immense knowledge which improved all aspects of my work.

I take this opportunity to thank Dr. Yi Huang for her support and technical contributions to this study. I am also grateful for her friendship and encouragement since our first encounter in 2014. My thanks extend to Dave Beckett, Heather Porter and Rachel Matthews for providing precious assistance with the laborious experimental work and to Chris Williams for his outstanding skills on machining operations which permitted the consistent production of all miniature specimens used in this investigation.

I am also grateful to Prof. Paulo R. Cetlin and Prof. Roberto B. Figueiredo for the friendship and mentoring since my undergraduate studies in UFMG. Your examples as professionals and idealists truly inspired my path towards a career in science and my achievements would not be possible without your help and support. My sincere thanks to CAPES Foundation in Brazil for sponsoring my PhD studies in the University of Southampton and thereby promote the research advancements presented in this doctoral thesis.

I would like to acknowledge and thank Prof. Yingchun Wang and her research group in Beijing Institute of Technology for conducting the dynamic tests with the Al-Mg-Sc alloy. My sincere thanks extend to Dr. Megumi Kawasaki for her kind assistance with the analyses of the rate controlling mechanism in superplasticity and to Prof. Małgorzata Lewandowska and Dr. Piotr Bazarnik for conducting all the TEM and STEM examinations shown in this study.

My deepest gratitude to my dear friends in Southampton who gracefully assisted me during the long hours and difficult moments of the study. Thanks for being my second family and sharing uncountable experiences along my 4-year journey in UK. I will always be with you whenever our good times are still remembered.

Finally, I specially thank my parents Anita and Antonio, my brother Gustavo, my family and friends in Brazil for the prayers, patience and assistance during my time overseas. Even if we were separated by the Atlantic Ocean, in each time I received your messages, I felt as if no time had passed and we were together. Thanks for sharing your thoughts and aspirations and allowing me to continue being part of your lives. I also wish to express my eternal gratitude to my grandmother, Ana, who passed away few months prior to my departure to England. She provided me with an example of perseverance in difficult moments and guided me into my faith and spirituality. I dedicate this work to her loving memory.

Definitions and Abbreviations

A – Dimensionless constant in the equation for high temperature deformation

ARB – Accumulative roll-bonding

C_0 – Speed of sound in the Hopkinson pressure bars

D – Diffusion coefficient

$D_{o,gb}$ – Frequency factor for grain boundary diffusion

D_c – Average crystallite size

D_{gb} – Coefficient for grain boundary diffusion

DSA – Dynamic strain ageing

DRX Dynamic recrystallization

DSC – Differential Scanning Calorimetry

E – Young's modulus

EDX – Energy-dispersive X-ray

EBSD – Electron backscatter diffraction

ECAP – Equal-channel angular pressing

FEM – Finite element modelling

FIB - Focused ion beam

FSP – Friction stir processing

G – Shear modulus

GBS – Grain boundary sliding

HAGBs – High-angle grain boundaries

HPT – High-pressure torsion

HSRS – High strain rate superplasticity

LAGBs – Low-angle grain boundaries

$\bar{L}$ – Average grain boundary spacing calculated using the linear intercept method

N – Number of revolutions in HPT processing

N_{ECAP} – Number of ECAP passes

OIM – Orientation imaging microscopy

OM – Optical microscopy

P_b – Driving pressure for grain boundary migration due to boundary energy

P_d – Driving pressure for grain boundary migration due to stored dislocations

P_{nom} – Nominal pressure applied in the disc surfaces during HPT processing

P_Z – Zener pinning pressure imposed on advancing grain boundaries by randomly distributed dispersoids

Q – Activation energy

Q_{gb} – Activation energy for grain boundary diffusion

R – Universal gas constant

RT – Room temperature

SAED – Selected Area Electron Diffraction

SFE – Stacking fault energy

SHPB – Split Hopkinson pressure bar

SPD – Severe Plastic Deformation

STEM – Scanning Transmission Electron Microscopy

T – Absolute Temperature

T_m – Absolute melting temperature

TEM – Transmission Electron Microscopy

TTT – Temperature-time-transformation diagram

UFG – Ultrafine-grained

V – Volume of the anvils

X Ratio between the equivalent diameter of a particular grain and the average equivalent diameter.

XRD – X-ray diffraction

a – Lattice parameter

a_{b} – Area of the cross section of the Hopkinson pressure bar

a_{s} – Area of the cross section of the specimen tested using the SHPB system

b – Burgers vector

c_d – Constant in the equation predicting the driving pressure for grain boundary migration due to stored dislocations

c_{w} – Specific heat capacity of the work-piece

d – Average grain size

d_{eq} – Area-weighted average grain diameter

d_s – Spatial grain size

f – Volume fraction of precipitates

fcc – Face-centred cubic structure

h – Thickness of the HPT disc

hcp – Hexagonal close-packed structure

k – Boltzmann's constant

k_p – Factor associated with the shape of the dispersoids (k_p = 3/2 for spherical particles).

k_y – Constant of yielding in the Hall-Petch relationship

$\mathrm{l_s}$ – Length of the specimen used during dynamic testing with the SHPB system

m – Strain rate sensitivity, $[\partial \log \sigma / \partial \log \dot{\varepsilon}]_T$

n – Stress exponent in the equation for high temperature deformation

p – Inverse grain size exponent in the equation for high temperature deformation

r – Radial distance measured from the centre of the HPT disc

r_p – Average radius of the precipitates

t – Time

ΔT_{HPT} – Variation in the temperature of the sample during HPT processing

γ – Interface energy of the boundary pinned by precipitates

ϕ – Intersecting angle which separates both parts of the channel in the ECAP die

ε – True strain

$\langle \varepsilon^2 \rangle^{1/2}$ – Lattice microstrain

$\varepsilon_{\mathrm{ECAP}}$ – Theoretical effective strain imposed after ECAP

ε_{ef} – Effective strain

ε_i – Incident strain pulse acquired during dynamic testing using the SHPB system

$\varepsilon_{\mathrm{HPT}}$ – Theoretical equivalent von Mises strain imposed during HPT

ε_r – Reflected strain pulse acquired during dynamic testing using the SHPB system

ε_t – Transmitted strain pulse acquired during dynamic testing using the SHPB system

$\dot{\varepsilon}$ – Strain rate

θ_{anvil} – Angle between the shallow depressions of the anvils and their inclined edges

θ_{mis} – Misorientation angle

λ – Steady-state subgrain size during deformation at high temperature

ρ – Dislocation density

ρ_{w} – Density of the work-piece

σ – True stress

σ_0 – Friction stress from the Hall-Petch relationship

σ_{iso} – Isothermal true stress calculated for the dynamic testing experiments

σ_{max} – Maximum true stress

σ_y – Yield stress

ψ – External curvature angle in the ECAP die

ψ_b – Dimensionless parameter for boundary stability - $\psi_b = \frac{k_p f d}{2r_p}$

ω – Angular velocity of the rotating anvil in HPT processing

ζ – Dimensionless constant in the equation predicting the steady-state subgrain size during deformation at high temperature

Chapter 1 Introduction

1.1 Background and Motivations

The processing of metallic materials through severe plastic deformation (SPD) methods has been extensively performed in the past three decades to produce bulk solids having exceptionally small grain sizes [1,2]. These materials normally exhibit remarkably improved mechanical properties compared with metals subjected to conventional metal forming due to the high density of dislocations and grain refinement introduced during SPD processing.

Although several SPD techniques are now available [3], most interest is centred on the procedures of equal-channel angular pressing (ECAP) [4] where a billet is repetitively pressed within a channel bent through an abrupt angle and high-pressure torsion (HPT) [5,6] where a thin disc is deformed by torsional straining under high hydrostatic pressures. These techniques require simple facilities and permit the processing of difficult-to-work materials by controlling the temperature and the imposed strain rate in the work-pieces [7].

The growing interest for more fuel-efficient vehicles has motivated the development of Al alloys especially designed for applications in the transportation industry [8,9]. After ECAP processing, pure aluminium displays superior mechanical strength and higher strain rate sensitivity compared with the coarse grained material [10]. Similar enhancements are also observed in SPD-processed Al-Mg alloys [11–15] which exhibit additional strengthening and grain refinement due to the presence of Mg solutes. However, these materials have unstable grain structures at elevated temperatures and any benefits in the mechanical properties attained by grain refinement are lost through recrystallization and grain coarsening [16–19]. With the aim of improving the microstructural stability, Al alloys may be alloyed with Sc additions because Al_3Sc dispersoids are effective in pinning the grain boundaries and preserving ultrafine-grained (UFG) structures even at high temperatures [20].

There have been several exploratory studies dedicated to examine the flow properties at high strain rates in different UFG metals [21–30]. Nevertheless, there are no reports at present available on the deformation of SPD-processed Al-Mg-Sc alloys at dynamic strain rates [31], even though conventional Al alloys with Sc additions display an exceptional capacity to resist the impact of projectiles [32,33]. Furthermore, there are only limited studies documenting the mechanical properties of UFG Al-Mg-Sc alloys at low deformation temperatures [34–37] and it is still unclear how grain refinement affects the flow mechanisms in this material for this range of temperatures.

Considering that the strain rate in superplasticity is inversely proportional to the square of the grain size [38], several studies have been conducted with the objective of producing nanostructured metals for use in superplastic forming operations at faster production rates [39]. The Al-Mg-Sc alloys have attracted notable attention from both the academia and the industry because of their high strength to density ratio, as well as their excellent superplastic properties, especially after severe plastic deformation [40,41]. The microstructural stability and the superplastic behaviour of Al-Mg-Sc alloys were studied extensively after ECAP processing [20,42–47].

After ECAP at RT, the Al-3Mg-0.2Sc alloy achieved a maximum elongation of ~2580 % after tensile testing at 723 K at $3.3 \times 10^{-3}\,s^{-1}$ [43]. By contrast, the Al-5Mg-0.2Sc-0.08Zr alloy processed by ECAP at ~600 K displayed a record elongation of ~4100 % after testing at $5.6 \times 10^{-2}\,s^{-1}$ at 723 K [45]. These results indicate that processing Al-Mg-Sc alloys through ECAP at high temperatures permits the achievement of higher ductilities but the reasons for this superior superplasticity remain a matter of debate. This motivates a more detailed assessment of the microstructural changes of Al-Mg-Sc alloys after ECAP at different temperatures and further heating at temperatures adequate for superplastic flow.

It has been consistently demonstrated that Al-Mg-Sc alloys processed by HPT at ambient temperature exhibit smaller grain structures than after ECAP processing [48–51]. Conversely, lower elongations to failure were obtained in the HPT-processed alloy for tests performed at 673 K [48,52]. This decrease in the superplastic ductilities is usually attributed to the use of miniature tensile specimens [48,49,53–55]; however, no information is provided about the microstructural changes in HPT-processed samples of Al-Mg-Sc alloys when exposed to elevated temperatures. Furthermore, although it is difficult to upscale the HPT samples, the use of miniature specimens also for the ECAP-processed alloy would permit an unequivocal comparison of the superplastic properties after HPT and ECAP.

It was revealed in recent investigations that the thermal stabilities in pure Ni [56] and stainless steel [57,58] are significantly enhanced by conducting HPT processing at high temperatures. Higher superplastic elongations were also documented for the AZ61 [59] and the Mg–9Al alloy [60] after HPT at 423 K. Nevertheless, there have been no studies to date dedicated to study the microstructural evolution and superplastic properties of Al-Mg-Sc alloys processed by HPT at a high temperature even though this processing route has emerged as a promising strategy to delay the grain growth kinetics in Al-Mg-Sc alloys and retain ultrafine grains at temperatures suitable for superplastic forming.

1.2 Aims and Objectives

This doctoral research aims to acquire knowledge about the mechanical properties and microstructural evolution of an Al-3Mg-0.2Sc alloy processed at different temperatures either by ECAP or HPT and determine, for each separate processing condition, the range of temperatures and strain rates in which this metal exhibits true superplastic flow. This investigation also aims to identify the deformation mechanisms over seven orders of magnitude of strain rate in the Al alloy both with and without processing by ECAP and reliably compare the superplastic elongations obtained after SPD processing.

The main objectives of this research are outlined as follows:

- To examine the flow properties and microstructural changes in an Al-3Mg-0.2Sc alloy both without and with processing by ECAP after mechanical testing under quasi-static and dynamic conditions.
- To measure the range of grain sizes in which plastic straining is primarily controlled by intragranular dislocation motion for Al-Mg-Sc alloys.
- To critically assess the influence of processing temperature on the microstructural evolution, thermal stability and superplastic properties of an Al-3Mg-0.2Sc alloy processed either by 8 passes of ECAP at 300 K or 10 ECAP passes at either 600 K.
- To investigate the influence of processing temperature on the hardening kinetics and microstructural evolution of an Al-3Mg-0.2Sc alloy processed by HPT at either 300 or 450 K.
- To critically evaluate the influence of processing temperature on the microstructural stability and superplastic behaviour of an Al-3Mg-0.2Sc alloy processed through 10 turns of HPT at either 300 or 450 K.
- To reliably compare the elongations to failure achieved in an Al-3Mg-0.2Sc alloy processed by either HPT or ECAP at different temperatures by conducting tensile tests on miniature specimens with identical dimensions.
- To identify the rate controlling mechanisms during superplastic flow for Al-Mg-Sc alloys with or without processing by SPD.

1.3 Thesis Structure

This doctoral thesis is composed of 8 chapters. Chapter 2 shows a comprehensive literature review which covers the fundamental concepts and potential applications of SPD processing. It also presents the principles of dynamic testing and provides a description about the most important microstructural aspects of Al-Mg-Sc alloys. The experimental procedures used in this investigation are presented in Chapter 3. Chapter 4 shows the flow properties and deformation mechanisms over seven orders of magnitude of strain rate in an Al-3Mg-0.2Sc alloy both with and without processing by ECAP. The microstructural stability and superplastic properties of this alloy after processing by ECAP or HPT are analysed in Chapters 5 and 6. Chapter 7 provides a general discussion on the influence of the nature of the SPD procedure and the processing conditions on the mechanical properties, thermal stability and superplastic characteristics of Al-Mg-Sc alloys. Finally, Chapter 8 presents the main conclusions obtained in this study and includes suggestions for future work.

Chapter 2 Literature Review

2.1 Severe Plastic Deformation

Severe plastic deformation (SPD) procedures refer to those metal forming techniques in which extremely high strains are imposed in bulk materials without changing significantly their dimensions after processing [4]. Using SPD methods, metals with superior mechanical properties are produced as a consequence of the intense straining and grain refinement during processing.

At temperatures below about half of the absolute melting temperature, T_m, the plastic flow in conventional crystalline metals occurs mainly by dislocation glide and the grain boundary strengthening is usually expressed in terms of the Hall-Petch relationship considering the yield stress, σ_y, and the average grain size, d, as follows [61,62]:

$$\sigma_y = \sigma_0 + k_y d^{\left(-\frac{1}{2}\right)} \tag{2.1}$$

where σ_0 is the friction stress and k_y is a constant of yielding. It follows from the Hall-Petch relationship that a reduction in the grain size leads to an increase in the mechanical strength of polycrystalline metals.

Conversely, recent studies have demonstrated that the Hall-Petch relationship may not accurately predict the grain boundary strengthening in metals with grain sizes in the ultrafine (100 nm to 1 μm) and nanocrystalline (<100 nm) ranges due to the increasing participation of different deformation mechanisms such as grain boundary sliding (GBS) and the emission and annihilation of extrinsic dislocations at grain boundaries [63–67]. Although there are only few experimental investigations showing direct or indirect evidence of these deformation mechanisms in nanostructured materials [68], there have been several exploratory studies using analytical models [69] and atomistic simulations [67,70] which consistently display the existence of these deformation mechanisms within this grain size regime. Furthermore, molecular dynamic simulations have also revealed that the stress required for the emission of dislocations from grain boundaries also depends on the local atomic structure of these contours [70,71] and non-equilibrium grain boundaries, usually developed during severe plastic deformation, are capable of emitting extrinsic dislocations with lower stress by comparison with equilibrium grain boundaries [72].

At high temperature regimes, plastic deformation occurs mainly by diffusion-controlled mechanisms such as dislocation climb, viscous glide and grain boundary sliding. It is feasible

to model the plastic flow at high temperatures and this leads to an equation in the conventional form for the strain rate under steady-state conditions, $\dot{\varepsilon}$:

$$\dot{\varepsilon} = \frac{ADG\boldsymbol{b}}{kT}\left(\frac{\mathbf{b}}{d}\right)^{p}\left(\frac{\sigma}{G}\right)^{n} \tag{2.2}$$

where D is the diffusion coefficient, G is the shear modulus, **b** is the Burgers vector, k is Boltzmann's constant, T is the absolute temperature, σ is the applied true stress, p and n are the exponents of the inverse grain size and the stress, respectively, and A is a dimensionless constant [38].

In the theoretical model for GBS in superplasticity, p = 2, n = 2, and A = 10 in Eq. 2.2 [38]. Additionally, the coefficient for grain boundary diffusion, D_{gb}, is the appropriate diffusion coefficient for Eq. 2.2 and may be expressed as:

$$D_{gb} = D_{o,gb}\, e^{\left(-\frac{Q_{gb}}{kT}\right)} \tag{2.3}$$

where $D_{o,gb}$ is the frequency factor and Q_{gb} is the activation energy for grain boundary diffusion. Accordingly, as evident in Eq. 2.2, the flow by GBS may be attained at faster strain rates by decreasing the grain size [39] and thereby the production of ultrafine-grained, UFG, metals through severe plastic deformation is recognised as a promising strategy to increase the production rates in superplastic forming [73].

The potential for achieving excellent properties in bulk solids through grain refinement by severe plastic deformation was first reported in 1988 where it was demonstrated the possibility of fabricating an UFG aluminium alloy using HPT processing [74]. This report was especially important to arouse international interest in this scientific field, and since then, an increasing number of research activities have been developed in this area with the objective of producing a large range of UFG materials by severe plastic deformation [1,2]. Even though this research topic is relatively new considering the long history of Metallurgy and Materials Science, the large number of citations and review papers published in journals with high-impact factors testifies to the importance of this area for the materials science community [75].

Inspired by the extraordinary properties of ultrafine-grained materials, many different SPD procedures have been developed as recently reported [3]. Among these techniques, equal-channel angular pressing (ECAP) [4], high-pressure torsion (HPT) [5,6], accumulative roll-bonding (ARB) [76] and multi-directional forging [77] are considered as well-established SPD processes capable of fabricating solids with grain sizes in the nanometre range [3,4].

Although various SPD techniques are now available, major focus has been dedicated to ECAP and HPT processing as they require simple facilities and permit the processing of difficult-to-work materials by controlling the temperature, the imposed pressure and the effective strain rate in the work-pieces [7]. High-pressure torsion is usually more effective than ECAP concerning the production of nanostructured grains. Nevertheless, HPT discs may display significant microstructural heterogeneity along their cross-sections, hindering the fabrication of large bulk solids with a satisfactory structural homogeneity [78]. Additionally, although the grain structures of the samples are not as refined after ECAP as in HPT processing, it is possible to produce billets with larger dimensions at higher production rates using the ECAP facilities now available [79].

In the following sections, the principles of ECAP and HPT processing will be presented in detail, as well as major achievements using both procedures to improve the mechanical and superplastic properties of metallic materials, especially focusing on aluminium alloys.

2.1.1 Equal-Channel Angular Pressing

2.1.1.1 Principles of ECAP

Equal-Channel Angular Pressing (ECAP) is an SPD procedure in which a sample is pressed by a plunger through a die containing a bent channel as illustrated in Figure 2.1 [80]. The channel angle, ϕ, is defined as the intersecting angle which separates both parts of the ECAP channel and the curvature angle, ψ, represents the angle at the external surface of the channel intersection. The coordinate system defined in Figure 2.1 is used to indicate planes and directions in the ECAP billets. Additionally, both parts of the ECAP channel have the same cross-sections and thereby the billets have nearly the same initial dimensions after processing by ECAP. Accordingly, it is possible to repetitively press these samples into the die without the requirement of any machining operation between passes.

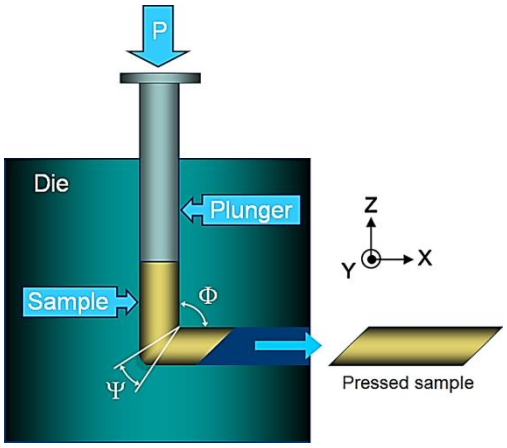

Figure 2.1 - Schematic illustration of the ECAP facility [80].

During ECAP processing, the billet is deformed by simple shear whilst passing through the die channel and the imposed effective strain, $\varepsilon_{ECAP,}$ depends upon the angles ϕ and ψ, as well as the number of passes through the die, $N_{ECAP,}$ as shown in the following relationship [81]:

$$\varepsilon_N = \frac{N_{ECAP}}{\sqrt{3}}\left[2\cot\left(\frac{\phi}{2}+\frac{\psi}{2}\right)+\psi\csc\left(\frac{\phi}{2}+\frac{\psi}{2}\right)\right] \quad (2.4)$$

It follows from Eq. 2.4 that the angle ϕ has major influence on the deformation attained during ECAP processing. In addition, the lower the channel angles, the higher the level of strain imposed in the ECAP-processed material. Both the accuracy of Eq. 2.4 and the deformation homogeneity along the work-pieces were already discussed in a number of reports which used experiments with coloured plasticine [82] and finite element modelling [7,83,84] to calculate the distribution of strain in different materials. The results of these studies showed excellent agreement with the strain values predicted using Eq. 2.4. Nevertheless, low values of strain were observed in the vicinity of the lower surfaces of the ECAP-billets and this strain inhomogeneity is attributed to frictional effects during processing. Furthermore, the strain distribution and workability of the ECAP billets strongly depends on their strain rate sensitivity [7].

The microstructural evolution and mechanical properties of materials processed by ECAP depend not only on the geometrical parameters of the dies, but also they depend upon the processing parameters such as the pressing speed [85], processing temperature [86] and back-pressure [87]. In addition, the billets may be rotated between each ECAP pass in order to activate different slip systems in the UFG metal during plastic straining and, accordingly, four fundamental processing routes were defined [88] as illustrated in Figure 2.2 [89].

It is readily apparent from Figure 2.2 that in route A the samples are not rotated between each pass, in route B_a the samples are periodically rotated 90° in opposite senses whereas in route B_c the samples are rotated 90° in the same sense after each ECAP pass. Finally, in route C the samples are rotated 180° between consecutive passes.

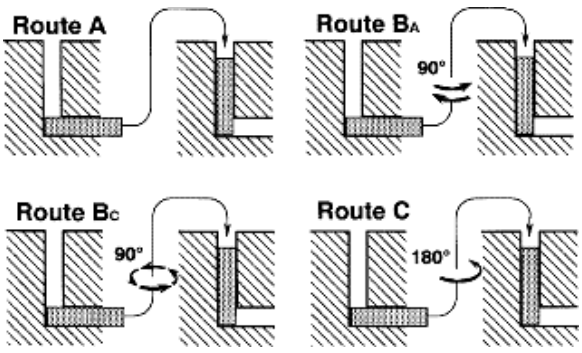

Figure 2.2 - Schematic illustration of the processing routes in ECAP [89].

The knowledge about the influence of the processing parameters is essential for applying the ECAP technique in difficult-to-deform materials such as magnesium alloys. Recent reports have demonstrated that the workability of this group of materials may be improved by using back-pressure during processing [87], as well as by refining the initial microstructure of the ECAP billets using conventional metal forming procedures such as hot rolling [90]. Additionally, further grain refinement in magnesium may be achieved by processing billets at high temperatures and gradually decrease the temperature of the ECAP die in the following passes [91].

2.1.1.2 Microstructural Evolution

There have being numerous investigations using advanced techniques such as Transmission Electron Microscopy (TEM) [92,93] and Electron Backscatter Diffraction (EBSD) [11,94] aiming to evaluate the microstructural evolution in polycrystalline materials processed by ECAP. These studies provide experimental evidence of grain refinement and increase in the fraction of high-angle grain boundaries, HAGBs, with increasing number of ECAP passes, as depicted in Figures 2.3 and 2.4 [94] for high-purity Al.

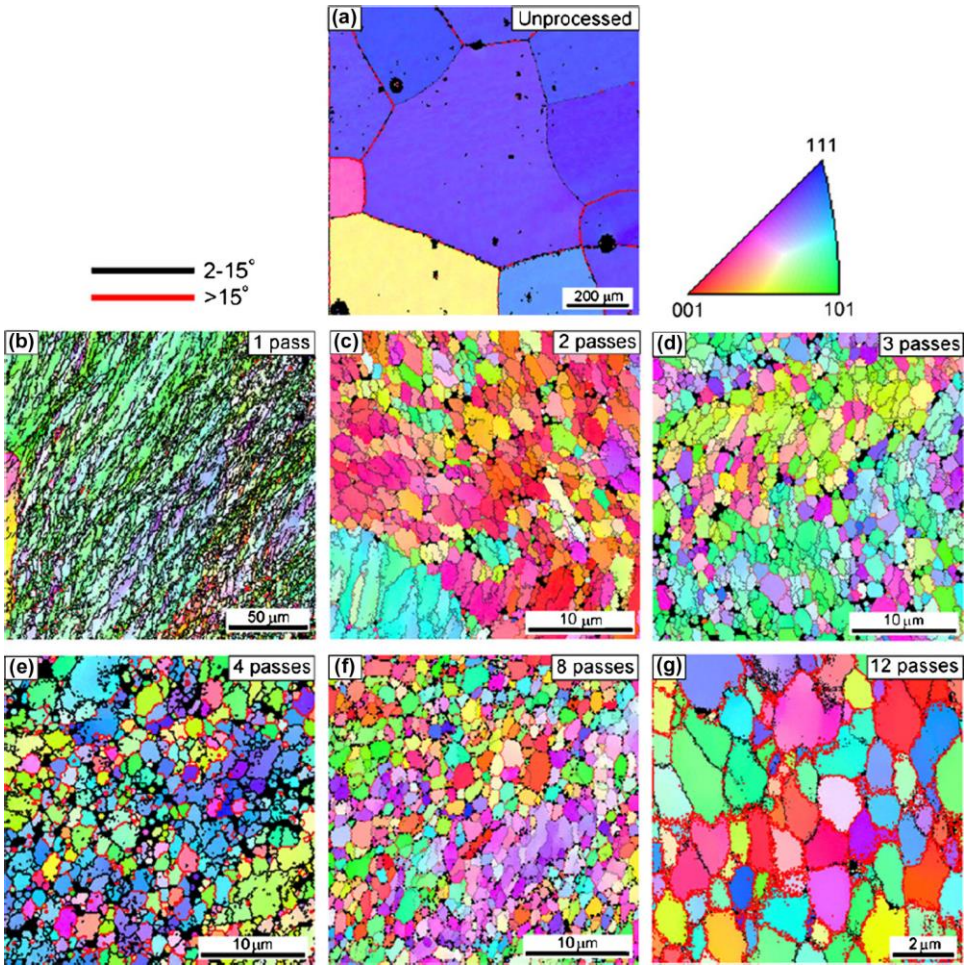

Figure 2.3 - Microstructural evolution in pure aluminium after ECAP [94].

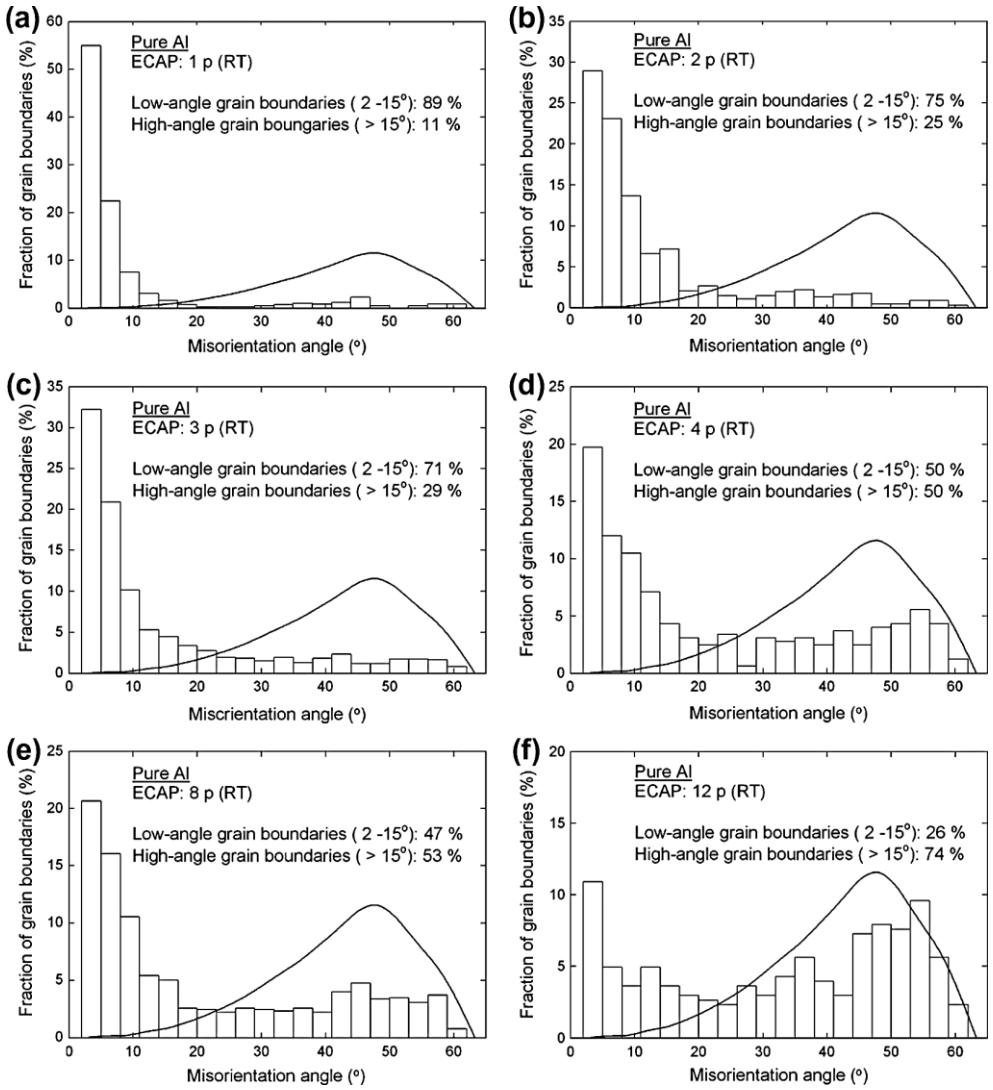

Figure 2.4 - Distribution of the misorientation angles in pure aluminium after ECAP [94].

Figure 2.3 shows that after processing pure aluminium using an ECAP die with $\phi = 90^{o}$ and $\psi = 20^{o}$ the initial coarse structures with an average grain size of ~1 mm are fully refined and the grain sizes after 8 and 12 passes are ~1.1 ± 0.6 and ~1.2 ± 0.6 μm, respectively, thus indicating no further refinement after 8 passes. Figure 2.4 displays that the fraction of high-angle grain boundaries monotonically increased with increasing number of ECAP passes in high-purity Al, although there is a significant fraction of boundaries with low misorientation angles even after 12 ECAP passes.

Despite the experimental evidences of grain refinement, formation of high-angle grain boundaries and increase in dislocation density during ECAP, the mechanisms of strengthening and grain refinement remain a matter of discussion in the scientific community. As described in a recent study [3], the most accepted grain refinement models under SPD conditions are dislocation density based models in which it is assumed that the dislocations developed during straining evolve to dislocation cell structures which progressively transform to ultrafine grains with HAGBs [95,96].

The overall morphology and distribution of grains in polycrystalline metals processed by ECAP depends upon the chosen processing route for face-centred cubic (fcc) metals as depicted in Figure 2.5 [92] and is strongly influenced by the initial grain size in hexagonal close-packed (hcp) metals as illustrated in Figure 2.6 [46].

It is apparent in Figure 2.5 from the observation of the TEM images in the Y plane associated with the correspondent Selected Area Electron Diffraction (SAED) patterns that a reasonably equiaxed array of grains is formed after four ECAP passes using route B_c. Nevertheless, in the case of high-purity Al processed by ECAP using routes A and C there are remaining banded structures with elongated grains and a considerable fraction of low-angle grain boundaries, LAGBs, even after four passes.

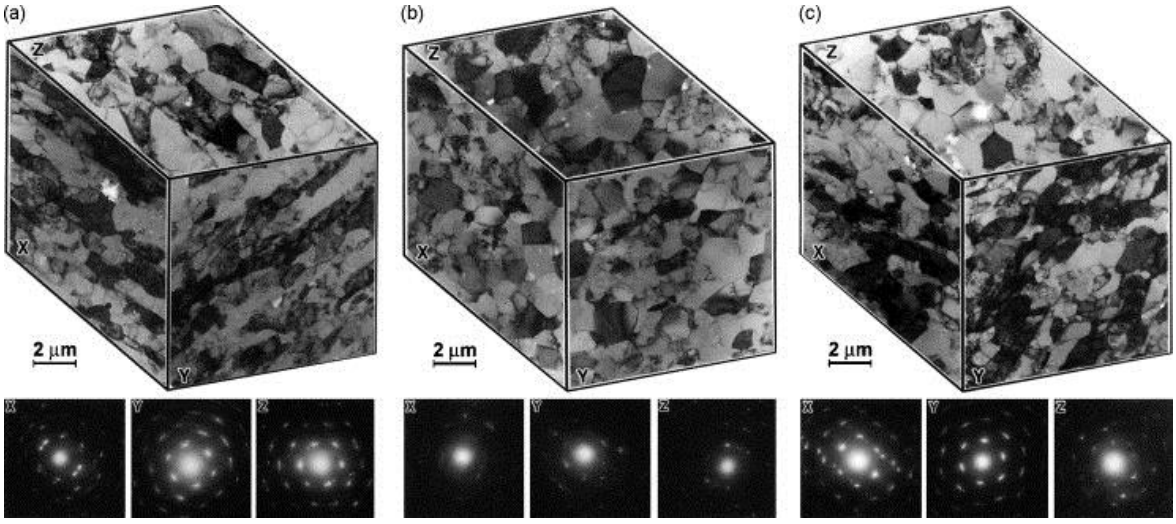

Figure 2.5 - Microstructures and SAED patterns on the X, Y and Z planes in pure aluminium after four ECAP passes for (a) route A, (b) route B_c and (c) route C [92].

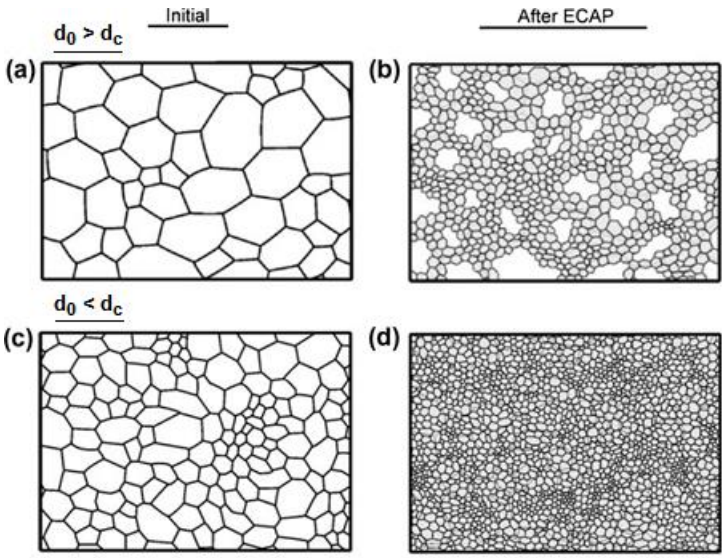

Figure 2.6 - Schematic illustration of the influence of the relation between the initial and the critical grain size in the grain refinement of magnesium processed by ECAP [97].

Figure 2.6 illustrates the significance of the initial grain size in the microstructural evolution in hcp metals. In the case of a relatively large initial grain size, new grains nucleate heterogeneously at the former grain boundaries, a necklace-like array of grains is developed and this bimodal structure remains even after multiple ECAP passes. Therefore, in order to obtain equiaxed and homogeneously distributed grains in magnesium alloys, the average grain size before ECAP processing shall lie below a critical level which may be achieved by conducting extrusion [97] or rolling [90] prior to severe plastic deformation.

2.1.1.3 Mechanical Properties and Superplasticity

The mechanical properties of materials processed by ECAP have been extensively investigated since the first developments of this technique. Ultrafine-grained metals usually have very high strength as predicted using the Hall-Petch relationship [61,62] and reduced ductility as a result of their high flow stress and low strain-hardening capability [3]. Although many studies confirm this dichotomy in nanostructured metals [98–100], extremely high strength and high ductility were reported when processing Cu [101] and Ti [102] by ECAP, as shown in Figure 2.7 [101]. The reason for the "paradox of strength and ductility in SPD-processed metals" was attributed to the increased contribution of grain boundary sliding during plastic deformation of UFG metals [101,103].

Superplasticity refers to the ability of a polycrystalline material to exhibit very high elongations when pulled out to failure in a tensile testing such that the measured elongation to failure is often equal or higher than 400 % with a measured strain rate sensitivity of ~0.5 [104]. Extraordinary superplastic properties have been reported in a large number of metals processed by ECAP with special concern on Al and Mg alloys [105] as demonstrated in Figure 2.8 [106] for an extruded ZK60 magnesium alloy.

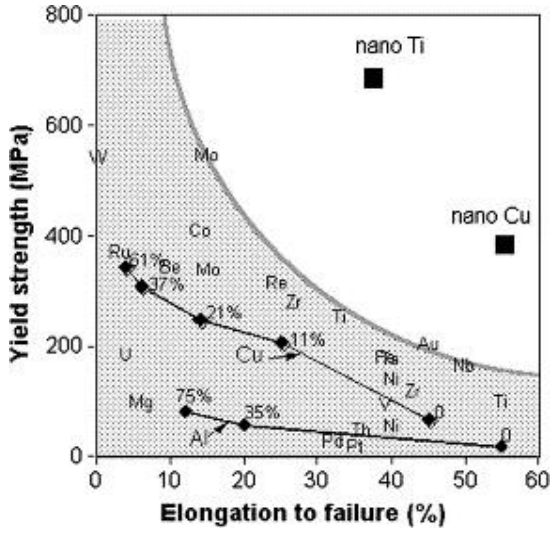

Figure 2.7 - The relationship between the yield strength and elongation to failure in coarse-grained metals and in the nanostructured Ti and Cu after ECAP [101].

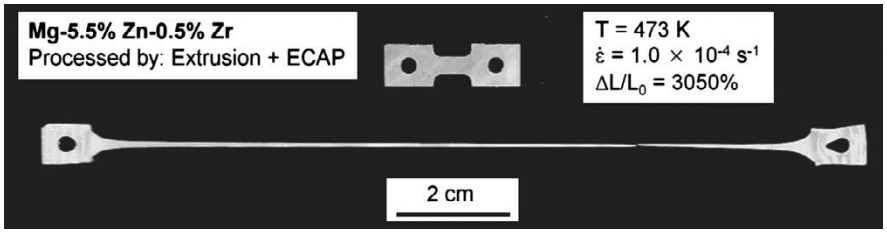

Figure 2.8 - Exceptional superplasticity in a commercial extruded ZK60 magnesium alloy after 2 ECAP passes at 473 K [106].

2.1.2 High-Pressure Torsion

2.1.2.1 Principles of HPT

High-Pressure Torsion (HPT) refers to the metal-working technique in which the microstructure of a usually thin disc is severely refined by imposing very high hydrostatic stresses and concurrent torsional straining [5].

The first investigations on processing by HPT were conducted by Professor Bridgman as reported in 1935 [107] and described in a very recent review [6]. In these classic experiments, thin discs of different materials were simultaneously compressed and twisted using hardened steel anvils such that these samples were twisted to greater angles without fracture than in the absence of hydrostatic stresses. The HPT anvils used by Bridgman did not provide any mechanical restriction to the lateral flow of the work-piece leading to its substantial thinning during processing.

Since this early investigation, different HPT facilities were developed and according to the geometry of the anvils and the mechanical restriction imposed to the radial flow of the sample, HPT processing is classified in three distinct categories termed constrained, quasi-constrained and unconstrained HPT, as depicted in Figure 2.9 [108].

It follows from Figure 2.9 that there is a more pronounced outflow and thinning in the work-piece in unconstrained HPT as the anvils do not provide sufficient restriction to the lateral flow besides the frictional forces in the upper and lower surfaces of the sample. By contrast, there is a physical barrier preventing the radial flow of the disc and usually higher torques are required during constrained and quasi-constrained HPT [108]. A recent study using finite element modelling (FEM) examined the distribution of strain and hydrostatic stress within the disc during processing by HPT under different constraining conditions [109]. These FEM simulations revealed that there are different regions of flow localization along the cross-section of the disc after 1 turn of HPT at constrained and quasi-constrained configurations. It is also apparent a more uniform strain distribution for the material processed by unconstrained HPT besides its undesirable thinning, as displayed in Figure 2.10.

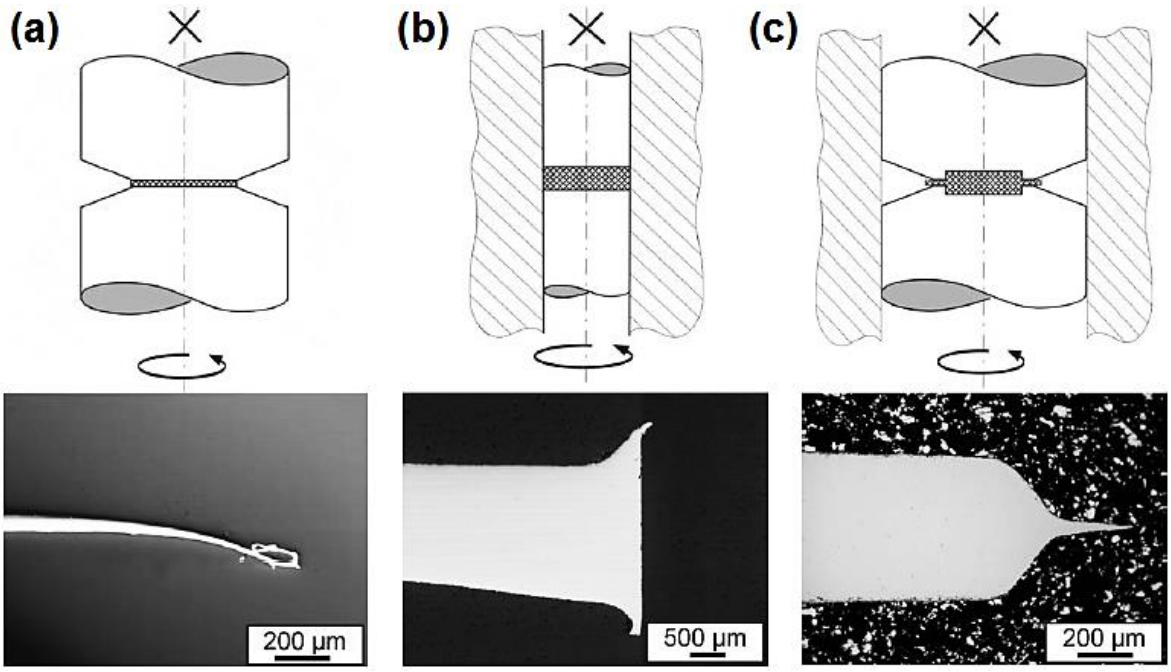

Figure 2.9 - Illustrations of the anvils and cross-sections of discs after processing by HPT using (a) unconstrained, (b) constrained and (c) quasi-constrained configurations [108].

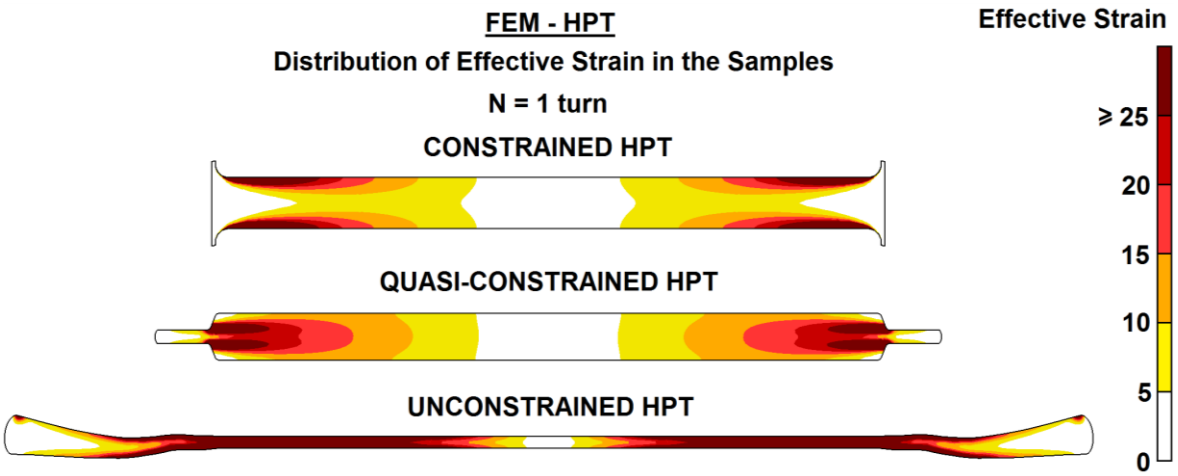

Figure 2.10 - Distribution of strain in discs subjected to 1 turn of HPT using the nominal pressure of 1.5 GPa, the rotation rate of 1.0 rpm and different anvil configurations [109].

In practice, HPT processing is mostly conducted using quasi-constrained configurations and consists of two stages based on the relative motion of the anvils and the sample as illustrated in Figure 2.11 [110]. Firstly, in the compression stage of HPT, a disc is placed in a shallow depression in the lower anvil and an increasing load is applied at the surface of the sample until the processing pressure is reached. Afterwards, in the compression-torsion stage, the applied axial load is maintained constant whereas the lower (or upper) anvil rotates with a selected rotation rate imposing substantial torsional straining within the processed material.

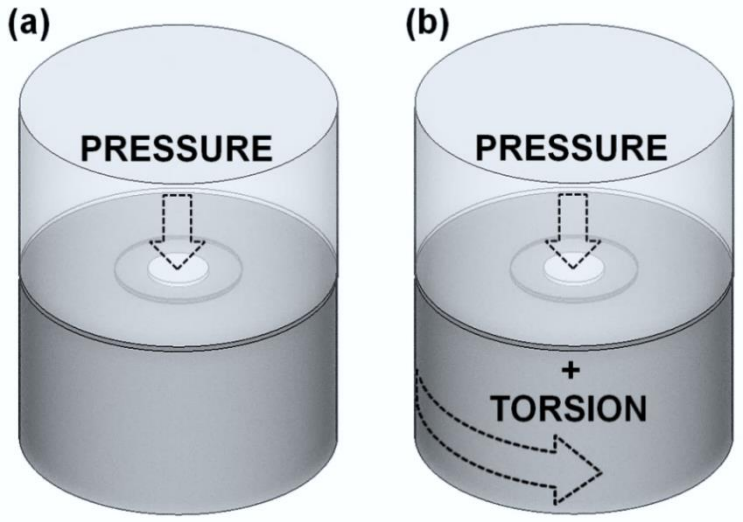

Figure 2.11 - Schematic illustration of (a) the compression stage and (b) the compression-torsion stage in HPT processing [110].

During the compression stage of HPT both the upper and lower surfaces of the disc become curved as a consequence of the elastic deformation of the anvils during processing and the gradient in the thickness of the work-piece depends upon the nominal pressure, P_{nom}, used during HPT processing [110,111]. Discs processed by HPT are deformed during the loading and unloading of the anvils thereby producing an inhomogeneous distribution of strain in the work-pieces such that the effective strain is higher near their edges. This heterogeneous distribution of strain is confirmed by means of microhardness measurements which depict a hardness peak in the centre of the samples compressed within the HPT anvils [110].

The equivalent von Mises strain, ε_{HPT}, imposed on HPT discs during the compression-torsion stage, also referred to as effective strain, ε_{ef}, in different FEM investigations [109–113], is given by the following relationship [114]:

$$\varepsilon_{HPT} = \frac{2\pi Nr}{h\sqrt{3}} \tag{2.5}$$

where N is the number of revolutions, r is the radial distance measured from the centre of the disc and h is the thickness of the work-piece. It follows from Eq. 2.5 that the equivalent strain is very heterogeneous along the sample diameter during processing by HPT. The accuracy of this theoretical relationship has been discussed in recent reports through the calculation of the internal and external work during HPT [115] and FEM simulations [112,116,117]. The simulation results demonstrate good agreement concerning the strain distribution predicted using Eq. 2.5, nevertheless there is a tendency for flow localization in the vicinity of the sample outflow.

2.1.2.2 Microstructural Evolution

In the past three decades, special attention has been dedicated to study the influence of the processing parameters and the fundamental material properties on the grain refinement and microstructural evolution in HPT processing [2,5].

Figure 2.12 [117] depicts the distribution of the effective strain rate on disc-shaped samples with a selected diameter and different thicknesses during HPT processing. The simulation results presented in Figure 2.12 show that higher strain rates are found in discs having smaller thickness. Furthermore, samples with higher diameter-to-thickness ratios exhibit more prominent strain rate gradients along the through-thickness direction which leads to more heterogeneous microstructures and local mechanical properties as experimentally verified using microhardness measurements [108] and optical microscopy (OM) images of bulk aluminium samples processed by high-pressure torsion [78].

In quasi-constrained HPT, the angle between the shallow depressions of the anvils and their inclined edges, θ_{anvil}, also plays a significant role in the distribution of microhardness [108] and plastic strain along the disc thickness as shown in Figure 2.13 [118]. Inspection of Figure 2.13 reveals that the equivalent strain is highly inhomogeneous at r = 5 mm for more vertical lateral walls of the anvil depressions (θ_{anvil} = 0 and 30°) compared with θ_{anvil} = 60°. Therefore, more homogeneous distributions of strain along the thickness of the HPT discs may be attained by using anvil depressions with more inclined lateral walls.

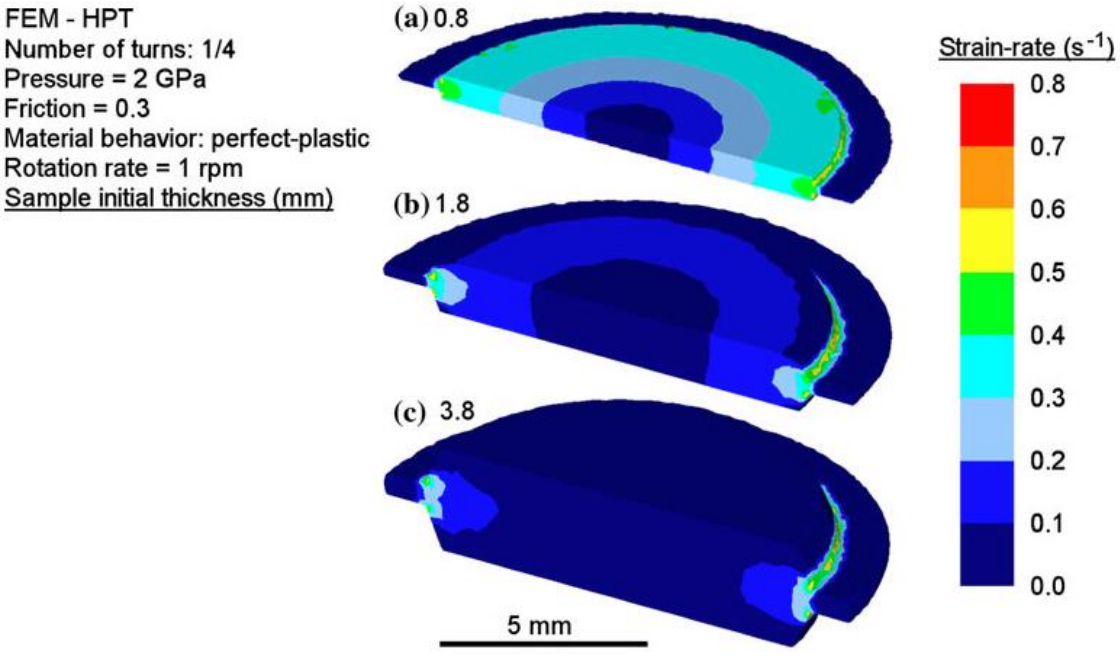

Figure 2.12 - Strain rate distribution on the half-disc surfaces considering samples with 10 mm in diameter and initial thicknesses of (a) 0.8, (b) 1.8 and (c) 3.8 mm [117].

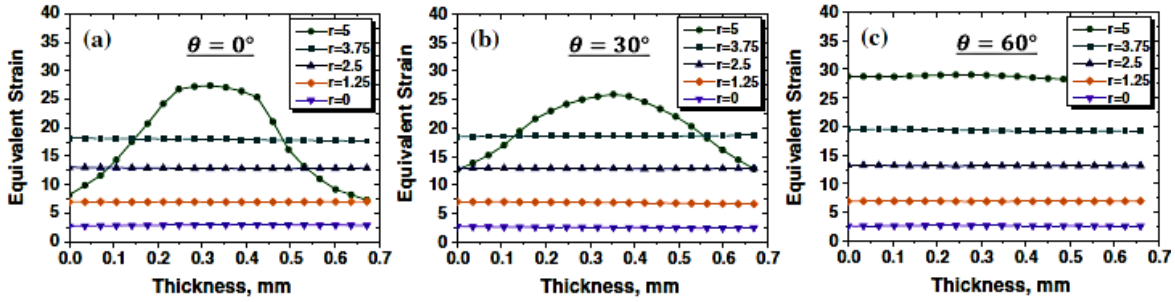

Figure 2.13 - Equivalent strain along the through-thickness direction in HPT discs at the radial coordinates of 0. 1.25, 2.5, 3.75 and 5 mm. The angles between the anvil depressions and their inclined edges, θ_{anvil}, are (a) 0, (b) 30 and (c) 60º [118].

There have been several studies showing the influence of the applied pressure [108,110,119,120], the processing temperature including the calculation of the temperature rise in HPT [56,109,115,121–125], the strain reversals [126], the anvil alignment [127] and the local strain rate [128] in processing metallic materials by high-pressure torsion.

Processing by HPT using higher processing pressures leads to more pronounced lateral flow and thinning of the samples [110]. Besides the operational requirement to apply a minimum processing pressure in order to avoid the slippage of the disc during HPT [108,129], experimental investigations demonstrated that the application of pressures beyond this minimum value does not modify significantly the distribution of grains and microhardness in metals after HPT processing [119,120].

Assuming that 90 % of the plastic work is converted into heat during deformation, the temperature rise, ΔT, as a consequence of the plastic deformation in adiabatic conditions is given by the following relationship [130]:

$$\Delta T = \frac{0.9}{\rho_w c_w} \int \sigma \, d\varepsilon \qquad (2.6)$$

where ρ_w and c_w are the density and the specific heat capacity of the work-piece, respectively. The sample heating during high-pressure torsion is not adiabatic and Eq. 2.6 fails to estimate ΔT in HPT processing. Nevertheless, recent reports have successfully predicted the temperature rise in the discs considering the heat losses to the massive anvils and the environment during processing [121,123,125].

During HPT processing, the disc is continuously strained and, accordingly, its temperature increases until a maximum temperature is achieved as shown in Figure 2.14 [121] for different angular velocities, ω, volume of the anvils, V, radii, r, and initial thicknesses, h, of the samples.

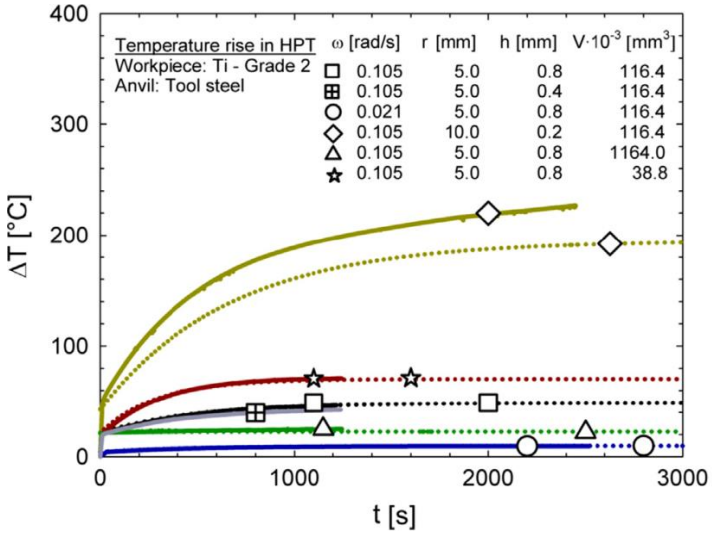

Figure 2.14 - Variation of temperature ΔT as a function of time t in discs of grade 2 titanium during quasi-constrained HPT processing [121].

The plots displayed in Figure 2.14 were obtained using FEM simulations (continuous lines) validated by experimental data and a general relationship (dotted lines) was derived in the same investigation [121]. There is good agreement between the equation and FEM results such that the difference of both predictions is within < 15 %. The maximum temperature in the work-piece in quasi-constrained HPT processing is directly proportional to the material flow stress, the angular velocity and the square of the sample radius. Furthermore, the variation of temperature in the samples during HPT may be reduced by using anvils with higher volumes and higher heat capacities. Additionally, the applied pressure and the sample thickness play a relatively minor role in the rise in temperature.

A simplified relationship for the variation of temperature, ΔT_{HPT}, with time t in HPT samples during processing was derived considering discs with a diameter of 10 mm and tool steel anvils with volumes for each anvil of ~58,200 mm^3 as follows [121]:

$$\Delta T_{\mathrm{HPT}} = 0.22\sigma\omega\left[1 + 1.28\left(1 - \mathrm{e}^{-(t/482)}\right)\right] \tag{2.7}$$

Using Eq. 2.7, it is possible to evaluate whether there is a significant increase in the temperature of the samples in HPT processing as higher grain sizes and decreased hardness values are obtained after HPT with increasing processing temperatures [56,124].

The grain refinement, precipitation and phase transformation in discs during high-pressure torsion has been evaluated using various techniques such as differential scanning calorimetry (DSC) [131], TEM [132] and EBSD [132,133]. Even though the plastic flow in HPT is essentially heterogeneous, fairly homogeneous microstructures and hardness distributions are attained in the discs after a sufficient number of turns as recently reviewed [134] and also displayed in Figure 2.15 [135].

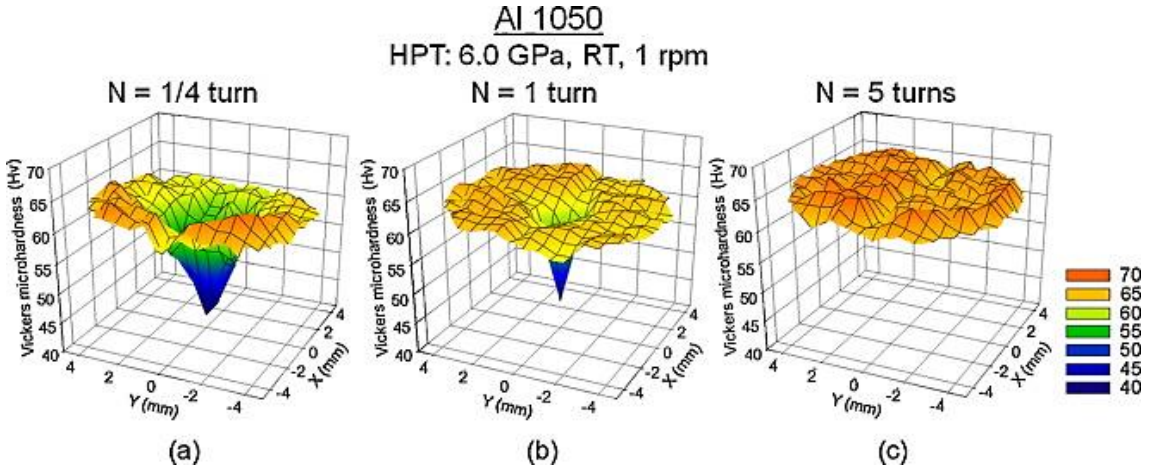

Figure 2.15 - Hardness evolution for commercial purity aluminium (Al-1050) after(a) 1/4 (b) 1 and (c) 5 turns in HPT processing [135].

As depicted in Figure 2.15, the Vickers microhardness values significantly increased and the hardness distribution is reasonably homogeneous after 5 turns of HPT processing using Al-1050 discs. The same behaviour was already reported in a number of investigations [134] and it was indicated the hardness distribution during HPT is strongly influenced by the ratio between the processing and melting temperatures of the processed material such that high ratios may lead even to softening in metals after HPT processing [136].

2.1.2.3 Mechanical Properties and Superplasticity

The mechanical properties of materials processed by HPT have been examined using hardness measurements [134] and conventional tensile testing using thin samples such that two tensile specimens are usually machined from each disc. These specimens are symmetrically located in the disc and their gauge sections are positioned at ~2 mm of the disc centre in order to avoid problems related to inhomogeneity in the centres of the discs [137,138]. Figure 2.16 [137] shows the stress-strain curves obtained from tensile tests performed at room temperature, RT, in Al-1% Mg specimens in the annealed condition, after HPT and after HPT processing and subsequent annealing.

Inspection of Figure 2.16 reveals that the ultimate tensile strength in Al-1% Mg samples after 10 turns of HPT is about four times the values obtained in the annealed condition. On the other hand, the ductility of this Al alloy significantly decreases after HPT and higher elongations are achieved through further annealing in detriment of the mechanical strength.

The potential for achieving extensive superplastic elongations after HPT processing has been extensively investigated in aluminium and magnesium alloys as recently reported [139]. Extremely high elongations are achieved in the Zn-22% Al alloy after the application of SPD procedures as shown in Figure 2.17[139] using datum points obtained elsewhere [140,141].

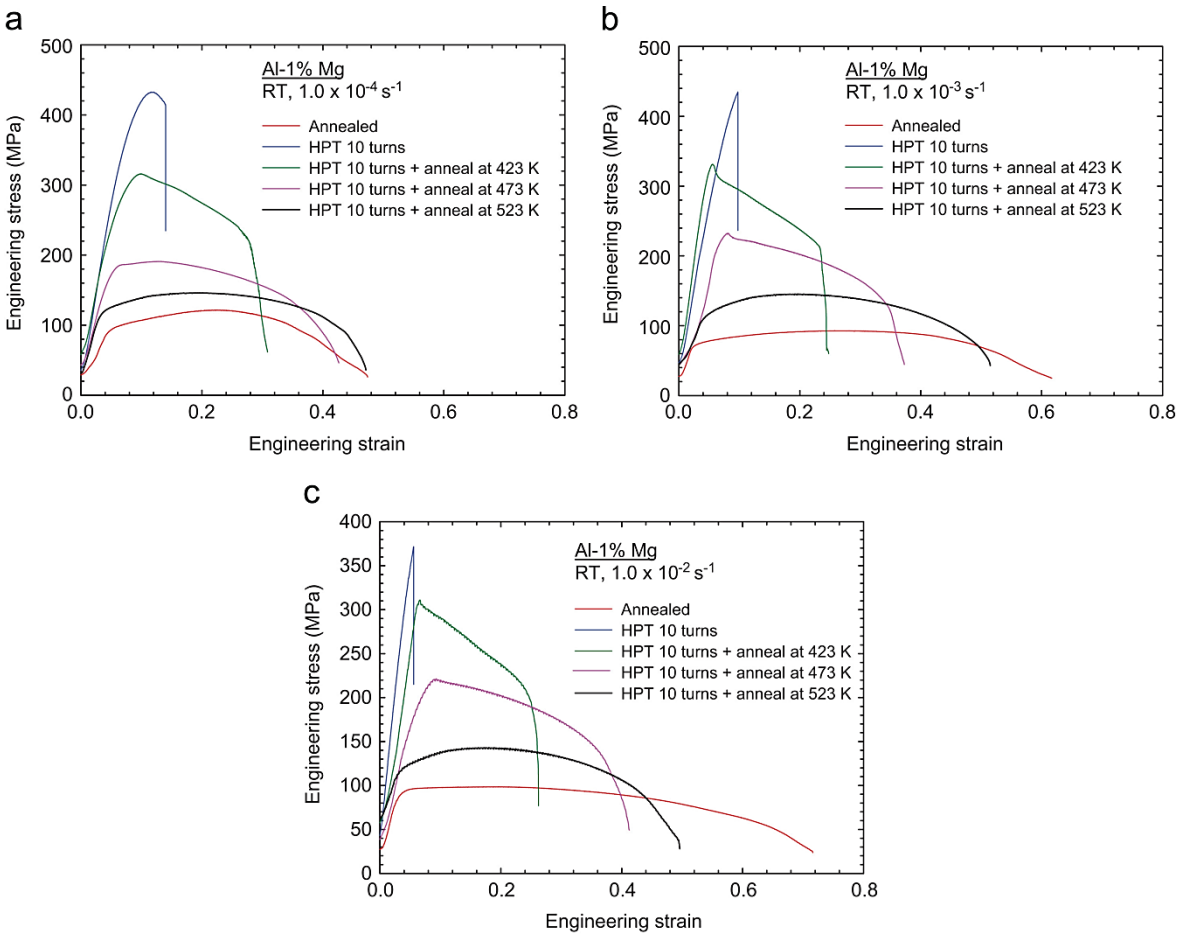

Figure 2.16 - Stress-strain curves for the annealed Al-1% Mg alloy, after 10 turns of HPT and after 10 turns of HPT and further annealing at 423, 473 and 523 K. The initial strain rates of the performed tensile tests were (a) 1.0×10^{-4}, (b) 1.0×10^{-3} and 1.0×10^{-2} s^{-1} [137].

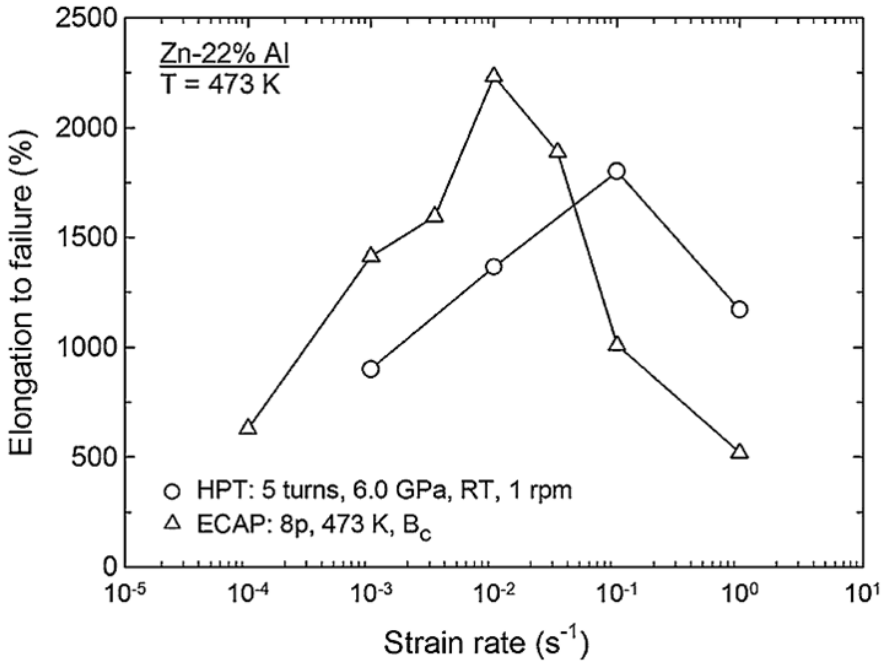

Figure 2.17 - A comparison of elongations to failure in a Zn-22% Al alloy processed either by ECAP [140] or HPT [141] and further tested at 473 K [139].

Figure 2.17 shows consistent evidence of superplastic flow in the Zn-22% Al alloy either after processing by ECAP or HPT. As the measured grain sizes in this aluminium alloy after ECAP and HPT were ~900 [140] and ~350 nm [141], respectively, it was expected that the samples processed by HPT would exhibit higher elongations than the samples processed by ECAP. Furthermore, according to Eq. 2.2, the superplastic region after HPT should be displaced to faster strain rates by comparing with ECAP.

It is readily seen in Figure 2.17 that after HPT the optimum superplastic behaviour occurs at faster strain rates by comparison with the same in the Zn-22% Al alloy processed by ECAP. However, the maximum elongation in ECAP is higher than in HPT. The reason for these apparently contradictory results is associated with the differences in the geometry of ECAP and HPT specimens. The HPT samples usually have smaller cross-sectional areas than ECAP specimens and an exploratory investigation using copper samples tested at room temperature has shown using experiments and FEM simulations [142] that both the uniform elongation and the post-necking elongation increase with increasing cross-sectional areas of the tensile work-pieces. Nevertheless, further tensile testing using samples with identical geometries are necessary in order to isolate the effect of the specimen size and also evaluate the intrinsic microstructural aspects which may affect the ductility and thermal stability of samples subjected to different SPD procedures.

2.2 Dynamic Testing

The mechanical properties and deformation mechanisms of UFG materials have been widely investigated using conventional mechanical testing techniques such as tensile and compression testing. Nevertheless, these testing methods are usually limited to strain rates within the range from $\sim 10^{-5}$ to $\sim 10^{1}$ s^{-1} and thereby different techniques are required to provide information about the mechanical behaviour of polycrystalline metals at extremely high strain rates, as illustrated in Figure 2.18 [143].

It is readily observed from the diagram depicted in Figure 2.18 that, at strain rates higher than $\sim 10^{1}$ s^{-1} up to $\sim 10^{4}$ s^{-1}, mechanical testing is usually conducted using the concept of pressure bars [144] through the compression split Hopkinson pressure bar (SHPB) system [145–147]. The basic idea of the dynamic testing using typical SHPB facilities is that the sample is compressed between two bars with comparatively higher yield stress, as displayed in Figure 2.19 [26]. Thereafter, the striker bar is propelled by a pressurized gas towards the incident bar and thus produces an elastic compression wave which propagates through the incident bar towards the compression specimen. Accordingly, this compression wave reaches the sample which is thereby plastically strained. Part of the wave is reflected to the incident bar and part goes through the transmitted bar.

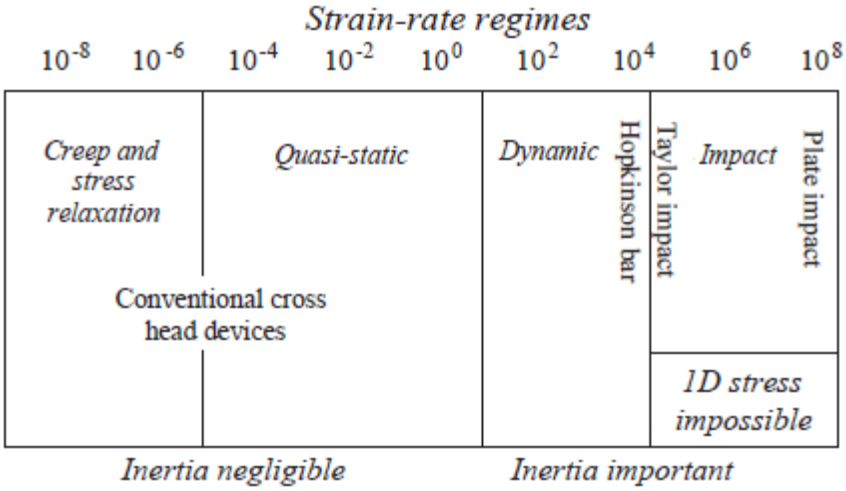

Figure 2.18 - Schematic diagram displaying the mechanical testing techniques used at different strain rate regimes (unit: s^{-1}) [143].

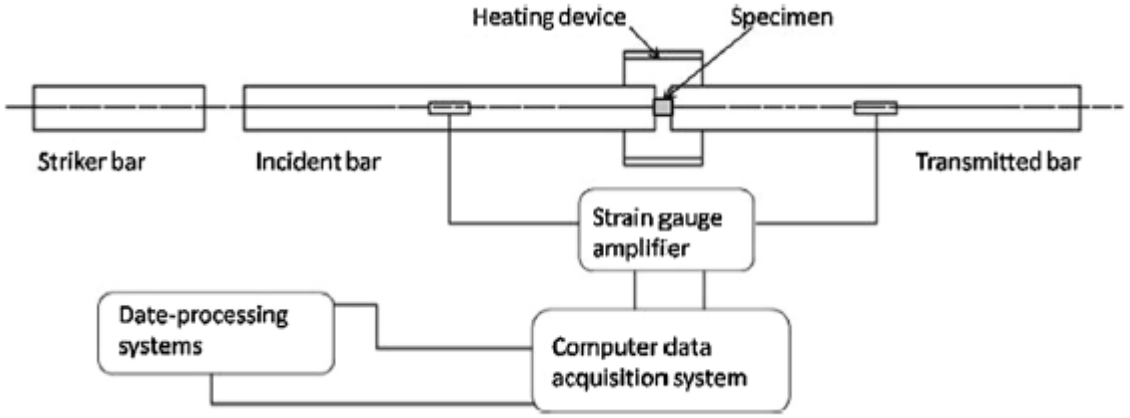

Figure 2.19 - Schematic illustration of the SHPB system [26].

The strain rate, $\dot{\varepsilon}$, the true strain, ε, and the true stress, σ, in samples tested by means of the SHPB system are calculated based on the incident, ε_i, reflected, ε_r, and transmitted, ε_t, strain pulses, as shown in the following relationships [148]:

$$\dot{\varepsilon}(t) = \frac{C_0}{l_s}[\varepsilon_i(t) - \varepsilon_r(t) - \varepsilon_t(t)] \tag{2.8}$$

$$\varepsilon(t) = \frac{C_0}{l_s}\int_0^t [\varepsilon_i(t) - \varepsilon_r(t) - \varepsilon_t(t)]\,dt \tag{2.9}$$

$$\sigma(t) = \frac{E\,a_b}{a_s}[\varepsilon_i(t) - \varepsilon_r(t) - \varepsilon_t(t)] \tag{2.10}$$

where t is the time, C_0 is the speed of sound in the bar, l_s is the length of the compression specimen, E is the Young's modulus of the bar, and a_b and a_s are the areas of the cross-section of the Hopkinson bar and the compression specimen, respectively.

In the past three decades, there has been an increasing interest in evaluating the mechanical properties under dynamic conditions in metals with extremely small grain sizes which are potential candidates for application in the aeronautical and aerospace industries [149]. Accordingly, numerous experimental techniques have being developed to acquire comprehensive data in miniature samples as well as reproduce experimental conditions similar to real ballistic impacts [143]. Among these procedures, dynamic indentation through non-deformable spherical balls, split Hopkinson pressure bars and Taylor impact tests have been widely used to evaluate the microstructural evolution and mechanical properties at dynamic strain rates in UFG metals such as titanium [26], magnesium [28] and aluminium alloys [23–25,150–152]. A very recent investigation demonstrated that currently no single dynamic testing technique may reflect the actual ballistic penetration behaviour of 7XXX series aluminium alloys. Nevertheless, it is also revealed that these methods are complementary in nature and provide direct correlation with the actual ballistic behaviour when the limitations and advantages of each procedure are considered [25].

The deformation at extremely high strain rates is generally associated with extensive twinning as well as with the formation of shear bands along the microstructure of fcc metals [153]. Microtwins are more likely to occur in metals with high stacking fault energy (SFE) whilst microbands are predominant in metals deformed at strain rates higher than $\sim 10^4$ s^{-1} [153]. Additionally, the volume fraction of twins and shear bands throughout the deformed metal increases with increasing grain sizes as experimentally observed in copper rods subjected to oblique shock loading [154].

During dynamic testing, straining occurs in a very short interval of time and thus the formation of shear bands is intrinsically adiabatic [21,22]. Nevertheless, the propagation of the these bands depends upon the strain, strain rate and temperature and may lead to intense grain refinement as well as to early failure of the deformed material [151]. Figure 2.20 [151] shows a typical shear band in the Al-Li alloy subjected to dynamic testing.

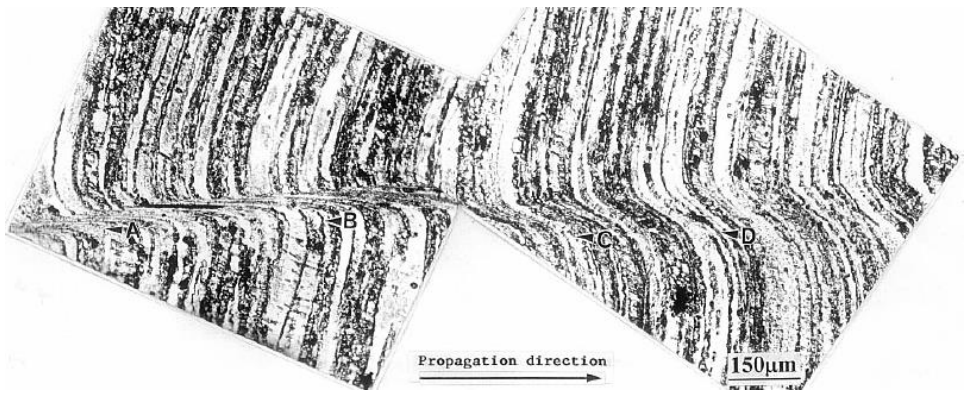

Figure 2.20 - Propagation of an adiabatic shear band in the Al-Li alloy subjected to dynamic testing using the SHPB system [151].

It is readily apparent from the optical image displayed in Figure 2.20 that a region with extremely localized strain develops during dynamic testing of the Al-Li alloy and propagates towards the shear direction. Examination of the microstructure of the Al-Li alloy through TEM revealed that significant grain refinement occurred within these localized shear bands during deformation, as depicted in Figure 2.21 [151].

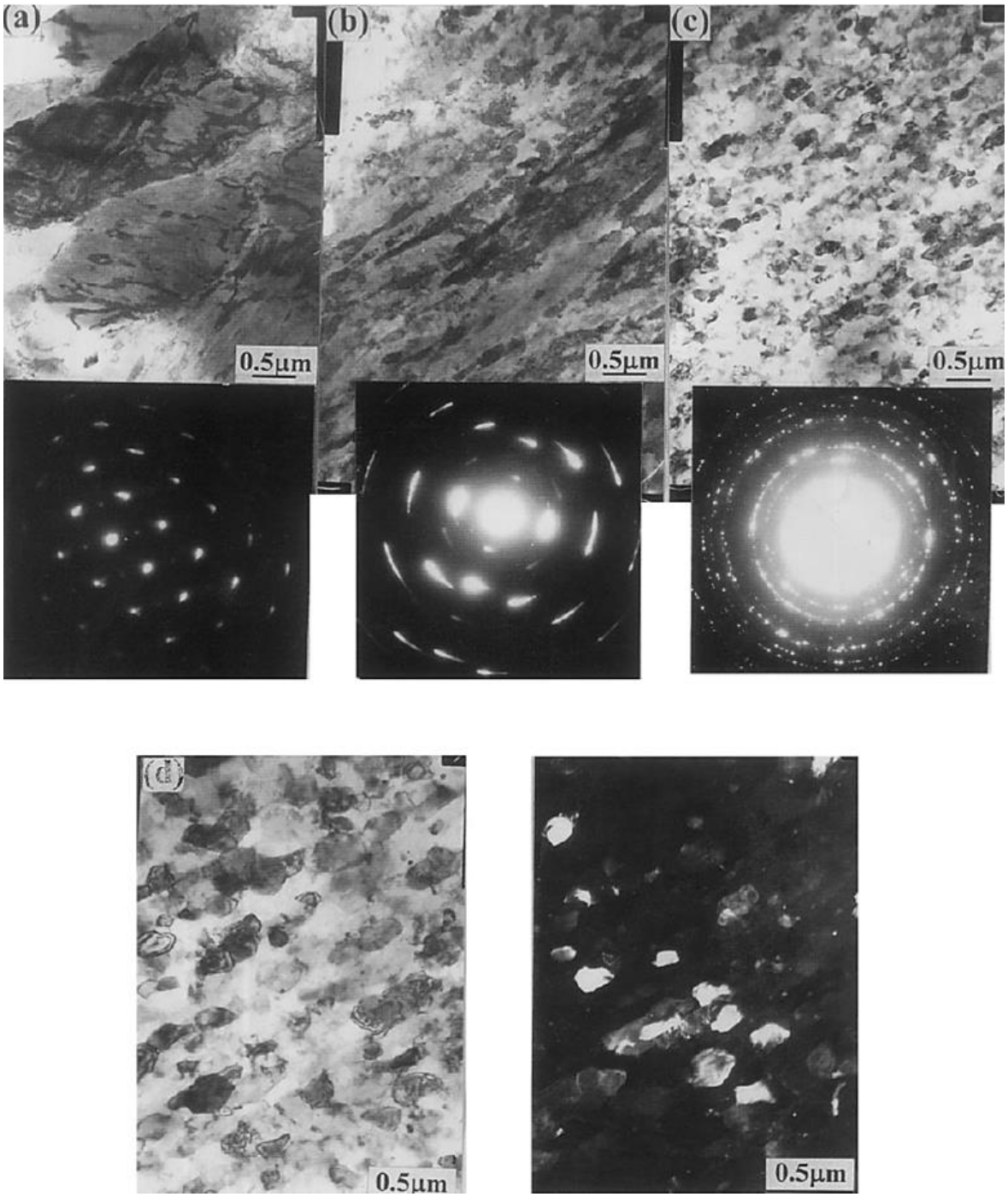

Figure 2.21 -TEM images displaying (a) the deformed structure in a region of homogeneous deformation, (b) elongated cells in a region adjacent to the shear bands and (c,d) ultrafine grains within the shear bands formed during dynamic testing of the Al-Li alloy [151].

Inspection from Figure 2.21 reveals that the interior of the shear bands was severely refined during dynamic testing such that the average grain boundary spacing after deformation was ~0.2 μm. In addition, these grain structures are nearly equiaxed and they are mostly formed by HAGBs as indicated by the well-defined ring in the SAED pattern of Figure 2.21 (c). Nonetheless, the region adjacent to the shear bands has elongated cells which did not evolve to grains with HAGBs and the region of homogeneous deformation is characterized by grains with an average size in the order of few micrometres.

Although shear banding is essentially adiabatic the temperature rise and the time in which the deformed material remains at elevated temperature in many cases is insufficient to justify the occurrence of the conventional thermally activated dynamic recrystallization during dynamic testing [21,22]. Therefore, the grain refinement within the shear bands is usually attributed to a mechanically-driven dynamic recrystallization process in which the increase of the misorientation angle, θ_{mis}, between adjacent subgrains at the regions inside the bands ultimately leads to the formation of very fine grains with HAGBs [22].

2.3 Al-Mg-Sc alloy

The increasing demand for more fuel-efficient and environmentally friendly vehicles has motivated the development of light-weight aluminium alloys especially designed for applications in the transportation industry [8,9]. Among these materials, Al-Mg alloys with Sc additions have attracted notable attention from both the academia and the industry because of their high strength to density ratio, as well as their excellent microstructural stability and superplastic properties [40,41]. Although many reports have demonstrated the superior mechanical properties of the Al-Mg-Sc alloys, the commercial applications of these alloys are still limited because of the relatively high cost of the Sc additions. Consequently, Sc-containing Al alloys are mostly used either in high performance sports equipment or in applications wherein the material cost plays a minor role in the total manufacturing and maintenance cost of the product (e.g. aircraft industry) [40].

Severe plastic deformation procedures have been successfully used to produce Al alloys with remarkably improved properties compared with conventional forming techniques, as summarized in a recent report [155]. Furthermore, many studies have been dedicated to develop UFG Al alloys suitable for manufacturing by superplastic forming and, among these metals, the Al-3Mg-0.2Sc alloy exhibited excellent superplastic properties after processing by SPD [43,156]. Accordingly, important studies concerning the microstructural aspects and mechanical properties of Al-Mg-Sc alloys are discussed in the following sections with special attention to the superplastic behaviour of these Al alloys after SPD processing.

2.3.1 Microstructural Aspects

Al-Mg based alloys have been extensively processed through SPD techniques and it was demonstrated that the presence of Mg in solid solution in these alloys leads to additional strengthening and grain refinement during SPD processing by comparison with the pure material, as the solute atoms increase the local shear stress needed for dislocation motion and also delay the recovery kinetics [11–15]. On the other hand, even though very fine structures are produced through the application of ECAP in Al-Mg alloys, the benefits on the mechanical properties attained by grain refinement are lost after recrystallization at relatively low temperatures [16–19], as depicted in Figure 2.22 [17] for the Al-3% Mg alloy subjected to 8 passes of ECAP using a die with $\phi = 120^{o}$ and the processing route A.

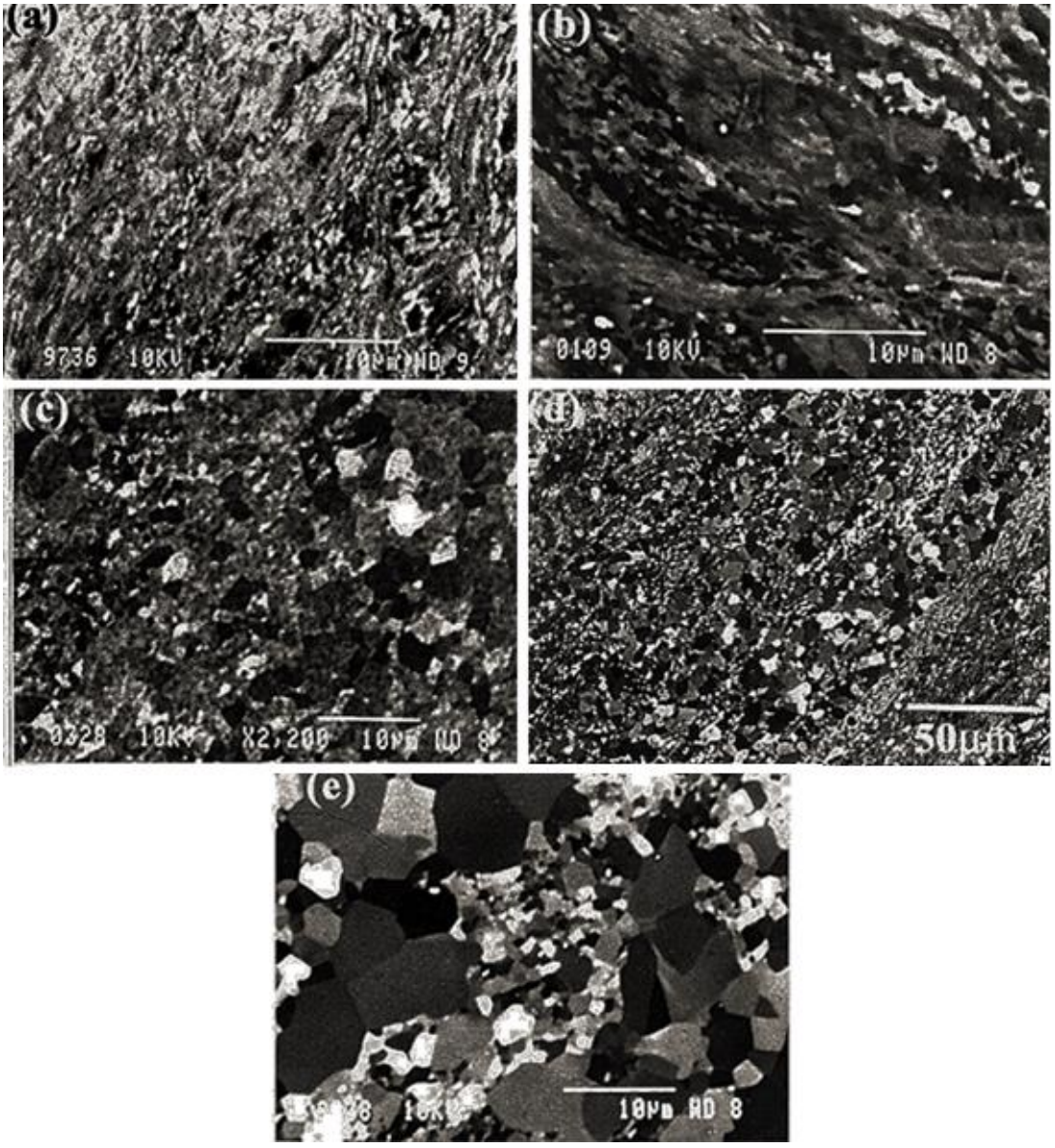

Figure 2.22 - SEM images showing the grain structures of the Al-3% Mg alloy processed by (a) ECAP and further annealed for (b) 1 h at 473 K, (c) 15 min at 523 K and (d,e) 1 h at 523 K [17].

Inspection from Figure 2.22 (a) reveals that the Al-3Mg alloy exhibits elongated grains and cell structures with width of 70-80 nm and 300-400 nm in length immediately after ECAP processing. Further TEM analysis also demonstrated that most of the grains produced using this processing route have LAGBs with $\theta_{mis} \leq 15^{o}$. After annealing at 523 K for 1 hour, it is clearly noted the inhomogeneous recrystallization of the microstructure which resulted in the formation of a duplex banded structure of recrystallized and deformed grains with grain sizes within the range of 5-10 μm and 0.5-1 μm, respectively.

Additions of scandium in Al-Mg alloys significantly enhance their microstructural stability such that Al-Mg-Sc alloys are capable of retaining ultrafine grains produced by severe plastic deformation at temperatures suitable for achieving optimum superplastic flow, as displayed in Figure 2.23 [20]. It is apparent in these plots that the grain sizes immediately after ECAP are significantly larger in pure Al by comparison with Al-3%Mg alloys both with and without Sc and Zr additions. This demonstrates the role of Mg on the reduction of the recovery rate and promotion of further grain refinement in SPD-processed Al-based alloys. Furthermore, it is clearly evident the grain stability benefits attained by the addition of Sc in an Al-3Mg alloy. Although, similar grain sizes (~200-300 nm) are achieved in both the Al-3Mg and the Al-3Mg-0.2Sc alloy after 8 passes of ECAP, significant grain coarsening is observed in the Al-3Mg alloy after annealing at $T \geq 473$ K. By contrast, the Al-3Mg-0.2Sc alloy processed by ECAP retains grains <1 μm even after annealing at $T \leq \sim 650$ K for 1 h.

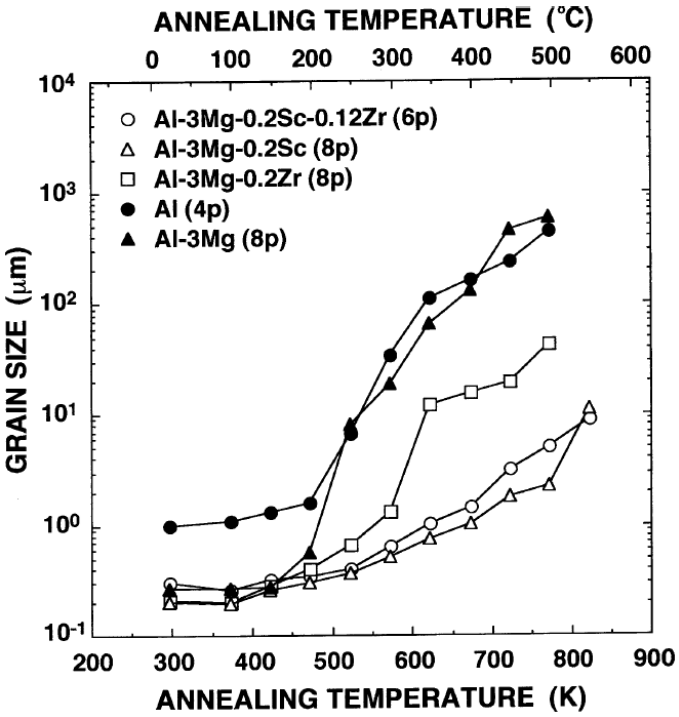

Figure 2.23 – Average grain size as a function of annealing temperature for the ECAP-processed pure Al and Al–3%Mg alloys both without and with Sc and Zr additions [20].

In order to better evaluate the reasons for the superior microstructural stability of Al alloys with Sc additions, it is important to understand which intermetallic phase is in thermodynamic equilibrium in diluted Al alloys as well as assess its precipitation kinetics and how this phase interacts with the moving grain boundaries.

Scandium in Al alloys with weight percentages (wt.%) of Sc inferior to ~0.6 % is present either in solid solution or in the form of Al_3Sc precipitates which have an ordered fcc structure with the Sc atoms associated with the vertices of the unit cell [40]. For the Al- 0.2wt.% Sc alloy, Sc atoms are completely dissolved in solid solution at equilibrium conditions for $T \geq$ ~865 K [157,158]. Conversely, incipient melting is reported for the Al-3Mg-0.2Sc alloy at temperatures slightly above 883 K and thereby the solution treatment of this metal has to be conducted with special accuracy and preferably within the range from ~878 to 883 K in order to maximize the scandium content in solid solution [43,159]. Furthermore, the cooling rate strongly influences the degree of Sc supersaturation in solution treated Al-Mg-Sc-Zr alloys. Higher cooling rates increase the amount of Sc in solid solution after heat treatment and this ultimately leads to faster precipitation kinetics and larger number density of Al_3Sc dispersoids during subsequent ageing treatment [160].

The precipitation of Al_3Sc dispersoids from the supersaturated solid solution in the Al-0.2Sc alloy may occur continuously or discontinuously depending upon the ageing temperature as demonstrated in the isothermal temperature-time-transformation, TTT, diagram of Figure 2.24 [158].

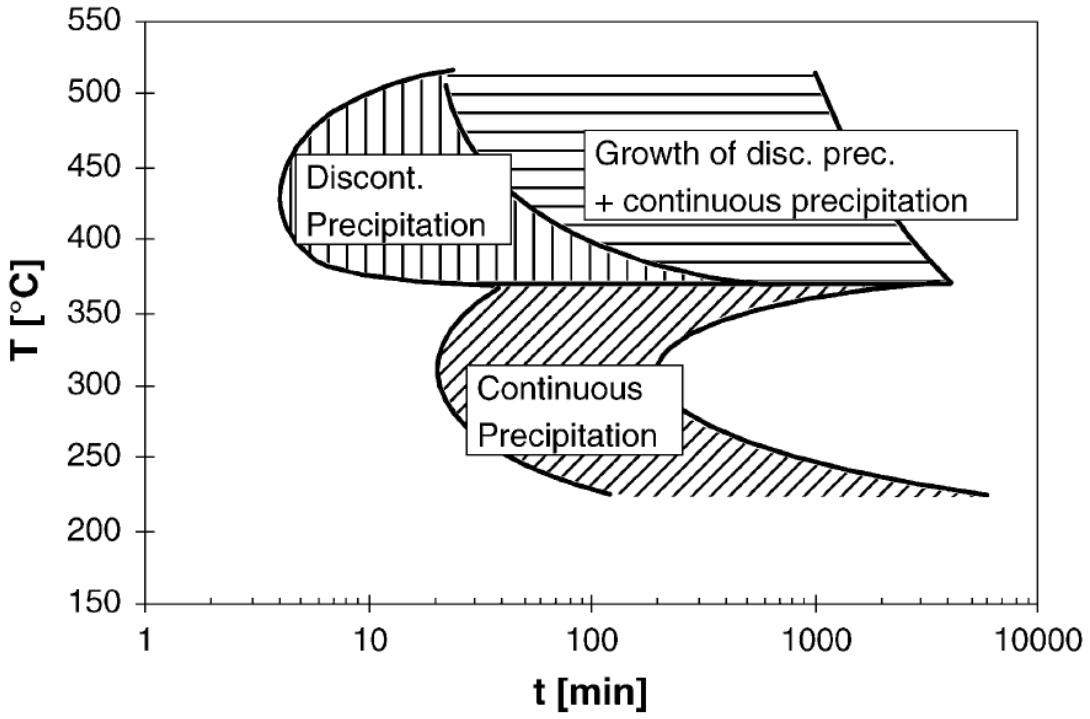

Figure 2.24 –Isothermal TTT diagram of precipitation in the Al-0.2Sc alloy after solution treatment at 873 K and further ageing [158].

It is readily apparent in Figure 2.24 that Al_3Sc dispersoids continuously precipitate in the microstructure of the Al-Sc alloy after heat treatment at T <350 °C (623 K), whereas ageing at $T \geq 370$ °C (643 K) leads to an inhomogeneous distribution of Al_3Sc phases which start precipitating after ageing times of the order of a few minutes. It also follows from the TTT diagram that the complete precipitation of Al_3Sc dispersoids may take ~3 h as in the material aged at 583 K up to more than 2 days as after ageing at 513 K. Furthermore, it is interesting to note that discontinuous precipitation is recognised as an undesired precipitation mode as produces coarser and more disperse Al_3Sc phases by comparison with continuous precipitation.

The Zener pinning pressure, P_Z, imposed on a moving grain boundary by randomly distributed precipitates is expressed as follows [161]:

$$P_Z = k_p \frac{f\gamma}{r_p} \tag{2.11}$$

where k_p is a factor associated with the shape of the dispersoids (k_p = 3/2 for spherical particles), γ is the interface energy of the pinned boundary, f is the volume fraction and r_p is the average radius of the precipitates. Although, several simplifications are assumed to derive Eq. 2.11 [161], this relationship provides relevant qualitative information about the influence of the size and volume fraction of precipitates on delaying recrystallization in polycrystalline materials. In addition, a recent investigation demonstrated that Eq. 2.11 displays good agreement with the results obtained using 3D FEM simulations [162].

Figure 2.25 shows the size and coherency of the Al_3Sc dispersoids formed in a solution treated Al- 0.25 wt.% Sc alloy during annealing for 1 h [163]. Inspection of these plots reveals that r_p < 20 nm and the precipitates are fully coherent with the Al matrix after annealing for 1 h at temperatures up to 450 °C (723 K). Furthermore, annealing at T > 723 K leads to coherency loss and significant coarsening of the precipitates, as also shown in a later study [164]. Also, precipitation of Al_3Sc particles mainly occurs prior to recrystallization in the coarse-grained Al-0.25Sc alloy and this allows an effective pinning of the moving boundaries. Nevertheless, after annealing at $T \geq 773$ K, the driving pressure for grain boundary migration overcomes the pinning pressure exerted by the dispersoids and this alloy fully recrystalizes.

Similar results were attained in an Al- 2.2at.%Mg- 0.12at.%Sc after ageing at $573 \leq T \leq 673$ K [165]. It is interesting to note that although longer heat treatment times were used in this study, the Al_3Sc precipitates continue coherent with the matrix and have average radii <20 nm even after ageing at 573 K for 1040 h or ageing at 673 K for ~9 days. In addition, a recent study using an Al-4.57Mg-0.2Sc-0.09Zr alloy showed that the Al_3Sc particles remain predominantly coherent with the matrix even after 8 ECAP passes at $T \geq 573$ K [166].

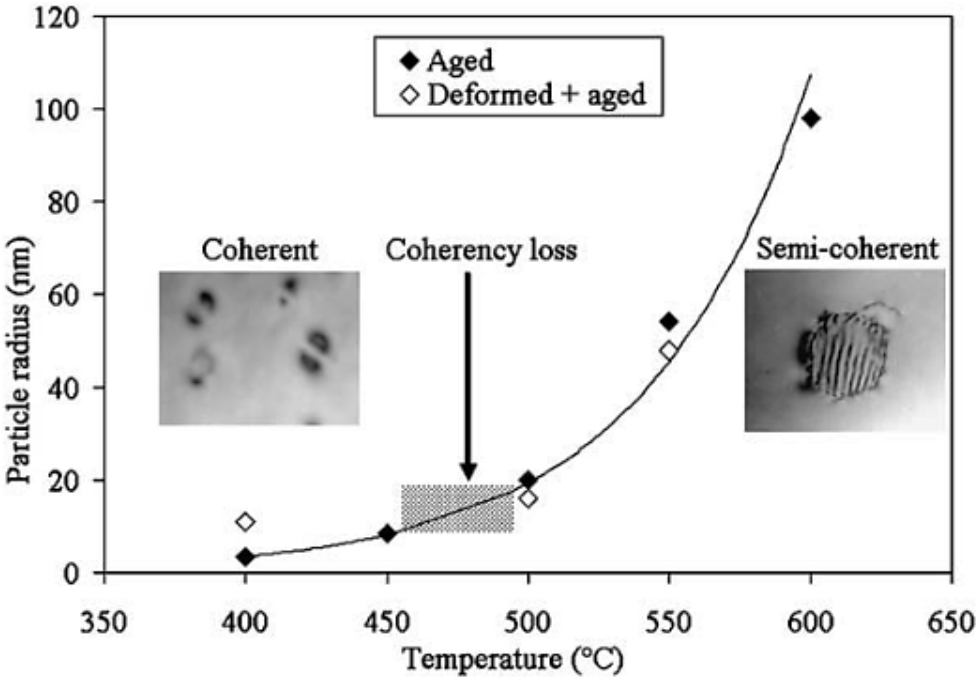

Figure 2.25 –Evolution of the size of the Al_3Sc dispersoids in an Al- 0.25 wt.% Sc alloy during annealing for 1 h [163].

The influence of pressing temperature on the microstructural evolution of Al-Mg-Sc alloys processed by ECAP was already examined in a number of studies [47,86,167–169] which demonstrated that the grain size after ECAP processing increases with increasing pressing temperatures. Also, finer grain structures were obtained processing Al-Mg-Sc alloys at high temperatures compared with Al-Mg alloys with similar Mg content [86]. Additionally, processing an Al-6Mg-0.3Sc alloy through ECAP at 573 K resulted in the development of a bimodal grain structure, as displayed in Figure 2.26 [169].

It is apparent in Figure 2.26 that processing an Al-6Mg-0.3Sc alloy by ECAP at 573 K leads to the formation of a very inhomogeneous grain distribution after 4 to 12 passes such that the grain sizes of the deformed and recrystallized regions were estimated as ~1 and ~8 μm, respectively. The onset of a bimodal structure is attributed to the combined effect of strain localizations during ECAP that increase the thermodynamic potential for recrystallization in highly deformed structures and the presence of Al_3Sc precipitates which hinder the grain boundary motion and act preventing recrystallization in regions with relatively lower density of dislocations [169].

By contrast, a recent investigation revealed that the area fraction of grains with ~1 μm is nearly 90% after processing an Al-5Mg-0.2Sc-0.08Zr alloy through 10 passes of ECAP at ~600 K [47]. Accordingly, the superior microstructural homogeneity achieved in the Al-5Mg-0.2Sc-0.08Zr alloy after ECAP is associated with the selection of a more efficient processing route (route Bc) as well as with the presence of fewer Mg solutes in this alloy.

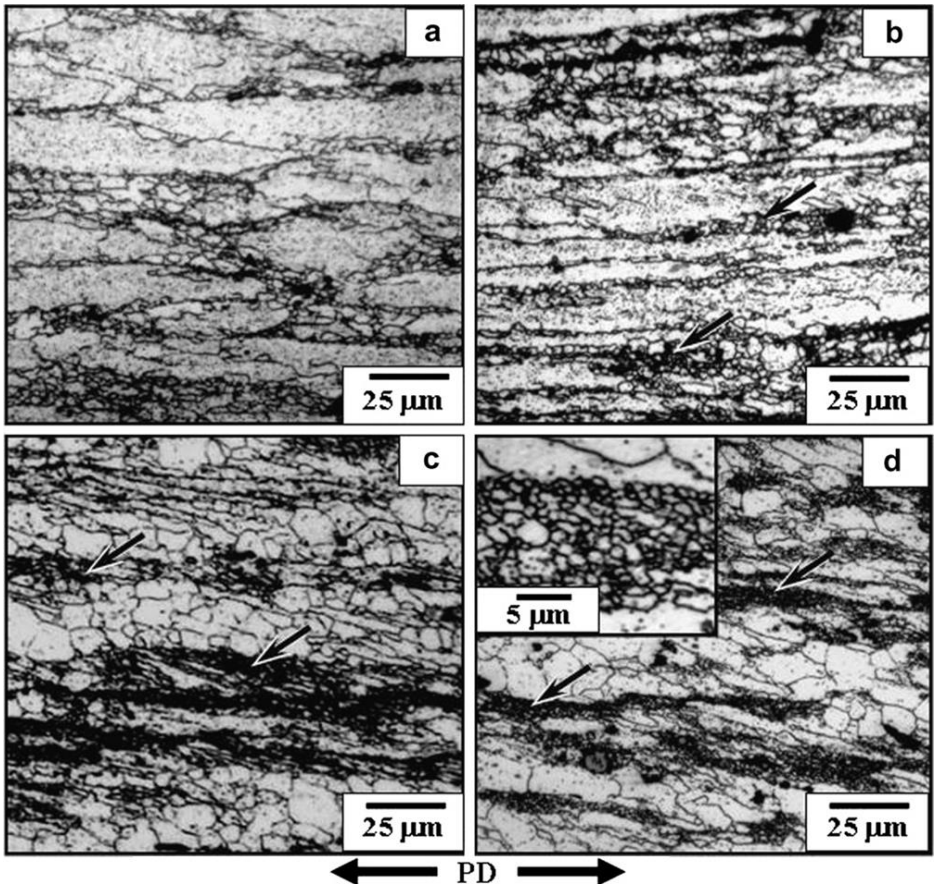

Figure 2.26 - Optical micrographs revealing the microstructure of an Al-6Mg- 0.3Sc alloy (a) before and after (b) 1, (c) 4 and (d) 12 ECAP passes at 573 K [169].

The microstructural evolution of Al-Mg-Sc alloys was already investigated after HPT using processing temperatures ranging from ~300 to 673 K [48,50,51]. It was demonstrated that processing Al-Mg-Sc alloys through HPT at room temperature leads to the formation of grain structures with mainly HAGBs and grain sizes within the range of 100-220 nm [48,50,51] which are smaller than the grains obtained after ECAP processing using the same initial temperature [20,43,156]. Furthermore, HPT processing of Al-Mg-Sc alloys at 473 K also results in the development of ultrafine grains with average sizes varying from ~150 to 350 nm [50,51].

A very recent study successfully examined the segregation and precipitation phenomena in the Al-5.7%Mg-0.32%Sc alloy processed by high-pressure torsion either at room temperature or at 473 K [51]. The HPT disc had a diameter of 20 mm and 2 mm in thickness. The processing was performed using a nominal pressure of 6 GPa and a rotation rate of 1 rpm. The results revealed that after HPT at RT part of the Mg originally in the Al-Mg solid solution segregates at the grain boundaries and triple junctions in the form of Mg-rich clusters. These segregations have diverse shapes and their size or thickness varies within the range of ~5-20 nm, as shown in the dark zones of the Scanning Transmission Electron Microscopy (STEM) images depicted in Figure 2.27 [51].

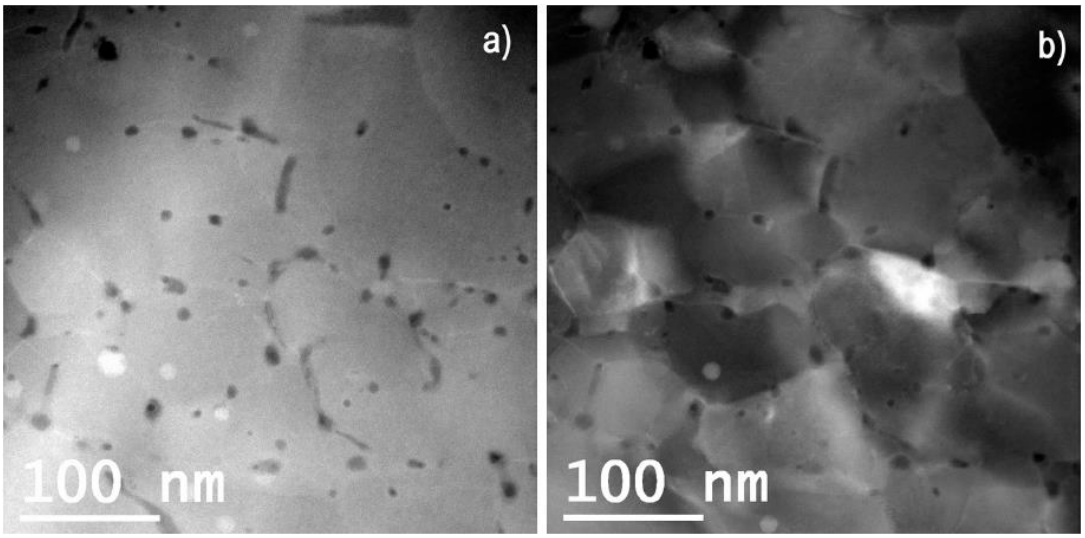

Figure 2.27 - STEM images with enhanced (a) atomic number and (b) diffraction contrast of the Al-Mg-Sc alloy processed by HPT at room temperature [51].

Processing the Al-5.7%Mg-0.32%Sc-0.4%Mn alloy through HPT at 473 K also leads to the segregation of Mg solutes along the grain boundaries and triple junctions. Nevertheless, the Al_3Mg_2 phase was not detected in the microstructure of this Al alloy even after processing at a high temperature [51]. In the same investigation, the Al-Mg-Sc alloy processed by HPT at room temperature was subsequently annealed for 2 h at 653 K, water-quenched and further annealed at 448 K for 15 days. After this sequence of heat treatments, the grain size increased to ~1-2 μm and Al_3Mg_2 phases developed along the grain boundaries of the HPT-processed material.

Similar Mg segregates were also found in the Al-Zn-Mg-Cu alloy processed by ECAP and it was demonstrated that the area fraction of these segregates increases with increasing number of ECAP passes [170]. Further analysis also indicated that these Mg segregates may hinder extrinsic dislocations emitted from grain boundaries in nanostructured Al-Mg-Sc alloys and thereby the presence of these Mg enriched regions provides additional strengthening in this Al alloy during plastic straining at low temperatures [34,171,172].

2.3.2 Mechanical Properties and Superplasticity

After SPD processing, Al-Mg-Sc alloys exhibit enhanced mechanical strength as a consequence of the increase in the density of dislocations, the intense grain refinement and also the influence of other relevant strengthening mechanisms such as solid solution and precipitation strengthening. Different models have been developed to calculate the effect of each strengthening mechanism on the yield stress and strain hardening behaviour of Al-Mg-Sc alloys after cold working, although the relative contribution of each of these mechanisms continues a matter of debate [35,173–175].

A recent investigation describing the application of friction stir processing, FSP, in an Al-Mg-Sc alloy demonstrated that ultrafine grains with mean grain sizes within the range of 0.39-0.63 μm were obtained through processing using this technique [35]. In addition, an evaluation of the additivity of the different strengthening mechanisms acting in this Al alloy was performed after microstructural characterization before and immediately after FSP. Although the predictions of the σ_y in the coarse-grained Al-Mg-Sc alloy were reasonably accurate, the linear additivity rule resulted into calculated values for the yield stress higher than the values obtained experimentally. It was proposed that the reason for this apparent discrepancy relies on the model assumption that the relative contribution of the grain boundary strengthening may be well predicted using a single value for the constant of yielding in the Hall-Petch relationship.

Different studies assessed the effect of ECAP processing on the mechanical strength and fatigue properties of Al-Mg-Sc alloys with 1.5 to 6% of Mg (% in weight) [176,177]. The results of these investigations revealed an either modest [177] or significant [176] enhancement of the fatigue properties in ECAP-processed Al-Mg-Sc alloys by comparison with the coarse-grained material subjected to conventional metal-working procedures. Nevertheless, an exceptional yield stress was recently documented for an Al-Mg-Sc alloy after processing through 20 turns of HPT at ambient temperature, as shown in Figure 2.28 [34].

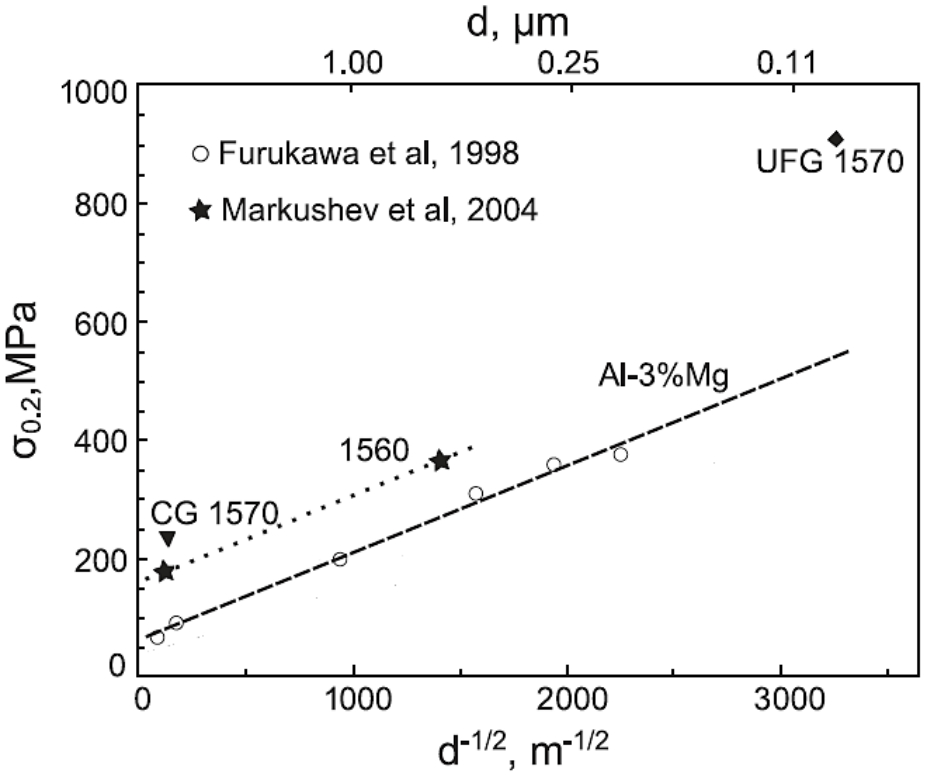

Figure 2.28 - The relationship between the yield stress and the grain size in the Al alloys: Al-3% Mg [178], Al1560 [179] and Al1570 [34].

It is apparent in Figure 2.28 that after high-pressure torsion the average grain size of the Al1570 alloy is < 100 nm and σ_y > 900 MPa. Furthermore, it is worth noting that according to this plot the yield stress of the HPT-processed Al1570 alloy even exceeds the predictions based on calculations using the Hall-Petch equation (Eq. 2.1) considering k_y obtained from experiments with the Al-3Mg alloy [178] and the Al1560 alloy [179] processed by ECAP. The extremely high strength obtained in this Al alloy is attributed to the additional strengthening provided by the grain refinement and the Mg segregation at grain boundaries during HPT which may difficult the emission and mobility of extrinsic dislocations [34].

There are numerous reports in the literature dealing with the processing of Al-Mg-Sc alloys through different metal-working procedures aiming the achievement of superior superplastic properties [43–46,48,49,53,73,156,159,180–187]. Systematic investigations about the influence of ECAP processing on the superplastic flow of an Al-3Mg-0.2Sc alloy revealed the optimum processing conditions which lead to higher elongations after tensile testing at elevated temperatures [43,156]. Accordingly, the highest elongations to date in Al-Mg-Sc alloys subjected to ECAP at RT were achieved after processing an Al-3Mg-0.2Sc alloy through 8 passes of ECAP using a die with ϕ = 90º and route B_c [43,156]. Furthermore, the influence of the tensile testing temperature and strain-rate on both the elongation and the flow stress in an Al-3Mg-0.2Sc alloy cold-rolled or processed by ECAP were also detailed examined, as depicted in Figures 2.29 and 2.30 [43], respectively.

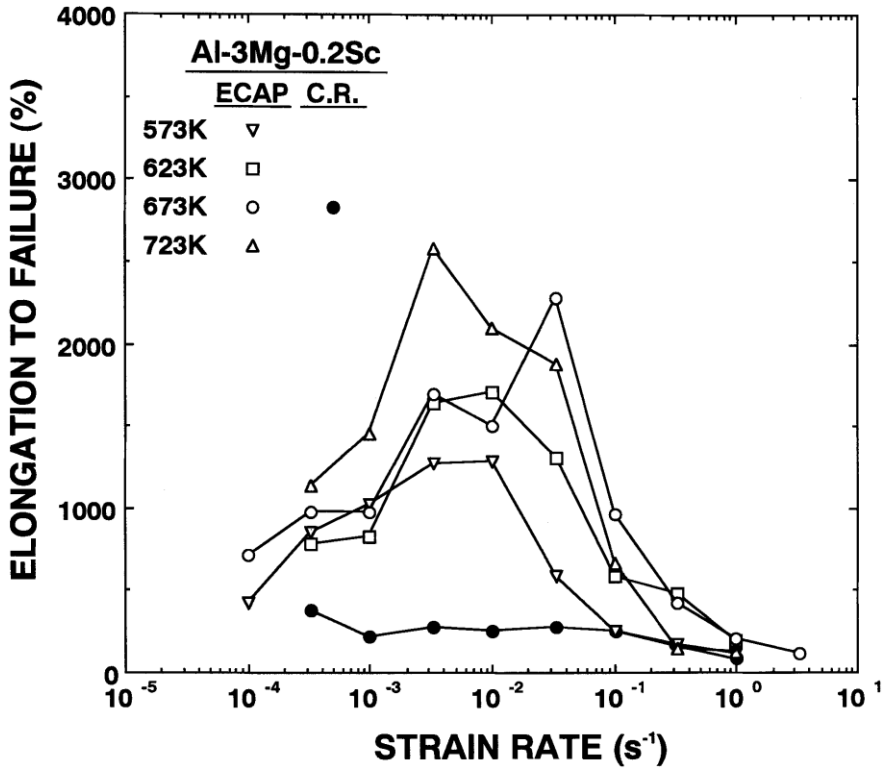

Figure 2.29 - The variation of the elongation to failure with strain rate for an Al-3Mg-0.2Sc alloy either processed by cold rolling (C.R.) or ECAP processing [43].

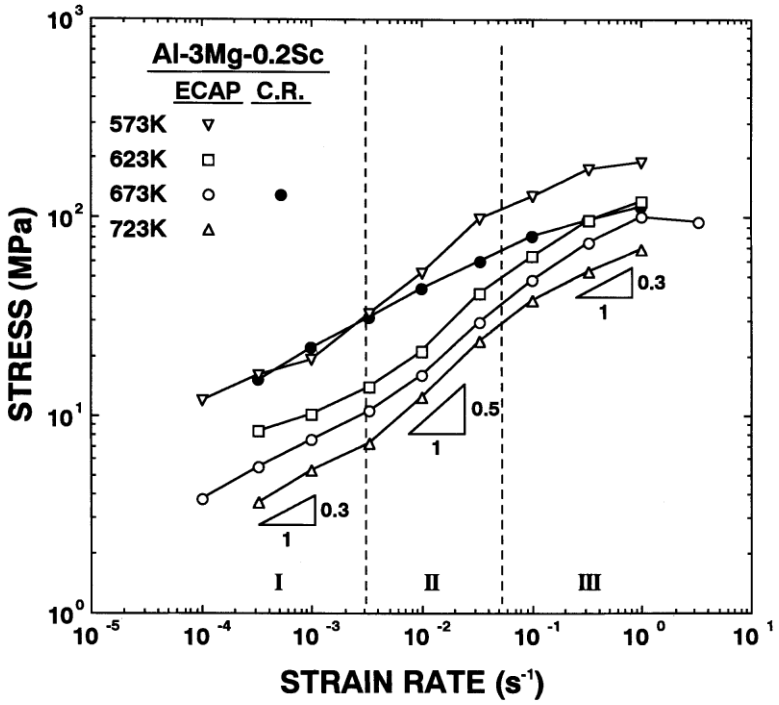

Figure 2.30 - The variation of the maximum flow stress with strain rate for an Al-3Mg-0.2Sc alloy either processed by cold rolling (C.R.) or ECAP processing [43].

As depicted in Figure 2.29, extremely high elongations were attained in the Al-3Mg-0.2Sc alloy after tensile testing, especially at strain rates from ~10^{-3} to 10^{-1} s^{-1} and at 673-723 K in which the ECAP-processed material attained elongations of >2000 %.

Figures 2.29 and 2.30 also display a clear correlation among the ductility of the ECAP-processed alloy and the slopes of the plots of flow stress vs strain rate. For superplastic metals, these curves usually have a sigmoidal shape and may be divided into three distinct regions. There is an intermediate region II associated with high elongations. Based on Eq. 2.2, having no change on the grain size during straining, this slope corresponds to the strain rate sensitivity, m (= $[\partial \log \sigma / \partial \log \dot{\varepsilon}]_T$), and m values of ~0.5 are associated with the occurrence of superplastic flow [38]. Nevertheless, transitions to regions I and III at low and high strain rates, respectively, lead to reduction in the elongations achieved during testing which may be associated with the occurrence of different deformation mechanisms other than GBS.

Additionally, it is readily noted the absence of superplasticity in the cold rolled Al-Mg-Sc samples as indicated by the very low elongations and the slope of ~0.3 at intermediate strain rates. Therefore, these remarkable results [43] conjugated with the experimental results obtained in a practical investigation of the superplastic forming in the same material under industrial conditions [73] confirmed the achievement of high strain rate superplasticity (HSRS) [188] in an Al-3Mg-0.2Sc alloy processed by ECAP at RT and it arises the opportunity of producing complex products in the superplastic forming industry at higher production rates using this SPD procedure as an intermediate manufacturing stage.

In addition to the investigations concerning the superplastic flow in Al-Mg-Sc alloys processed by ECAP at RT, numerous studies were conducted processing Al-Mg-Sc alloys using several other metal forming techniques aiming the achievement of better superplastic ductility through microstructural refinement [45,46,48,49,53,181–187,189]. Table 2.1 shows the grain sizes obtained in Al-Mg-Sc alloys after the application of cold rolling, forging, ECAP, HPT and friction stir processing. Furthermore, it is also depicted the testing temperature and strain rate wherein the highest elongation was achieved in each selected study.

It is apparent from Table 2.1 that although very high elongations were obtained after tensile testing in Al-Mg-Sc alloys subjected to conventional metal-working procedures, the strain rates in these tests were lower by comparison with the values reported for the SPD-processed material at optimum superplastic conditions. In addition, the temperature in which the highest elongations were experimentally found is generally lower for the experiments conducted using Al-Mg-Sc alloys processed through SPD procedures.

An Al-3Mg-0.2Sc alloy was subjected to 8 passes of ECAP at RT using routes A or B_c and higher maximum elongations were achieved by in the material processed through route B_c (~2580 %) [43,156]. As discussed based on SAED patterns obtained in TEM examinations [43], the lower ductility at superplastic conditions after ECAP using route A resulted from the relatively lower fraction of HAGBs compared with the Al alloy processed using route B_c.

An Al1570 alloy was processed by ECAP at 598 K using a conventional ECAP facility with an L-shaped channel with a circular cross-section [183]. After 16 ECAP passes, tensile specimens were machined from the processed billets and tested at 723 K and at 5.6×10^{-2} s^{-1} such that very high elongations to failure (~2000 %) were attained after plastic deformation.

It follows from Table 2.1 that an elongation of ~4100% was obtained after processing an Al-5Mg-0.18Mn-0.2Sc-0.08Zr alloy by ECAP at 598 K (~0.64 T_m) [45]. It is interesting to note that this study was conducted using an ECAP die with a channel angle of 90^o and a rectangular cross-section (150 × 30 mm). Furthermore, the elongation to failure of ~4100 % corresponds to the highest elongation reported to date in all aluminium alloys.

The world record elongation of aluminium alloys (~4100 %) was attributed to the presence of ultrafine, stable and homogeneously distributed grains in the microstructure of the Al-5Mg-0.2Sc-0.08Zr alloy processed by ECAP at 598 K which also displayed an elevated fraction of high-angle grain boundaries (HAGBs ≈ 87 %) immediately after severe plastic deformation, as measured using EBSD analysis. Additionally, the almost absence of coarse phases after ECAP processing at an elevated temperature is believed to contribute to inhibit cavitation in the Al-Mn-Mg-Sc-Zr specimens during tensile testing.

Table 2.1 - Reports of superplasticity in Al-Mg-Sc alloys.

Alloy or composition (wt.%)	Metal-working procedure	Grain size (μm)	Superplasticity			Reference
			Testing temperature (K)	Strain rate (s^{-1})	Maximum elongation (%)	
Al-5.76Mg-0.32Sc-0.3Mn	Cold rolling + annealing at 748 K for 45 min	~1	748	1.4×10^{-2}	1130	Nieh et al. (1998) [181]
Al-6.1Mg-0.3Mn-0.25Sc-0.1Zr	Cold-rolling + annealing at 573 K for 1 h	~2.5	798	5.0×10^{-3}	3250	Cao et al. (2015) [186]
Al-5.5Mg-2.2Li-0.2Sc-0.12Zr-	ECAP: $\phi = 90^{o}$, 643K, 12 passes, route B_c	~0.3-0.4	673	1.0×10^{-1}	1500	Islamgaliev et al. (2003) [182]
Al-3Mg-0.2Sc	ECAP: $\phi = 90^{o}$, RT, 8 passes, route A	---	673	3.3×10^{-2}	1170	Komura et al. (2001) [156]
Al-3Mg-0.2Sc	ECAP: $\phi = 90^{o}$, RT, 8 passes, route B_c	~0.2	723	3.3×10^{-3}	2580	Komura et al. (2001) [43]
Al-5.8Mg-0.3Mn-0.32Sc-0.2Si-0.1Fe	ECAP: $\phi = 90^{o}$, 598 K 16 passes, route B_c	~1[a]	723	5.6×10^{-2}	2000	Musin et al. (2004) [183]
Al-5Mg-0.18Mn-0.2Sc-0.08Zr-	ECAP: $\phi = 90^{o}$, 598 K 10 passes, route B_{cz} [b]	~1	723	5.6×10^{-2}	4100	Avtokratova et al. (2012) [45]
Al-5.8Mg-0.4Mn-0.32Sc-0.1Zr	ECAP: $\phi = 90^{o}$, 598 K 8 passes, route B_{cz} [b] + warm rolling at 598 K	~1	723	1.4×10^{-1}	2330	Avtokratova et al. (2015) [189]
Al-6.1Mg-0.3Mn-0.25Sc-0.1Zr	Free Forging	~3.7	748	1.0×10^{-3}	1590	Duan et al. (2015) [187]
Al-5.3Mg-0.49Mn-0.23Sc-0.14Fe-0.06Zr	Friction stir processing	~2.2	748	1.0×10^{-1}	1500	Liu et al. (2012) [185]
Al-3Mg-0.2Sc	HPT: 6 GPa, 5 turns, RT	~0.15	673	3.3×10^{-2}	500	Sakai et al. (2005) [48]
Al-3Mg-0.2Sc	HPT (bulk sample): 1 GPa, 2 turns, RT	~0.13	573	3.3×10^{-3}	1600	Horita and Langdon (2008) [49]
Al-3Mg-0.2Sc	HPT (ring sample): 1.25 GPa, 1 turn, RT	~0.22	573	3.3×10^{-3}	1510	Harai et al. (2009) [53]

[a] Grain size measured after annealing at 443 K for 4 h.

[b] ECAP was conducted using plate samples.

Inspection of Table 2.1 reveals that, in general, superior elongations are attained in Al-Mg-Sc alloys processed by ECAP at warm-to-hot conditions. The Al-3Mg-0.2Sc alloy processed by ECAP at RT has an average grain size of ~0.2 μm immediately after processing and achieves an elongation of ~2580% after tensile testing at 723 K at 3.3×10^{-3} s^{-1} [43]. By contrast, the Al-5Mg-0.2Sc-0.08Zr alloy has a mean grain size of ~1 μm after ECAP at 598 K, however, this materials exhibits enhanced superplastic properties with an elongation of ~4100% after testing at 5.6×10^{-2} s^{-1} at 723 K [45]. These apparent contradictory results may be justified by a larger proportion of high-angle grain boundaries as well as an improved microstructural stability in the material processed by ECAP at 598 K.

It is also clearly noted in Table 2.1 that the overall elongations to failure achieved after ECAP are significantly higher than the elongations obtained after different variations of HPT processing at room temperature, even though smaller grain sizes are attained immediately after high pressure torsion. Although these differences are usually attributed to the comparatively lower cross-sectional areas of the HPT specimens [48,49,53], no information is provided about the grain sizes after the annealing of HPT samples at the tensile testing temperatures and more factors may contribute to reduce the ductility of the HPT processed Al-Mg-Sc alloy at superplastic conditions. In addition, there is no available data on the literature concerning the range of temperatures and strain-rates in which GBS accommodated by intragranular slip is the main deformation mechanism in Al-Mg-Sc alloys processed by HPT.

The apparent contradictory results obtained after processing Al-Mg-Sc alloys using ECAP and HPT motivate more investigations dedicated to provide a better understanding of the significance of stored energy during plastic deformation as well as the influence of the dimensions of the tensile specimens on the superplastic behaviour and mechanical properties after severe plastic deformation.

Chapter 3 Experimental Material and Procedures

3.1 Material and Solution Treatment

An Al-3% Mg-0.2% Sc (in wt. %) alloy was used in the current study. This material was supplied by China Rare Metal Material Corporation (Jiangxi Province, China) in the form of forged bars having lengths of ~130 mm and diameters of ~10 mm.

Solution treatment was conducted in the as-received Al-3Mg-0.2Sc alloy using similar conditions as in other investigations with the same material [43,159]. Accordingly, the Al-Mg-Sc bars were heat treated at 880 ± 2 K for 1 h and then quenched in water in order to develop a uniform distribution of grains and maximize the scandium content in solid solution.

3.2 SPD Processing

3.2.1 ECAP Processing

Billets with lengths of ~65 mm were cut from the solution treated bars, lubricated with MoS_2 and then processed through either 8 passes of ECAP at room temperature (~300 K) or 10 passes of ECAP at 600 ± 5 K using route B_c wherein each billet is rotated by 90° in the same sense between passes [88]. The ECAP procedure was conducted using a pressing speed of ~2 mm s^{-1} and a solid die having an internal channel angle of 90° and an outer arc of curvature of ~20°. These angles introduce an equivalent strain of ~1 on each ECAP pass [81].

3.2.2 HPT Processing

Discs with ~1 mm thickness were cut from the solution treated bars and then ground down to ~0.82 mm using abrasive papers. Afterwards, they were processed by HPT under quasi-constrained conditions [112] either at ambient temperature (~300 K) or 450 ± 5 K. The temperature of 450 K was attained by incorporating a heating element around the anvils and this parameter was measured and controlled using a thermocouple placed within the upper anvil at a position of ~10 mm from the work-piece as described in earlier studies [59,60,190]. Initially, in the compression stage of HPT [110], the discs were compressed within the anvils under a nominal pressure of 6 GPa and then held at the HPT facility for ~1 and ~10 min for the procedures conducted at ~300 and ~450 K, respectively. Thereafter, the lower anvil was rotated at a constant rate of 1 rpm for a total of 0.5, 1, 2, 5, 10, 20, 30, 60 and 100 turns to examine the microstructural evolution of the Al-3Mg-0.2Sc alloy. Additionally, some discs were only compressed within the HPT anvils using P_{nom} = 6 GPa.

3.3 Post-SPD Annealing

Following ECAP processing, billets of the Al-3Mg-0.2Sc alloy subjected to 8 ECAP passes at ~300 K or to 10 passes at ~600 K were cut into discs with thicknesses of ~1 mm. Thereafter, these samples were annealed at temperatures ranging from 423 to 773 K for 1 h and then cooled in air. The same annealing procedure was also performed in the Al alloy processed through 10 turns of HPT at different temperatures.

Additionally, billets of the Al-3Mg-0.2Sc alloy processed by 8 passes of ECAP at ambient temperature were also annealed for ~10 min at either 523 or 673 K and then air cooled.

3.4 Mechanical Testing

3.4.1 Dynamic Testing using the Split Hopkinson Pressure Bar

Cylindrical samples with lengths of ~5 mm and diameters of ~5 mm were machined from both the solution treated and the ECAP-processed material such that their longitudinal axes lay along the pressing direction. These specimens were tested dynamically at temperatures from ~298 to 673 K using a strain rate of 4.0×10^3 s^{-1} in a SHPB facility through the same procedure described earlier [26]. Prior to dynamic testing, the compression samples were heated in a tubular furnace and held at the required temperature for ~10 min. Furthermore, all dynamic testing was performed on at least two different samples under the same experimental condition to ensure data reproducibility.

The strain rate, $\dot{\varepsilon}$, strain, ε, and stress, σ, during dynamic testing were initially calculated based on the incident, reflected and transmitted strain pulses using the relationships presented in Eqs. 2.8, 2.9 and 2.10, respectively [148]. Thereafter, as dynamic testing using the SHPB is adiabatic, the temperature rise, ΔT, during plastic straining was calculated using Eq. 2.6 with $\rho_w = 2.7 \times 10^3$ kg m^{-3} and $c_w = 9 \times 10^3$ J kg^{-1} K^{-1} [191] and the isothermal true stress, σ_{iso}, henceforth denoted the true stress was estimated using the following relationship [24]

$$\sigma_{iso}(t) = \sigma(t) - \frac{\partial \sigma}{\partial T} \Delta T(t) \tag{3.1}$$

where $\partial\sigma/\partial T$ is calculated based on the experimental data obtained in the current study for the solution treated and the ECAP-processed Al-3Mg-0.2Sc alloy.

3.4.2 Microhardness Measurements

Billets of the Al-3Mg-0.2Sc alloy subjected to 8 passes of ECAP at ~300 K were cut along their transversal (plane X) and longitudinal (plane Y) directions. These samples were ground using abrasive papers and polished using 1 μm diamond paste and 0.06 μm silica colloidal to obtain mirror-like surfaces along the ECAP planes X and Y. Thereafter, microhardness measurements were taken along these planes using an FM300 microhardness tester equipped with a Vickers indenter under a load of 200 gf and a dwell time of 15 s, as schematically depicted in Figure 3.1 [192].

The hardness measurements in plane Y were recorded along longitudinal lines at positions corresponding to vertical distances of 0.5, 1.0, 2.0, 3.0, 4.0, 5.0, 6.0, 7.0, 8.0, 9.0 and 9.5 mm to the upper surface. These measurements were recorded parallel to the pressing direction at equal intervals of 1 mm covering a total distance of 40 mm from the rear to the front of each ECAP billet. For the plane X, hardness values were recorded over the surface of the sample following a rectilinear grid pattern with a spacing of 0.3 mm between each separate indentation. The same procedure was used to measure the hardness values along the plane X in the Al-3Mg-0.2Sc alloy processed through 10 passes of ECAP at ~600 K.

Following HPT processing at different temperatures, discs were ground and polished using the same procedure described for the ECAP-processed samples. Afterwards, the microhardness distribution in the mid-section parallel to the upper and lower surfaces of each disc was recorded at the positions displayed in Figure 3.2 [126].

Values of the Vickers microhardness were recorded using the same conditions described for the metal processed by ECAP. The circles in Figure 3.2 display the positions in which the Vickers microhardness was evaluated along the diameter of the samples. The hardness values at these positions were calculated as the average of the values obtained from four indentations separated by a distance of 0.15 mm from these selected points. In addition, hardness measurements over the entire disc surfaces were taken following a rectilinear grid pattern with indentations separated by 0.3 mm.

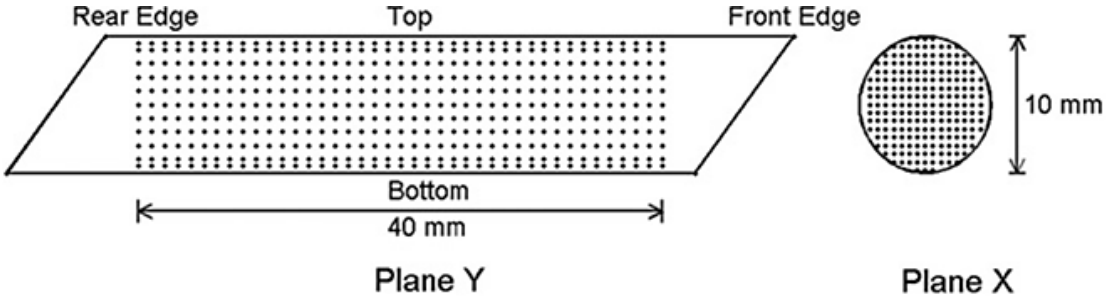

Figure 3.1 - Schematic illustration of the positions of the hardness measurements in the ECAP-processed material on the longitudinal plane Y and the cross-sectional plane X [192].

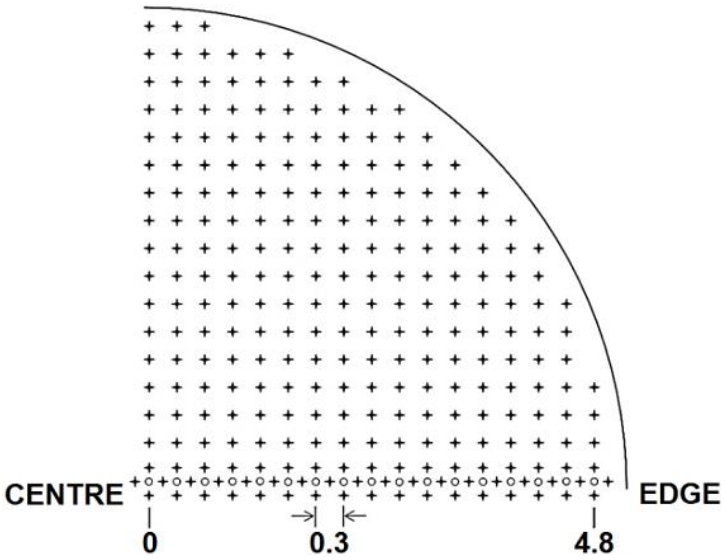

Figure 3.2 - One-quarter of an HPT disc displaying the positions of the hardness measurements along (∘) the diameter and (+) the surface of the discs [126].

The distribution of the Vickers microhardness was also recorded along the diameter of discs processed by 10 turns of HPT as well as through the Z direction on the longitudinal plane Y of ECAP-processed billets after annealing for 1 h at temperatures from 423 to 773 K. Furthermore, the average microhardness of the post-SPD annealed Al-3Mg-0.2Sc alloy was estimated using the hardness measurements recorded along the diameters of the samples. It is important to note that, for the material processed by HPT, the hardness values near the edges of the sample are associated with larger surface areas and therefore an area-weighted average microhardness was considered for these discs.

3.4.3 Tensile Testing

For mechanical testing, tensile specimens were machined from the solution treated bars as well as from the billets of the Al-3Mg-0.2Sc processed by 8 passes of ECAP at room temperature and 10 ECAP passes at ~600 K, as detailed depicted in Figure 3.3. Discs with thicknesses of ~1.0 mm were cut from these billets and ground using abrasive papers to thicknesses of ~0.8 mm. Two specimens were machined from each disc using electrical discharge machining and then further polished to obtain mirror-like surfaces and thicknesses of ~0.6 mm. Thereafter, these work-pieces were pulled to failure using a Zwick Z030 testing machine operating at a constant rate of cross-head displacement. Tests were conducted in both the solution treated and the Al alloy processed by ECAP at testing temperatures ranging from 298 to 773 K using initial strain rates from 3.3×10^{-4} to 3.3×10^{-1} s^{-1}. All samples were held at the required temperature for ~10 min prior to application of the load and the temperatures were held constant to within ±2 K during testing.

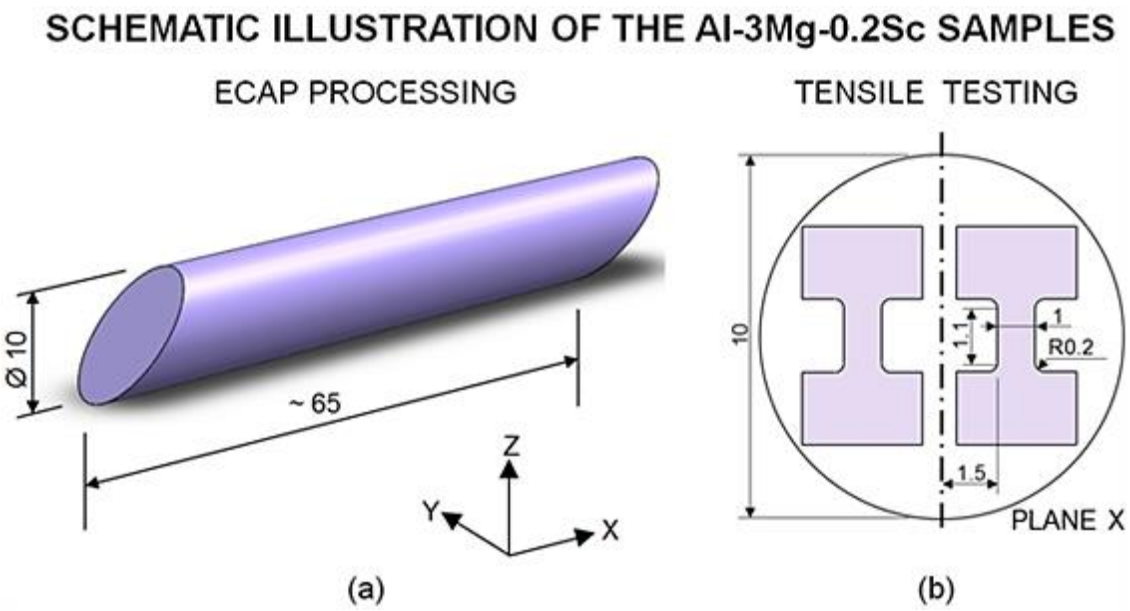

Figure 3.3 - Schematic illustration of the samples used during (a) ECAP processing and (b) tensile testing (unit: mm).

After HPT processing, the surfaces of the discs became curved as a consequence of the elastic distortion of the HPT anvils [110]. Accordingly, the upper and lower surfaces of the HPT-processed samples were ground and polished to a thickness of ~0.60 mm to remove any surface irregularities. Afterwards, tensile specimens with the same geometry displayed in Figure 3.3 were cut from the HPT-processed discs and further pulled to failure at temperatures from 473 to 723 K and at strain rates from 3.3×10^{-4} to 1 s^{-1}. Similarly to the ECAP-processed samples, the HPT specimens were held at the testing temperature for ~10 minutes prior to the load application and during tensile testing the temperature was held constant to within ±2 K. Additional tensile testing was performed in the Al-3Mg-0.2Sc alloy at 298 K using an initial strain rate of 1.0×10^{-3} s^{-1}.

The load and displacement data were recorded during tensile testing, converted into plots of engineering stress and engineering strain and then converted to plots of true stress and true strain by considering homogeneous deformation along the gauge section of the Al-Mg-Sc specimens. The elastic distortion of the testing machine was corrected by equating the elastic portion of the engineering stress and engineering strain curves to the elastic modulus of the material.

The initial thickness of the specimens was measured using a digital calliper and a Wild M420 stereoscope was used to obtain images of the tensile specimens just after tensile testing and to measure the final length in the gauge section of the samples.

3.5 Microstructural Characterization

3.5.1 Optical Microscopy (OM)

The microstructures of the unprocessed Al-3Mg-0.2Sc alloy in both the solution treated and the dynamic tested conditions were observed along the plane X, indicated in Figure 3.3, using an Olympus BX51 optical microscope. The sample preparation involved grinding using abrasive papers followed by polishing using 1 μm diamond paste and 0.06 μm silica colloidal. Thereafter, the polished samples were etched using an aqueous solution of 5% HBF_4 to reveal the grain boundaries and other microstructural features. The average grain boundary spacing, $\bar{L}$, was estimated in the OM images using the linear intercept method.

3.5.2 Scanning Electron Microscopy (SEM) and Electron Backscattered Diffraction (EBSD)

The grain structures of the Al-Mg-Sc alloy were examined by scanning electron microscopy (SEM) and orientation imaging microscopy (OIM) through electron backscattered diffraction (EBSD). Samples for SEM and EBSD analysis were prepared using the same procedure described for examination by OM, however, using a longer preparation time during final polishing with silica colloidal.

The microstructure of the Al-3Mg-0.2Sc alloy after SPD processing, heat treatment and mechanical testing at different conditions was observed using a JSM6500F thermal field emission SEM. EBSD patterns with information about the local crystal orientation were collected on a regular grid using step sizes as small as 0.03 μm and these were ultimately used to generate orientation maps. A cleaning procedure, including grain dilatation, was performed on each of these maps, henceforth denoted OIM images. Low-angle grain boundaries (LAGBs) were defined as having misorientation differences between adjacent points from 2° to 15° and high-angle grain boundaries (HAGBs) had misorientations >15°. The OIM analysis generated graphical displays of texture using pole figures from each measurement area. In addition, the distributions of the correlated misorientation angles and the area-weighted grain diameters were calculated for selected conditions.

Following tensile testing, observations of the surface of the fractured specimen and the topography along the gauge area were conducted using a JSM6500F thermal field emission SEM operating at 15 kV. The images obtained by scanning electron microscopy were used to measure the average grain boundary spacing and calculate the spatial grain size, d_s, using the expression $d_s = 1.74\ \bar{L}$ [193].

Additional SEM examinations were conducted in samples prepared by Ar-ion milling using a Hitachi IM4000 system. These analyses were performed using a Hitachi SU70 scanning electron microscope in the solution treated material and the HPT-processed alloy annealed for 1 h at 673 K.

3.5.3 Transmission Electron Microscopy (TEM) and Scanning Transmission Electron Microscopy (STEM)

Samples of the HPT-processed Al-3Mg-0.2Sc alloy were selected for microstructural examination using a JEOL 1200EX TEM and a Hitachi 5500 STEM operating at 30 kV. Discs with ~3 mm in diameter were punched at positions located at ~3.5 mm from the centre of both the HPT-processed samples and the work-pieces further annealed at 673 K for 1 h. Afterwards, these discs were electropolished using a Struers Tenupol-5 system with an electrolytic solution of 70% CH_3OH and 30% HNO_3 at ~280 K and analysed by STEM and TEM.

3.5.4 X-ray Diffraction (XRD)

The microstructures of the Al-3Mg-0.2Sc alloy subjected to ECAP and HPT processing at different temperatures were examined using a Bruker D2 Phaser X-ray diffractometer equipped with a copper target using Cu Kα (wavelength = 0.15406 nm) radiation. Billets of the material processed by ECAP were cut into discs with thicknesses of ~1 mm. Afterwards, these samples as well as the discs processed by HPT were prepared for examination by X-ray diffraction (XRD) through grinding using abrasive papers followed by polishing using 1 μm diamond paste and 0.06 μm silica colloidal. Furthermore, the surfaces of the polished samples were etched for ~10 s using an aqueous solution of 5% HBF_4.

XRD patterns were recorded for the entire surface of the samples through θ-2θ scans conducted from 2θ = 30-110° using a step size of 0.02°. The lattice microstrain, $\langle \varepsilon^2 \rangle^{1/2}$, the average crystallite size, D_c, and the lattice parameter, a, were calculated based on the Rietveld method [194] using Maud software for profile fitting and these parameters were used to estimate the dislocation density, ρ, using the relationship [195,196]

$$\rho = \frac{2\sqrt{3}\,\langle \varepsilon^2 \rangle^{1/2}}{D_c\,\mathbf{b}} \tag{3.2}$$

Furthermore, energy-dispersive X-ray (EDX) spectroscopy examinations were conducted using SEM, STEM and TEM systems equipped with EDX detectors. These analyses aimed at verifying the presence of Al_3Sc dispersoids within the microstructure of Al-3Mg-0.2Sc samples processed under different conditions.

Chapter 4 Influence of Grain Size on the Flow Properties of an Al-Mg-Sc Alloy Both Without and With Processing by ECAP

4.1 Introduction

The Al-Mg-Sc alloys have attracted significant attention because of their high specific strength as well as their excellent superplastic properties [40,41]. Although the superplastic behaviour of Al-Mg-Sc alloys was studied extensively after processing by conventional metal-working techniques and ECAP [42–46], there are only limited studies documenting the mechanical properties of UFG Al-Mg-Sc alloys at low deformation temperatures [34–37].

Recent investigations have demonstrated the exceptional capacity of Al alloys with Sc additions to resist the impact of high speed projectiles [32,33] which makes this material an important candidate for use in the structure of spacecraft. Although several studies were reported evaluating the flow properties at high strain rates in different UFG metals [21–30], there are no reports up to the publication of these doctoral studies available on the deformation of SPD-processed Al-Mg-Sc alloys at dynamic strain rates [31].

Accordingly, this investigation was initiated to assess the mechanical properties and deformation mechanisms in both the coarse and UFG Al-Mg-Sc alloy tested under quasi-static and dynamic conditions. The influence of grain size on the mechanical behaviour of this metal was also examined based on the Hall-Petch relationship as presented throughout this chapter.

4.2 Experimental Results

4.2.1 Mechanical Properties

Representative plots of true stress vs true strain obtained through dynamic testing using the SHPB system are shown in Figure 4.1 for samples with and without processing by 8 passes of ECAP at ambient temperature. The curves show that processing by ECAP leads to superior mechanical strength at all testing temperatures. In addition, the curves of the solution treated material display significant work-hardening at 298 K whereas the curves at

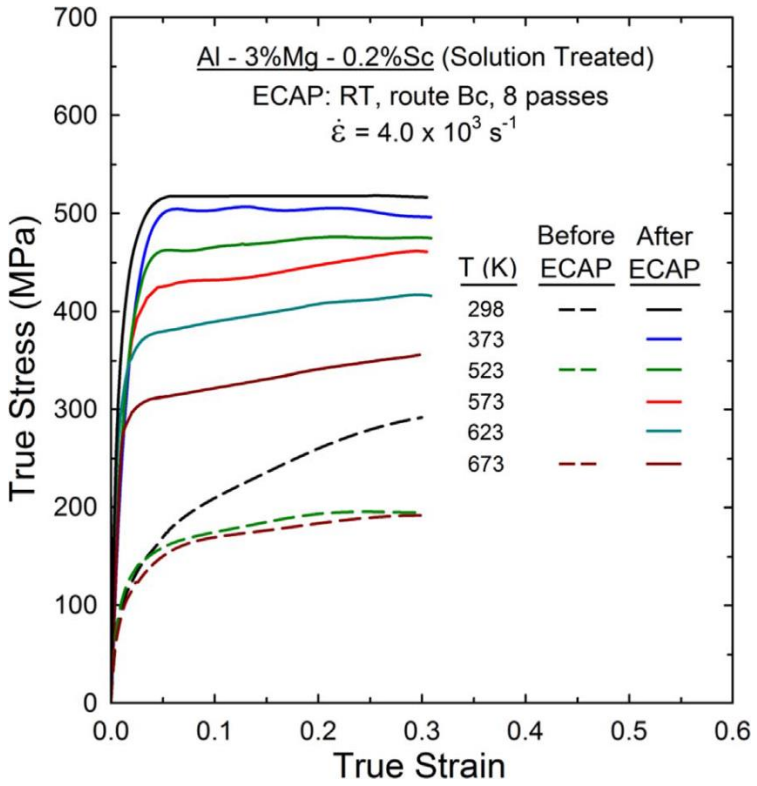

Figure 4.1 - True stress vs true strain curves for samples of the solution treated Al-3Mg-0.2Sc alloy (broken lines) before and (solid lines) after processing by 8 ECAP passes at ~300 K and further dynamic testing at 4.0×10^3 s^{-1} within the temperature range from 298 to 673 K.

523 and 673 K exhibit only minor work-hardening and achieve similar true stresses of ~200 MPa at ε = 0.3. There is an apparent saturation in the true stress at ~520 MPa for the ECAP-processed alloy tested at 298 K and there are only minor decreases in the flow stresses for $T \leq 573$ K.

To visualize more clearly the temperature sensitivity of stress in the Al-Mg-Sc alloy, Figure 4.2 displays the variation of the true stress at ε = 0.05 with the testing temperature. The experimental points displayed in Figure 4.2 include the experimental data obtained during both the dynamic tests and the tensile tests performed using miniature samples at the strain rates of 3.3×10^{-3} and 3.3×10^{-1} s^{-1}.

Inspection of Figure 4.2 reveals that the true stress monotonically decreases with increasing temperatures for the Al-3Mg-0.2Sc alloy, however the rate that the stress varies with temperature, $\frac{\partial \sigma}{\partial T}$, strongly depends upon the strain rate and the microstructure of the metal prior to mechanical testing. Nevertheless, for both the solution treated and the ECAP-processed material the flow stress is more sensitive to temperature variations at low strain rates. Additionally, this temperature sensitivity is more pronounced in the Al-3Mg-0.2Sc alloy after ECAP compared with the unprocessed material.

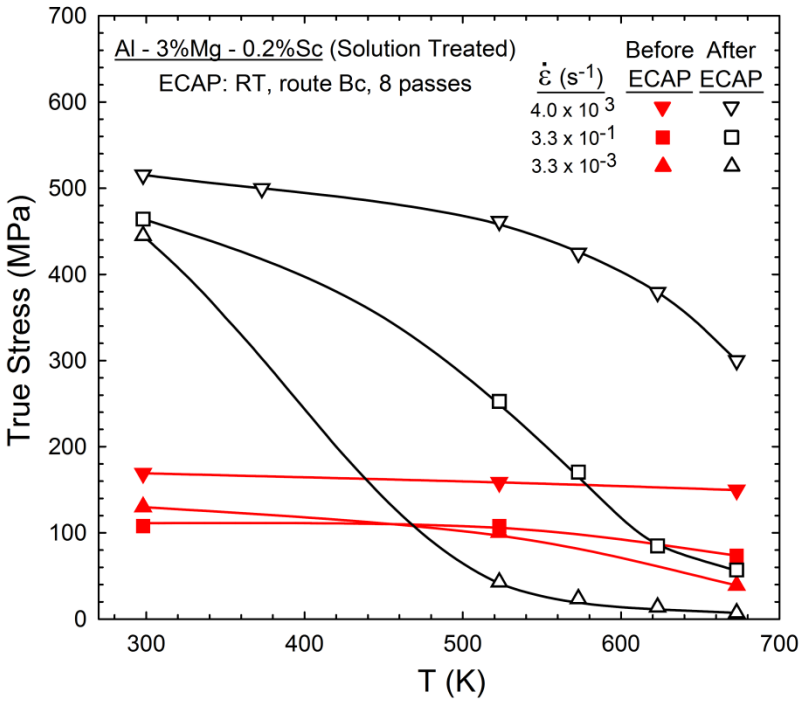

Figure 4.2 - Variation of the true stress at ε = 0.05 with the temperature for samples of the solution treated Al-3Mg-0.2Sc alloy (closed symbols) before and (open symbols) after processing by 8 passes of ECAP at ~300 K and further mechanical testing.

It is apparent from Figure 4.2 that the flow stress at ε = 0.05 for the unprocessed material is ~160 MPa for specimens tested at 4.0×10^3 s^{-1}, regardless of the testing temperature. Conversely, the Al-Mg-Sc alloy processed by ECAP depicts higher temperature sensitivity of stress during dynamic testing, especially for $T \geq 523$ K. It follows from Figure 4.2 that the flow stresses in the ECAP-processed alloy tensile tested at $\dot{\varepsilon} = 3.3 \times 10^{-1}$ s^{-1} are lower than in the unprocessed material for $T >$ ~623 K. The same transition from strengthening to softening is also observed for the samples tested at $\dot{\varepsilon} = 3.3 \times 10^{-3}$ s^{-1} at a deformation temperature of ~470 K, although the absence of experimental datum points at $298 < T < 523$ K does not permit a rigorous prediction of the transition temperature.

In order to provide information on the deformation mechanisms, Figure 4.3 shows the variation with strain rate of the true stress at ε = 0.05 for samples tested at different absolute temperatures, *T*, in (a) the solution treated condition and (b) after ECAP processing. The slopes of these curves correspond to the strain rate sensitivity, *m*, and it is apparent that there is a negative strain rate sensitivity of $m \approx -0.04$ for the unprocessed alloy tested at room temperature for strain rates below ~3.3×10^{-1} s^{-1}. This negative value of *m* is associated with the occurrence of dynamic strain ageing (DSA) in the Portevin-Le Chatelier effect [137,197–200]. Inspection of Figure 4.3 (a) shows that $m > 0$ in the solution treated alloy from 3.3×10^{-4} to 3.3×10^{-1} s^{-1} at 523 and 673 K, the slopes of the curves increase with increasing *T* and decreasing $\dot{\varepsilon}$, and the value of *m* is ~0.2 at strain rates below ~3.3×10^{-2} s^{-1}.

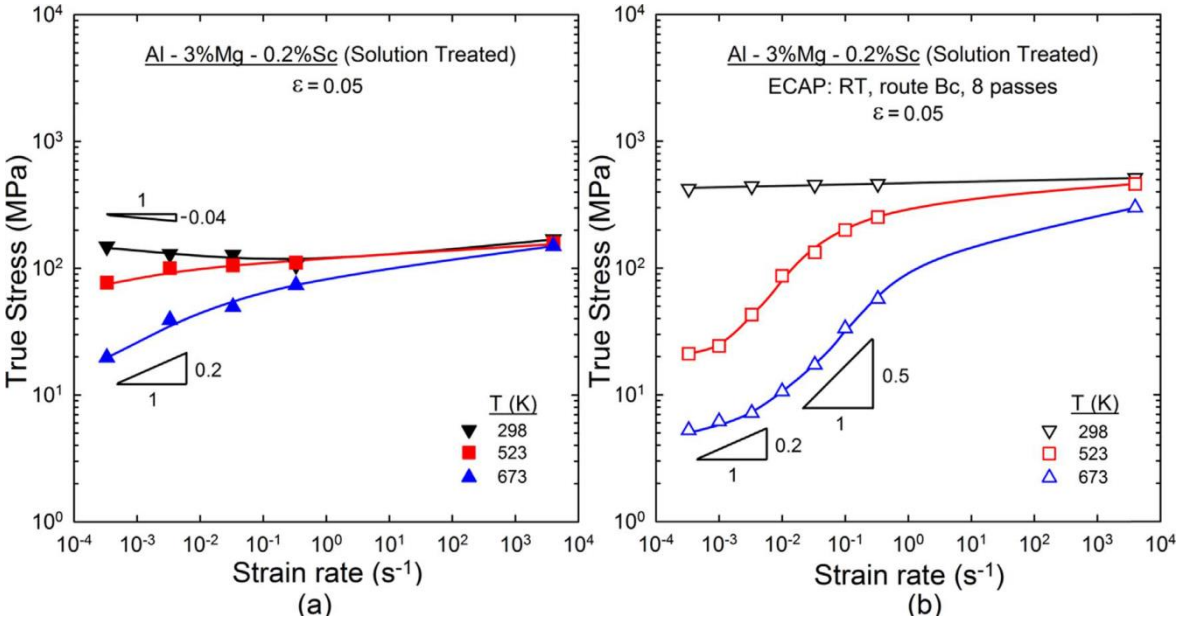

Figure 4.3 - Variation of the true stress at a true strain of 0.05 with the strain rate for samples of the solution treated Al-3Mg-0.2Sc alloy (a) before and (b) after processing by ECAP and further mechanical testing within the temperature range from 298 to 673 K.

In Figure 4.3 (b) for the ECAP-processed material there is an approximate sigmoidal relationship at the two higher temperatures which is similar to the three regions of flow generally observed in superplastic metals [201]. At the lowest strain rates at $\dot{\varepsilon} \leq 1.0 \times 10^{-3}\ s^{-1}$ the curves have a slope of ~0.2 whereas at faster strain rates, up to $\dot{\varepsilon} \approx 3.3 \times 10^{-1}\ s^{-1}$ for the specimens tested at 523 K, the slope is $m \approx 0.5$. At even faster strain rates, the values of m remain positive but tend to decrease with increasing strain rate.

4.2.2 Grain Structure and Texture of the Coarse-Grained Al-Mg-Sc Alloy

Figure 4.4 displays the microstructure of the Al-3Mg-0.2Sc alloy after solution treatment observed by (a) OM using polarised light and (b) SEM using a HITACHI SU-70 system operating at 10 kV with a photo-diode backscattered electron detector in the composition mode (PDBSE-CP). Inspection of Figure 4.4 (a) reveals that the solution treated metal has a fairly homogeneous microstructure with $\bar{L} \approx 300$ μm. There are few particles with diameters < 300 nm within selected areas of the grains of this Al alloy as apparent in Figure 4.4 (b). EDX examinations conducted in the unprocessed material also revealed that these particles are Al_3Sc precipitates that were not completely dissolved in this Al-Mg-Sc alloy during solution treatment. Nevertheless, it is important to note that although few coarse Al_3Sc dispersoids were observed after heat treatment, Sc is mostly present in the form of a solid solution in the unprocessed material. This is confirmed through EDX analysis conducted in 10 different locations in the solution treated metal which displayed average wt. % of Mg and Sc of ~3 % and ~0.19 %, respectively, very close to the nominal composition of each element.

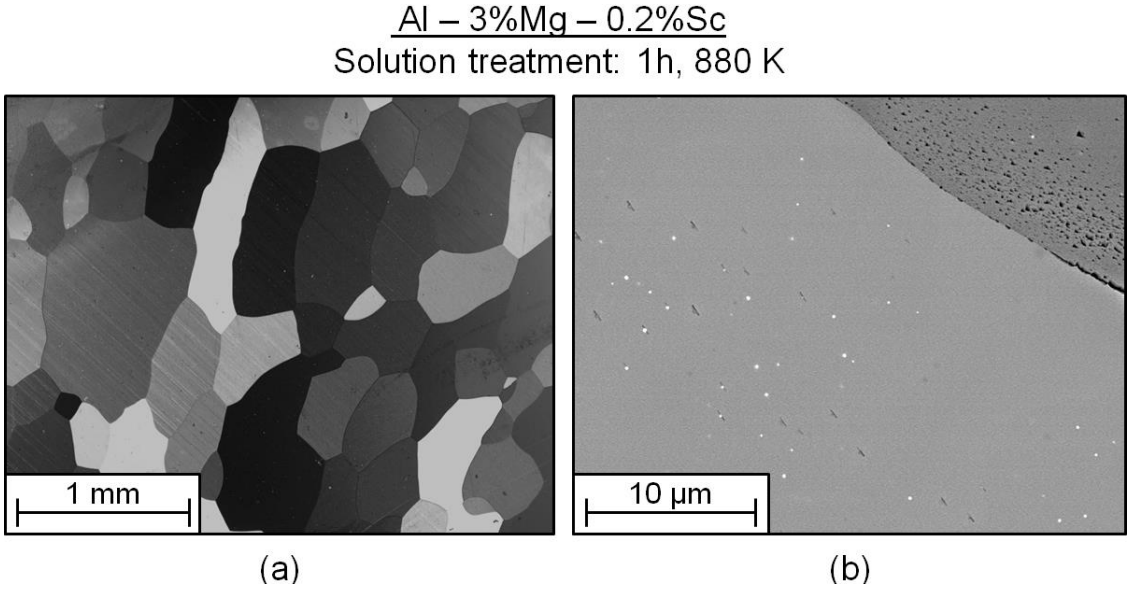

Figure 4.4 - Microstructure of the solution treated Al-3Mg-0.2Sc alloy observed through (a) optical microscopy and (b) scanning electron microscopy.

Figure 4.5 shows the microstructure of the solution treated Al-3Mg-0.2Sc alloy after dynamic testing at 298 and 673 K. It is readily seen in Figure 4.5 that the microstructure of the unprocessed material after dynamic testing is clearly formed by two different types of grain structures. Firstly, there is a group of grains which underwent significant straining during deformation at high strain rates, as observed in the darker regions of Figures 4.5 (a) and (c) for the samples deformed at 298 and 673 K, respectively. In addition, the area fraction of these highly strained grains is inferior in the material deformed at 673 K compared with the same alloy tested at room temperature. Furthermore, shear bands developed inside the original boundaries of these deformed grains and some of these bands even cross each other, as depicted in the top-right position of Figure 4.5 (b). Finally, examination of Figures 4.5 (a) and (b) also reveals the existence of a second group of grains, distinguished by grain structures free of internal features with shapes very similar to the original grains displayed in Figure 4.4 (a).

Typical OIM images are shown in Figure 4.6 obtained along the X plane in the middle-section of (a) the unprocessed alloy and after dynamic testing at (b) 298 and (c) 673 K. It is apparent from Figure 4.6 (a) that the microstructure of the solution treated material is mostly formed by grain structures with HAGBs and there is no evidence of substructures with LAGBs within these grains. Furthermore, it is also noted that the grain structures of the unprocessed metal do not depict a preferable orientation and each grain has a well-defined orientation, as there is no colour gradient inside the grains. By contrast, Figures 4.6 (b) and (c) shows that the originally coarse-grained metal has its microstructure refined during dynamic testing. It is also apparent that the shear band formation shown in Figures 4.5 (b) and 4.6 (b) promotes grain refinement during straining at $\dot{\varepsilon} = 4.0 \times 10^3\ s^{-1}$.

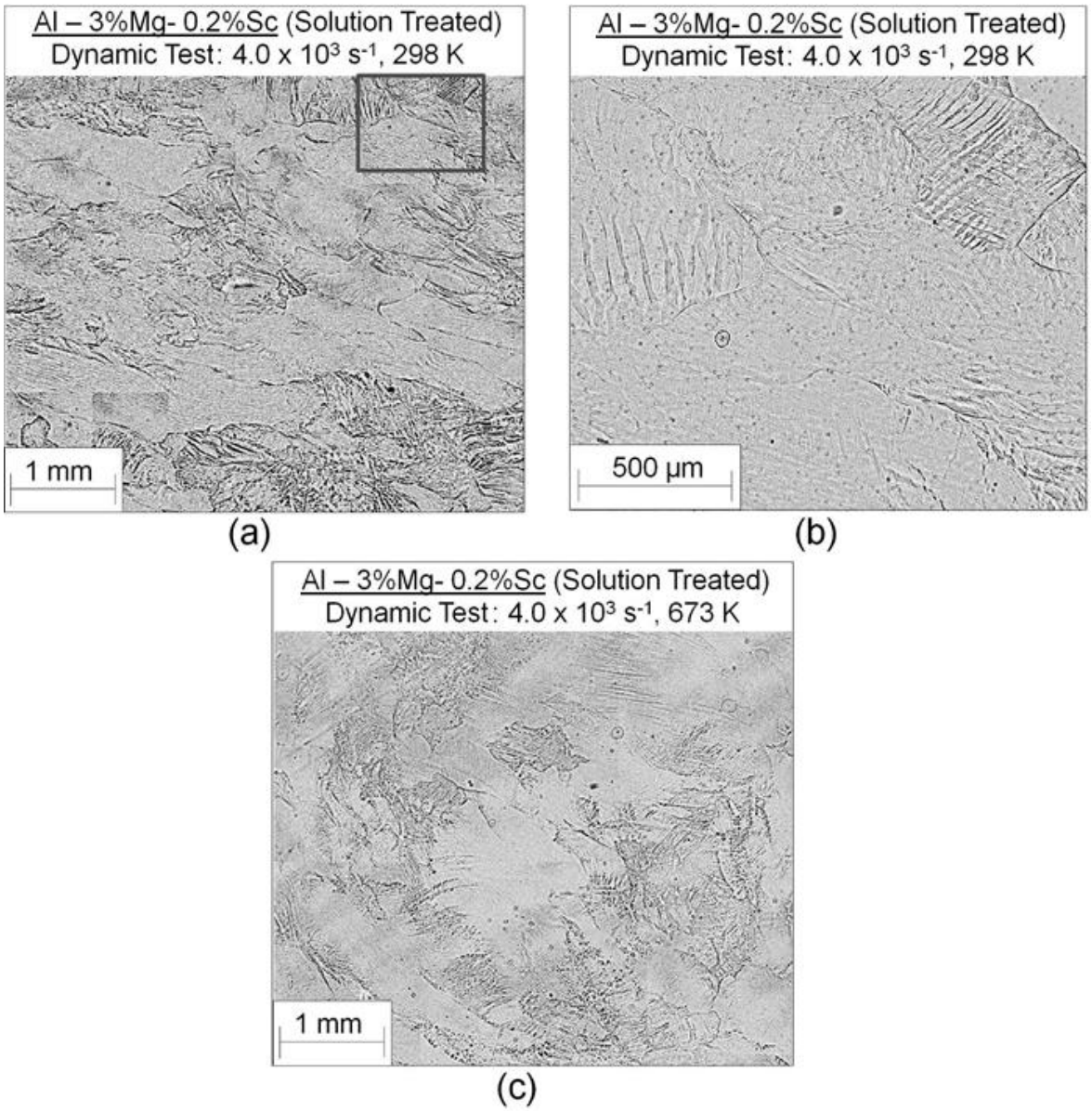

Figure 4.5 - The OM images for the solution treated Al-3Mg-0.2Sc alloy after dynamic testing at 4.0×10^3 s^{-1} at (a,b) 298 K and (c) 673 K.

In Figures 4.6 (b) and (c), there is evidence for the development of substructure with LAGBs in the highly strained areas and there are strong texture gradients which reflect abrupt changes in the local misorientations. These structures initially form LAGBs but eventually evolve into grains with HAGBs through mechanically-induced dynamic recrystallization (DRX) [21,22,153]. It also follows from Figures 4.6 (b) that some grains essentially preserve their original sizes and have a very high density of LAGBs. There is a distinct texture in these grains with the {110} planes parallel to the *X* plane. Similarly, Figure 4.6 (c) shows many large grains with the same texture as in Figure 4.6(b) but with a lower density of LAGBs. The textures of the unprocessed alloy are presented as {111} pole figures in Figure 4.7 both (a) without and (b and c) with dynamic testing.

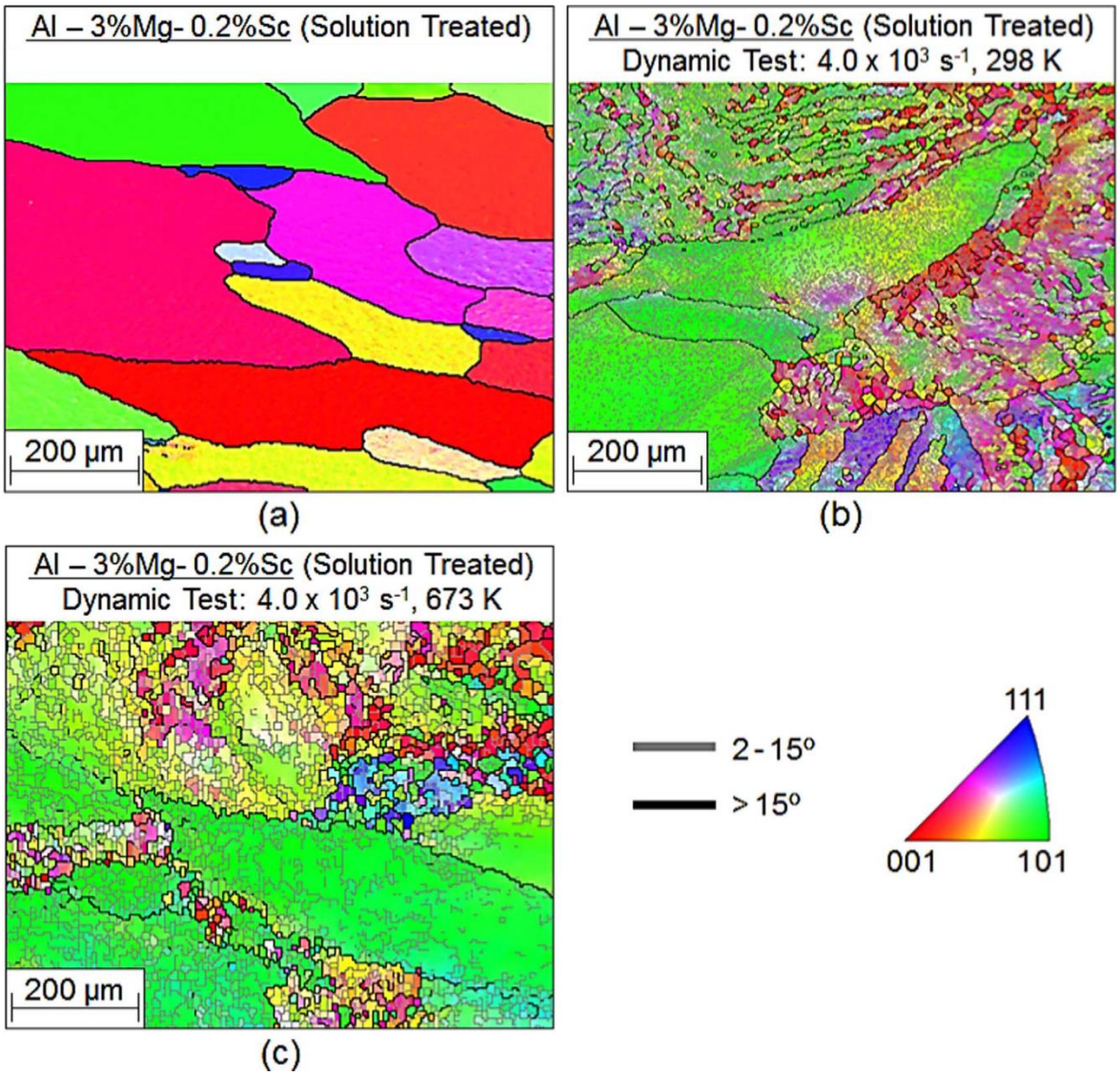

Figure 4.6 - OIM images for (a) the solution treated Al-3Mg-0.2Sc alloy and after dynamic testing at 4.0×10^3 s^{-1} at (b) 298 and (c) 673 K.

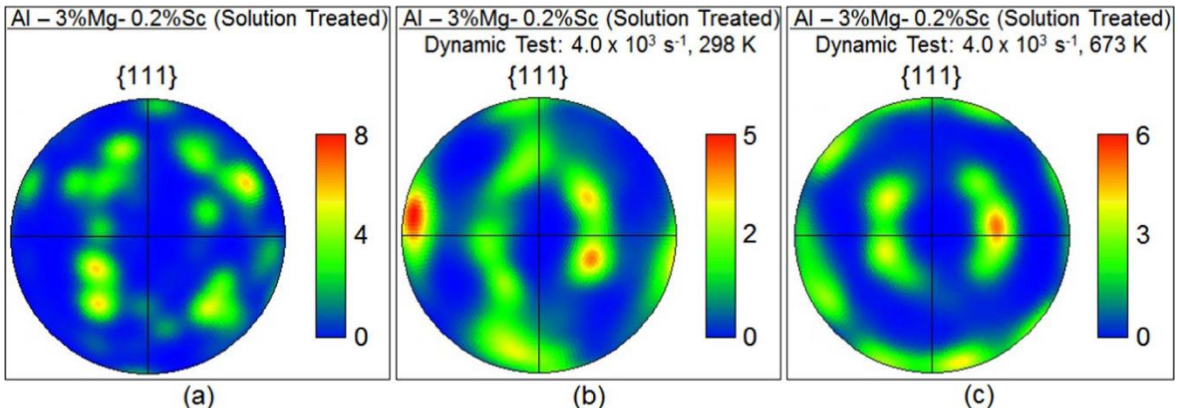

Figure 4.7 - Texture represented as {111} pole figures for (a) the solution treated Al-3Mg-0.2Sc alloy and after dynamic testing at 4.0×10^3 s^{-1} at (b) 298 and (c) 673 K.

It is readily seen in Figure 4.7 that the alloy has a random texture after solution treatment but it develops a deformation texture after dynamic testing at (b) 298 and (c) 673 K. This texture is typical of fcc metals with high stacking fault energies after compression testing and it is characterized by a fibre-type texture where the compression axis is the fibre axis [202,203]. As is evident from Figures 4.7 (b) and (c), both samples show a strong texture component around {110} and, for the alloy tested at 298 K, there is also a weak texture component around {100}.

4.2.3 Grain Structure and Texture of the ECAP-Processed Al-Mg-Sc Alloy

The microstructure of the Al-Mg-Sc alloy was intensively refined by 8 ECAP passes to give $\bar{L} \approx 250$ nm as measured from SEM images where this is comparable to the grain size of ~200 nm reported earlier for the same alloy using transmission electron microscopy after processing through similar conditions [43]. Figure 4.8 shows typical OIM images of the ECAP-processed alloy (a) after annealing at 673 K for 10 min, (b) after tensile testing at 3.3×10^{-3} s^{-1} at 673 K and (c and d) after dynamic testing at 4.0×10^{3} s^{-1} at 298 and 673 K, respectively. Additionally, it is worth mentioning that the short-term annealing was conducted with the aim of reproducing the microstructural changes that occurred during the period of time in which the samples were heated inside the tubular furnace just prior to mechanical testing.

It follows from Figure 4.8 (a) that the banded structures formed during ECAP evolve into nearly equiaxed grains during annealing at 673 K for 10 min and, in addition, there is a large fraction of subgrains with an average size of ~0.6 μm. In Figure 4.8 (b) the ECAP-processed alloy pulled to failure at 3.3×10^{-3} s^{-1} at 673 K shows mostly grains with HAGBs. EBSD scanning was performed in the gauge area of a tensile specimen which underwent an elongation of ~980 %. As elongations >400 % were observed in this condition [105], the randomness of the texture and the high misorientations between neighbouring grains strongly suggest that the material processed by 8 passes of ECAP at ambient temperature deforms by grain boundary sliding (GBS) at this testing temperature and strain rate.

It is apparent in Figures 4.8 (c) and (d) that a strong texture component develops around {110} after dynamic testing regardless of the testing temperature. It is also interesting to note that the grains are equiaxed and primarily consist of HAGBs although there is a significant fraction of LAGBs. Furthermore, it is evident from Figures 4.8 (a) and (d) that limited grain coarsening occurs during dynamic testing at an elevated temperature as $\bar{L} \approx 0.8$ μm after testing at 4.0×10^{3} s^{-1} at 673 K.

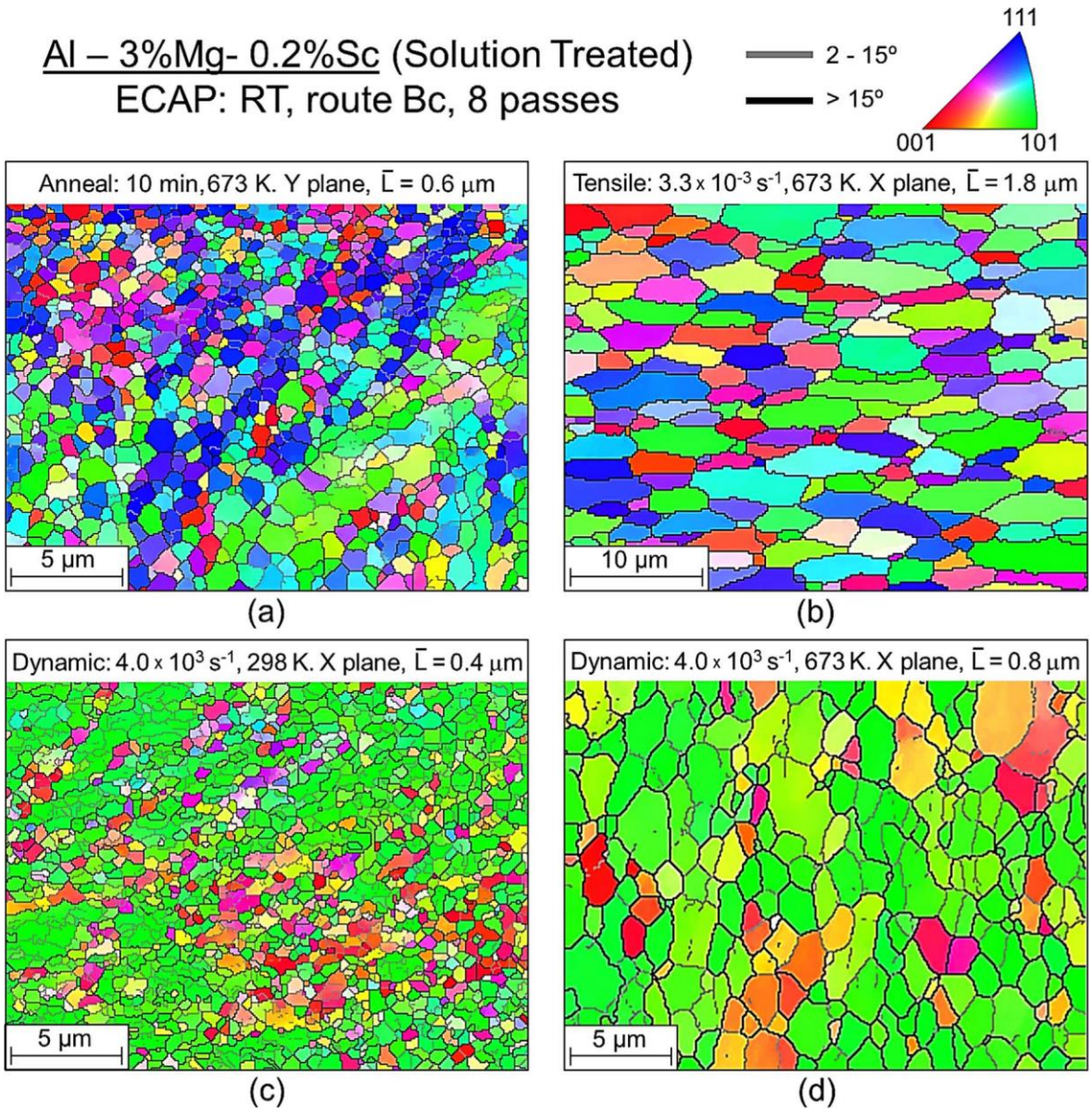

Figure 4.8 - OIM images of the ECAP-processed Al-3Mg-0.2Sc alloy after (a) annealing at 673 K for 10 min, (b) tensile testing at 3.3×10^{-3} s^{-1} at 673 K and dynamic testing at 4.0×10^{3} s^{-1} (c) at 298 and (d) at 673 K.

The fractions of boundaries are plotted in Figure 4.9 as a function of the misorientation angles for the samples tested under the same conditions as in Figure 4.8: these histograms depict the correlated pixel-to-pixel misorientation distributions with a cut-off angle of 2° [204] and the superimposed solid curves represent the Mackenzie theoretical distribution [205]. It is apparent from Figure 4.9 (a) that the alloy has a high fraction of LAGBs (~30 %) after ECAP and annealing at 673 K. Similarly, after dynamic testing there are also large fractions of LAGBs as shown in Figures 4.9 (c) and (d) and the material also has a larger fraction of HAGBs with misorientation angles >50° compared with the material annealed for 10 min.

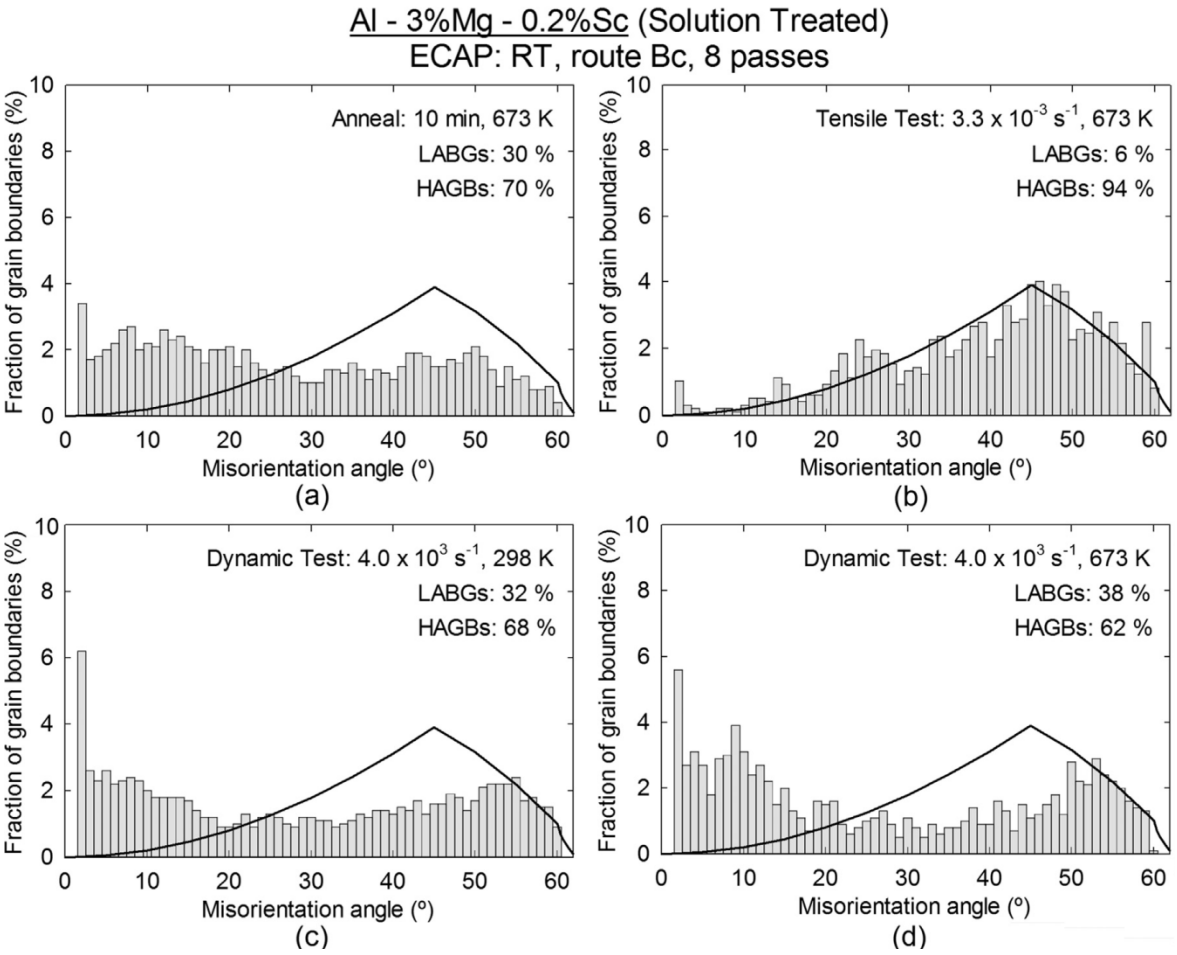

Figure 4.9 - Histograms of the misorientation angles for the ECAP-processed Al-3Mg-0.2Sc alloy after (a) annealing at 673 K for 10 min, (b) tensile testing at 3.3×10^{-3} s^{-1} at 673 K and dynamic testing at 4.0×10^{3} s^{-1} (c) at 298 and (d) at 673 K.

It is readily seen in Figure 4.9 (b) that testing in tension at 673 K with a strain rate of 3.3×10^{-3} s^{-1} gives results that conform closely with the Mackenzie distribution [205] thereby demonstrating that the alloy develops a random texture during tensile straining. By contrast, there are very significant deviations from the theoretical curves after dynamic testing in Figures 4.9 (c) and (d) so that a strong texture develops under these conditions as shown by the corresponding {111} pole figures for the four different testing conditions in Figure 4.10.

In Figure 4.10 (a) there is a typical ECAP shear texture [206–209] after ECAP and annealing. Conversely, the pole figure after tensile testing in Figure 4.10 (b) exhibits a relatively small intensity index as well as a random distribution and this is similar to the same alloy processed by 8 ECAP passes using a die with a channel angle of 60° and further tested in tension [210]. By contrast, Figures 4.10 (c) and (d) reveal a strong compression texture with the same characteristics described in Figures 4.7 (b) and (c) after dynamic testing. Accordingly, as already noted for the OIM images in Figures 4.8 (c) and (d), the {110} planes are mostly parallel to the *X* plane which is normal to the compression axis.

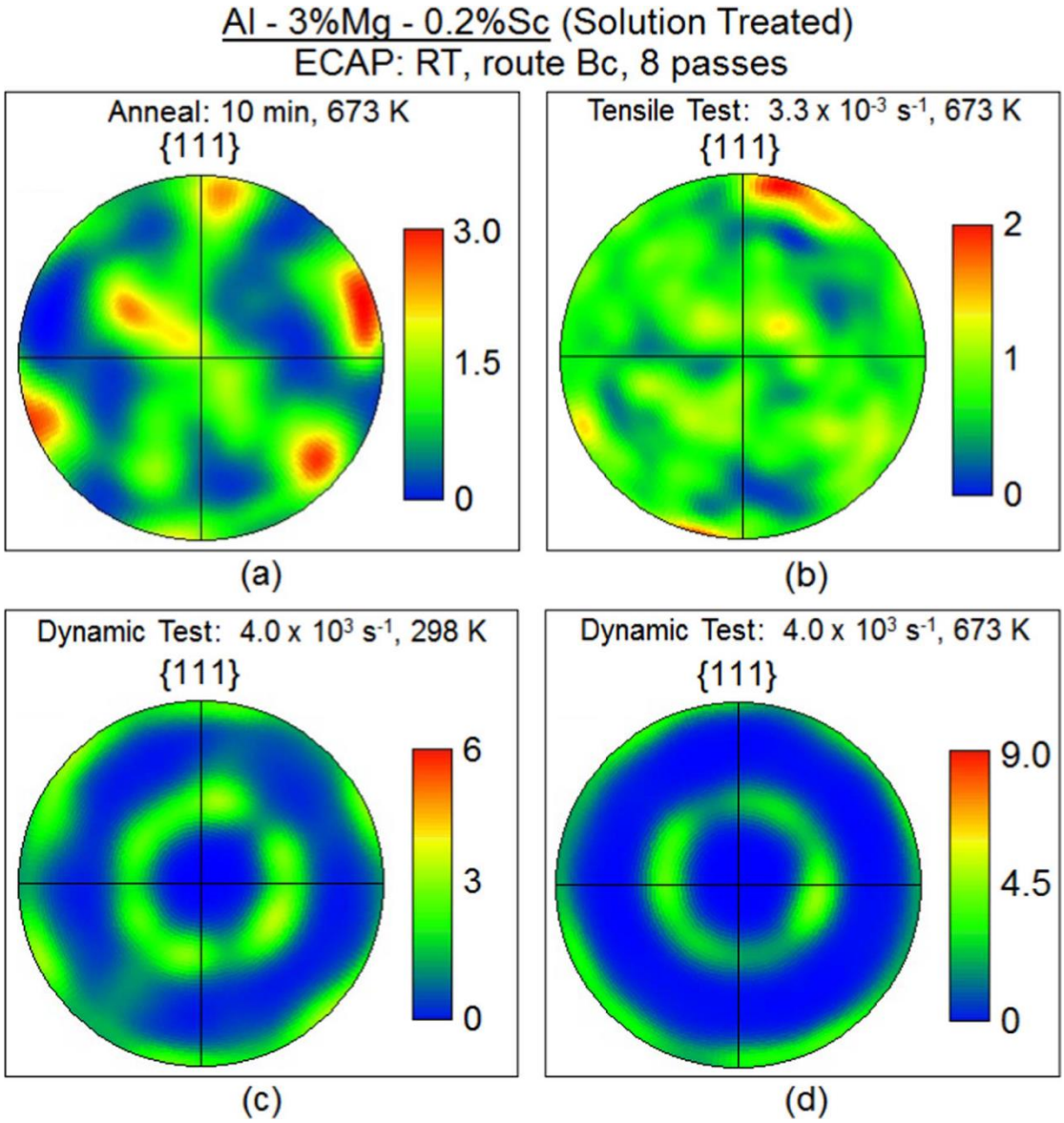

Figure 4.10 - Texture represented as {111} pole figures for the ECAP-processed Al-Mg-Sc alloy after (a) annealing at 673 K for 10 min, (b) tensile testing at 3.3×10^{-3} s^{-1} at 673 K and dynamic testing at 4.0×10^{3} s^{-1} (c) at 298 and (d) at 673 K.

4.3 Discussion

4.3.1 Application of the Hall-Petch Relationship in Al-Mg-Sc Alloys

The plots depicted in Figures 4.1, 4.2 and 4.3 confirm the superior mechanical strength of the UFG Al-Mg-Sc alloy during deformation at ambient temperature regardless of the testing strain rate. It is well established that the ECAP-processed alloy displays excellent superplastic properties at elevated temperatures [43] and also a significantly higher strength when tested using the SPHB facility by comparison with the coarse-grained material or with a UFG Al-1.5% Mg alloy [24]. The reasons for these exceptional mechanical properties are

associated both with the strengthening effects of the Al-Mg solid solution and the presence of many grain boundaries due to the SPD processing and with the presence of Al_3Sc precipitates which enhance the strength and the grain boundary stability of this aluminium-based alloy [40,211]. Furthermore, it is important to note that Al-Mg alloys without Sc or similar additions exhibit substantial grain growth at temperatures above 500 K [16,17,212] and this is deleterious for the material strength and ductility at high temperatures.

There are numerous reports discussing the validity of the Hall-Petch relationship (Eq. 2.1) for materials with grain sizes in the submicrometre range [63–65,67,213,214]. In order to verify whether the grain boundary strengthening predicted by the Hall-Petch relationship remains consistent for the UFG Al-3Mg-0.2Sc alloy, Figure 4.11 plots the yield stress, σ_y, against the inverse square root of the grain boundary spacing using both the experimental data obtained in this investigation and data from other studies conducted on commercially pure aluminium [215–218], Al-Mg alloys [24,137,178,219–222] and Al-Mg-Sc alloys [34–36,47,223].

It is apparent from Figure 4.11 that pure aluminium (Al 1100) has inferior strength compared with Al-Mg alloys regardless of the grain size. There is also a breakdown in the Hall-Petch relationship at $\bar{L}^{-0.5} \approx 1600\ m^{-0.5}$ which corresponds to $\bar{L} \approx 0.4\ \mu m$ for commercially pure aluminium. On the other hand, Al-Mg alloys have higher yield stresses by comparison with Al 1100 as a direct consequence of the solid solution strengthening effect obtained by the addition of Mg solutes [11–15]. Furthermore, Al-Mg alloys display a delayed breakdown in the Hall-Petch relationship which occurs for grain sizes <0.15 μm. By contrast,

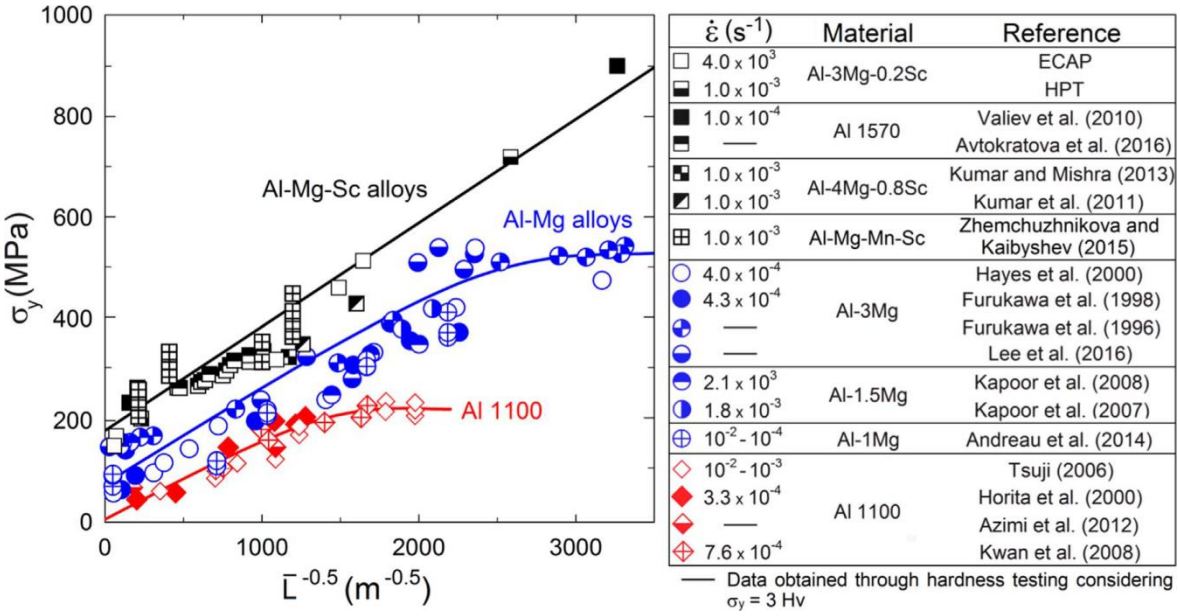

Figure 4.11 - The Hall-Petch relationship in commercially pure aluminium [215–218], Al-Mg alloys [24,137,178,219–222] and Al-Mg-Sc alloys [34–36,47,223].

the evidence in Figure 4.11 infers that the grain boundary strengthening predicted using the Hall-Petch equation remains accurate for Al-Mg-Sc alloys over the full range of grain sizes evaluated in this and other studies ($\bar{L}$ > 0.1 μm).

In the current study, the solution treated Al-3Mg-0.2Sc alloy was also processed through 10 turns of HPT at ambient temperature and ultrafine-grained structures with an average size of ~0.14 μm were obtained after processing. Tensile testing was conducted in the HPT-processed metal at room temperature and at 1.0×10^{-3} s^{-1} using miniature specimens with the same geometry displayed in Figure 3.3 (b). The results show that this alloy has a yield stress of ~720 MPa after HPT processing and follows the same trend predicted by the Hall-Petch relationship. In addition, the Al 1150 alloy undergoes further grain refinement and achieves an extraordinary yield stress of ~900 MPa, in excellent agreement with the theoretical prediction considering the pile up of dislocations at the vicinity of HAGBs.

The absence of a breakdown in the Hall-Petch relationship suggests that the deformation is primarily controlled by intragranular dislocation motion and the contribution from the emission and annihilation of extrinsic dislocations at the non-equilibrium grain boundaries may be diminished by the presence of Mg segregation at HAGBs and triple junctions [34]. Thus, high concentrations of Mg solutes were detected at grain boundaries in SPD-processed Al-Mg alloys [51,170–172]. There was also some evidence from SEM in the present study for a thin discontinuous layer of Mg segregates along the grain boundaries in the ECAP-processed Al-Mg-Sc alloy after dynamic testing but a more comprehensive study is now needed to fully substantiate this effect. Nevertheless, as predicted by molecular dynamic simulations [70–72], the local atomic structure along HAGBs has a major influence on the stress required for the emission of dislocations and in practice the segregation of Mg along the boundaries serves to reduce the boundary energy and improve the stability of these grain structures [224,225]. High concentration of Mg at HAGBs may also suppress the emission of extrinsic dislocations through solute drag [34]. In addition, it is important to note that Mg segregation is not observed in the Al-3Mg alloy after HPT which underwent instead dissolution of Mg atoms in solid solution during processing [219].

It is apparent from Figure 4.11 that Al-Mg-Sc alloys have superior mechanical strength by comparison with other Al-Mg alloys having similar Mg contents. This is due to the presence of the Al_3Sc dispersoids which act as obstacles for dislocation glide [40]. The experimental data in Figure 4.11 was obtained from Al-Mg-Sc alloys processed using different procedures, testing temperatures and strain rates and the experimental points represented by the open squares are for the ECAP-processed alloy tested at 4.0×10^{3} s^{-1}. This confirms that intragranular dislocation slip remains active even at extremely high strain rates.

4.3.2 The Deformation Mechanisms in the Coarse and UFG Al-Mg-Sc Alloys

Al-Mg-Sc alloys deform through different mechanisms depending on grain size, temperature and strain rate. In general, polycrystalline metals develop adiabatic shear bands during deformation at dynamic strain rates [22,26,28,153] and strain localization within these shear bands promotes a mechanically-driven grain refinement [21,22]. In this study, strain localization and local grain refinement were observed in the coarse-grained material after dynamic testing. Therefore, the prominent work hardening of the unprocessed alloy during dynamic deformation at ambient temperature is attributed to an increase in the dislocation density and the formation of small grains which act as effective barriers to dislocation motion.

Conversely, the coarse-grained Al-3Mg-0.2Sc alloy does not display substantial work hardening during dynamic straining at high temperatures. Although, there is also evidence of grain refinement during dynamic testing at 673 K, the originally solution treated metal exhibits a lower density of LAGBs mostly organized as subgrains. Thereby, the existence of a steady state flow stress and the subgrain formation indicate the occurrence of dynamic recovery during dynamic straining at high temperatures.

Figure 4.3 shows that the coarse-grained alloy exhibits a negative strain rate sensitivity ($m \approx -0.04$) when testing at 298 K at strain rates lower than $\sim 3.3 \times 10^{-1}$ s^{-1}. Similarly, coarse-grained Al-Mg alloys with different magnesium contents also display $m < 0$ which is due to the occurrence of DSA wherein the flow stress is controlled by interactions between mobile dislocations and solute atom atmospheres [198–200,226–228]. The presence of solutes requires an increment of the local shear stress to promote the movement of dislocations with their solute atmospheres and hence, after application of additional stresses, these dislocations are released and then require lower stresses to continue their movement leading to flow instability. This instability has been demonstrated both in experiments [137,198,200,229] and in computational modelling [230].

It is apparent from Figure 4.3 that m increases with increasing temperatures and is ~ 0.2 at a strain rate of $\sim 10^{-3}$ s^{-1}. This value of m is consistent with deformation controlled by dislocation climb at 673 K for strain rates from 3.3×10^{-4} to $\sim 10^{-2}$ s^{-1} and this is in good agreement with data reported for a coarse-grained Al-Mg alloy in mechanical testing [231].

Exceptional grain refinement was attained in the Al-3Mg-0.2Sc alloy after processing through 8 passes of ECAP such that the deformed metal has an average grain boundary spacing of ~0.25 μm as measured from typical SEM images. Consequently, different deformation mechanisms were operative during plastic deformation by comparison with the coarse-grained metal. Inspection of Figure 4.3 (b) shows also that $m \approx 0$ for the

ECAP-processed alloy deformed at 298 K which also suggests the occurrence of DSA. In practice, serrated flow and profuse micro-shear bands were observed in Al-Mg-Si [232] and Al-Mg-Mn-Sc [36,37] alloys processed by ECAP and mechanically tested under conditions similar to those in the present investigation and there was also evidence in this work for limited serrated flow at low temperatures and strain rates for the Al-3Mg-0.2Sc alloy processed by ECAP at room temperature.

Furthermore, grain refinement may be beneficial for the ductility of Al-Mg-Sc alloys at low temperatures as the average distance between micro shear bands in the UFG metal is significantly smaller than the distance between shear bands in the coarse-grained alloy [37]. Accordingly, plastic deformation is more diffuse in a microstructural level for the ECAP-processed material and thereby severe plastic deformation may be effectively used to delay the incipient failure caused by strain localization in Al-Mg alloys during dynamic strain ageing.

It follows from Figure 4.3 (b) that $m \approx 0.2$ for the UFG Al-Mg-Sc alloy deformed at *673* K at $\dot{\varepsilon} \leq 3.3 \times 10^{-3}$ s^{-1} and $m \approx 0.5$ for faster strain rates, up to $\dot{\varepsilon} \approx 3.3 \times 10^{-1}$ s^{-1}. Nevertheless, there is significant grain coarsening in the ECAP-processed specimens tested at high temperatures and low strain rates as observed in Figure 4.8 (b) for the Al alloy pulled to failure at 3.3×10^{-3} s^{-1} at 673 K ($\bar{L} \approx 1.8$ μm). Therefore, the m values shall not be used as a direct evidence of the deformation mechanism in the UFG Al-3Mg-0.2Sc alloy deformed at $T \geq 523$ K at strain rates below $\sim 3.3 \times 10^{-3}$ s^{-1}.

There is consistent evidence supporting the occurrence of GBS in the UFG metal tested at 3.3×10^{-3} s^{-1} at 673 K even though $m < 0.5$. As depicted in Figures 4.8 (b), 4.9 (b) and 4.10 (b), the Al-3Mg-0.2Sc alloy develops a random texture during plastic straining at this testing condition which is typical for Al alloys during grain boundary sliding [210,233]. In addition, a superplastic elongation to failure of ~980 % is attained after tensile testing at 3.3×10^{-3} s^{-1} at 673 K in good agreement with an early study [43]. This evidence therefore indicates that the primary deformation mechanism in the ECAP-processed Al-3Mg-0.2Sc alloy at 673 K and at $\dot{\varepsilon} < \sim 3.3 \times 10^{-2}$ s^{-1} is Rachinger GBS [234]. Furthermore, as diffusivity increases with increasing temperatures and Al-Mg-Sc alloys have excellent grain boundary stability, it is naturally expected that GBS will be operative at faster strain rates [105] which is confirmed in Figure 4.3 (b) as the superplastic regime extends to higher strain rates in the material tested at 673 K compared with the metal tested at 523 K.

During deformation at high temperatures, subgrains tend to be developed within the grains and it is well established, for both metals [235] and ceramics [236], that the average subgrain size, λ, is dependent upon stress through the relationship

$$\lambda = \zeta \mathbf{b} \left(\frac{\sigma}{G}\right)^{-1} \quad (4.1)$$

where **b** is the Burgers vector, G is the shear modulus and ζ is a constant having a value of ~20.

Grain coarsening was observed in the UFG Al-3Mg-0.2Sc alloy after plastic deformation at various strain rates and elevated temperatures. Figure 4.12 shows a plot of grain size against the modulus-compensated stress, σ/G, for different temperatures and strain rates where the value of σ corresponds to the maximum flow stress in ECAP for an Al-1.5Mg alloy [24] and the Al-3Mg-0.2Sc alloy used in this investigation. The two lower broken lines labelled $\bar{L}_{(0,298\ K)}$ and $\bar{L}_{(0,673\ K)}$ refer to the measured grain sizes in the Al-Mg-Sc alloy of ~250 and ~600 nm immediately after ECAP and after ECAP and annealing at 673 K for 10 min, respectively. Additionally, the solid line represents the theoretical prediction for λ in Al-Mg alloys using Eq. 4.1 with ζ = 20, **b** = 2.86×10^{-10} m and G (MPa) = $(3.022 \times 10^4) - 16T$ [237].

The experimental data from testing conditions in which grain softening is observed in Al-Mg alloys are represented as open symbols in Figure 4.12. It is apparent that $\bar{L} < \lambda$ for the Al-3Mg-0.2Sc alloy tested at 523 K and $\bar{L} \approx \lambda$ for the Al-1.5Mg samples deformed in equivalent conditions. In addition, $\bar{L} << \lambda$ for the ECAP-processed Al-Mg-Sc alloy pulled to failure at 673 K. It is well stablished that GBS is accommodated by dislocation slip [238–240] and thereby the presence of LAGBs delays this accommodation process, leads to an incipient opening of cavities and cracks at triple junctions and ultimately promotes premature failure in materials during plastic straining [241]. Accordingly, subgrains are almost absent in the ECAP-processed Al-3Mg-0.2Sc alloy deformed at 3.3×10^{-3} s^{-1} at 673 K as confirmed in Figure 4.12 (b) and thus both the high diffusivity at 673 K and the faster accommodation process during GBS permit the achievement of an extensive superplastic elongation of ~980 % at this testing condition.

It is readily noted from Figure 4.12 that $\bar{L} \geq \lambda$ for UFG Al-1.5Mg and the Al-3Mg-0.2Sc alloy subjected to dynamic testing. It is also apparent from the OIM images in Figure 4.8, and from the histograms in Figure 4.9, that the ECAP-processed samples tested at 4.0×10^3 s^{-1} have higher fractions of LAGBs by comparison with the annealed Al alloy. In addition, these LAGBs are mostly organized as subgrains and are more pronounced in the material tested at 673 K. It also follows from Figure 4.12 that the subgrain sizes after dynamic testing are slightly larger than immediately before testing. Nevertheless, in addition to the strong

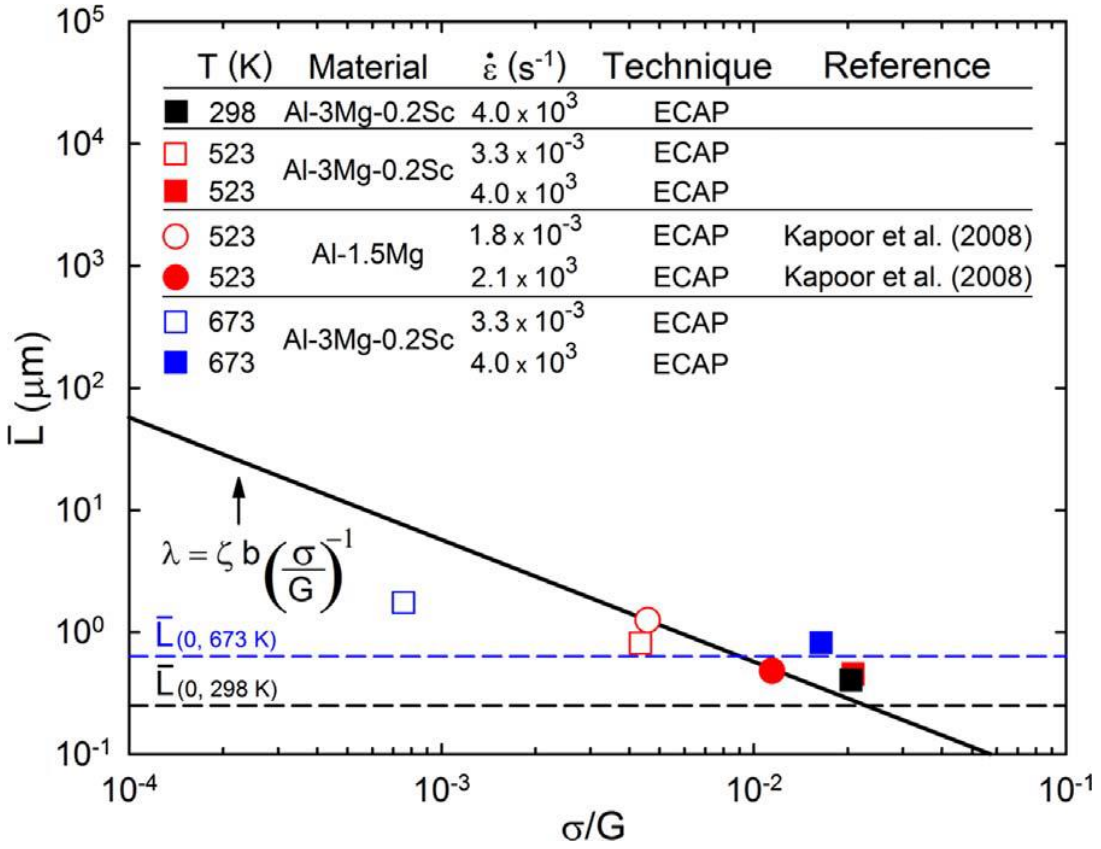

Figure 4.12 - Average grain boundary spacing, $\bar{L}$, vs modulus-compensated stress, σ/G, for the Al-1.5Mg alloy [24] and the Al-3Mg-0.2Sc alloy processed by ECAP and mechanically tested at various temperatures and strain rates: the two broken lines denote the measured grain sizes in the Al-Mg-Sc alloy immediately after ECAP ($\bar{L}_{(0,298\ K)}$) and after ECAP and annealing at 673 K for 10 min ($\bar{L}_{(0,673\ K)}$) and the solid line represents the theoretical prediction for λ using Eq. 4.1.

deformation texture, the DRX grains are equiaxed and homogeneously distributed as shown in Figures 4.8 (c) and (d). Also, the ECAP-processed alloy exhibits excellent strength and only very limited grain coarsening even after extensive straining at very high strain rates. Therefore, as the Al-3Mg-0.2Sc alloy preserves the grain refinement attained during ECAP processing and no cracks are visible in the compressed samples, it is concluded that the UFG Al-3Mg-0.2Sc alloy is a potential candidate for applications demanding light-weight materials with good ductility and high impact resistance.

4.4 Summary and Conclusions

1. An Al-3% Mg-0.2% Sc alloy was processed by ECAP at room temperature to produce a grain size of ~250 nm. This grain size increased to ~600 nm after annealing for 10 min at 673 K. Mechanical testing was conducted in both the solution treated and the ECAP-processed metal at different temperatures over a very wide range of strain rates up to dynamic testing at 4.0×10^3 s^{-1}.
2. Excellent mechanical properties were achieved after ECAP processing. The results confirm the validity of the Hall-Petch relationship down to grain sizes of ~0.1 μm.
3. Profuse shear banding and grain refinement were observed in the coarse-grained material during dynamic testing. The ECAP-processed alloy exhibited only minor coarsening and a reasonably uniform distribution of grains after testing at 4.0×10^3 s^{-1}.
4. Dynamic strain ageing occurred in both the coarse and UFG Al-Mg-Sc alloy when deforming at 298 K for strain rates below ~10^{-1} s^{-1}. The results suggest dislocation climb as the rate-controlling mechanism for the coarse-grained alloy at 673 K and at strain rates from ~10^{-4} to ~10^{-2} s^{-1}. In the ECAP-processed alloy, the strain rate sensitivity was ~0.5 at low strain rates which is consistent with superplastic flow.

Chapter 5 Influence of Processing Temperature on the Thermal Stability and Superplastic Behaviour of an Al-Mg-Sc Alloy Processed by ECAP

5.1 Introduction

There have been numerous studies showing the superplastic properties of Al-Mg-Sc alloys processed by ECAP [43,45,156,159,180,182,183,189]. The Al-3Mg-0.2Sc alloy subjected to 8 passes of ECAP at room temperature achieves an elongation of ~2580 % after tensile testing at 3.3×10^{-3} s^{-1} at 723 K [43]. Conversely, a record elongation of ~4100 % was attained in the Al-5Mg-0.2Sc-0.08Zr alloy processed through 10 passes of ECAP at 598 K and subsequently pulled to failure at 723 K at 5.6×10^{-2} s^{-1} [45]. It is worth mentioning that finer grain sizes are obtained after ECAP at ambient temperature [43] and the Al-5Mg-0.2Sc-0.08Zr alloy processed by ECAP at an elevated temperature displays excellent microstructural stability as demonstrated in recent investigations [45,47].

These readily distinct superplastic behaviours motivated the studies presented in this chapter which aims to examine the influence of processing temperature on the thermal stability and mechanical properties of an Al-Mg-Sc alloy processed by ECAP. The microstructural evolution and stored energy of the ECAP-processed Al-3Mg-0.2Sc alloy during plastic deformation and further annealing is evaluated through SEM, EBSD and XRD analysis. Furthermore, it is important to note mechanical testing is performed using miniature tensile specimens with the same geometry normally used for HPT samples to permit a direct comparison of the elongations to failure.

5.2 Experimental Results

5.2.1 Microstructural Stability of the ECAP-Processed Al-Mg-Sc Alloy

5.2.1.1 Microhardness Measurements

Figure 5.1 shows the variation of the Vickers microhardness recorded along the *Z* direction on the longitudinal plane *Y* of Al-3Mg-0.2Sc billets in the solution treated condition and after processing by ECAP at different temperatures. For simplification purposes, samples of the Al alloy immediately after 8 passes of ECAP at 300 K and 10 ECAP passes at 600 K are henceforth also denoted as ECAP-RT and ECAP-HT material, respectively.

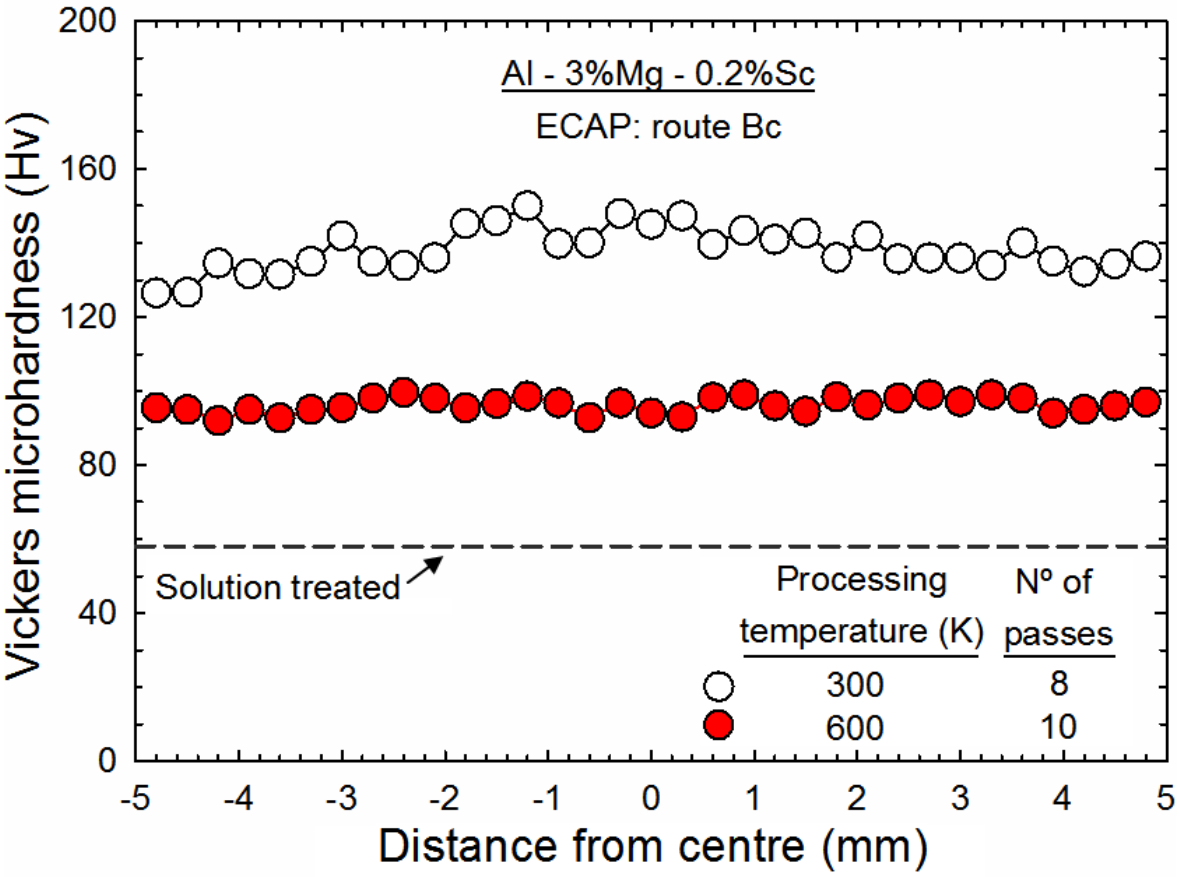

Figure 5.1 - Variation of the Vickers microhardness recorded along the Z direction on the longitudinal plane Y of Al-3Mg-0.2Sc billets processed by ECAP at either 300 or 600 K.

Inspection of Figure 5.1 reveals that the hardness of the unprocessed metal is ~58 Hv and after ECAP processing there is a substantial increase in the microhardness values along the diameter of the billets. After 8 passes of ECAP processing, hardness values of ~150 Hv are apparent in the central region of the sample and the hardness decreases with increasing distance from the centre of the ECAP billet such that the Vickers microhardness is ~130 Hv at radial positions located at >4 mm from its centre. It also follows from Figure 5.1 that the hardness distribution along the diameter of the ECAP-RT material processed at room temperature is locally inhomogeneous as noticed by the variations of the Vickers microhardness. By contrast, the Al-3Mg-0.2Sc alloy has an average microhardness of ~96 Hv after processing by 10 passes of ECAP at 600 K and its hardness distribution is essentially uniform along the Z direction of the billets.

Hardness measurements were taken over the longitudinal plane Y and the cross-sectional plane X of the Al-3Mg-0.2Sc billets processed by 8 passes of ECAP at 300 K and 10 passes of ECAP at 600 K following a rectilinear grid pattern as illustrated in Figure 3.1. Accordingly, colour-coded contour maps were constructed using these measurements as shown in Figures 5.2 and 5.3.

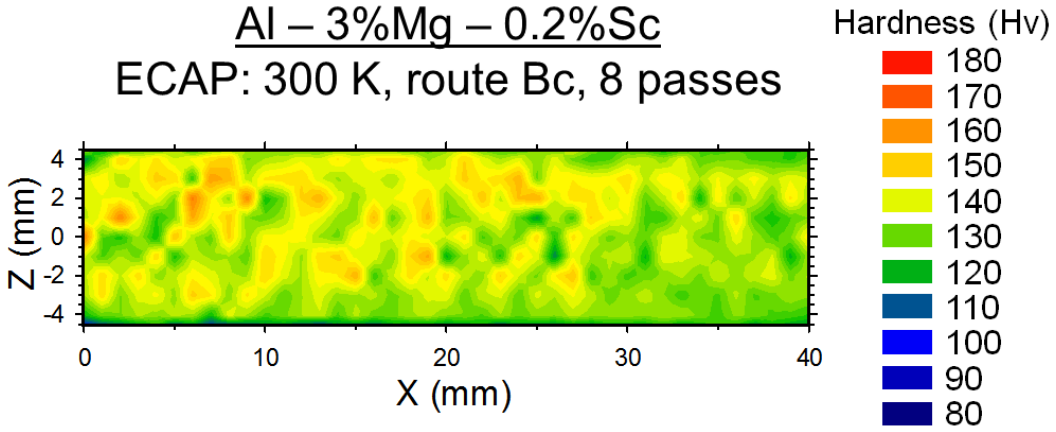

Figure 5.2 - Colour-coded contour maps showing the distributions of the Vickers microhardness over the longitudinal plane Y of the Al-3Mg-0.2Sc billet subjected to 8 passes of ECAP processing at room temperature.

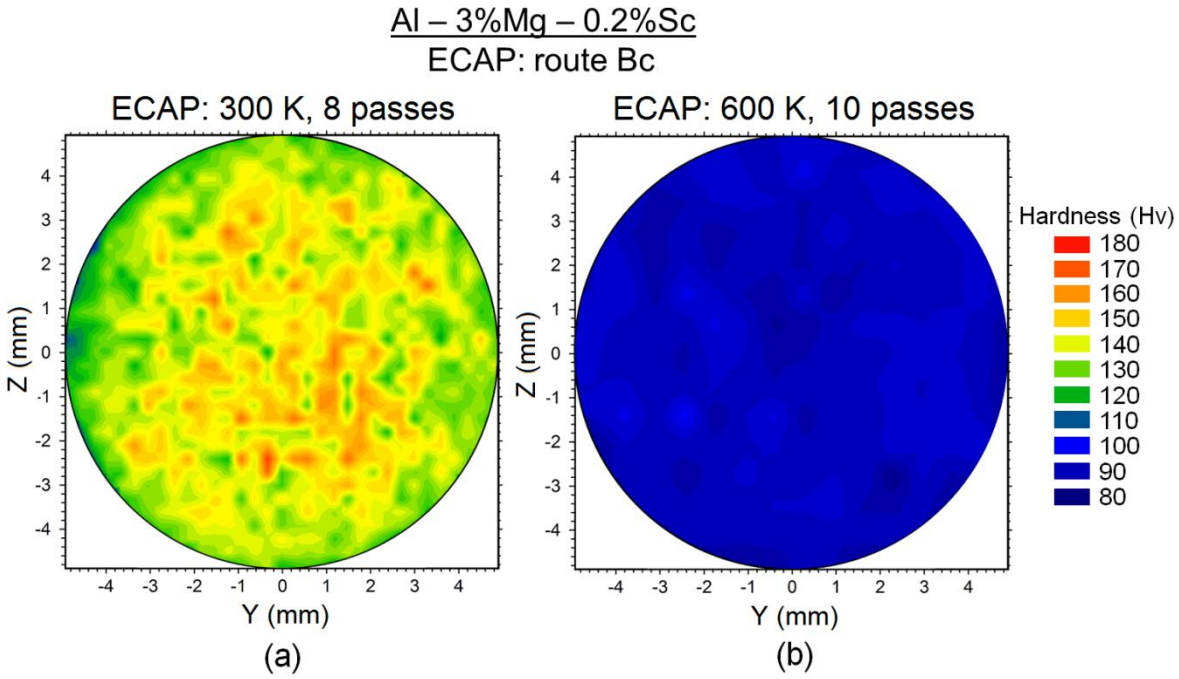

Figure 5.3 - Colour-coded contour maps showing the distributions of the Vickers microhardness over the cross-sectional plane X of the Al-3Mg-0.2Sc billets processed by (a) 8 passes of ECAP at 300 K and (b) 10 passes of ECAP at 600 K.

Examination of Figures 5.2 and 5.3 (a) reveals that hardness values ranging from ~120 to 150 Hv are found over the longitudinal surface and the cross-section of the billets after processing by 8 passes of ECAP at room temperature. In addition, low hardness values are displayed close to the head of the billets at X ≈ 40 mm. It is interesting to note that the local variations of the Vickers microhardness apparently follow a periodic pattern such that there are regions with nearly constant hardness along a direction with an inclination of ~45° in relation to the X direction. Conversely, it is clearly seen in Figure 5.3 (b) that the

microhardness distribution is fairly homogeneous along the entire cross-section of the ECAP-HT billet which displays hardness values within the interval from ~90 to 100 Hv.

A comparison between Figures 5.1 and 5.3 shows that there is excellent agreement between the colour-coded contour maps and the hardness measurements taken in the longitudinal plane of the ECAP-processed alloy and this consistently confirms the representativeness of the plots depicted in Figure 5.1. Following ECAP processing, cylinders with ~5 mm in height were cut from the processed billets and then annealed for 1 h at temperatures ranging from 423 to 773 K. These cylinders were ground and polished down to their middle-sections to obtain mirror-like surfaces along the ECAP planes Y. Afterwards, hardness measurements were taken through the Z direction in order to evaluate the variation of the Vickers microhardness in samples of an Al-Mg-Sc alloy processed by ECAP at either 300 or 600 K after further annealing as displayed in Figures 5.4 and 5.5, respectively.

It is readily noted from the plots depicted in Figures 5.4 that post-SPD annealing leads to a significant decrease in the hardness values of the Al-3Mg-0.2Sc alloy processed by ECAP at 300 K. Furthermore, the distribution of the Vickers microhardness for the ECAP-RT billets becomes fairly homogeneous with increasing annealing temperatures. By contrast, it is

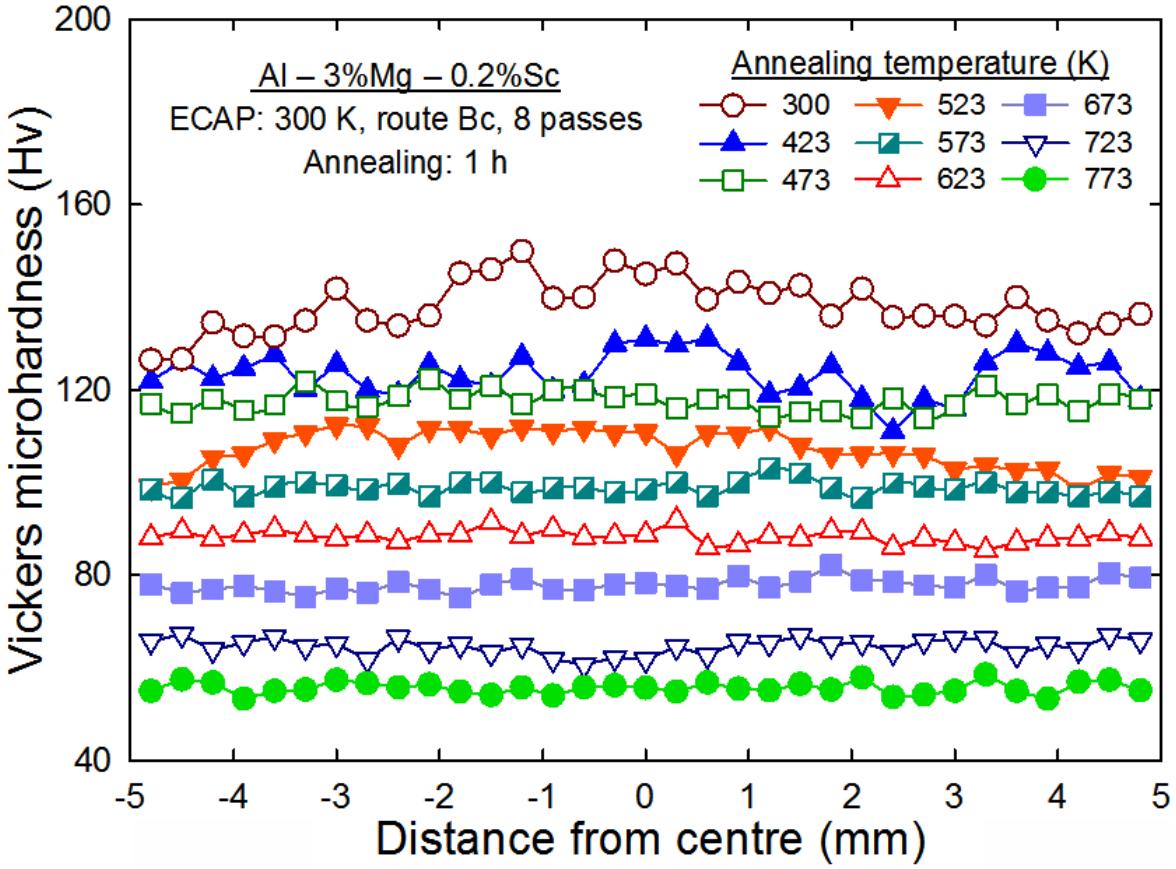

Figure 5.4 - Variation of the Vickers microhardness recorded along the Z direction on the longitudinal plane Y of Al-3Mg-0.2Sc billets after processing by ECAP at 300 K and further annealing.

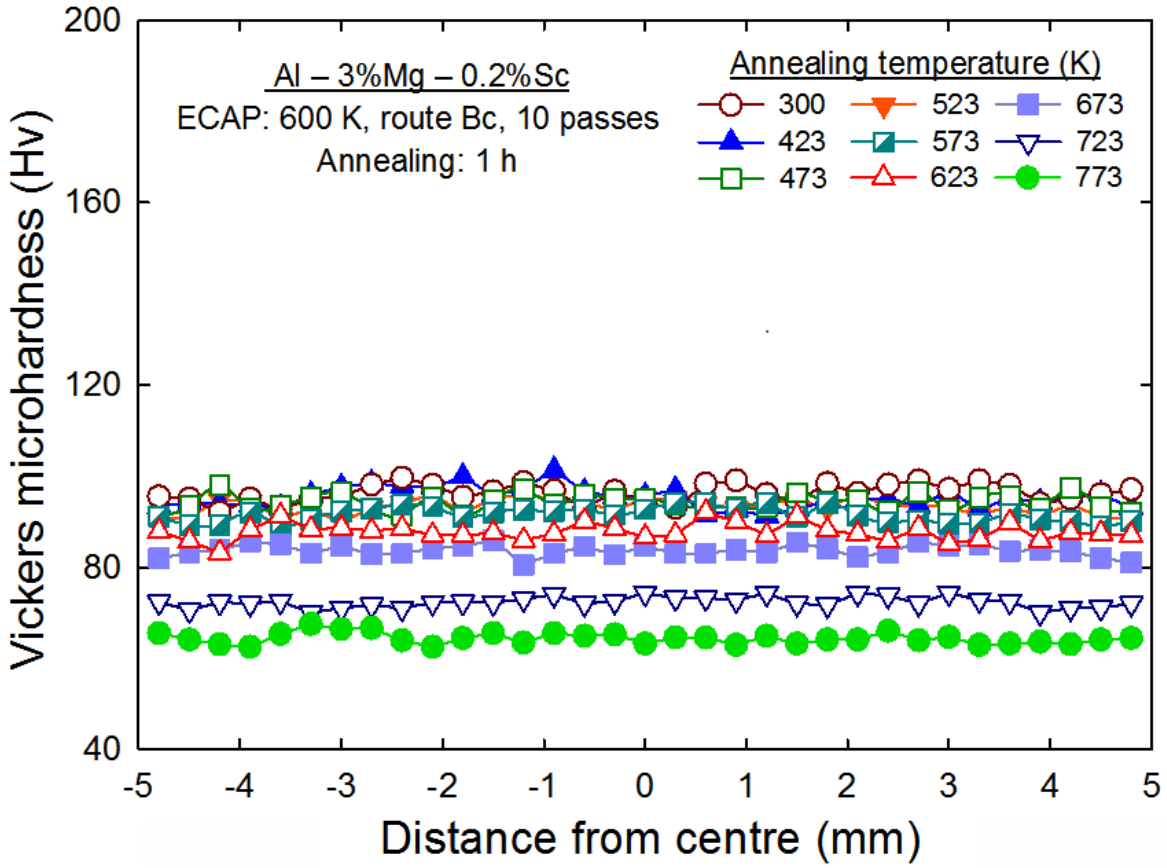

Figure 5.5 - Variation of the Vickers microhardness recorded along the Z direction on the longitudinal plane Y of Al-3Mg-0.2Sc billets after processing by ECAP at 600 K and further annealing.

evident in Figure 5.5 that there are no significant changes in the overall microhardness distributions of the Al alloy processed by ECAP at 600 K and further annealed for 1 h at $T \leq 573$ K, although the hardness values noticeably decrease after annealing at $T \geq 623$ K.

In order to show more clearly the evolution of the Vickers microhardness after post-ECAP annealing, Figure 5.6 displays the variation of the average microhardness as a function of annealing temperature for the Al-3Mg-0.2Sc alloy processed by 8 passes of ECAP at 300 K and 10 passes of ECAP at 600 K and subsequently annealed for 1 h at different temperatures. It follows from Figure 5.6 that the average microhardness of the ECAP-RT material continuously decreases with increasing annealing temperatures and this occurs at slightly faster rates for $T > \sim 473$ K. By contrast, it is clearly observed in Figure 5.6 that the average hardness values of the Al-3Mg-0.2Sc alloy processed by ECAP at an elevated temperature remain almost unchanged after annealing up to $T \approx 623$ K.

The results displayed in Figure 5.6 demonstrate that the material processed at 600 K exhibits superior average microhardness compared with the Al alloy processed by ECAP at 300 K after annealing at $T > \sim 623$ K. It is also apparent that the Vickers microhardness vs

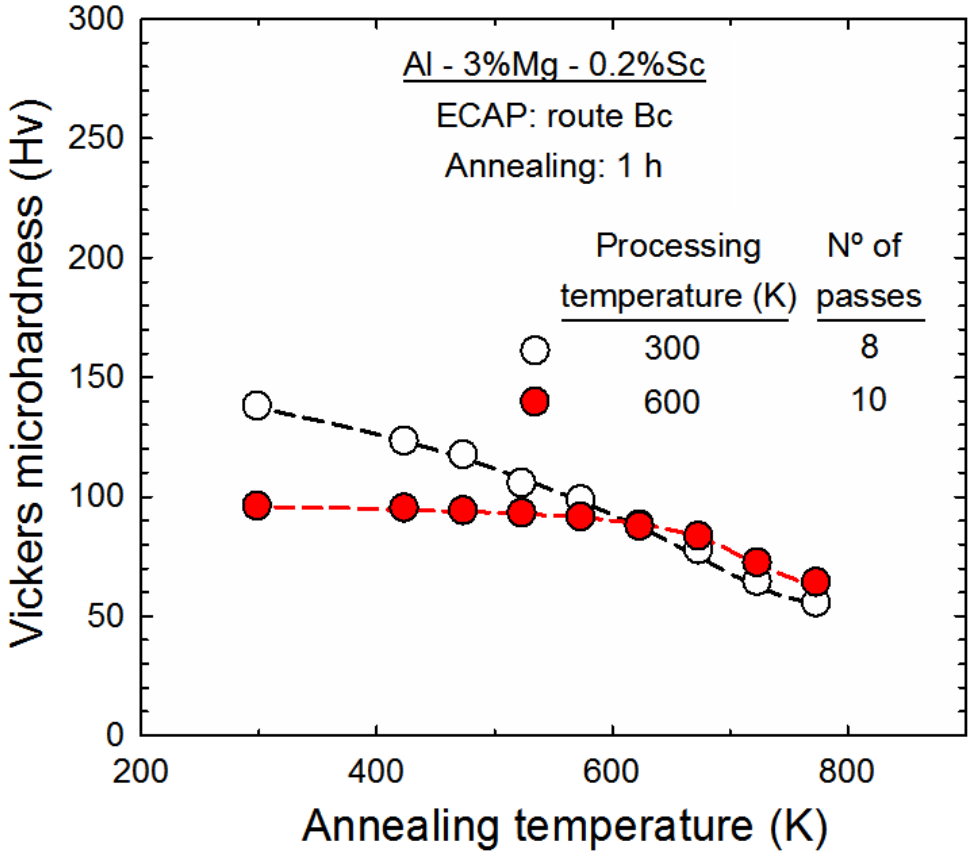

Figure 5.6 - Average microhardness as a function of annealing temperature for the Al-3Mg-0.2Sc billets processed by 8 passes of ECAP at 300 K and 10 passes of ECAP at 600 K and annealed for 1 h at different temperatures.

annealing temperature plots have similar slopes for the Al-Mg-Sc alloy processed by ECAP at both temperatures after heat treatment for 1 h at $T \geq 673$ K.

5.2.1.2 Microstructural Evolution

Figure 5.7 shows typical SEM images obtained along the plane Y in the middle-section of the Al-3Mg-0.2Sc alloy immediately after processing by either (a) 8 passes of ECAP at 300 K or (b) 10 passes of ECAP at 600 K. It follows from Figure 5.7 that reasonably uniform arrays of ultrafine grains were developed in the Al-3Mg-0.2Sc alloy during ECAP processing at either 300 or 600 K. The grain structures of the ECAP-RT material are slightly elongated and have an average size of ~250 nm as measured in Figure 5.7 (a) using the linear intercept method. By contrast, the same Al alloy exhibits fairly equiaxed grains with $\bar{L} \approx 600$ nm after processing by 10 passes of ECAP at 600 K.

The grain structures along the longitudinal plane Y of the Al-3Mg-0.2Sc billets processed by ECAP were also examined from OIM images obtained through EBSD scans performed using step sizes of 40 and 75 nm for the processing temperatures of 300 and 600 K, respectively, as shown in Figure 5.8.

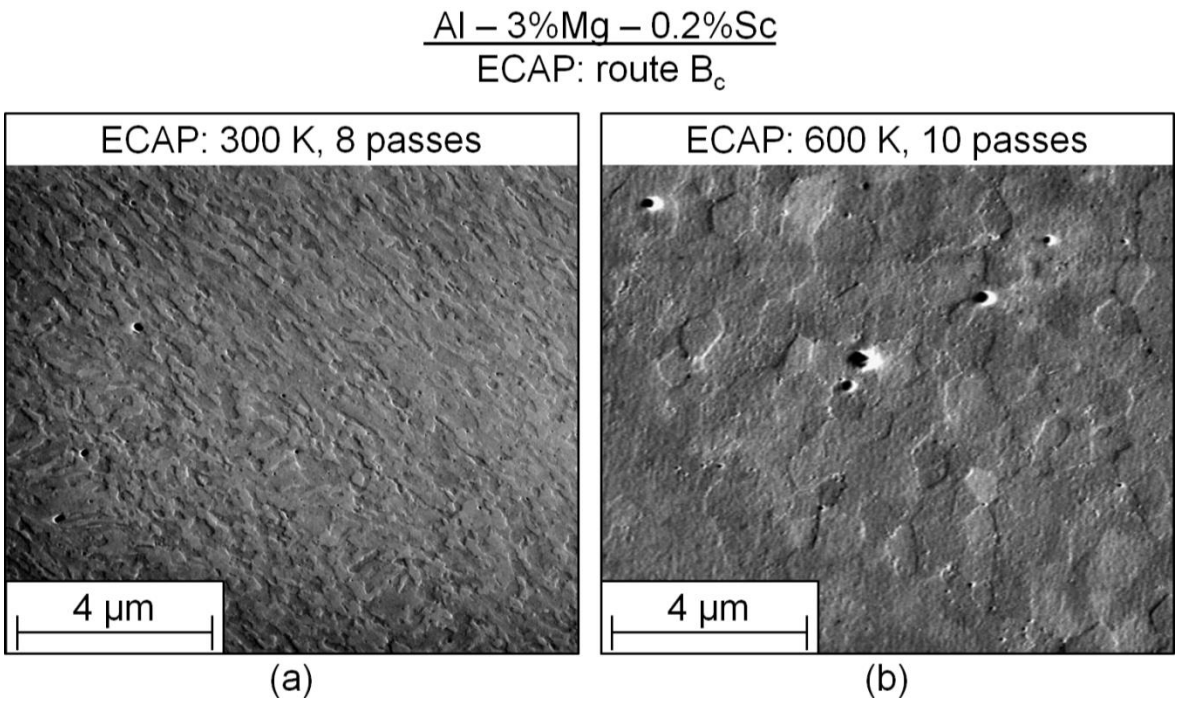

Figure 5.7 - SEM images of the Al-3Mg-0.2Sc alloy processed either by (a) 8 passes of ECAP at 300 K or (b) 10 passes of ECAP at 600 K.

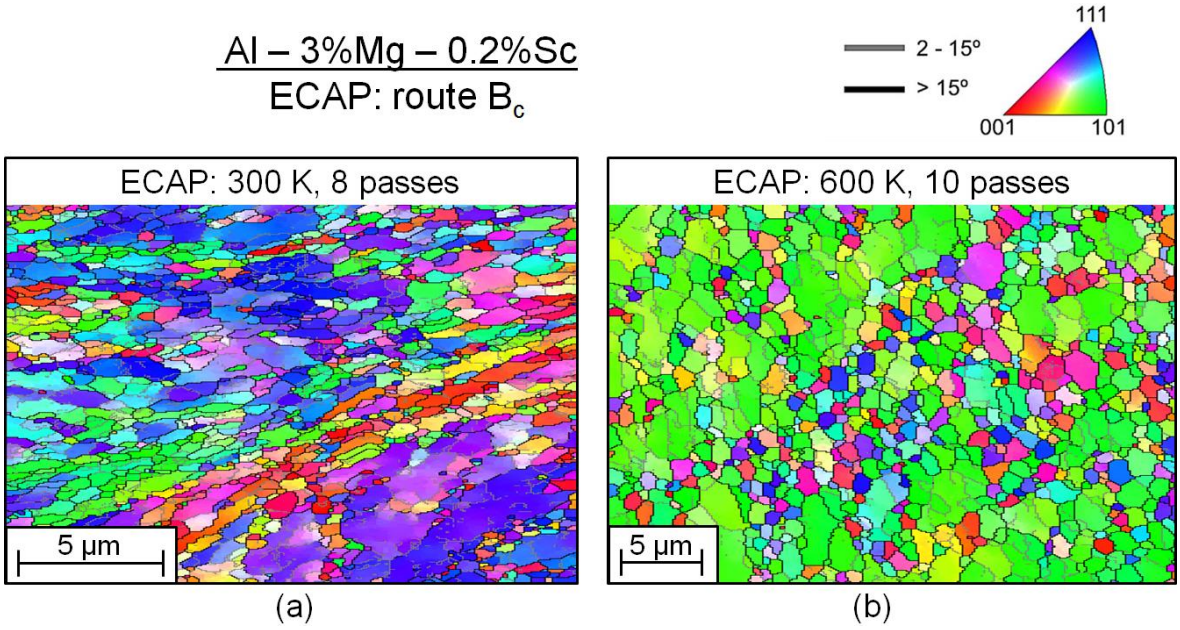

Figure 5.8 - OIM images of the Al-3Mg-0.2Sc alloy processed either by (a) 8 passes of ECAP at 300 K or (b) 10 passes of ECAP at 600 K.

Inspection of Figure 5.8 (a) reveals that the microstructure of the Al alloy processed by ECAP at ambient temperature is mostly formed by ultrafine grains with HAGBs. Conversely, it is also evident in Figure 5.8 (a) that representative areas of the ECAP-processed material were not fully refined and continue having large fractions of substructures with LAGBs even after 8 passes of ECAP using route B_c. Similarly to Figure 5.7 (a), it is also apparent in the OIM

image that the grain structures after 8 ECAP passes at 300 K are elongated and $\bar{L} \approx 250$ nm as estimated considering intercepts with misorientation angles higher than 15°.

It follows from Figure 5.8 (b) that the ECAP-HT alloy exhibits equiaxed grains with sizes in the submicrometre range together with a group of larger grains having a significant fraction of subgrains with LAGBs and a strong texture component around {110}. In addition, an average grain boundary spacing of ~0.63 μm was calculated using the OIM image displayed in Figure 5.8 (b) in good agreement with the measurements from typical SEM images.

The microstructural stability of the Al-3Mg-0.2Sc alloy was examined by conducting systematic EBSD scans in the material processed by ECAP and subsequently heat treated at different temperatures. Figures 5.9 and 5.10 display representative OIM images of the Al-3Mg-0.2Sc alloy processed by ECAP at 300 and 600 K, respectively, and further annealed at temperatures ranging from 523 to 773 K for 1 h.

It is apparent in Figure 5.9 (a) that annealing at 523 K for 1 h leads to minor changes on the grain structures of the material processed by 8 ECAP passes at room temperature as the average grain boundary spacing increases to ~0.4 μm and the ultrafine grains have less extreme aspect ratios. Furthermore, Figures 5.9 (b) and (c) demonstrate that, although additional grain coarsening occurs in the ECAP-RT metal after annealing for 1 h at 623 and 673 K, respectively, the microstructure of this Al alloy continues having an essentially uniform array of grains with HAGBs, with the exception of some areas with a strong texture component around {111} which display a large fraction of structures with LAGBs.

By contrast, it is clearly revealed in Figures 5.9 (d) and (e) that there is abnormal grain growth in the Al-3Mg-0.2Sc alloy processed by 8 passes of ECAP at 300 K and annealed for 1 h at $T \geq 723$ K as indicated by the formation of a bimodal distribution of grains. Additionally, it is apparent in these OIM images that the fine grain structures with few micrometres in size are now generally limited by LAGBs and the area fraction of coarse grains with $\bar{L} \geq 10$ μm noticeably increases with increasing annealing temperatures.

Figure 5.10 shows that there are no significant changes in the overall distributions of grains in the Al-Mg-Sc alloy processed by 10 passes of ECAP at 600 K after annealing for 1 h at $T \leq 673$ K, except for some limited grain coarsening. In contrast with the ECAP-RT material, abnormal grain growth is not observed in this Al alloy after ECAP processing at 600 K and subsequent annealing at $T \geq 723$ K. On the other hand, it is noted in Figure 5.10 (e) that, although the grain size distribution is apparently uniform after annealing for 1 h at 773 K, grain coarsening occurs at faster rates compared with the metal annealed at lower temperatures and there is a concomitant increase in the fraction of structures with LAGBs.

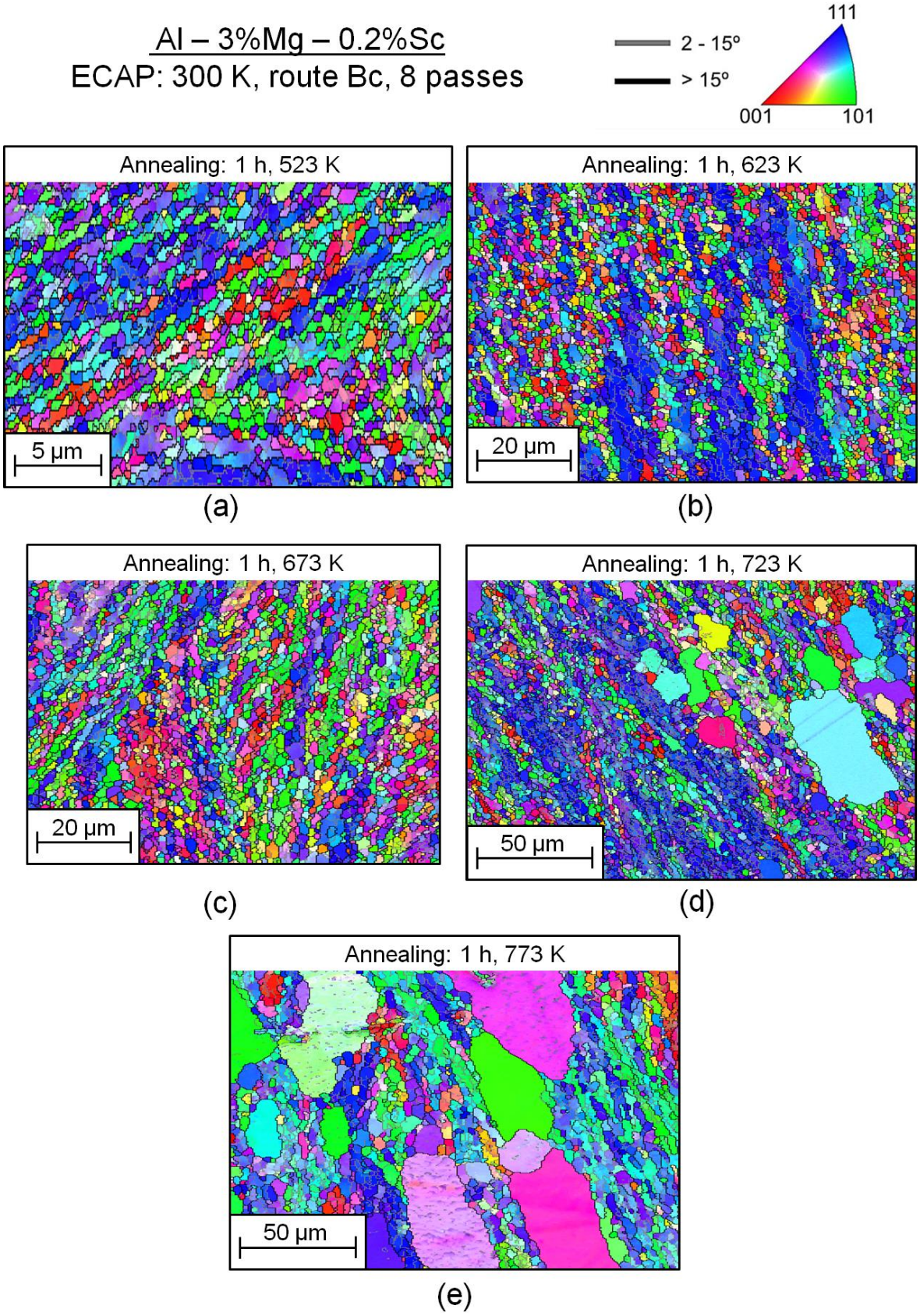

Figure 5.9 - OIM images of the Al-3Mg-0.2Sc alloy processed by 8 passes of ECAP at 300 K and subsequently annealed at (a) 523, (b) 623, (c) 673, (d) 723 and (e) 773 K for 1 h.

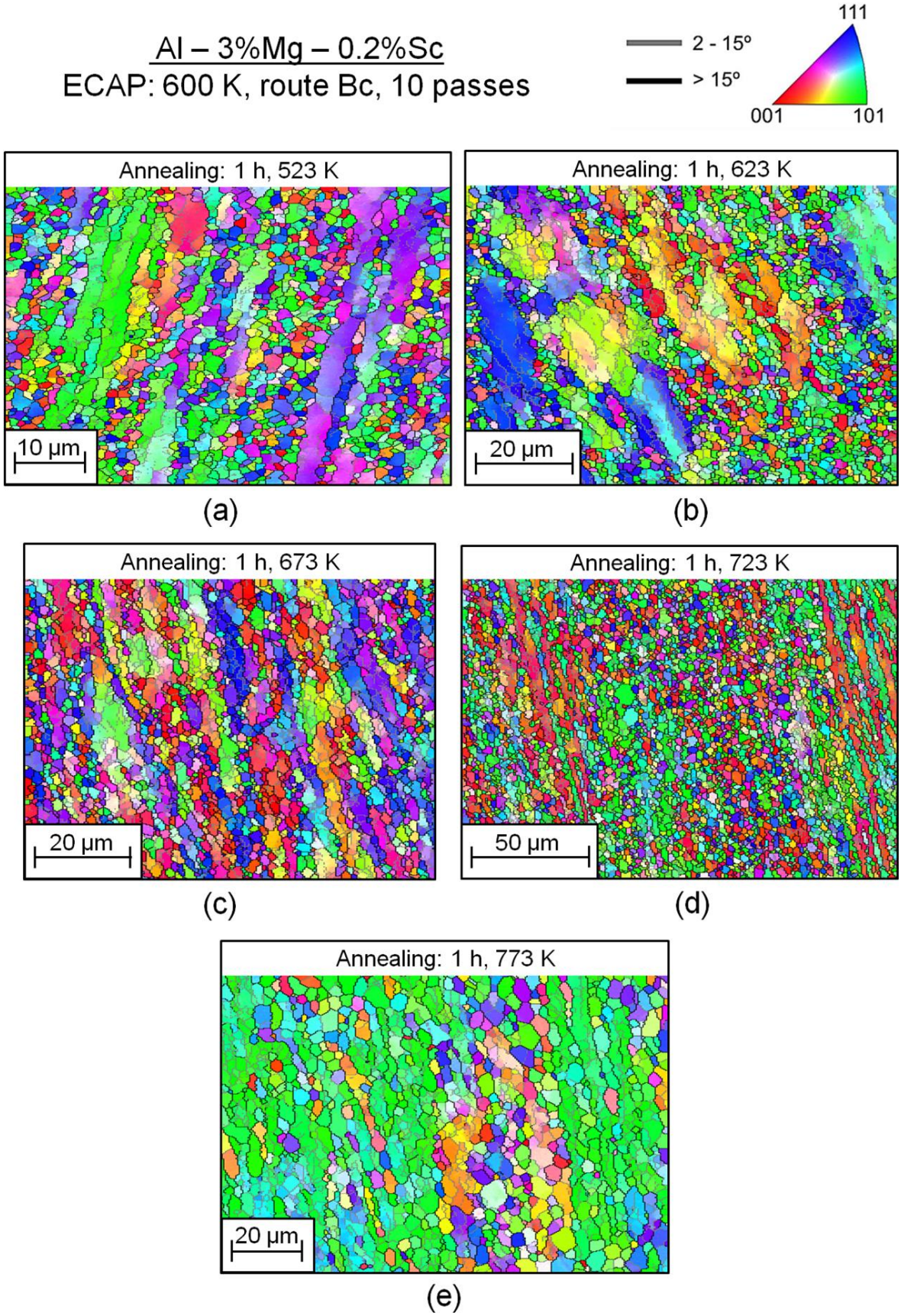

Figure 5.10 – OIM images of the Al-3Mg-0.2Sc alloy processed by 10 passes of ECAP at 600 K and subsequently annealed at (a) 523, (b) 623, (c) 673, (d) 723 and (e) 773 K for 1 h.

The grain sizes of the Al-3Mg-0.2Sc alloy immediately after ECAP processing and after annealing for 1 h at different temperatures were measured in the OIM images depicted in Figures 5.8, 5.9 and 5.10 using the linear intercept method. Accordingly, in order to directly compare the influence of processing temperature on the thermal stability after ECAP, Figure 5.11 shows the variation of the average grain boundary spacing, $\bar{L}$, as a function of annealing temperature for the material processed by ECAP at either 300 or 600 K and further annealed for 1 h at temperatures ranging from 523 to 773 K.

It is readily seen in Figure 5.11 that there is only a limited grain coarsening in the ECAP-processed metal after annealing at 523 K, regardless of the processing temperature. Conversely, the growth rate of the grain structures with HAGBs noticeably increases during annealing at $T > 623$ K for the Al-Mg-Sc alloy processed by ECAP at 300 K as the originally UFG metal has grains with $\bar{L} \geq 1$ μm after annealing for 1 h at $T \geq 673$ K.

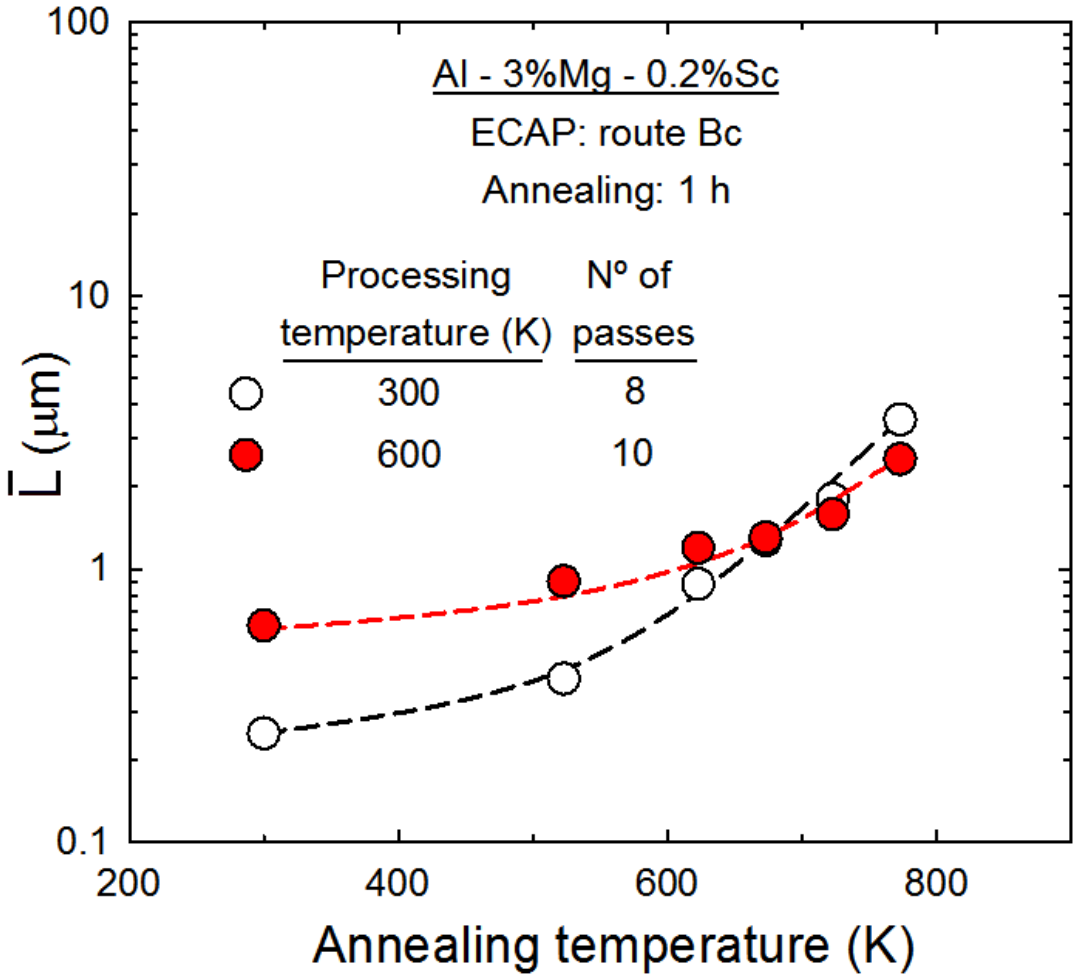

Figure 5.11 – Average grain boundary spacing, $\bar{L}$, as a function of annealing temperature for the Al-3Mg-0.2Sc alloy processed by ECAP at different temperatures and further annealed for 1 h at temperatures ranging from 523 to 773 K.

Inspection of Figure 5.11 also reveals that, although the Al-Mg-Sc alloy processed by 10 passes of ECAP at 600 K has coarser grains compared with the ECAP-RT metal, its microstructure is more thermally stable as only minor grain growth is observed during annealing for 1 h at temperatures up to ~723 K. After heat treatment at T > 673 K, the material processed by ECAP at 300 K exhibits larger grains by comparison with the Al alloy processed by ECAP at 600 K, as evident from the plots shown in Figure 5.11. Additionally, it is important to note that the rate of grain coarsening in the metal processed by ECAP at 600 K increases for annealing temperatures higher than 723 K, however $\bar{L}$ < 3 μm even after annealing at 773 K.

It follows from the OIM images depicted in Figures 5.8 that the microstructure of the Al-3Mg-0.2Sc alloy was intensively refined during ECAP processing. Nevertheless, it is also noted that even after annealing, there are regions in the microstructure not fully developed having grains with few micrometres in size and a large fraction of substructures with LAGBs. Furthermore, it is also apparent in Figure 5.9, that annealing at $T \geq 723$ K leads to the onset of a bimodal distribution of grains and the estimation of grain size based on the mean linear intercepts may underestimate this microstructural parameter.

In order to provide a more quantitative representation of the different distributions of grains with HAGBs after different processing and heat treatment conditions, histograms of the area fraction of grain diameters for the ECAP-processed alloy before and after post-SPD annealing are shown in Figure 5.12. The calculations of the individual grain diameters were performed using the OIM images depicted in Figures 5.8, 5.9 and 5.10 based on the equivalent circle diameter method in which the diameter of each grain is defined as the diameter of a circle with the same area as its corresponding grain [161].

It is readily seen in Figure 5.12 (a) that ~74 % of the analysed area of the Al-3Mg-0.2Sc alloy immediately after ECAP processing at 300 K corresponds to grains with diameters < 1 μm, whereas this area fraction is ~43 % for the ECAP-HT material. It also follows from Figure 5.12 (a) that a significant number of grains has an equivalent diameter higher than 2 μm for both processing temperatures and therefore the values of the area-weighted average grain diameter calculated based on these distributions are superior to the values estimated for the grain sizes using the linear intercept method.

The results displayed in Figures 5.12 (e) demonstrate that the histograms of the Al alloy processed by ECAP at either 300 or 600 K and further annealed at 723 K are very similar considering equivalent diameters up to ~10 μm. Nevertheless, it is evident in Figures 5.12 (e) and 5.12 (f) the presence of exceptionally coarse grains in the material processed by ECAP at room temperature and heat treated at $T \geq 723$ K. These grains have diameters higher

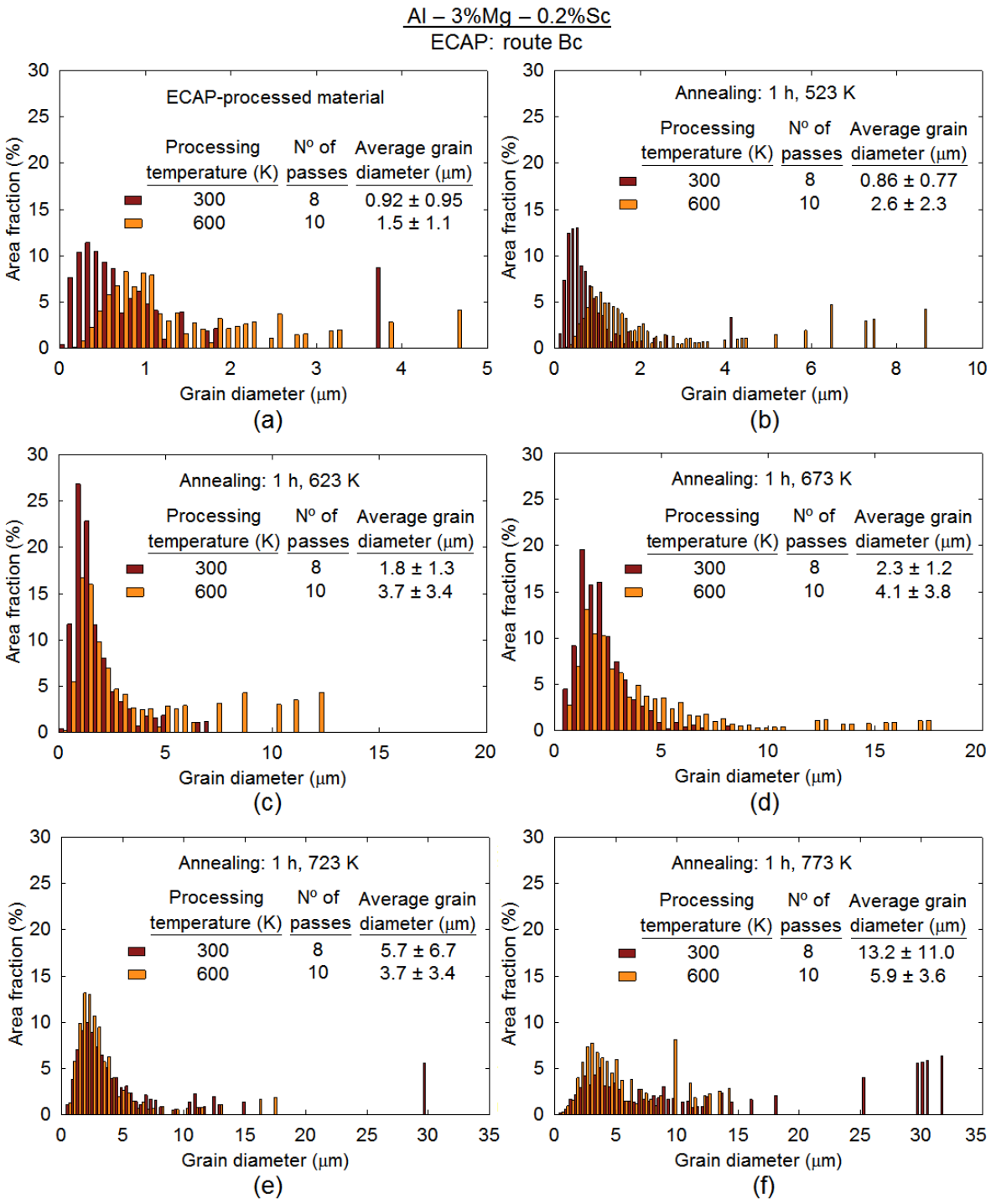

Figure 5.12 - Histograms of the area fraction of grain diameters for the Al-3Mg-0.2Sc alloy (a) immediately after processing by ECAP at either 300 or 600 K and after further annealing at (b) 523, (c) 623, (d) 673, (e) 723 and (f) 773 K for 1 h.

than 10 μm and correspond to 15 and 42 % of the area fraction of the OIM images displayed in Figures 5.9 (d) and 5.9 (e), respectively. In addition, it is relevant to note the presence of few grains with equivalent diameters higher than 10 μm in the metal processed by ECAP at 600 K and further annealed at $T \geq 723$ K, however, there is a large fraction of LAGBs within these structures and thus it is unlikely that they are associated with abnormal coarsening.

Figure 5.13 shows the variation of the average grain diameter, d_{eq}, calculated using the histograms displayed in Figure 5.12, with the annealing temperature for the Al-3Mg-0.2Sc alloy processed by ECAP and further annealed for 1 h within the temperature interval from 523 to 773 K. A comparison of the plots in Figures 5.11 and 5.13 reveals the grain size measurements using the linear intercept method gives lower values for the average grain size than the procedure used to calculate d_{eq}, especially for the annealing conditions displaying duplex structures. Conversely, both plots show the same general trend for the evolution of grain sizes after annealing, regardless of the procedure used in these estimations.

It is clearly seen in Figure 5.13 that the metal processed by ECAP at 300 K has lower grain diameters compared with the ECAP-HT material after annealing at $T \leq 673$ K. Furthermore, the rate of grain coarsening in the Al alloy subjected to 8 passes of ECAP at room temperature drastically increases during heat treatment at $T \geq 723$ K as a result of the onset of abnormal grain growth.

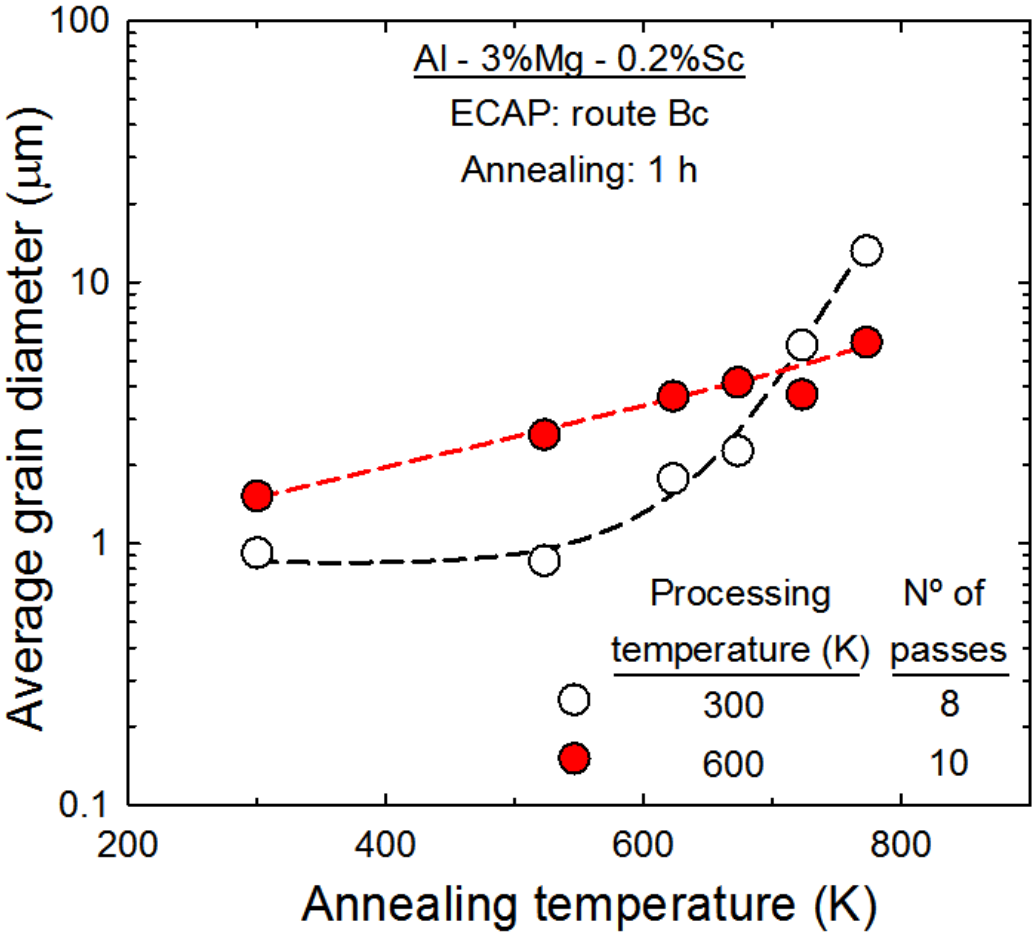

Figure 5.13 – Area-weighted average grain diameter as a function of annealing temperature for the Al-3Mg-0.2Sc alloy processed by ECAP at different temperatures and further annealed for 1 h at temperatures ranging from 523 to 773 K.

The fractions of grain boundaries are plotted in Figure 5.14 as a function of the misorientation angles for the Al alloy processed under the same conditions as in Figure 5.12. Inspection of Figure 5.14 reveals that the correlated pixel-to-pixel misorientation distributions [204] of the ECAP-processed alloy do not conform closely with the Mackenzie distribution [205] due to the development of a defined texture during ECAP processing and the presence of substructures with LAGBs. The material processed by 10 ECAP passes at 600 K exhibits a higher fraction of HAGBs by comparison with the same metal immediately

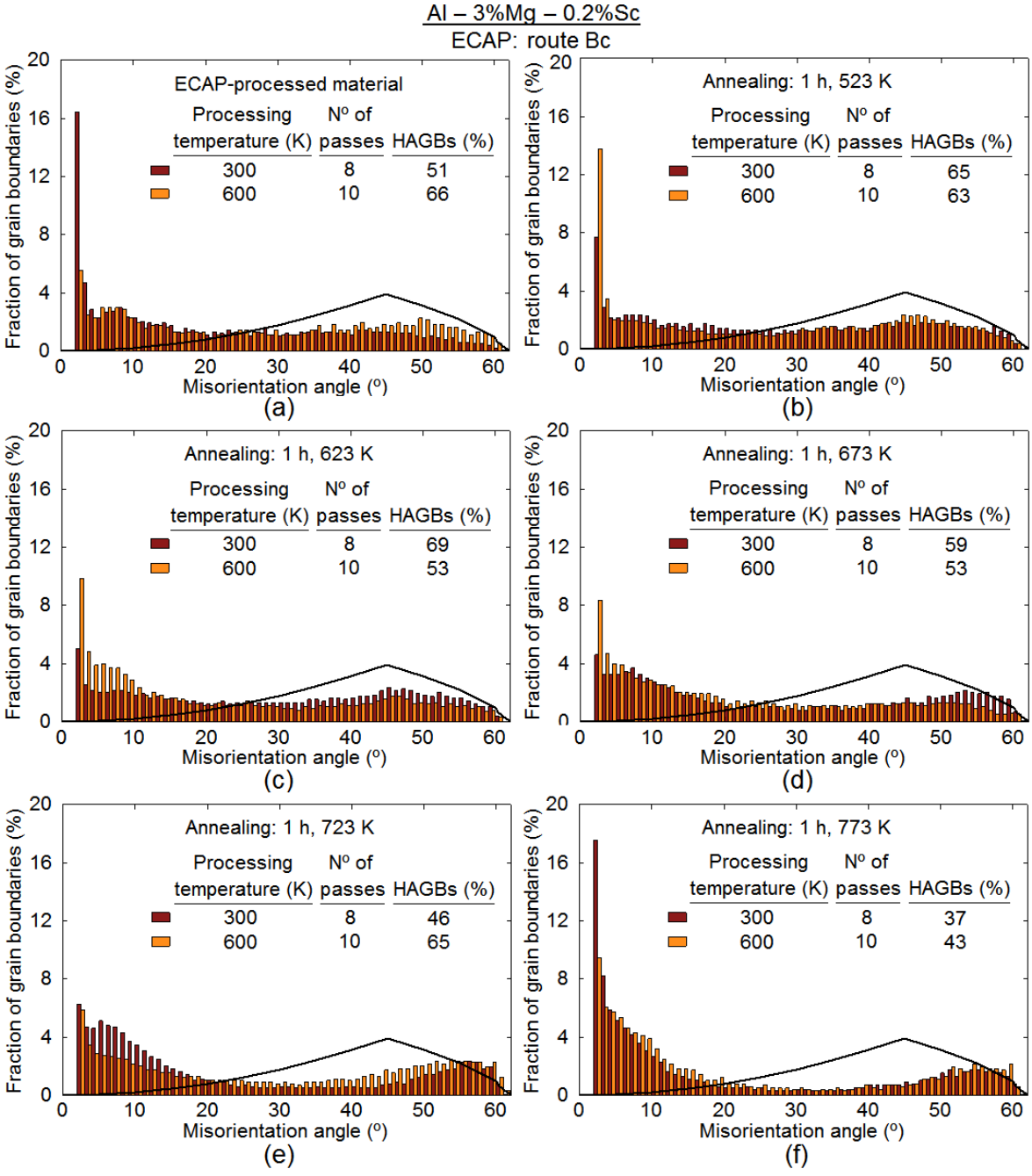

Figure 5.14 - Histograms of the misorientation angles for the Al-3Mg-0.2Sc alloy (a) immediately after processing by ECAP at either 300 or 600 K and after further annealing at (b) 523, (c) 623, (d) 673, (e) 723 and (f) 773 K for 1 h.

after ECAP at ambient temperature. Conversely, the proportion of HAGBs in the Al-Mg-Sc alloy processed at 300 K increases after annealing for 1 h at temperatures up to 623 K and this becomes even larger than in the material processed by ECAP at 600 K after annealing at equivalent conditions.

The results in Figure 5.14 demonstrate that there is a significant increase in the fraction of LAGBs in the material processed by ECAP at 300 K after annealing at $T \geq 673$ K, whereas samples processed at 600 K continue having relatively low fractions of substructures even after post-SPD heat treatment at 723 K. Also, it is interesting to note that the fractions of HAGBs substantially decrease during annealing for 1 h at 773 K for the Al-3Mg-0.2Sc alloy processed by ECAP at both conditions and their misorientation distributions become very similar although their microstructures are considerably distinct.

XRD patterns were recorded along the cross-sectional plane X of the Al-3Mg-0.2Sc billets immediately after ECAP processing. Thereafter, these patterns were used to determinate the lattice microstrain, the average crystallite size and the dislocation density for the ECAP-processed alloy and the values obtained from these calculations are shown in Table 5.1.

It follows from Table 5.1 that average crystallite sizes of ~160 and 270 nm were estimated for samples processed by ECAP at either 300 or 600 K, respectively. It is important to note that these values are significantly lower than the average grain sizes estimated for the alloy processed by ECAP at equivalent conditions and this may be attributed to the presence of substructures with LAGBs as D_c corresponds to the size of domains in the microstructure which coherently scatter X-ray [242]. Furthermore, the results obtained from XRD examinations reveal that the density of dislocations in the metal processed by ECAP at 300 K is slightly higher than in the same alloy after ECAP a 600 K.

Table 5.1 - Lattice microstrain, $\langle \varepsilon^2 \rangle^{1/2}$, average crystallite size, D_c, and dislocation density, ρ, for the Al-3Mg-0.2Sc alloy processed by ECAP at different temperatures.

Metal-working procedure	Microstrain (%)	Crystallite size (nm)	Dislocation density ($m^{-2} \times 10^{13}$)
ECAP: 300 K, route Bc, 8 passes	0.042 ± 0.002	160 ± 3	3.2 ± 0.2
ECAP: 600 K, route Bc, 10 passes	0.058 ± 0.004	270 ± 8	2.6 ± 0.3

5.2.2 Tensile Properties and Microstructure of the ECAP-Processed Al-Mg-Sc Alloy

Samples of the Al-3Mg-0.2Sc alloy were subjected to either 8 passes of ECAP at 300 K or 10 passes at 600 K and thereafter tested in tension using a wide range of temperatures and strain rates to investigate the influence of processing temperature on the flow properties of this Al alloy. Figure 5.15 shows representative plots of true stress vs true strain for samples processed by ECAP at different temperatures and further pulled to failure at 523 and 723 K using strain rates ranging from 3.3×10^{-4} to 3.3×10^{-1} s^{-1}.

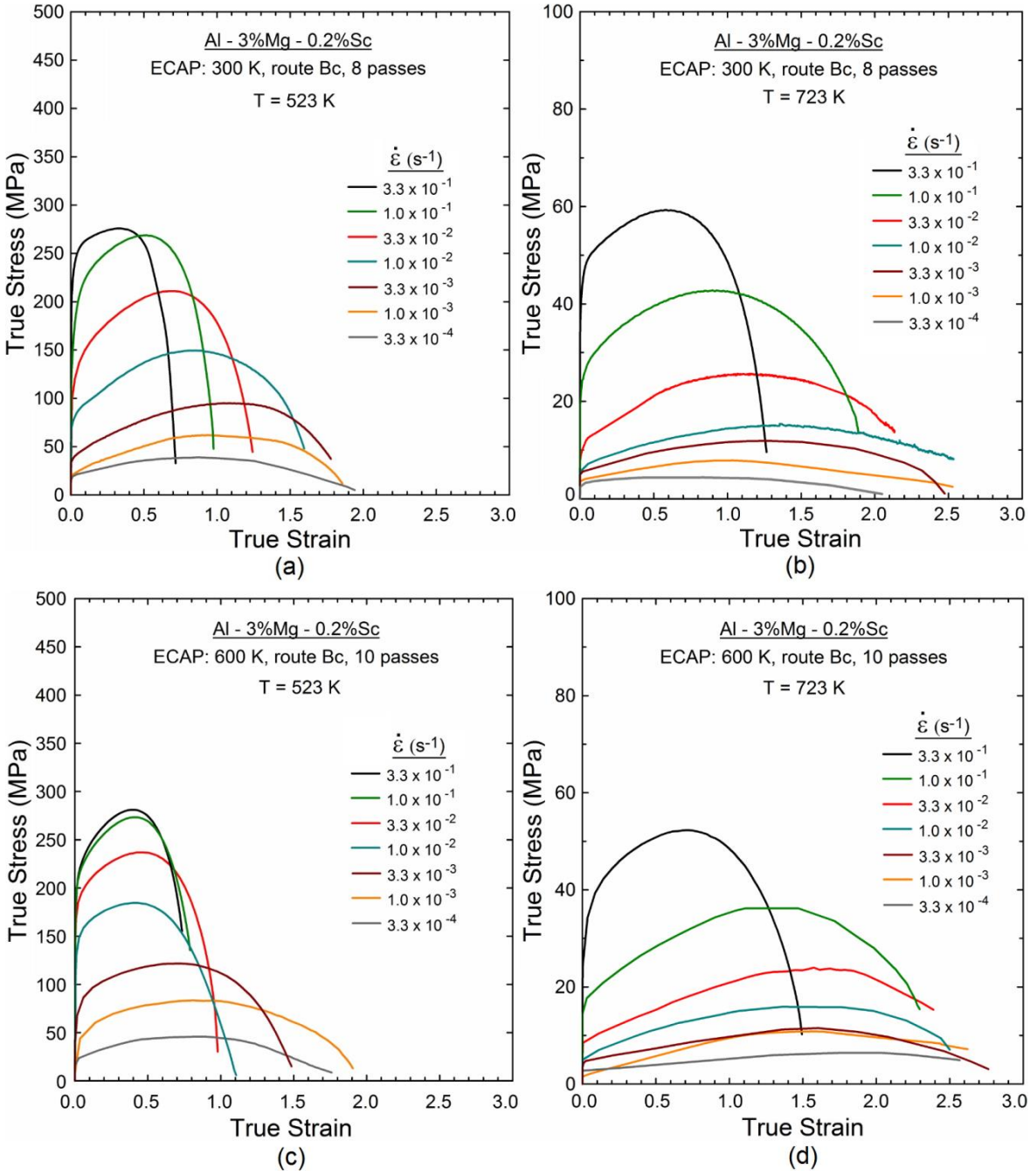

Figure 5.15 - True stress vs true strain curves of the Al-3Mg-0.2Sc alloy processed by either 8 passes of ECAP at 300 K and pulled to failure at (a) 523 and (b) 723 K or 10 passes of ECAP at 600 K and tested in tension at (c) 523 and (d) 723 K.

The results displayed in Figure 5.15 demonstrate that the mechanical behaviour of the Al-3Mg-0.2Sc alloy processed by ECAP at either 300 or 600 K is strongly influenced by the testing temperature and strain rate. Inspection of Figures 5.15 (a) and (c) reveals that the ECAP-RT material generally exhibits lower yield stresses and superior ductility compared with the Al alloy processed by ECAP at 600 K when tested in tension at 523 K at equivalent strain rates. It is noted from these plots that true strains higher than 1.5 are attained in the metal processed by ECAP at 300 K for tests conducted at 523 K using $\dot{\varepsilon} \leq 1.0 \times 10^{-2}$ s^{-1}, whereas this is only achieved in the ECAP-HT material during tensile testing at 523 K for $\dot{\varepsilon} \leq 1.0 \times 10^{-3}$ s^{-1}.

It is readily apparent in Figures 5.15 (b) and (d) that there is a major reduction in the flow stresses for the ECAP-processed alloy deformed at 723 K for all strain rates used in this investigation. It is also visible from these plots that significantly higher values of true strain are achieved in this Al-Mg-Sc alloy after increasing the deformation temperature from 523 to 723 K as plastic strains superior to 1.5 are now attained during tensile testing at initial strain rates up to 1.0×10^{-1} s^{-1}. Further examination of Figures 5.15 (b) and (d) shows that, in contrast with the results obtained during plastic straining at 523 K, the ECAP-HT material tested at 723 K mostly exhibits lower flow stresses and superior maximum strains by comparison with the Al alloy processed by ECAP at ambient temperature and deformed at similar conditions.

Figures 5.16 and 5.17 show the shapes of Al-3Mg-0.2Sc specimens after high temperature tensile testing for the material originally subjected to either 8 passes of ECAP at 300 K or 10 ECAP passes at 600 K, respectively. Additionally, the values of the elongation to failure are also displayed for each testing condition.

It follows from Figures 5.16 (a) and 5.17 (a) that the material processed by ECAP at room temperature displays superior elongations to failure compared with the ECAP-HT alloy after mechanical testing at 523 K using comparable strain rates, except for $\dot{\varepsilon} = 3.3 \times 10^{-1}$ s^{-1}. It is clearly seen in these images that elongations higher than 400 % are attained in the miniature tensile specimens of the ECAP-RT material tested at 523 K for $\dot{\varepsilon} \leq 1.0 \times 10^{-2}$ s^{-1}, whilst superplastic elongations are only achieved at $\dot{\varepsilon} \leq 1.0 \times 10^{-3}$ s^{-1} in samples originally processed by ECAP at 600 K.

The results depicted in Figures 5.16 (b) and 5.17 (b) readily show there is a substantial increase in the elongation values obtained in the ECAP-processed alloy after tensile testing at 723 K. In addition, superplastic elongations are now achieved at considerably faster strain rates as elongations to failure superior to 400 % are obtained in specimens of both the ECAP-RT and ECAP-HT material when tested at 723 K using initial

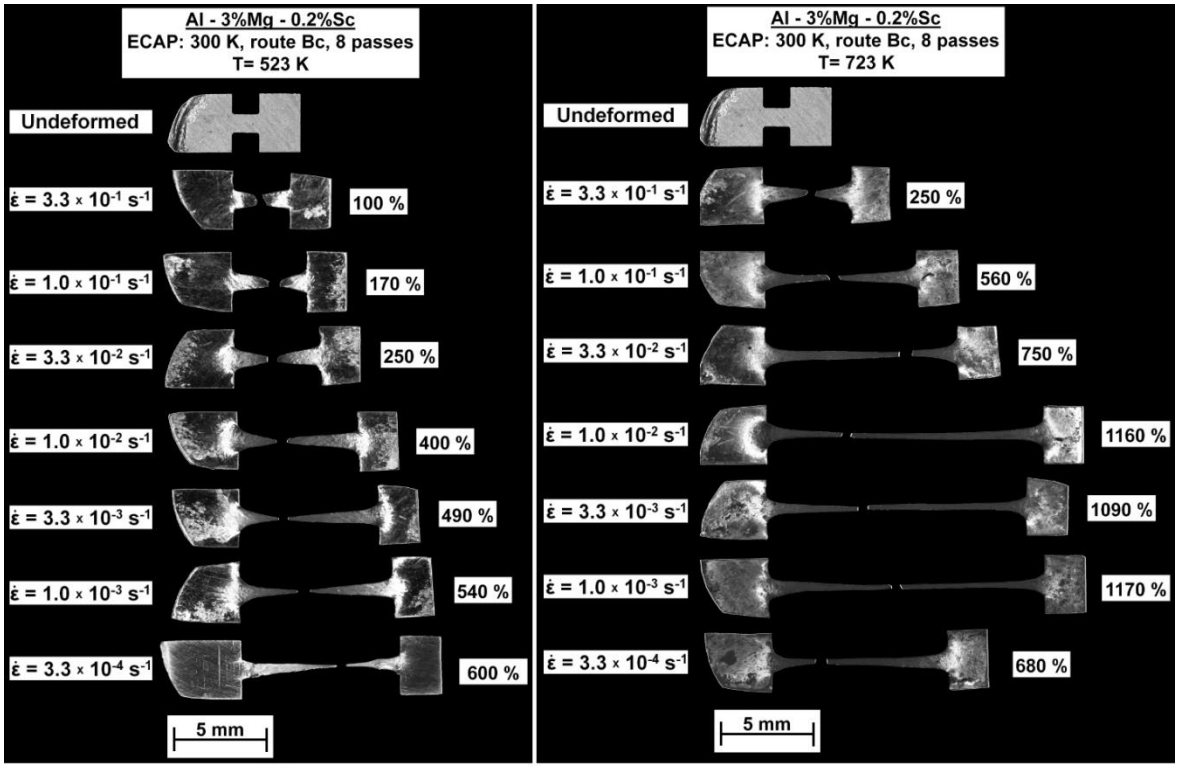

Figure 5.16 - Samples of the Al-3Mg-0.2Sc alloy subjected to 8 passes of ECAP at 300 K and further pulled to failure at (a) 523 and (b) 723 K.

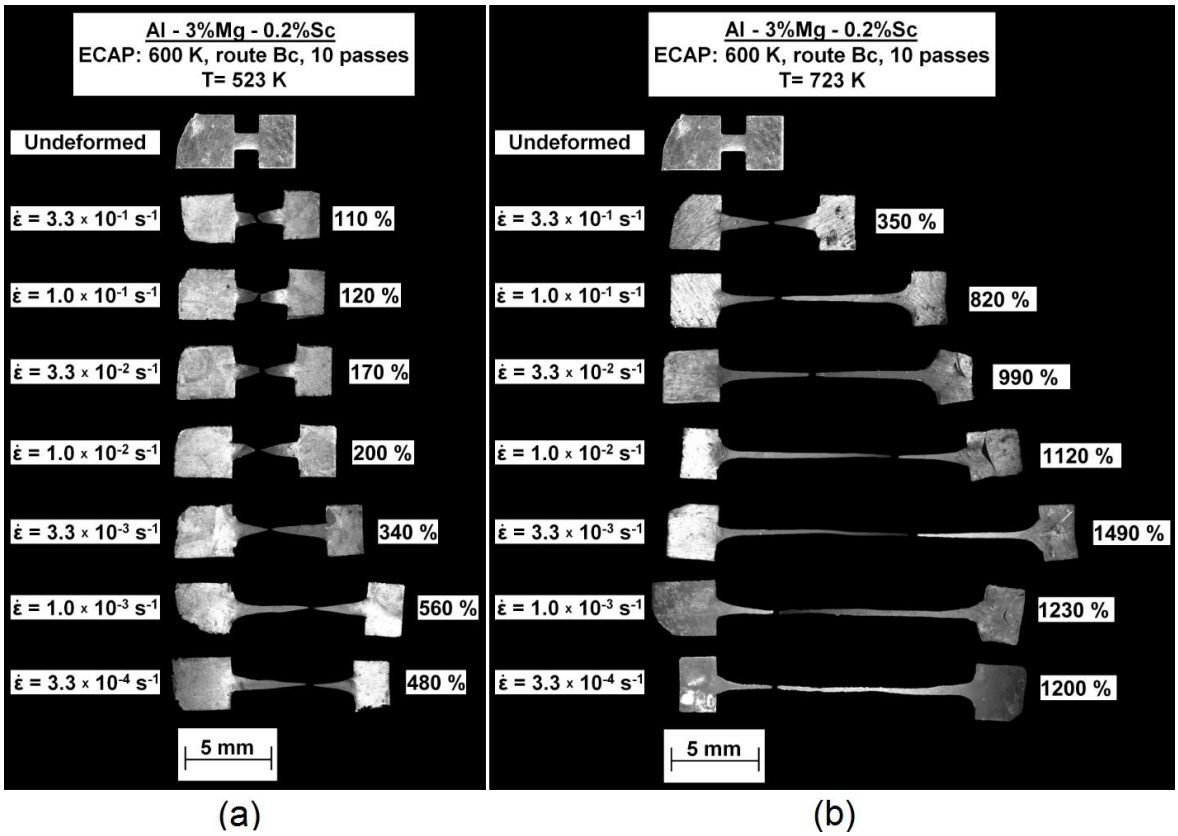

Figure 5.17 - Samples of the Al-3Mg-0.2Sc alloy subjected to 10 passes of ECAP at 600 K and further pulled to failure at (a) 523 and (b) 723 K.

strain rates up to 1.0×10^{-1} s^{-1}. A more detailed examination of these images reveals that the width of the miniature specimens exhibiting elongations higher than 1000 % is nearly the same all over their gauge sections and there is no evidence of a localized necking in the vicinity of their fracture tip.

It is also important to note that the Al alloy processed by 10 passes of ECAP at 600 K exhibits higher elongations than the ECAP-RT metal after tensile testing at 723 K using equivalent strain rates. A maximum elongation of ~1490 % was attained in the ECAP-HT material pulled to failure at 723 K at 3.3×10^{-3} s^{-1}, whereas the metal processed by ECAP at 300 K displays an elongation of ~1090 % at the same testing condition.

Figure 5.18 shows the elongations to failure obtained in miniature specimens of the Al-3Mg-0.2Sc alloy processed by ECAP at either (a) 300 or (b) 600 K and subsequently tested in tension at temperatures ranging from 523 to 773 K using strain rates from 3.3×10^{-4} to 3.3×10^{-1} s^{-1}.

It is readily observed in Figure 5.18 (a) that the elongation values of the ECAP-RT alloy consistently increase with decreasing strain rates and increasing temperatures for tests conducted at $T \leq 623$ K. Elongations to failure higher than 400 % were measured in samples tested at $\dot{\varepsilon} \geq 1.0 \times 10^{-2}$ s^{-1} at $T \geq 573$ K, indicating the occurrence of high strain rate superplasticity in the Al-Mg-Sc alloy originally processed by 8 ECAP passes at 300 K. Additionally, it is interesting to note that a superplastic elongation of ~530 % was attained in the ECAP-RT material tested at 623 K using an exceptionally high strain rate of 1.0×10^{-1} s^{-1}.

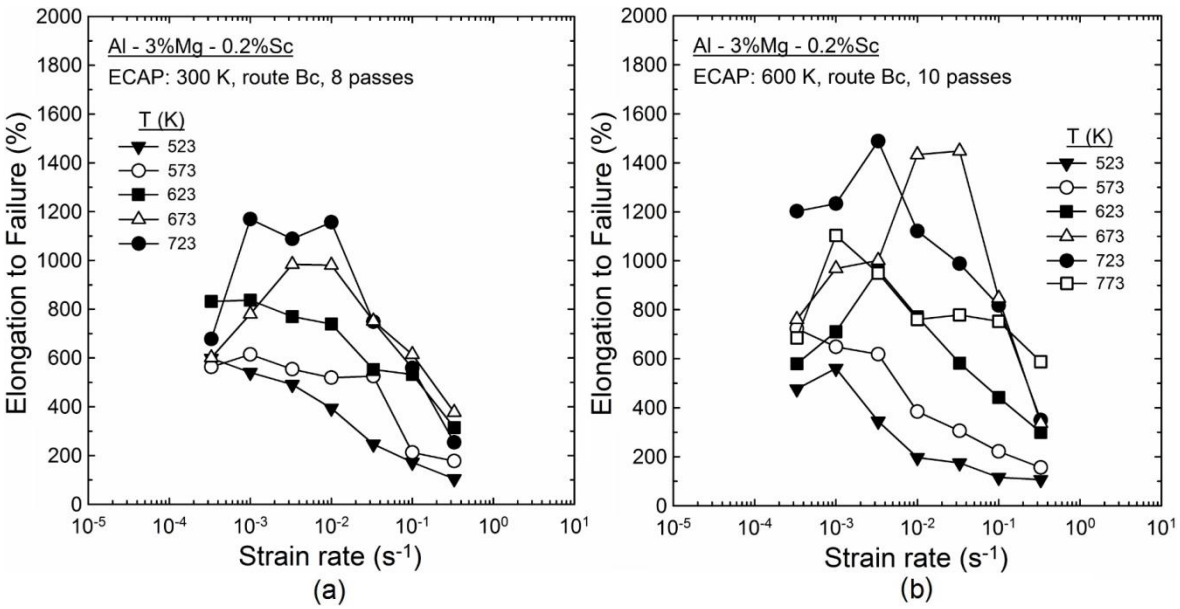

Figure 5.18 - Elongation to failure vs strain rate for the Al-3Mg-0.2Sc alloy processed by either (a) 8 passes of ECAP at 300 K or (b) 10 passes of ECAP at 600 K and further tested in tension at temperatures from 523 to 773 K.

The results shown in Figure 5.18 (a) demonstrate that, in general, the elongations of the ECAP-RT metal continue increasing with increasing testing temperatures for $T \geq 673$ K. Elongations to failure superior to 1000 % were achieved in specimens tested at 723 K within the strain rate interval from 1.0×10^{-3} to 1.0×10^{-2} s^{-1}. Conversely, it is evident in these plots that the Al-Mg-Sc alloy processed by ECAP at 300 K and further pulled to failure at $T \geq 673$ K at 3.3×10^{-4} s^{-1} exhibits inferior ductility compared to the metal tested at 623 K using the same initial strain rate. It is also worth mentioning the ECAP-RT material was not subjected to tensile testing at temperatures higher than 723 K as there are consistent evidences in the literature that the Al-3Mg-0.2Sc alloy processed by ECAP using similar processing conditions does not display superplastic elongations at 773 K [20].

Inspection of Figure 5.18 (b) reveals that elongations to failure higher than 400 % were observed in the ECAP-HT material after tensile testing at $T \leq 573$ K. However, these superplastic elongations were attained in a narrower range of strain rates by comparison with the Al alloy processed by ECAP at room temperature. It is also apparent in these plots that increasing the testing temperature to 623 K leads to an overall increase in the elongation values together with an extension of the interval of strain rates in which the ECAP-HT alloy exhibited superplastic elongations.

The experimental data in Figure 5.18 (b) consistently show that the Al-Mg-Sc alloy processed by ECAP at 600 K displays superior elongations in comparison to the ECAP-RT alloy when tested in tension at $T \geq 673$ K. Elongations to failure ≥ 1000 % were achieved in samples of the ECAP-HT material pulled to failure at $T \geq 673$ K using strain rates up to 3.3×10^{-2} s^{-1}. It is also observed in these plots that superplastic elongations were attained for the entire range of strain rates used in this study in specimens of the ECAP-HT metal tested at 773 K. Nevertheless, these elongation values are significantly lower than the values obtained in the same alloy pulled to failure at 723 K, except for $\dot{\varepsilon} = 3.3 \times 10^{-1}$ s^{-1}.

Figure 5.19 shows the variation of the flow stress at $\varepsilon = 0.3$ with the initial strain rate for samples of the Al-3Mg-0.2Sc alloy processed by either (a) 8 passes of ECAP at 300 K or (b) 10 passes of ECAP at 600 K and tested in tension at temperatures ranging from 523 to 773 K. The experimental datum points depicted in Figure 5.19 were plotted using logarithmic scales for both the strain rate and the true stress and thereby, the local slope of these curves represents the apparent strain rate sensitivity, m, of this alloy at each testing condition.

It is readily seen in Figure 5.19 (a) that the curve corresponding to the ECAP-RT material deformed at 523 K has a sigmoidal shape and displays a slope of ~0.3 for $\dot{\varepsilon} < 1.0 \times 10^{-3}$ s^{-1}. It is also apparent that m values of ~0.5 are observed at this temperature for strain rates ranging from 1.0×10^{-3} to 1.0×10^{-2} s^{-1} and these values decrease with increasing

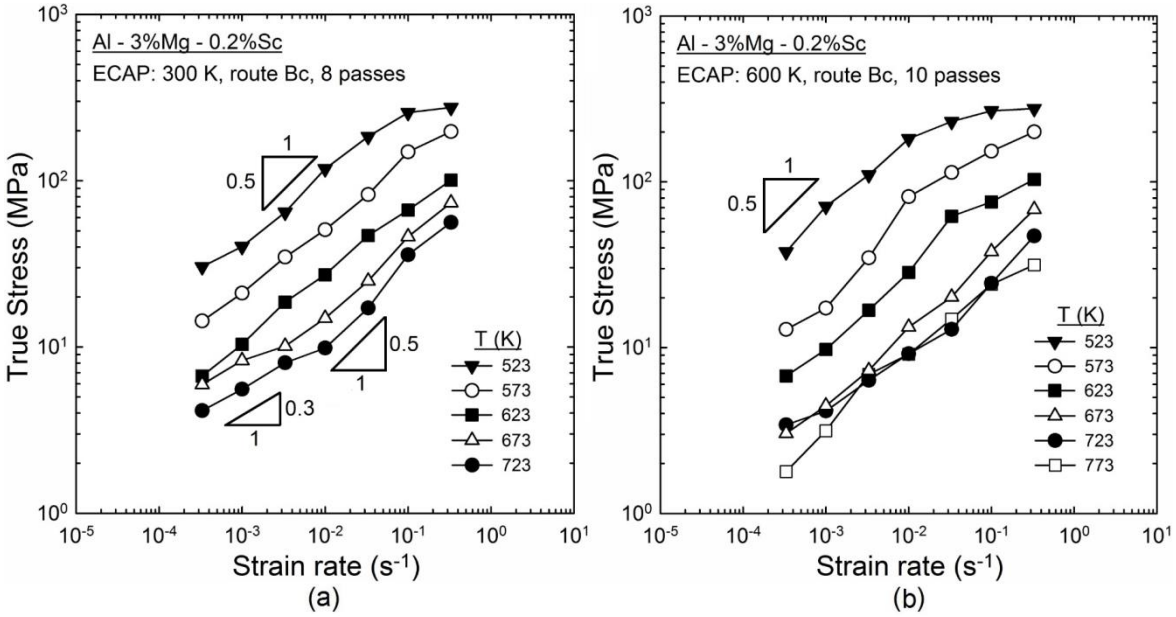

Figure 5.19 - Variation of the true stress at a true strain of 0.3 with the strain rate for samples of the Al-3Mg-0.2Sc alloy processed by either (a) 8 passes of ECAP at 300 K or (b) 10 passes of ECAP at 600 K and further pulled to failure within the temperature range from 523 to 773 K.

strain rates for $\dot{\varepsilon} > 1.0 \times 10^{-2}$ s^{-1}. Furthermore, it is noted in Figure 5.19 (a) that the region in the true stress vs strain rate plots associated with $m \approx 0.5$ expands towards faster strain rates at higher testing temperatures as evident for samples tested at 673 K within the strain rate interval from 3.3×10^{-3} to 1.0×10^{-1} s^{-1}.

It follows from Figure 5.19 (b) that the Al-3Mg-0.2Sc alloy processed by 10 passes of ECAP at 600 K exhibits higher flow stresses compared with the ECAP-RT metal when tested at 523 K using the same initial strain rate. This is also observed for samples tested at 573 K for $\dot{\varepsilon} > 3.3 \times 10^{-3}$ s^{-1}, although the differences in the true stress are almost negligible for tests performed at 1.0×10^{-1} and 3.3×10^{-1} s^{-1}. In addition, $m \approx 0.5$ for the ECAP-HT material deformed either at 523 K using $\dot{\varepsilon} \leq 1.0 \times 10^{-2}$ s^{-1} or at 573 K for strain rates within the range from 1.0×10^{-3} to 1.0×10^{-2} s^{-1}.

These results demonstrate that samples of the Al-Mg-Sc alloy processed by ECAP at either 300 or 600 K display very similar true stresses at $\varepsilon = 0.3$ when pulled to failure at 623 K at $\dot{\varepsilon} \leq 1.0 \times 10^{-2}$ s^{-1}. By contrast, the flow stresses of the ECAP-HT material are significantly reduced by increasing the testing temperature from 623 to 673 K such that this metal consistently exhibits lower flow stresses than the ECAP-RT alloy deformed at $T \geq 673$ K using comparable strain rates. It is also interesting to note that there is no significant difference in the true stress values for the ECAP-HT material tested at 723 and 773 K for $3.3 \times 10^{-3} \leq \dot{\varepsilon} \leq 1.0 \times 10^{-1}$ s^{-1}, although higher elongations are observed after testing at 723 K.

Examinations by SEM were conducted in samples of the ECAP-processed alloy after tensile testing at elevated temperatures to assess the distribution and overall morphology of the grains at the surface of deformed specimens. Figures 5.20 and 5.21 show the surface topography at the gauge area of Al-3Mg-0.2Sc specimens originally processed by ECAP at different temperatures and afterwards pulled to failure at 523 and 723 K, respectively.

It is now recognised that superplasticity occurs through the relative motion of adjacent grains in GBS [243]. Accordingly, the grain structures stand out on the surface of tensile specimens during superplastic flow and this is clearly visible in the SEM images in Figures 5.20 and 5.21. After tensile testing at 523 K at 3.3×10^{-3} s^{-1}, the ECAP-RT alloy exhibits a

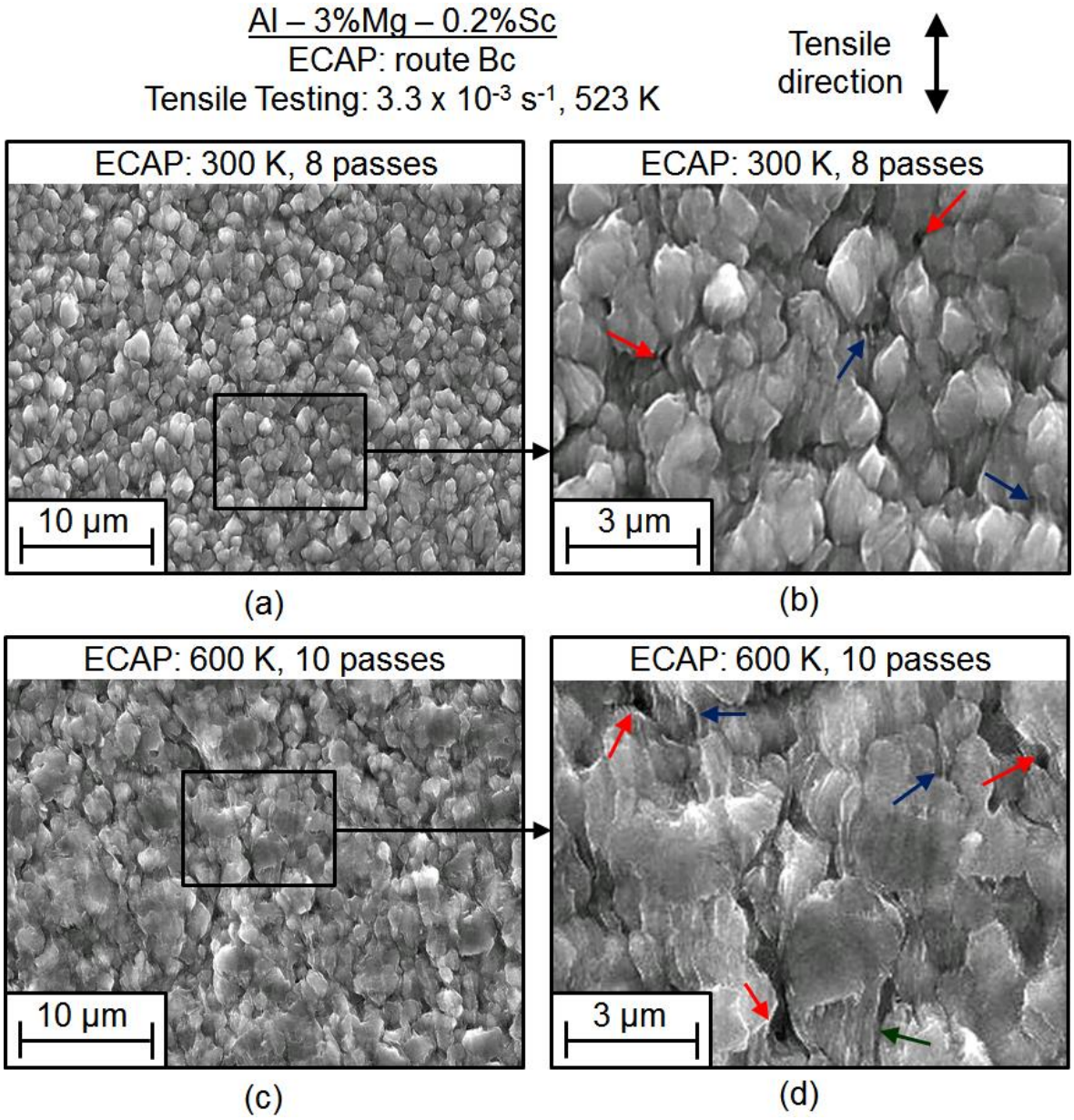

Figure 5.20 – SEM images taken along the gauge area of Al-3Mg-0.2Sc samples processed either by (a,b) 8 passes of ECAP at 300 K or (c,d) 10 passes of ECAP at 600 K and further pulled to failure at 3.3×10^{-3} s^{-1} at 523 K.

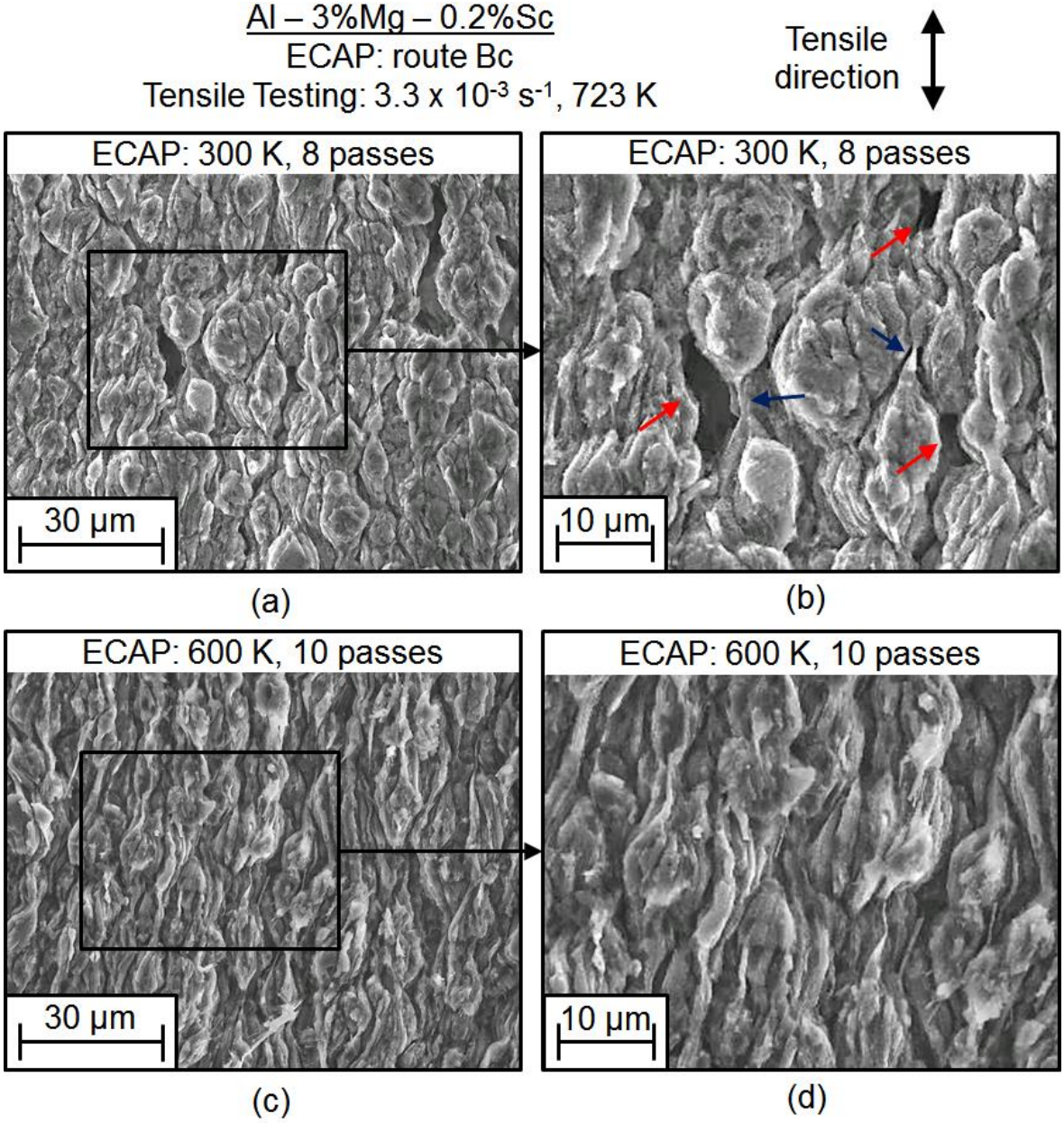

Figure 5.21 - SEM images taken along the gauge area of Al-3Mg-0.2Sc samples processed either by (a,b) 8 passes of ECAP at 300 K or (c,d) 10 passes of ECAP at 600 K and further pulled to failure at 3.3×10^{-3} s^{-1} at 723 K.

reasonably uniform microstructure formed by nearly equiaxed grains with an average size of ~0.8 μm. It is also apparent in Figure 5.20 (b) the formation of cavities at triple junctions and grain boundaries together with fibre structures nearly parallel to the tensile direction as indicated using red and blue arrows, respectively.

Figures 5.20 (c) and (d) show that the grain structures of the ECAP-HT alloy are essentially equiaxed with $\bar{L} \approx 1.1$ μm and there is intense cavitation during tensile testing at 3.3×10^{-3} s^{-1} at 523 K. Furthermore, the Al alloy originally processed by ECAP at 600 K has a more inhomogeneous distribution of grains and displays larger pores by comparison with the ECAP-RT material deformed at equivalent conditions. These SEM images also demonstrate

that grain boundary sliding is more obvious for grains with sizes in the submicrometre range, although GBS is also observed in coarser grains, as verified by the presence of striated bands after intense plastic deformation and indicated in Figure 5.20 (d) using a green arrow.

It is readily seen in Figure 5.21 that the microstructures of the Al-3Mg-0.2Sc alloy processed by ECAP at different temperatures are fairly homogeneous after testing at 723 K at 3.3×10^{-3} s^{-1}. In addition, average grain sizes of ~3.8 and ~3.5 μm were estimated using the linear intercept method for the metal initially processed by ECAP at either 300 or 600 K, respectively. It is worth mentioning that, although similar grain sizes were measured after tensile testing at 723 K, the ECAP-RT specimen attained an elongation of ~1090 %, whereas the sample originally processed by ECAP at 600 K displayed a superplastic elongation of ~1490 % and thereby was kept at the furnace of the testing machine for additional ~20 min.

It is clearly visible in Figure 5.21 (b) that some grains on the surface of the ECAP-RT material are separated by large and elongated cavities lying parallel to the tensile direction as shown using red arrows. The grain structures of the ECAP-processed alloy are somewhat elongated along the tensile direction and the fibre structures, already identified in Figure 5.20 for tests conducted at 523 K, are noticeably more abundant after tensile testing at 723 K as evident in Figure 5.21.

The grains structures along the gauge area of selected samples of the Al-Mg-Sc alloy processed by ECAP and subsequently tested in tension were also evaluated using EBSD scans performed using a step size of 400 nm. Figure 5.22 shows representative OIM images and corresponding {111} pole figures for specimens originally processed either by (a) 8 passes of ECAP at 300 K or (b) 10 passes of ECAP at 600 K and pulled to failure at 3.3×10^{-3} s^{-1} at 723 K.

Inspection of Figures 5.21 and 5.22 demonstrates that there is excellent agreement concerning the size and distributions of grains in the ECAP-processed alloy tested at 723 K as observed through SEM and EBSD analyses, respectively. These results also reveal that the grains of the polycrystalline metal deformed at superplastic conditions are slightly elongated in a direction parallel to the tensile axis and are homogeneously distributed all over the gauge area of the samples. Additionally, the Al-Mg-Sc alloy develops a random texture during plastic straining at 3.3×10^{-3} s^{-1} at 723 K as evident in the {111} pole figures of Figure 5.22.

It follows from Figures 5.22 (a) and (b) that the microstructures of the ECAP-processed material are mostly formed by grains having HAGBs and substructures with LAGBs are basically absent after tensile testing at 723 K. The same procedure for measuring the grain sizes in the SEM images was also used in these OIM images to give $\bar{L}$ values of ~4.0 and ~3.6 μm for the alloy initially processed by ECAP at 300 and 600 K, respectively. It is also interesting to note the presence of cavities mainly at triple junctions and HAGBs as indicated

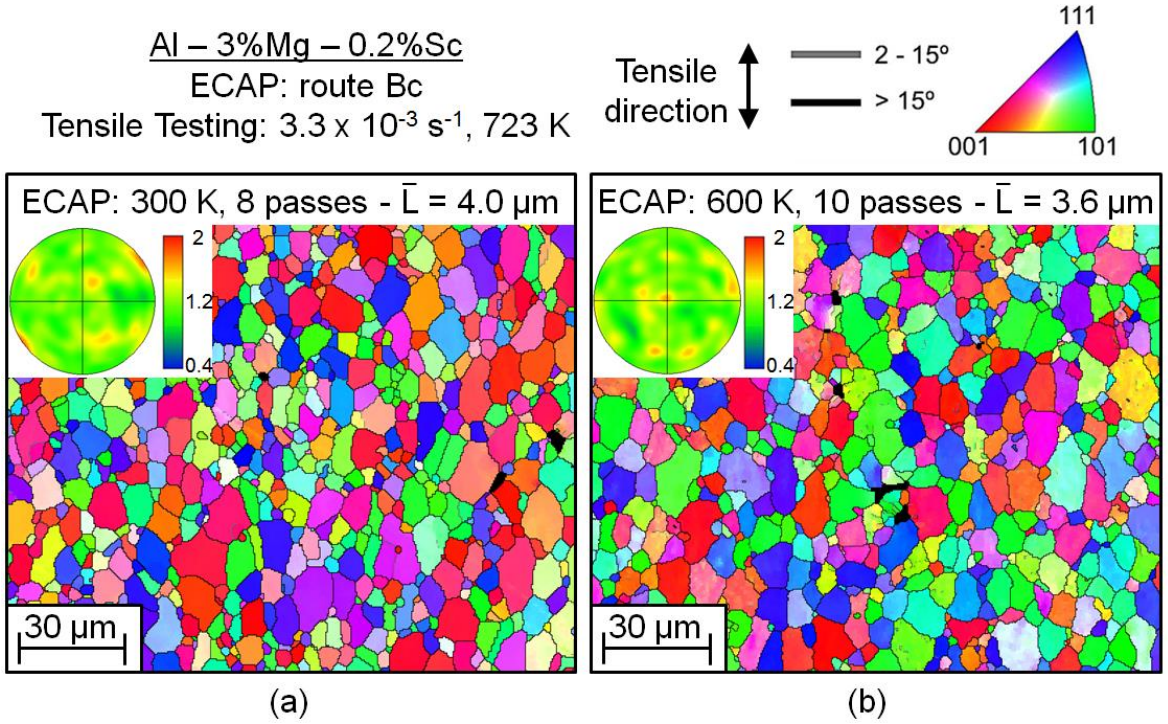

Figure 5.22 - OIM images and corresponding {111} pole figures of the gauge area of Al-3Mg-0.2Sc specimens processed either by (a) 8 passes of ECAP at 300 K or (b) 10 passes of ECAP at 600 K and tested in tension at 3.3×10^{-3} s^{-1} at 723 K.

through the unindexed areas coloured in black for both OIM images.

Figure 5.23 shows histograms of both (a) the area fraction of grain diameters and (b) the misorientation angles for the ECAP-processed Al-3Mg-0.2Sc alloy after tensile testing at 3.3×10^{-3} s^{-1} at 723 K. It is clearly seen in Figure 5.23 (a) that the samples subjected to ECAP

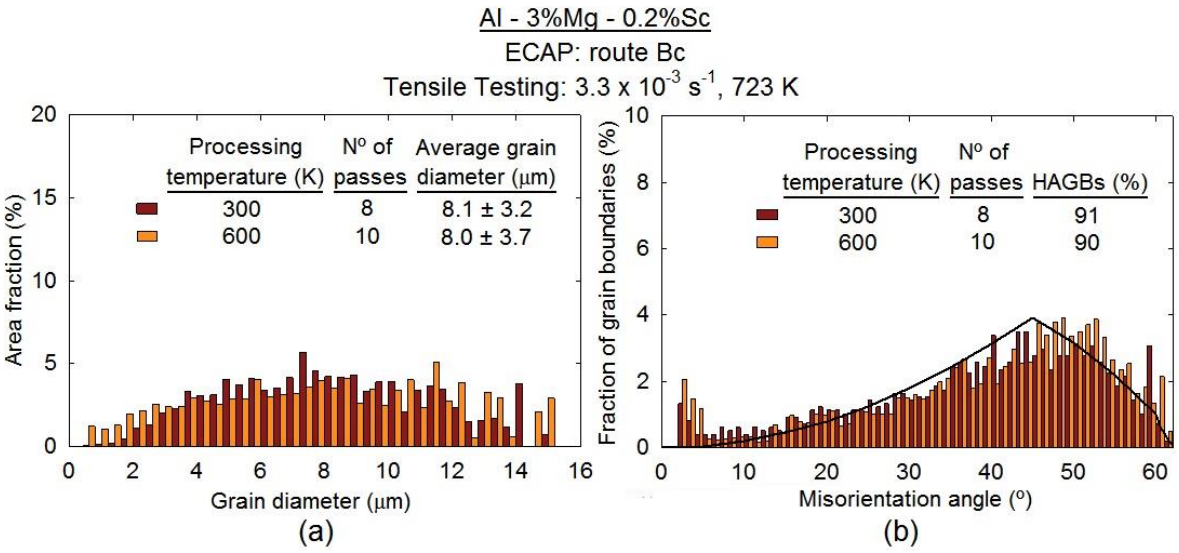

Figure 5.23 – Histograms of (a) the area fraction of grain diameters and (b) the misorientation angles for the ECAP-processed Al-3Mg-0.2Sc alloy immediately after tensile testing at 3.3×10^{-3} s^{-1} at 723 K.

at either 300 or 600 K have very similar distributions of grain diameters and exhibit an area-weighted average grain diameter of ~8 μm after extensive plastic deformation at superplastic conditions.

Inspection of Figures 5.12 (e) and 5.23 (a) reveals that the analysed samples of the metal annealed for 1 h at 723 K have sharper distributions of grain diameters compared with the specimens tested at superplastic conditions, considering grains with diameters lower than 20 μm. The annealed material has a large fraction of grains with ~2 μm in diameter, whilst the deformed samples of the Al-Mg-Sc alloy exhibits similar area fractions for grain diameters ranging from 4 to 12 μm. Nevertheless, it is important to note that there is no evidence of abnormally coarse grains in the ECAP-RT metal after tensile testing at 723 K, even though this material was held at the testing temperature for ~1.1 h.

The results in Figure 5.23 show that there is an excellent correlation between the histograms of misorientation angles and the Mackenzie distribution [205] thereby demonstrating that the ECAP-processed Al-Mg-Sc alloy develops an essentially random texture during plastic deformation at 723 K with an initial strain rate of 3.3×10^{-3} s^{-1}. It is also noted that more than 90 % of the grain structures in these samples have HAGBs, whereas the same material exhibits fractions of LAGBs higher than 35 % after annealing at 723 K for 1 h as revealed in Figure 5.14 (e).

It follows from Figures 5.21 and 5.22 that reasonably similar grain sizes were measured from images of the Al-Mg-Sc specimens obtained using conventional SEM and EBSD scans and this confirms that the average grain boundary spacing can be reliably and efficiently predicted through examination of the topography of samples after plastic deformation. Accordingly, several SEM images were taken along the gauge area of specimens of the Al-3Mg-0.2Sc alloy in order to compare the kinetics of grain coarsening during high temperature testing for the material originally processed by ECAP at 300 or 600 K and these results are displayed in Figure 5.24.

The plots depicted in Figure 5.24 demonstrate that significant grain growth occurs during plastic straining at elevated temperatures for the ECAP-processed alloy. In addition, the values of the average grain size increase with increasing temperatures and decreasing strain rates during tensile testing. These results also indicate that higher coarsening rates are observed in samples strained for shorter periods of time, as especially apparent in the ECAP-RT material. Nevertheless, there are only minor differences in the grain sizes after plastic deformation with strain rates lower than $\sim 1.0 \times 10^{-2}$ s^{-1} and thereby for a retention time in the furnace exceeding 1000 s.

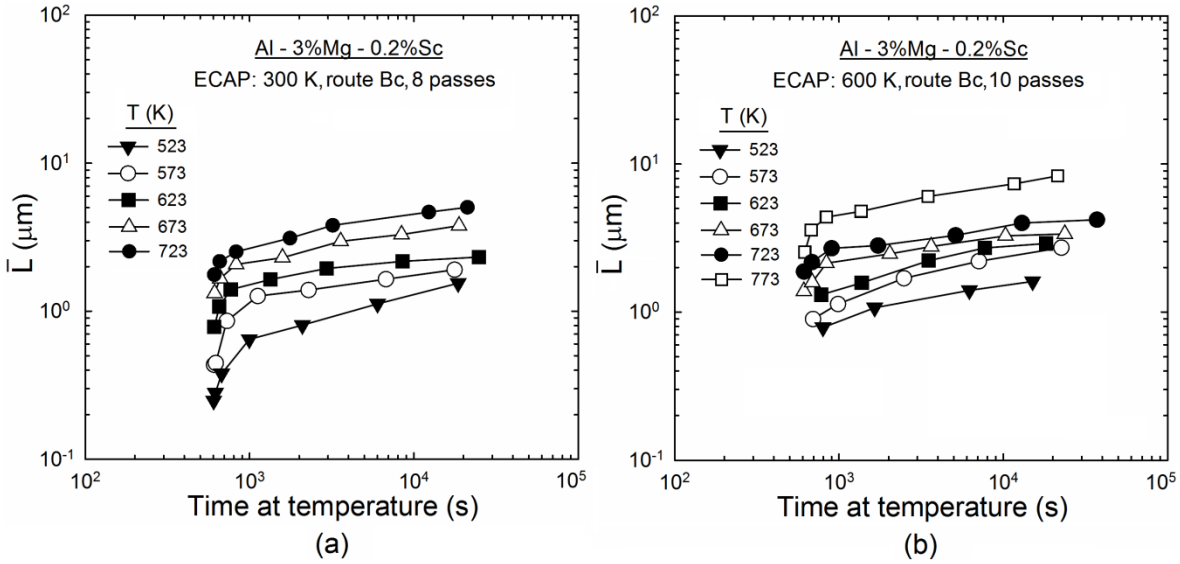

Figure 5.24 - Average grain boundary spacing, $\bar{L}$, as a function of time at temperature for samples of the Al-3Mg-0.2Sc alloy processed either by (a) 8 passes of ECAP at 300 K or (b) 10 passes of ECAP at 600 K and tested in tension at temperatures ranging from 523 to 773 K.

A comparison of Figures 5.24 (a) and (b) also reveals that the Al alloy processed by 8 passes of ECAP at ambient temperature has smaller grains compared with the ECAP-HT metal after tensile testing at $T \leq 573$ K. Additionally, samples processed by ECAP at both processing temperatures display similar grain sizes after deformation at 623 K and the ECAP-RT alloy generally exhibits coarser grain structures for tests performed at $T \geq 673$ K for comparable testing times. It is also interesting to note from these experimental results that the Al-Mg-Sc alloy originally processed by ECAP at 600 K shows very limited grain growth during plastic straining at temperatures up to 723 K. However, the values of the average grain size prominently increase for specimens tested at 773 K with testing times higher than 1000 s.

5.3 Discussion

5.3.1 Effect of Processing Temperature on the Grain Refinement and Thermal Stability of an Al-Mg-Sc Alloy Processed by ECAP

This study consistently demonstrates that processing through 8 passes of ECAP at 300 K leads to smaller grain sizes (~0.25 μm) and a higher average microhardness (~140 Hv) in the Al-3Mg-0.2Sc alloy by comparison with ECAP at 600 K. These results show reasonable agreement with earlier investigations that examined the grain structures after ECAP in Al-Mg-Sc alloys having slightly different chemical compositions [20,47,169,184,244] and are

directly associated with the increasing contribution of softening mechanisms during and immediately after plastic straining at higher temperatures.

There have been several studies in which UFG structures were successfully attained in Al-Mg-Sc alloys after ECAP [43,45,156,159,180,182,183,189]. Nevertheless, it should be noted that ECAP processing at elevated temperatures was performed in commercial Al-Mg-Sc alloys with high Mg contents (>5 wt. %) [45,167,182,183,189,245]. These metals exhibit a more severe strain localization during ECAP compared with the Al-3Mg-0.2Sc alloy and thereby displayed extensive cracking after few passes at temperatures below 423 K [244,245]. By contrast, the material used in the present work was able to withstand 8 passes of ECAP at RT and 10 passes of ECAP at 600 K with negligible macroscopic cracking and this permits a direct assessment of the effect of processing temperature on the microstructure and mechanical properties of identical Al-Mg-Sc alloys after ECAP.

It is also important to note that commercial Al-Mg-Sc alloys were generally heat treated at T < 800 K for extended periods (>6 h) prior to ECAP processing at high temperatures and this leads to the formation of nano-sized Al_3Sc dispersoids [45,166,167,182,183,189,245]. As a result, these precipitates interact with mobile dislocations and delay the recovery kinetics during severe plastic deformation [167,245,246]. In this investigation, the Al-3Mg-0.2Sc alloy was solution treated for 1 h at 880 K to maximize the Sc content in solid solution [43,159] and only few undissolved precipitates were observed in the unprocessed alloy. Also, billets were exposed to the processing temperature for total times inferior to 5 min and quenched in water immediately after each ECAP pass at 600 K. Thus, it is not believed there was significant precipitation during ECAP at an elevated temperature as the minimum incubation period observed in the TTT diagram in Figure 2.24 is ~20 min at 573 K [158].

It has been demonstrated through systematic TEM analysis that the microstructure of the Al-3Mg-0.2Sc alloy is formed by mixed areas of both elongated and fairly equiaxed grains with an average size of ~200 nm after 8 passes of ECAP at room temperature [20,244]. Observations of SAED patterns also indicated that these UFG structures are essentially separated by HAGBs, although the misorientations relative to each individual grain boundary were not determined in these examinations. EBSD scans performed using the same Al-Mg-Sc alloy revealed that the ECAP-RT material has an average grain boundary spacing of ~250 nm. This value is slightly higher than previous measurements using TEM images, however, it should be noted that only HAGBs were considered as intercepts for the OIM images. Conversely, it readily follows from the results displayed in Figures 5.8 (a) and 5.14 (a) that the Al-3Mg-0.2Sc alloy was not entirely refined during processing as this material continues having relatively coarse grains with a large fraction of LAGBs (~49 %).

The local inhomogeneities in this material even after 8 passes of ECAP at RT are also clearly visible in the hardness distributions in Figures 5.1, 5.2, and 5.3 (a) and are inherent to a more difficult grain refinement process in Al alloys with large amounts of Mg [11,244,247]. The addition of Mg in solid solution reduces the stacking fault energy and ultimately delays the recovery kinetics during plastic deformation [11,14,247]. Furthermore, it is demonstrated in Chapter 4 that $m \approx 0$ for the Al-3Mg-0.2Sc alloy deformed at ~300 K and this leads to intense shear localization and the development of strain inhomogeneities during ECAP [7,248]. Therefore, although different slip systems are activated during each ECAP pass using route B_c and this sensibly diminishes the overall microstructural heterogeneity with increasing number of passes [249], some areas in the microstructure of the Al-3Mg-0.2Sc alloy underwent lower straining levels which reflects the local variations in the Vickers microhardness and the presence of a high fraction of substructures.

Careful inspection of the OIM image in Figure 5.8 (b) reveals that the Al-3Mg-0.2Sc alloy exhibits reasonably equiaxed grains with an average size of ~0.6 μm after 10 passes of ECAP at 600 K. Similarly to the ECAP-RT material, it is apparent that representative areas of this microstructure were not fully refined after processing; however, these areas have a distinct texture and well-defined subgrains with approximately the same size as the HAGBs structures. It is also relevant to note that ECAP at 600 K leads to a more homogeneous microhardness distribution by comparison with processing at ambient temperature.

Grain refinement of Al-Mg-Sc alloys during ECAP at high homologous temperatures also involves the formation of deformation bands which gradually transform into HAGBs structures after mutual crossing in successive ECAP passes [77,167,169]. Although this process is mechanically driven and not thermally activated [22,77], recovery may occur concomitantly and after processing when the billet is still confined within the ECAP die. As a result, deformation bands created during ECAP at $T > 0.5T_m$ are more diffusive and dislocations rearrange into substructures with lower energy configurations after each pass. This delays the kinetics of grain refinement and increases the minimum grain size attained after ECAP in consistence with the current findings.

Furthermore, Figures 4.13 and 5.19 indicate that the strain rate sensitivity of Al-Mg-Sc alloys increases with increasing temperatures and $m > 0.2$ at $573 < T < 623$ K for strain rates close to the rate of deformation during ECAP calculated as ~1 s^{-1} using an analytical equation [250]. This leads to a more homogeneous distribution of strain after each pass and contributes to generate a uniform array of equiaxed grains after ECAP at 600 K. It is worth mentioning that the presence of Al_3Sc dispersoids significantly reduces the rate of grain refinement during ECAP [246]. This explains why, despite the lower Mg content, the solution

treated Al-3Mg-0.2Sc alloy exhibits lower grain sizes after ECAP at ~600 K compared with other Al-Mg-Sc alloys homogenised prior to processing [45,183,189,251].

Although the Al-3Mg-0.2Sc alloy showed considerably distinct microstructures and hardness distributions after ECAP at either 300 or 600 K, these samples have similar dislocation densities of $\sim 3 \times 10^{13}$ m^{-2}. These values are perfectly consistent with measurements performed using TEM images for Al-Mg-Sc alloys with ~5 wt.% Mg after ECAP processing at ~600 K [45,251]. This confirms that grain boundary strengthening plays a major role on the mechanical strength of UFG Al-Mg-Sc alloys as the grain structures of samples processed by ECAP at different temperatures have very distinguishable sizes and arrangements and this results in higher microhardness values for the ECAP-RT metal.

This investigation clearly reveals that the microstructure of the Al-3Mg-0.2Sc alloy processed by 10 passes of ECAP at 600 K displays enhanced thermal stability compared with the UFG structures developed during ECAP at $T \approx 0.3\ T_m$. After annealing for 1 h at $T \leq 623$ K, both the average microhardness and the grain size of the ECAP-HT material are essentially unchanged, whereas samples processed at RT display significant grain coarsening and reduction in the Vickers microhardness. Consequently, the metal originally processed at 600 K has superior mechanical properties and smaller grain sizes after annealing at $T \geq 673$ K. It should also be noted the development of a bimodal distribution of grains due to the occurrence of abnormal coarsening in the ECAP-RT alloy annealed at $T \geq 723$ K.

The reasons for the superior microstructural stability in Al-Mg-Sc alloys processed by ECAP at high homologous temperatures may be assessed by calculating the driving and restraining pressures for grain boundary migration. The formation and migration of HAGBs in severely deformed materials is primarily driven by the reduction of the strain energy stored in the form of dislocations and grain boundaries [77,252]. Accordingly, the driving pressure due to stored dislocations, P_d, is expressed as follows [161]:

$$P_d = c_d\ \rho\ G\ \mathbf{b}^2 \tag{5.1}$$

where c_d is a constant of ~ 0.5.

The driving pressure for grain migration due to release of the boundary energy, P_b, may be estimated in Al-Mg alloys by considering the interface energy of a HAGB, γ, as 0.324 Jm^{-2} [253] and the area of grain boundaries per unit volume ($\sim 3/d$) using the following relationship [161]:

$$P_b = \frac{3\gamma}{d} \tag{5.2}$$

The driving pressures for grain boundary migration for the ECAP-processed alloy were estimated using Eqs. 5.1 and 5.2 with **b** = 2.86 × 10^{-10} m and G = 25.42 GPa [237]. The values of P_d and P_b are shown in Table 5.2 and were calculated considering the dislocation densities in Table 5.1 and the average grain diameters in Figure 5.12 (a). It follows from Table 5.2 that samples processed by ECAP at either 300 or 600 K display similar stored energies due to dislocations. By contrast the ECAP-RT alloy has a considerably higher driving pressure for grain boundary motion due to the lower size of the grains developed during ECAP at 300 K.

It has been documented that Al-Mg alloys with comparable amounts of magnesium but without Al_3Sc dispersoids exhibit average grain boundary spacings of ~0.2-0.3 μm after several ECAP passes at room temperature [16,17,19,212]. As a result, these alloys also display extremely high values of P_b which eventually gives rise to discontinuous recrystallization and the formation of duplex structures after annealing for 1 h at temperatures of ~500-550 K [16,17]. The microstructural changes normally observed in Al alloys without dispersoids after severe plastic deformation at low temperatures and subsequent annealing are schematically represented in Figure 5.25.

The microstructures of Al alloys after ECAP processing at $T \approx 0.3\ T_m$ essentially consist of arrays of UFG structures developed by mutual crossing of deformation bands after consecutive ECAP passes. Typically, there are also few areas not fully refined having substructures with LAGBs. As illustrated in Figure 5.25, recovery occurs during annealing at relatively low temperature, generally for T_1 up to ~500 K, and this leads to annihilation and rearrangement of dislocations, but does not change the overall size of the submicrometre grains formed during ECAP [16,17].

Furthermore, ECAP-processed solid solutions without pinning particles exhibit discontinuous recrystallization at intermediate annealing temperatures (T_2) [16,17]. This softening mechanism is originated by the local microstructural heterogeneities observed after ECAP at low temperatures as there are remaining coarse grains with LAGBs mixed

Table 5.2 -Driving pressure for grain boundary migration due to stored dislocations, P_d, and boundary energy, P_b, for the Al-3Mg-0.2Sc alloy processed by ECAP at different temperatures.

Metal-working procedure	P_d (MPa)	P_b (MPa)
ECAP: 300 K, route Bc, 8 passes	0.03	1.06
ECAP: 600 K, route Bc, 10 passes	0.03	0.65

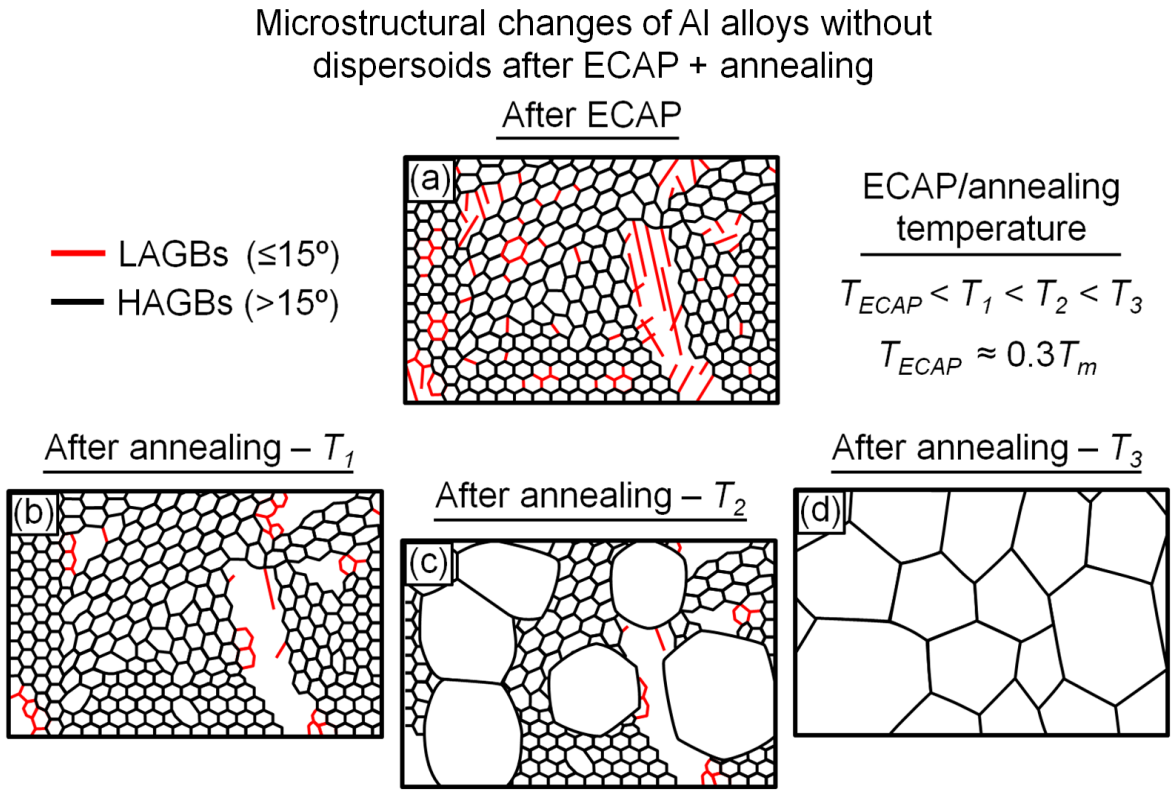

Figure 5.25 –Schematic representation of the microstructural changes of Al alloys without dispersoids after ECAP processing at a low homologous temperature and subsequent annealing.

with UFG structures [254]. Grains preferentially recrystallize in areas with higher stored energies which, in this case, are mainly regions with high fractions of non-equilibrium HAGBs. As a result, the material annealed under this condition may exhibit a bimodal distribution of grains composed of large recrystallized structures and areas containing ultrafine grains and structures not fully developed during ECAP. Nevertheless, annealing for extended periods or higher temperatures (T_3) results in a uniform distribution of fully recrystallized grains as suggested in Figure 5.25 and confirmed elsewhere [16,212,254].

In this investigation, the Al-3Mg-0.2Sc alloy was processed by ECAP in the solution treated condition to avoid the deleterious effect of Al_3Sc precipitates on the kinetics of grain refinement [246], but also to permit precipitation of extremely fine dispersoids during post-ECAP heat treatment [43,159]. The presence of nanoparticles significantly reduces the thermodynamic potential for recrystallization due to the restraining pressure, P_Z, exerted by these phases on the moving boundaries [161,252]. The values of P_Z for the Al-3Mg-0.2Sc alloy after annealing for 1 h at different temperatures were calculated using Eq. 2.11 with k_p = 1.5 and γ = 0.324 Jm^{-2} and are shown in Table 5.3. The volume fraction of Al_3Sc dispersoids, f, was estimated using the Al-Sc phase diagram and considering equilibrium conditions during annealing [40]. Also, the average precipitate radius, r_p, was taken from measurements performed in TEM images of Al-Sc alloys after annealing at equivalent conditions [255,256].

Table 5.3 - Volume fraction of Al_3Sc phase, f, average radius of the precipitates, r_p, and Zener pinning pressure, P_Z, for the Al-3Mg-0.2Sc alloy after annealing for 1 h at different temperatures.

T (K)	f (%) [a]	r_p (nm)	P_Z (MPa) [d]
573	0.50	1.0 [b]	2.43
623	0.48	1.8 [b]	1.29
673	0.46	3.5 [c]	0.64
723	0.43	9.5 [c]	0.26
773	0.33	21.5 [c]	0.08

[a] Calculated from the Al-Sc phase diagram considering equilibrium conditions during annealing [40].
[b] Average radius of Al_3Sc particles formed in an Al-0.3Sc alloy after ageing for ~1 h [255].
[c] Average radius of Al_3Sc particles formed in an Al-0.25Sc alloy after annealing for ~1 h [256].
[d] Calculated using Eq. 2.11 for $\gamma = 0.324$ Jm^{-2} [253].

It is readily observed in Table 5.3 that a relatively high fraction of precipitates with $r_p \approx 1.0$ nm are formed after annealing at 573 K and this gives $P_Z \approx 2.43$ MPa for the Al-3Mg-0.2Sc alloy. Nonetheless, the values for the restraining pressure considerably decrease with increasing temperatures due to coarsening and dissolution of precipitates. This is more evident after heat treatment at $T \geq 723$ K as $P_Z < 0.3$ MPa.

The susceptibility for grain boundary migration may be assessed by summing the contributions of the driving and restraining pressures ($\Delta P = P_d + P_b - P_Z$) displayed in Tables 5.2 and 5.3. Furthermore, it is also possible to evaluate whether abnormal grain coarsening occurs during heat treatment of alloys having second-phase particles through calculation of a dimensionless parameter for boundary stability, ψ_b, expressed as follows [161,257]:

$$\psi_b = \frac{k_p \, f \, d}{2 r_p} \tag{5.3}$$

The model used to derive Eq. 5.3 considers the existence of a dispersion in the distribution of grain sizes prior to annealing and defines the parameter size ratio, X, alternatively expressed as the ratio between the equivalent diameter of a particular grain and the average equivalent diameter [161,257]. It has been demonstrated that, for minimum size ratios higher than a critical value, abnormal grain growth arises when $0.25 < \psi_b < 1$ and this phenomenon occurs simultaneously with normal growth for $0.1 < \psi_b < 0.25$. In addition, there is some broadening of grain size distribution for values of ψ_b within the range from 0 to 0.1

and no growth should occur for $\psi_b > 1$. It is also important to note that the minimum size ratio needed to initiate abnormal coarsening increases with increasing ψ_b and $X > 10$ for $0.9 < \psi_b < 1$. The values of ΔP and ψ_b were calculated for the Al-3Mg-0.2Sc alloy processed by ECAP at either 300 or 600 K considering the different distributions of Al_3Sc dispersoids generated during subsequent annealing for 1 h and these results are shown in Table 5.4.

Table 5.4 reveals that the ECAP-HT material exhibits lower values of ΔP compared with the same alloy processed at ambient temperature and this is consistent with its superior microstructural stability. Also, ΔP is negative for $T \leq 623$ K and thereby grain growth should not occur at these annealing conditions. These results are consistent with the microstructural observations after annealing up to 523 K; however, billets processed at ~300 K display sizable grain coarsening after heat treatment at 623 K and this is probably associated with the local inhomogeneities of the microstructure after ECAP that were not considered in the calculations of the driving pressures.

It is readily observed in Table 5.4 that $\Delta P > 0.8$ MPa for the ECAP-RT metal after annealing for 1 h at $T \geq 723$ K, whereas the maximum value of ΔP in samples originally processed at 600 K does not exceed 0.60 MPa. It is also indicated that ψ_b varies from 0.91 to 0.11 for samples processed at 300 K and further annealed at $T \geq 673$ K. These values are within the interval for abnormal coarsening in alloys with second-phase particles [161,257]

Table 5.4 -Sum of the driving and restraining pressures for grain boundary migration, ΔP, and dimensionless parameter for boundary stability, ψ_b, for the Al-3Mg-0.2Sc alloy processed by ECAP at either 300 or 600 K and further annealed at different temperatures.

Metal-working procedure	T (K)	$\Delta P = P_d + P_b - P_Z$ (MPa)	ψ_b
ECAP: 300 K, route Bc, 8 passes	573	-1.34	3.45
	623	-0.20	1.83
	673	0.45	0.91
	723	0.83	0.37
	773	1.01	0.11
ECAP: 600 K, route Bc, 10 passes	573	-1.75	5.62
	623	-0.61	2.98
	673	0.03	1.49
	723	0.42	0.60
	773	0.60	0.18

and this phenomenon is consistently verified in this study for the ECAP-RT metal annealed for 1 h at $T \geq 723$ K. Nevertheless, it should be noted the absence of abnormal grain growth after annealing at 673 K and this may be explained by the requirement of a minimum size ratio greater than 10 to activate this mechanism for $\psi_b \approx 0.9$ [257].

Although ψ_b is within the range from ~0.18 to 0.60 for $T \geq 723$ K, there is no evidence of formation of a bimodal distribution of grains in the Al-3Mg-0.2Sc alloy processed by ECAP at $T \approx 0.6T_m$ for all annealing conditions used in this investigation. On the other hand, this material exhibits lower values of ΔP and a more uniform microstructure compared with the ECAP-RT material. Accordingly, it is possible that abnormal coarsening is only at its initial stage after annealing for 1 h and extended heat treatment times would result in the development of duplex structures. It is also worth noting that the onset of abnormal grain growth was recently observed in an Al-5Mg-0.2Sc-0.08Zr alloy processed by 10 ECAP passes at ~600 K after annealing for 1 h at ~750 K [47].

In order to summarize and extend the findings obtained in this investigation to other materials, Figures 5.26 and 5.27 show schematic representations of the microstructural changes in supersaturated Al alloys containing dispersoid elements after ECAP at either room temperature (~$0.3T_m$) or ~$0.6\ T_m$, respectively, and further annealing.

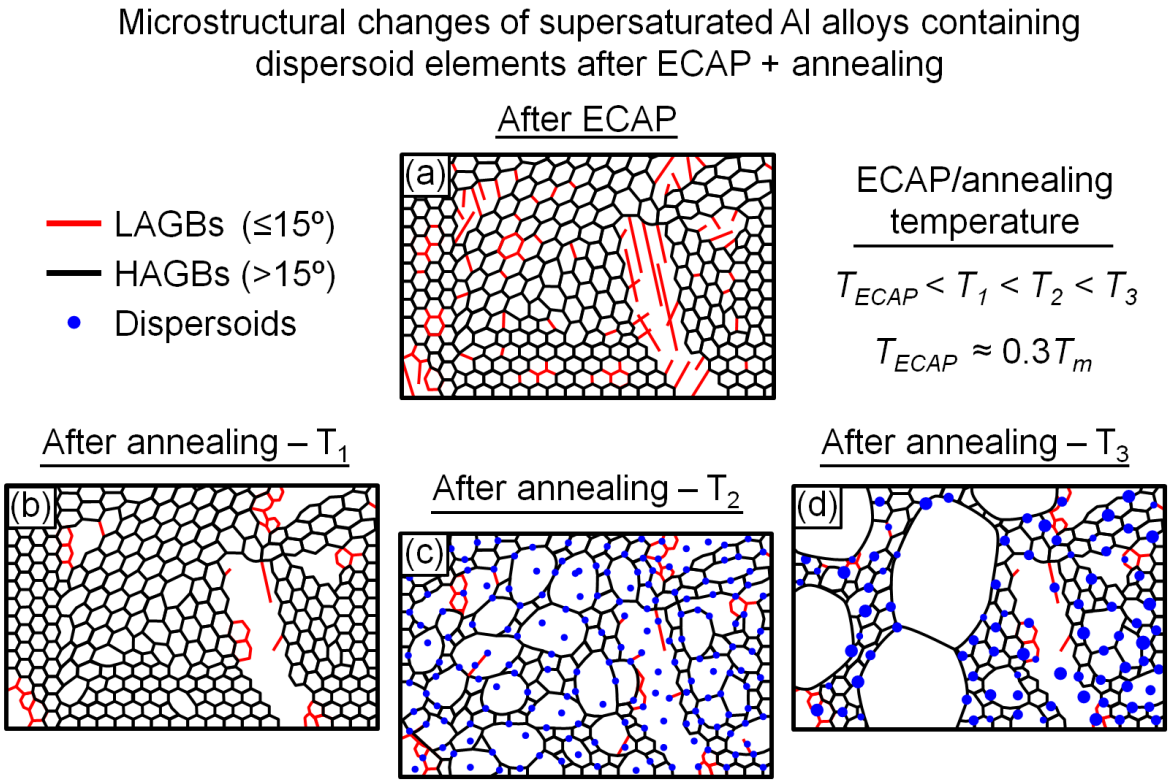

Figure 5.26 - Schematic representation of the microstructural changes of supersaturated Al alloys containing dispersoid elements after ECAP processing at room temperature and subsequent annealing.

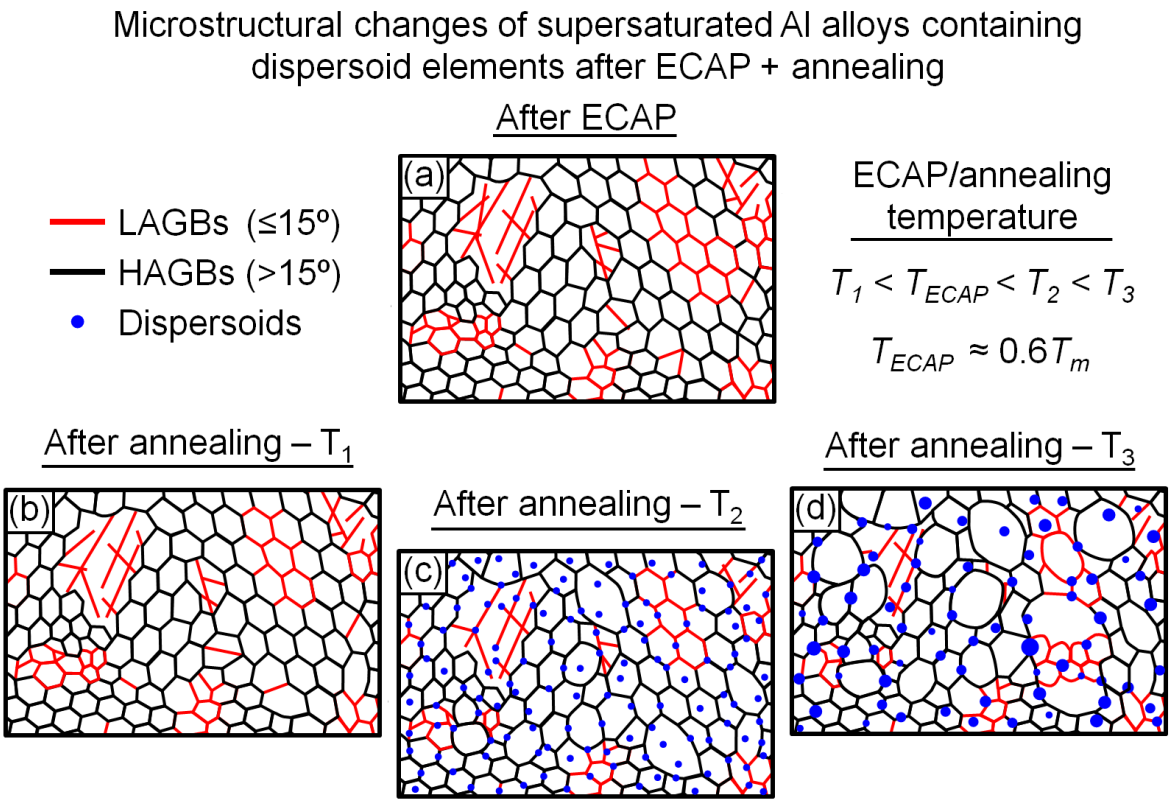

Figure 5.27 - Schematic representation of the microstructural changes of supersaturated Al alloys containing dispersoid elements after ECAP processing at a high homologous temperature and subsequent annealing.

Figure 5.26 illustrates that supersaturated Al alloys containing dispersoid forming elements exhibit similar microstructures in comparison to conventional alloys after ECAP at RT [16,17,20]. After annealing at T_1 up to $\sim 0.55T_m$, both the density of dislocations and the average microhardness are significantly reduced due to recovery, although the average grain size remains essentially the same as after deformation.

As represented in Figure 5.26 (c), continuous static recrystallization occurs simultaneously with homogeneous precipitation of fine dispersoids during annealing at a moderate temperature (T_2) [77]. The Zener drag pressure applied by precipitates in a particular boundary reduces its growth rate and this permits coarsening in other areas whereby precipitates are not yet hampering the grain boundaries. As a result, the microstructure develops uniformly during this process, as confirmed in this investigation for the ECAP-RT material heat treated for 1 h at 623 and 673 K. By contrast, annealing at higher temperatures ($T_3 > 0.75T_m$) leads to abnormal grain coarsening due to the accelerated ageing kinetics together with the occurrence of discontinuous precipitation in Al alloys with dispersoid elements [158,163,256,258,259].

After consecutive passes of ECAP at ~$0.6T_m$, the grain structures of Al-Mg-Sc alloys have larger sizes and are more homogeneously distributed compared with processing at ambient temperature and this is schematically illustrated in Figure 5.27 (a). As a consequence, very limited recovery occurs during annealing for 1 h up to $T_1 \approx 0.6T_m$, as verified through hardness measurements. Furthermore, the homogeneous precipitation of nanodispersoids at intermediate temperatures (T_2) effectively hinders the boundaries of ultrafine grains such that only minor coarsening is observed after annealing under these conditions.

It should also be noted that ECAP processing at higher homologous temperatures results in lower driving pressures due to boundary energies and this significantly delays the kinetics of grain growth. Accordingly, Al alloys containing dispersoids may not exhibit abnormal grain growth during annealing at T_3, even if there exist significant coarsening and heterogeneous nucleation of precipitates at this temperature. This is consistent with the results obtained in this study for an Al-Mg-Sc alloy processed by ECAP at 600 K, although it is believed that annealing for extended periods of time or at T > 773 K would eventually give rise to abnormal coarsening.

There have been several exploratory studies demonstrating that the ductility of UFG metals may be considerably improved by developing bimodal grain structures which preserve most of the strengthening benefits achieved during severe plastic deformation [260–263]. Although the present results show that the average microhardness of the ECAP-RT metal significantly decreases after annealing for 1 h at 723 K, heat treatments for shorter times could lead to a less prominent decline in this mechanical property together with enhancement in the ductility at low temperatures.

It is concluded therefore that Al-Mg-Sc alloys display superior thermal stability after 10 passes of ECAP at 600 K and thereby are more suitable for applications at high temperatures. Nevertheless, the less stable nature of the grains developed during processing at ambient temperature may be utilized for tailoring the microstructure through controlled annealing treatments to ultimately achieve good combinations of strength and ductility.

5.3.2 Superplastic Characteristics of Al-Mg-Sc Alloys Processed by ECAP

The individual values of elongation in Figure 5.18 were used to construct colour-coded maps showing the variations of this indicator of superplasticity with strain rate and temperature. Furthermore, broken lines were added to these plots to clearly delineate the regime of true superplastic flow [105], as displayed in Figure 5.28 for the Al-3Mg-2Sc alloy originally processed by ECAP at either (a) 300 or (b) 600 K.

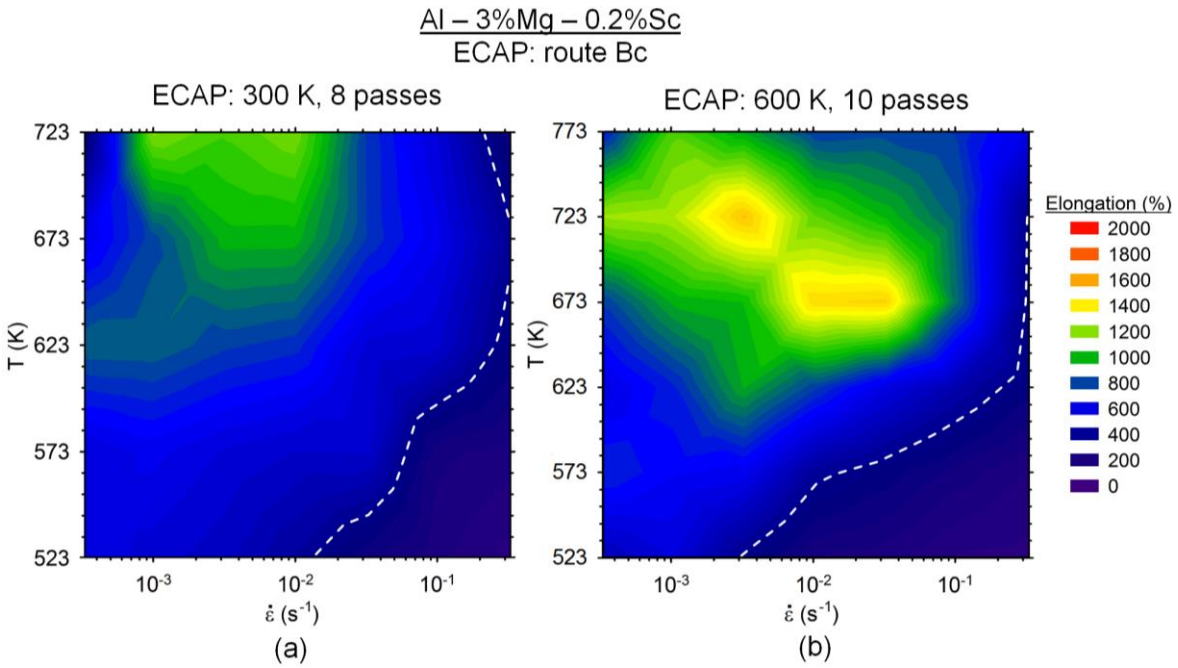

Figure 5.28 - Colour-coded contour maps showing the elongations to failure for the Al-3Mg-0.2Sc alloy processed by either (a) 8 passes of ECAP at 300 K or (b) 10 passes of ECAP at 600 K: the broken lines delineate the minimum elongation normally observed after true superplastic flow [105].

The results in Figure 5.28 demonstrate that the ECAP-HT material exhibits superior elongations and therefore enhanced superplastic properties compared with the alloy processed at 300 K and further tested at $T > 623$ K. Elongations to failure higher than 1000 % were observed after deformation at $T \geq 673$ K at strain rates up to $\sim 10^{-1}$ s^{-1} for the metal processed at 600 K, whereas these were only achieved at 723 K for the ECAP-RT alloy at strain rates from 1.0×10^{-3} to 1.0×10^{-2} s^{-1}. By contrast, it is clearly visible from these maps that the Al alloy processed by ECAP at RT displays improved ductility during testing at low homologous temperatures (~ 0.55-$0.65 T_m$) as the regime of superplastic flow extends to faster strain rates in comparison to the ECAP-HT metal.

As evident in Figures 5.11 and 5.24, these findings are perfectly consistent with the measurements of the average grain sizes in ECAP-processed samples after either static annealing or high temperature straining, respectively. It follows from the theoretical model for grain boundary sliding [38] that superplastic flow may be attained at faster strain rates by decreasing the size of grains with HAGBs as confirmed in several UFG metals [105,139]. Therefore, the superior low temperature superplasticity of the Al-3Mg-0.2Sc alloy after ECAP at 300 K may be attributed to its capacity to retain smaller grains than the ECAP-HT material, even after long exposures to temperatures up to ~ 623 K.

Nevertheless, it is also demonstrated in this study that ECAP processing at lower temperatures leads to smaller grain sizes but also higher driving pressures for grain

boundary motion. As a result, the UFG metal originally processed at RT displays significant grain growth after heating at $T \geq 673$ K and its microstructures become coarser than in specimens of the ECAP-HT metal at comparable temperatures. This explains the more extensive elongations achieved in Al-Mg-Sc alloys processed by ECAP at high temperatures [45] and the absence of true superplastic elongations in samples processed at RT and further tested at 773 K [20].

It is well established that superplastic elongations in UFG materials are generally associated with $m \geq 0.5$ [105]. This is also apparent in this investigation as m values higher than 0.5 were calculated for the Al-3Mg-0.2Sc alloy processed by ECAP during deformation in a wide range of strain rates and temperatures. Nevertheless, careful examination of Figures 5.19 and 5.28 reveals that strain rate sensitivities lower than 0.5 were also obtained in tensile specimens exhibiting elongations to failure superior to the minimum value usually attained after superplastic flow [105]. It should be further noted that the randomness of the texture together with the increase in the fraction of HAGBs (> 90%) during deformation reliably confirm the occurrence of GBS for ECAP-processed samples tested at 3.3×10^{-3} s^{-1} at 723 K.

Although these results are apparently contradictory, they are consistent with Eq. 2.2 as the slope of the plots true stress vs strain rate shall not be taken as $(1/n)$ when there are significant differences in the grain sizes during plastic straining at a particular temperature. The values of the flow stress in Figure 5.19 were taken at $\varepsilon = 0.3$ and all specimens were held at the testing temperature for ~10 min prior to application of the load. As a consequence, samples tested at 3.3×10^{-4} s^{-1} remained in the furnace for ~28 min up to achieving $\varepsilon = 0.3$, whilst this was attained after ~16 and 12 min for tests performed at either 1.0×10^{-3} or 3.3×10^{-3} s^{-1}, respectively. Therefore, the apparent decrease in the m values may have arisen due to significant grain coarsening and overestimation of flow stress for specimens tested at superplastic conditions for sufficiently high temperatures and slower strain rates [264,265].

In this investigation, the linear intercept method was used to measure the average grain size of the Al-3Mg-0.2Sc alloy processed by ECAP after all tensile testing conditions. This provides the opportunity to truthfully identify the rate controlling flow process in all samples exhibiting elongations higher than 400 % is GBS. For this reason, the temperature and grain size compensated strain rate, $(\dot{\varepsilon}kT/D_{gb}G\mathbf{b})(d/\mathbf{b})^2$, was plotted against the normalized stress, (σ/G), using Eqs. 2.2 and 2.3 with $p = 2$, and $D = D_{gb}$ [38]. These plots were constructed for samples of the ECAP-processed alloy which displayed superplastic elongations using σ as the maximum flow stress, σ_{max}, and d as the spatial grain size, d_s, as shown in Figure 5.29. Similarly to the earlier analyses [105,139,266,267], these calculations were performed using basic parameters for pure Al where $D_{o,gb} = 1.86 \times 10^{-4}$ m^2 s^{-1}, $Q_{gb} = 86$

kJ mol^{-1}, **b** = 2.86 × 10^{-10} m and G (MPa) = (3.022 × 10^{4}) – 16T [237]. A solid line labelled $\dot{\varepsilon}_{sp}$ is also plotted in Figure 5.29 showing the theoretical prediction of the rate of superplasticity in conventional materials as calculated using Eq. 2.2 with n = 2 and A = 10 [38].

It is demonstrated in Figures 5.29 (a) and (b) that there is excellent agreement between the experimental datum points obtained for the Al-3Mg-0.2Sc alloy processed by ECAP and the theoretical model for superplasticity, regardless of the processing temperature. Furthermore, there is a general consistency with the predicted stress exponent of n = 2, including for samples which apparently displayed m < 0.5 after testing at $\dot{\varepsilon} \leq 1.0 \times 10^{-2}$ s^{-1}.

It should also be noted that there are comprehensive analyses showing that the temperature and grain size compensated strain rate in UFG metals tested using miniature specimens tend to lie below the predicted line for conventional superplasticity and may differ from these predictions up three orders of magnitude [139,266,267]. By contrast, it is readily observed in Figure 5.29 that the results obtained in this investigation are more consistent with the theoretical predictions and lie slightly above the solid line labelled $\dot{\varepsilon}_{sp}$.

The origin of these differences is also associated with grain coarsening of UFG materials during plastic flow at high temperatures. In general, due to limited availability of experimental data, the grain sizes used in plots similar to Figure 5.29 are taken from measurements performed immediately after severe plastic deformation [139,266,267]. Nevertheless, UFG metals usually exhibit grain growth during tensile testing at high temperatures and this is particularly more prominent in samples processed by HPT [56,219].

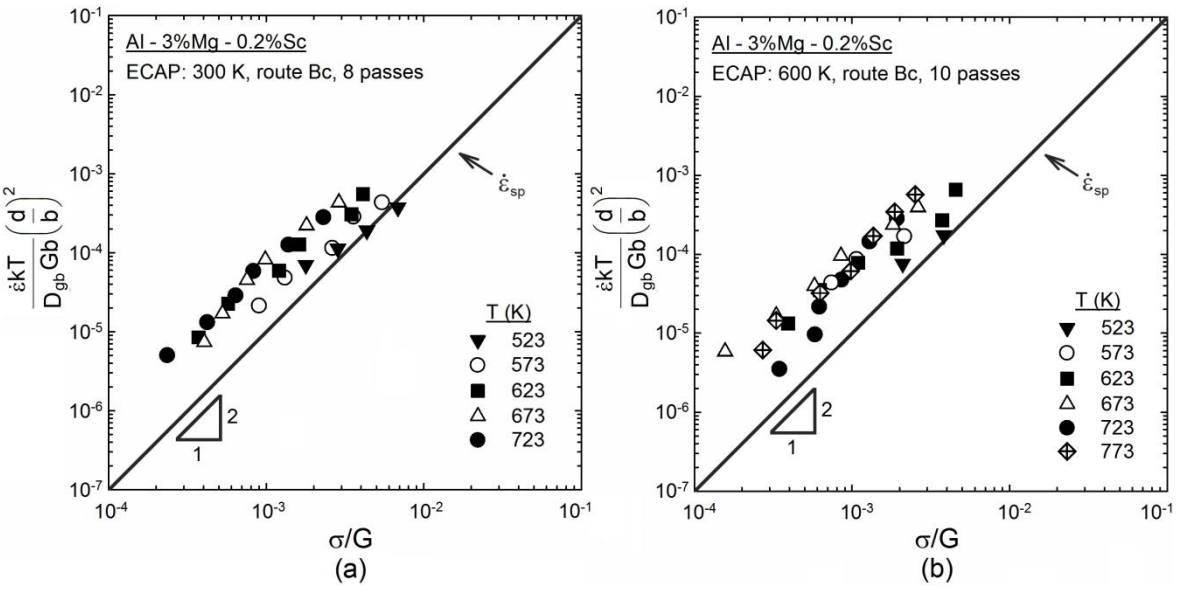

Figure 5.29 - Temperature and grain size compensated strain rate plotted as a function of normalized stress for the Al-3Mg-0.2Sc alloy processed by either (a) 8 passes of ECAP at 300 K or (b) 10 passes of ECAP at 600 K.

As a result, the strain rate in these plots may be considerably underestimated, even though σ is normally taken as the yield stress, σ_y.

In this study, the temperature and grain size compensated strain rates were calculated using the spatial grain size after deformation together with the maximum true stress in each testing condition. Accordingly, even though additional grain coarsening may occur in Al-Mg-Sc specimens after reaching σ_{max}, this procedure permits a more accurate assessment of the rate controlling mechanism during superplastic flow, as apparent in Figure 5.29.

The activation energy for superplastic flow where accommodation by dislocation climb is rate controlling was calculated through semi-logarithmic plots of $(1/GT)(\sigma/d)^2$ vs $1/T$ as shown in Figure 5.30 for the Al-3Mg-0.2Sc alloy processed by ECAP at different temperatures. These plots were constructed for samples displaying superplastic elongations and tested in tension at strain rates ranging from 3.3×10^{-4} to 1.0×10^{-2} s^{-1}.

Inspection of Figure 5.30 demonstrates that the calculated values for the activation energies, Q, for the ECAP-processed material range from ~99 to 125 kJ mol^{-1} for all processing temperatures. Although, there is some scattering in the experimental data, the values estimated for the activation energy for superplastic flow display reasonable consistency with the earlier analysis performed with the same metal after ECAP at RT (~120 kJ mol^{-1}) [43]. It should also be noted that, in this study, the values calculated for Q lie within the range for grain boundary diffusion in pure Al (~86 kJ mol^{-1}) [237] and interdiffusion in conventional Al-Mg alloys (~130.5 kJ mol^{-1}) [268]. These apparently high values of Q_{gb} may follow from the hindrance of HAGBs due to the presence of Al_3Sc dispersoids [269], but further investigations are needed to substantiate this effect during GBS.

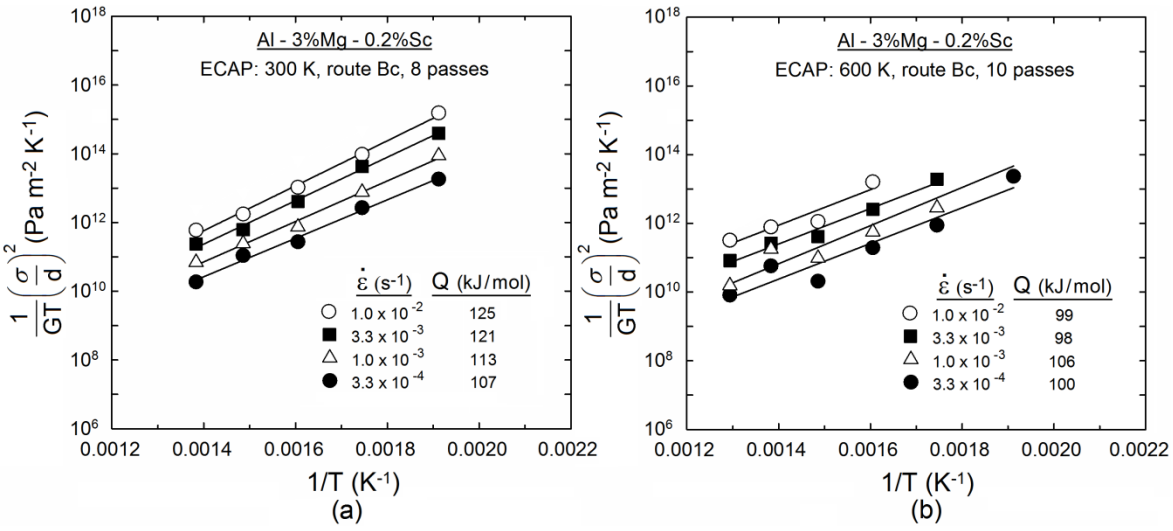

Figure 5.30 - Estimation of the activation energy for superplastic flow using an analysis based on Eq. (2.2) for the Al-3Mg-0.2Sc alloy processed by either (a) 8 passes of ECAP at 300 K or (b) 10 passes of ECAP at 600 K.

It is also demonstrated in Figure 5.30 that the Al alloy originally processed by ECAP at 600 K displays lower activation energies compared with the same metal processed at RT and these differences may be associated with the testing conditions selected for these estimations. Samples of the ECAP-RT material exhibited elongations slightly superior to 400 % after tensile testing at 523 K and it is probable that other deformation mechanisms operated simultaneously with GBS. Conversely, the ECAP-HT metal consistently displayed superplastic elongations after tests performed at 773 K whereby the high diffusion rates facilitate the accommodation during GBS. Therefore, the use of experimental datum points displaying elongations marginally superplastic at low temperatures could lead to overestimation of Q for the ECAP-RT alloy.

It is now well established that grain boundary sliding is accommodated by intragranular slip within the adjacent grains [238–240]. In practice, the presence of subgrains within HAGBs originates hindrance of dislocation motion during superplastic flow and this may significantly delay the rate of accommodation [241]. For this reason, superior superplastic elongations are generally attained in polycrystalline materials with grains sizes inferior to the steady state subgrain size, λ, predicted using Eq. 4.1.

Therefore, in order to evaluate whether the extensive grain growth observed in this investigation was sufficient to permit the development of subgrains during deformation at high temperatures, Figure 5.31 shows a plot of average grain boundary spacing, $\overline{L}$, vs the modulus-compensated stress, σ/G, for the Al-3Mg-0.2Sc alloy processed by ECAP and further tested in tension at various temperatures and strain rates: The solid line represents the theoretical prediction for λ in Al-Mg alloys using Eq. 4.1 with $\zeta = 20$, $\mathbf{b} = 2.86 \times 10^{-10}$ m and G (MPa) = $(3.022 \times 10^4) - 16T$ [237].

Several important conclusions may be drawn from examination of Figure 5.31.

First, the average grain sizes measured in Al-Mg-Sc specimens with superplastic elongations lie mostly below the predicted line for the steady-state subgrain size in Al-Mg alloys. This suggests that subgrains are basically absent in the microstructures of the ECAP-processed metal at the final stages of superplastic straining, as consistently confirmed through EBSD analyses performed after testing at 3.3×10^{-3} s^{-1} at 723 K.

Second, the grain sizes for samples exhibiting elongations inferior to 400 % lie close to the line for the steady state subgrain size in Al-Mg alloys calculated using Eq. 4.1. This is consistent with a comprehensive investigation using a Zn-22% Al alloy which demonstrates that, in conventional alloys, the transition from the superplastic regime to region III whereby the ductilities are reduced at higher strain rates normally occurs when a level of stress is achieved at which $\overline{L} \approx \lambda$ [270].

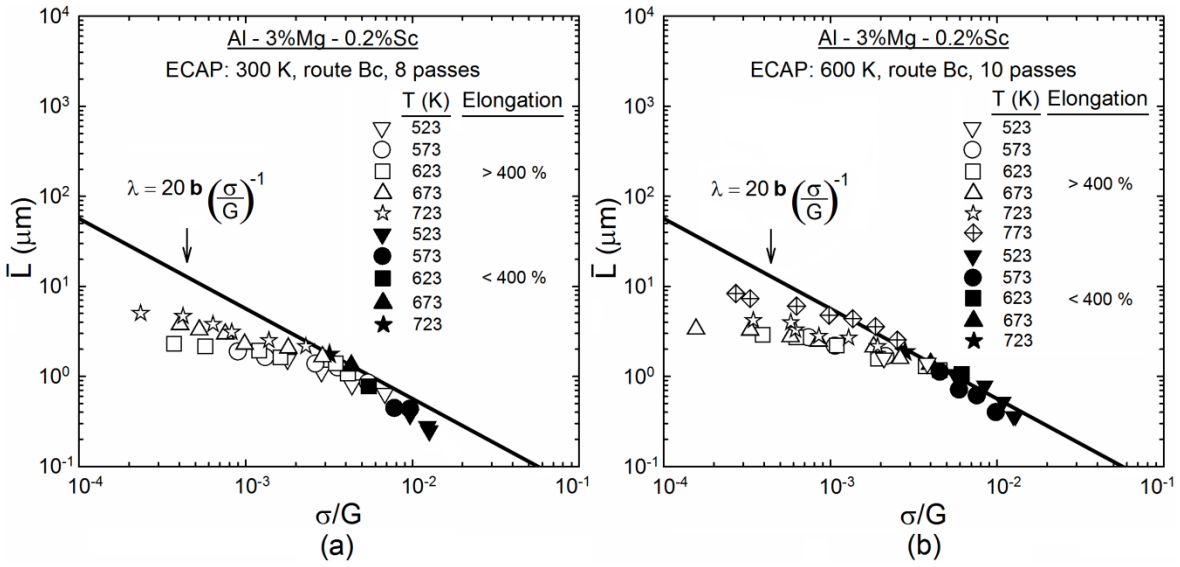

Figure 5.31 - Average grain boundary spacing, $\bar{L}$, vs modulus-compensated stress, σ/G, for the Al-3Mg-0.2Sc alloy processed by either (a) 8 passes of ECAP at 300 K or (b) 10 passes of ECAP at 600 K after tensile testing at various temperatures and strain rates: the solid line represents the theoretical prediction for λ using Eq. 4.1.

Third, a comparison of Figures 5.28 and 5.31 indicates that specimens having $\bar{L} > \lambda$ tend to withstand lower strains without failure during tensile testing at $T \geq 523$ K. This directly follows from the more difficult accommodation process when subgrains develop within sliding grains during superplastic flow. However, it is relevant to note that samples of the ECAP-RT metal tested at 523 K using $\dot{\varepsilon} \geq 3.3 \times 10^{-2}$ s^{-1} do not display elongations higher than 400 %. Although subgrains are unlikely to form under these experimental conditions, the diffusion rates at $T \approx 0.55T_m$ may have not been sufficient to capably accommodate GBS for these particularly high strain rates.

Furthermore, superplastic elongations were consistently attained in specimens of the ECAP-HT alloy with $\bar{L} > \lambda$ after testing at 773 K using strain rates superior to 10^{-2} s^{-1}. As the rate of lattice self-diffusion increases with increasing temperatures, dislocation climb also occurs at faster rates during deformation at higher temperatures. Therefore, although significant grain coarsening occurred in the ECAP-HT metal at $T \approx 0.8T_m$ possibly permitting the formation of substructures with LAGBs, the faster rate of dislocation climb at this temperature facilitates the accommodation in GBS and prevents incipient failure due to inter-linkage of cavities. For this reason, the presence or absence of subgrains shall not be solely used as a criterion to evaluate the effectiveness of accommodation during superplasticity.

In this investigation, all tensile tests were performed using miniature specimens having the same geometry shown in Figure 3.3 (b) and initial thicknesses of ~0.6 mm. Tensile tests at comparable conditions were previously performed using conventional Al-3Mg-0.2Sc samples with gauge length of ~5 mm and cross-sectional areas of ~2 × 3 mm^2 after 8 passes of ECAP at RT [43]. In addition, there is available data on the literature for the elongations obtained for the Al-5Mg-0.2Sc-0.08-Zr alloy processed by 10 ECAP passes at ~600 K and further tested in tension using specimens with a width of ~3 mm and a gauge length of ~6 mm [45].

A comparison of the elongations to failure obtained in these studies [43,45] with the results hereby presented consistently shows that the use of miniature specimens leads to significantly lower superplastic elongations after tensile testing. Elongations higher than 2000 % were attained using specimens with regular dimensions after testing at $T \geq 623$ K, whereas these elongations did not exceed 1500 % for miniature specimens of the ECAP-processed alloy. Nevertheless, it should be noted that these results are mutually consistent in terms of the range of strain rates and temperatures displaying elongations higher than the minimum threshold for superplasticity [105].

It has been demonstrated through experiments performed with UFG Cu that the elongations to failure are reduced by a factor of ~1.7 by decreasing the sample thicknesses from 1 to 0.35 mm [142]. Accordingly, although it is also shown that the elongations slightly decrease with increasing gauge length to width ratios, the apparently lower ductility measured after tensile testing at superplastic conditions using miniature specimens may be attributed to their extremely small thicknesses of ~0.6 mm compared with standard ECAP samples with ~1.5-2 mm in thickness [43,45].

It is worth mentioning that the use of miniature tensile specimens has become a regular procedure after HPT processing due to limitations associated with the reduced size of the discs after severe plastic deformation [34,54,271,272]. Therefore, the results obtained in this study also provide a reliable reference for comparison between the tensile properties of UFG materials processed by ECAP and HPT as further considered in the following chapters of this doctoral thesis.

From this comprehensive analysis, it is therefore concluded that, although ECAP at higher temperatures gives less refined grain structures, the Al-3Mg-0.2Sc alloy processed by 10 passes of ECAP at 600 K exhibits superior microstructural stability and thereby enhanced superplastic properties compared with the same alloy after ECAP at RT for tests performed at $T \geq 673$ K. Nevertheless, the ECAP-RT material displayed improved superplasticity at low homologous temperatures, as grain growth was less prominent at these testing conditions.

5.4 Summary and Conclusions

1. An Al-3% Mg-0.2% Sc alloy with an initial grain size of ~300 μm was subjected to ECAP at different temperatures to produce grain sizes of ~0.25 μm after 8 passes of ECAP at 300 K and ~0.60 μm after 10 passes of ECAP at 600 K. Microhardness measurements and EBSD analyses were performed immediately after processing and after static annealing for 1 h at temperatures up to 773 K. Tensile testing was conducted in miniature specimens of the UFG alloy at different temperatures using strain rates from 3.3×10^{-4} to 3.3×10^{-1} s^{-1}.
2. The Al alloy processed by ECAP at RT displays finer grain structures and a higher average microhardness (~140 Hv) than after ECAP at 600 K. This follows from the increasing contribution of recovery for samples processed by ECAP at higher temperatures which delays the kinetics of grain refinement and increases the minimum grain size achieved after ECAP.
3. The Al-3Mg-0.2Sc alloy processed ECAP at 600 K exhibits lower driving pressures for grain boundary migration and therefore an enhanced microstructural stability compared with the UFG metal processed by ECAP at RT. As a result, this material displays higher hardness values and smaller grain sizes compared with the alloy processed at room temperature after further annealing for 1 h at $T \geq 623$ K.
4. The microstructure of the Al alloy processed by ECAP at 300 K displays abnormal grain coarsening leading to the development of duplex structures after heat treatment at $T \geq 723$ K. This is attributed to the reduction of the pinning pressures due to coarsening of Al_3Sc dispersoids together with the occurrence of discontinuous precipitation during static annealing.
5. High superplastic ductilities were attained in samples of the ECAP-processed metal at temperatures from 523 to 773 K. The alloy originally processed at 600 K exhibited superior elongations at $T \geq 673$ K due to its enhanced thermal stability compared with the UFG metal processed by ECAP at RT. The highest elongation to failure was recorded as ~1490 % at 723 K when using a strain rate of 3.3×10^{-3} s^{-1}.
6. High strain rate superplasticity was consistently observed in the Al alloy processed by ECAP after testing at $T \geq 623$ K. The material processed at 300 K also displayed elongations higher than 400 % after testing at 523 and 573 K for initial strain rates $\geq 10^{-2}$ s^{-1}. The improved superplasticity at low homologous temperatures follows from the less pronounced grain coarsening at these conditions.

7. Analysis of the data confirms a stress exponent of n = 2 for samples of the ECAP-processed metal having superplastic elongations, as predicted using the theoretical model for superplastic flow in conventional alloys, and all experimental results are reasonably consistent with this model within one order of magnitude of strain rate. The calculated activation energies for superplasticity range from ~99 to 125 kJ mol^{-1} for all processing temperatures and are slightly higher than for grain boundary diffusion in pure Al (~86 kJ mol^{-1}).
8. The use of miniature specimens results in significantly lower elongations than in conventional ECAP samples for tensile tests performed at superplastic conditions. This follows from the reduced thicknesses of ~0.6 mm of the miniature specimens compared with standard ECAP samples.

Chapter 6 Influence of Processing Temperature on the Thermal Stability and Superplastic Behaviour of an Al-Mg-Sc Alloy Processed by HPT

6.1 Introduction

There have been studies showing that processing Al-Mg-Sc alloys by HPT leads to enhanced mechanical strength and additional grain refinement compared with processing by ECAP [48–50,53]. An Al-3Mg-0.2Sc alloy was processed through 5 turns of HPT at room temperature to produce a fairly homogeneous array of grains with an average size of ~0.15 μm [48], whereas an average grain size of ~0.25 μm was attained in the same metal after 8 passes of ECAP at 300 K.

By contrast, the elongations to failure in Al-Mg-Sc alloys after HPT at RT and further tensile testing at 673 K [48,52] are lower than in the ECAP-processed material, and although the reduced ductility in HPT-processed metals is commonly attributed to the use of tensile specimens with small thicknesses [48,49,53–55], no information is provided about the microstructural changes in HPT-processed samples of Al-Mg-Sc alloys when exposed to elevated temperatures. Additionally, there are insufficient data available concerning the range of strain rates and temperatures in which Al-Mg-Sc alloys processed by HPT display true superplasticity.

Recent investigations have demonstrated that HPT processing at high temperatures results in slightly larger grain sizes and lower hardness values in stainless steel [57,58], Mg alloys [59,60] and pure Ni [56] compared with processing at ambient temperature. Conversely, these materials usually have more stable microstructures when annealed after HPT [56–58] and exhibit higher superplastic elongations, as documented for the AZ61 [59] and the Mg–9Al alloy [60]. Accordingly, processing by HPT at high temperatures has emerged as a promising strategy to delay the grain growth kinetics in Al-Mg-Sc alloys and retain ultrafine grains at temperatures adequate for superplastic forming.

Both the absence of sufficient data regarding the microstructural evolution in HPT-processed Al-Mg-Sc alloys and the opportunity of enhancing the thermal stability and superplastic properties of this metal by conducting HPT at an elevated temperature motivated the studies presented in this chapter. Therefore, this investigation was initiated to evaluate the influence of processing temperature on the microstructural stability and

mechanical properties of an Al-3Mg-0.2Sc alloy processed through 10 turns of HPT at either 300 or 450 K and provide new information concerning the range of temperatures and strain rates wherein the HPT-processed samples exhibit superplastic flow.

For this purpose, the HPT-processed alloy was systematically annealed for 1 h at temperatures ranging from 423 to 773 K and its mechanical properties and microstructural evolution were examined using microhardness measurements together with SEM, EBSD and TEM analyses. The dislocation density immediately after HPT was estimated through XRD examinations and the size, coherency and distribution of Al_3Sc precipitates after annealing at 673 K were assessed through TEM and HRTEM analyses. Furthermore, miniature tensile specimens with similar dimensions as in the ECAP-processed metal were machined from the HPT-processed discs and further pulled to failure at temperatures ranging from 473 to 723 K.

6.2 Experimental Results

6.2.1 Microstructural Stability of the HPT-Processed Al-Mg-Sc Alloy

6.2.1.1 Microhardness Measurements

Prior to HPT processing, the solution treated samples had a uniform thickness of ~0.82 mm and this was reduced to ~0.70 mm at the centre and ~0.63 mm at the edge of the discs processed through 10 turns of HPT due to the material outflow and the elastic distortions of the anvils [110,112]. Figures 6.1 and 6.2 show the variation of the Vickers microhardness recorded at the middle-section position with distance from the centre of the Al-3Mg-0.2Sc discs subjected to HPT processing at either 300 or 450 K, respectively.

It follows from Figure 6.1 that there is a general increase in the hardness values of the Al alloy after compression within the HPT anvils, as indicated by the datum points represented using semi-filled squares (N = 0 turns). This hardness distribution has the same overall shape observed in other investigations using copper [273] and the AZ31 alloy [110] as there is a microhardness peak at the centre of the disc and the hardness tend to increase with increasing distance from the centre for radii > 1 mm [110].

After 0.5 turn of HPT at RT, there is a significant increase in the Vickers microhardness recorded along the diameter of the disc and hardness values higher than 160 Hv are readily observed at the edge of the HPT-processed sample. In addition, it is clearly noted that the microhardness increases with increasing distance from the centre of the disc such that processing through 0.5 turns of HPT results in the most inhomogeneous microhardness distribution among all processing conditions used in this investigation.

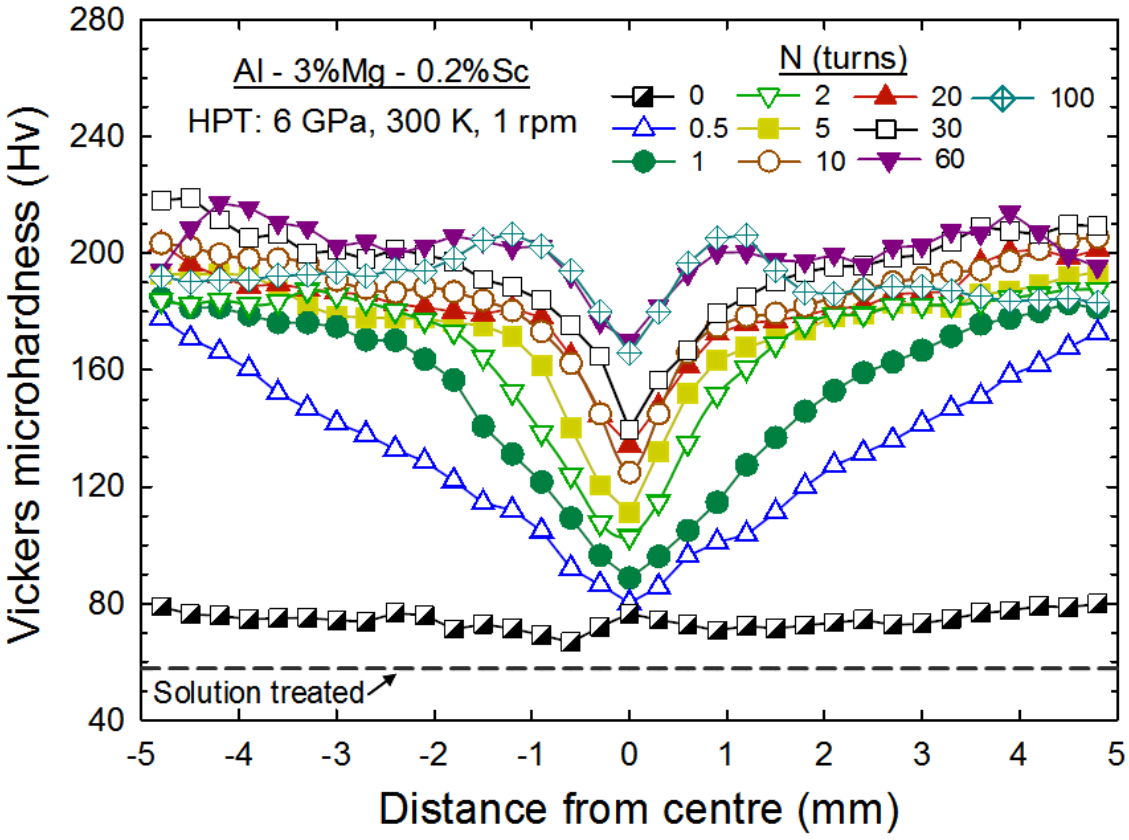

Figure 6.1 - Variation of the Vickers microhardness recorded at the middle-section position with distance from the centre of the Al-3Mg-0.2Sc discs processed by HPT at 300 K.

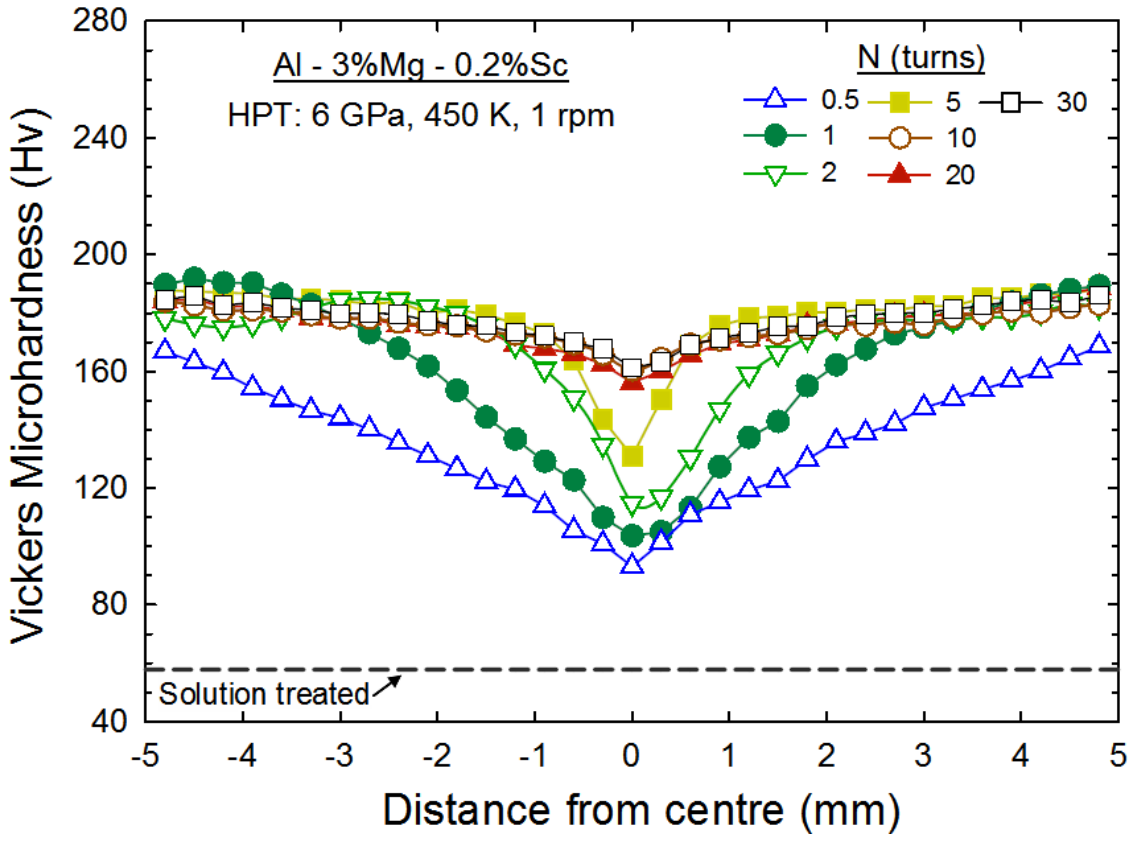

Figure 6.2 - Variation of the Vickers microhardness recorded at the middle-section position with distance from the centre of the Al-3Mg-0.2Sc discs processed by HPT at 450 K.

It is also revealed in Figure 6.1 that additional torsional straining up to 30 HPT turns leads to further increase in the Vickers microhardness up to a maximum value of ~ 220 Hv. Furthermore, the local mechanical properties tend to become less heterogeneous with increasing number of turns, although a completely uniform microhardness distribution was not achieved after HPT at 300 K. It should also be noted that the values of the Vickers microhardness at the periphery of the Al-Mg-Sc disc decrease after 60 turns of HPT and this extends to inner regions of the sample after processing through a total of 100 HPT turns as hardness values of ~190 Hv were recorded at radii > 2 mm.

Inspection of Figure 6.2 demonstrates that the hardness evolution for the material processed by HPT at an elevated temperature displays the same general trend observed in Figure 6.1 for samples processed at RT. Nevertheless, it is evident from these plots that increasing the processing temperature to 450 K results in faster hardening kinetics, more homogeneous hardness distributions and lower values for the saturation microhardness (~185 Hv) attained during HPT processing. After 10 turns of HPT, the Al-3Mg-0.2Sc alloy develops a reasonably uniform microhardness distribution with hardness values of ~160 and 185 Hv at the centre and edge of the deformed disc, respectively. It is also apparent that there is no further hardening or softening after 10 HPT turns as the distributions of the Vickers microhardness remain essentially unchanged after processing through 20 and 30 turns of HPT at 450 K.

In order to evaluate in detail the microhardness distribution in the middle-section position, hardness measurements were taken over the entire disc surfaces following a rectilinear grid pattern as illustrated in Figure 3.2. Accordingly, colour-coded contour maps were constructed using these measurements for Al-3Mg-0.2Sc discs processed through (a) 1 and (b) 10 turns of HPT at either 300 or 450 K as shown in Figures 6.3 and 6.4, respectively.

The microhardness values displayed in Figures 6.3 and 6.4 are consistent with the hardness distributions in Figures 6.1 and 6.2 thereby validating the assumption of axial symmetry in the hardness evolution during HPT processing. It is readily seen from these maps that the microhardness distributions for samples processed through 1 turn of HPT exhibit a doughnut-like pattern in which there is a ring of higher hardness values in the range of ~170-190 Hv and a central region with microhardness within the interval of 90-150 Hv. Comparison of Figures 6.3 (a) and 6.4 (a) also reveals that the Al-3Mg-0.2Sc alloy processed through 1 turn of HPT at 450 K (~0.5 T_m) displays higher hardness values than after 1 HPT turn at ~0.3 T_m considering equivalent radial positions.

After 10 turns of HPT processing, the hardness distributions become more uniform and there is a general increment in the Vickers microhardness recorded at the middle-section

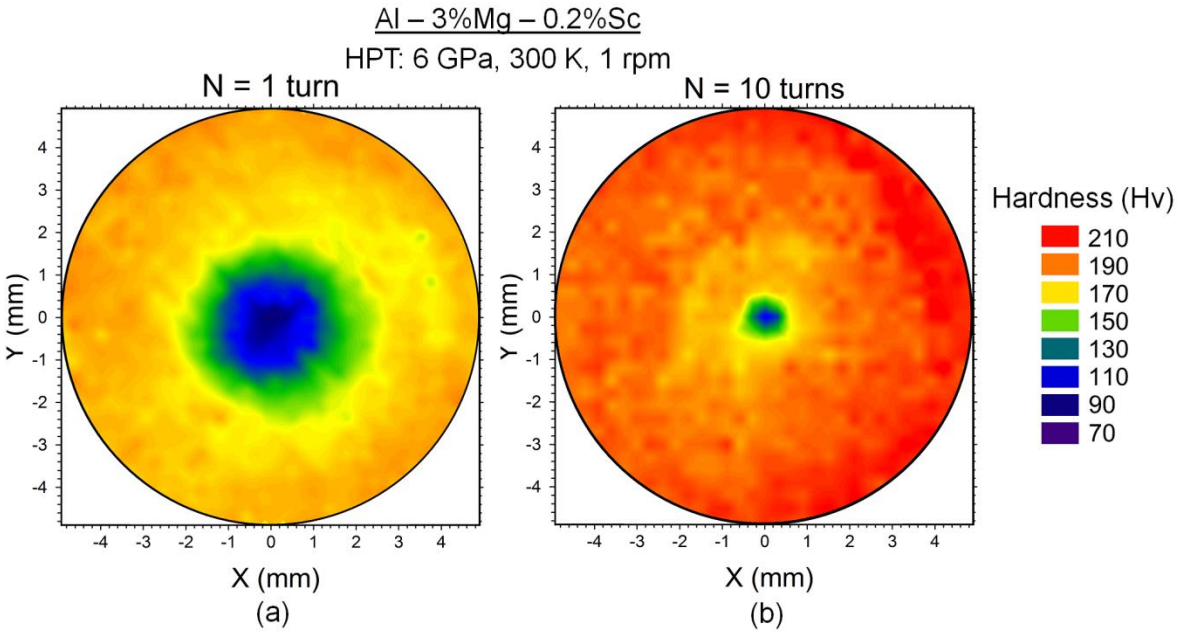

Figure 6.3 - Colour-coded contour maps showing the distributions of the Vickers microhardness over the surfaces of Al-3Mg-0.2Sc discs processed through (a) 1 and (b) 10 turns of HPT at 300 K.

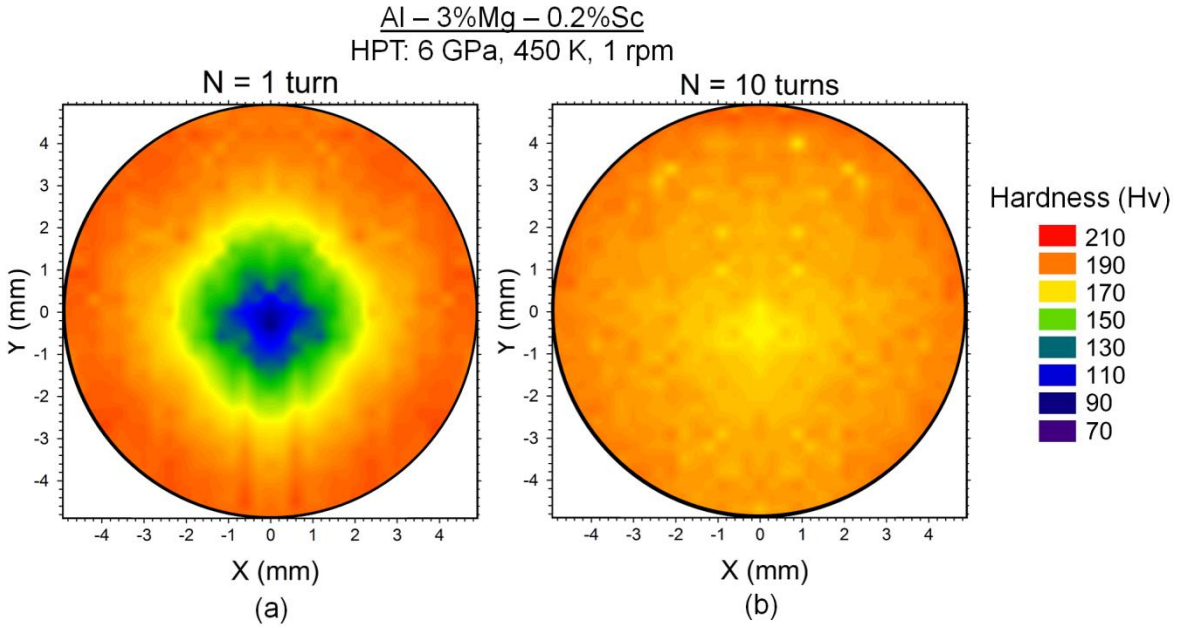

Figure 6.4 - Colour-coded contour maps showing the distributions of the Vickers microhardness over the surfaces of Al-3Mg-0.2Sc discs processed through (a) 1 and (b) 10 turns of HPT at 450 K.

position in samples of the Al-3Mg-0.2Sc alloy. Although hardness values < 150 Hv are still detected at the central region of the disc processed at RT, these are confined to smaller areas having diameters of ~1 mm. By contrast, the Vickers microhardness is limited within the interval of 170-190 Hv throughout the entire surface of the Al-Mg-Sc disc processed by 10 turns of HPT at 450 K.

The variation of Vickers microhardness along the diameters of samples of the Al-3Mg-0.2Sc alloy processed through 10 HPT turns at either 300 or 450 K and further annealed at temperatures ranging from 423 to 773 K are depicted in Figures 6.5 and 6.6, respectively, where the hardness measurements of the HPT-processed discs are represented by open circles. For simplification purposes, samples of the Al alloy immediately after 10 HPT turns at either 300 or 450 K are henceforward denoted as HPT-RT and HPT-HT material.

The results displayed in Figure 6.5 reveal that there is no apparent change in the hardness distribution of the HPT-RT metal after annealing for 1 h at 423 K. After heat treatment at 473 K, there is a substantial decrease in the microhardness of the HPT-processed material and the hardness distribution becomes fairly homogeneous, except at the central area of the disc wherein the hardness measurements are similar to those observed immediately after processing at 300 K. Additionally, annealing at $T \geq 523$ K results in a further reduction of the Vickers microhardness as well as a more uniform hardness distribution in the HPT-RT samples. Conversely, local hardness variations of the order of ~10 Hv are evident in the middle-section of the Al alloy annealed for 1 h at 623 and 673 K.

It follows from Figure 6.6 that post-HPT annealing at temperatures up to 473 K leads to a slight decrease in the hardness recorded along the diameter of the Al-3Mg-0.2Sc samples

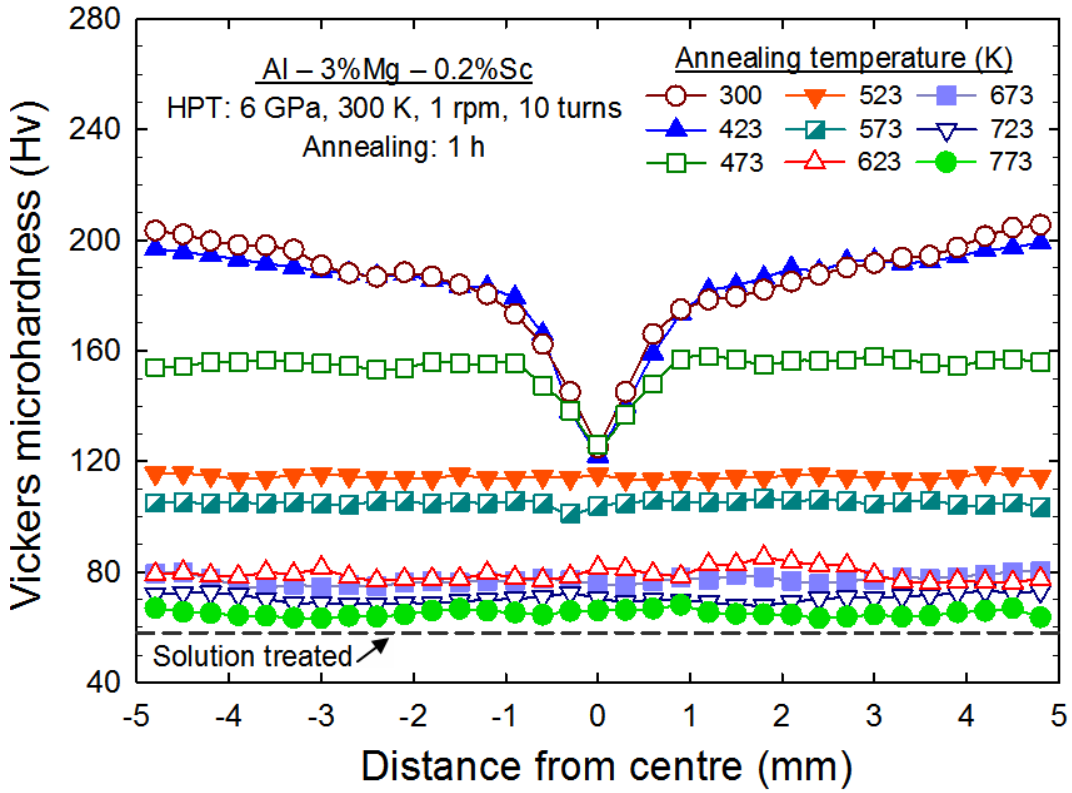

Figure 6.5 - Variation of the Vickers microhardness recorded at the middle-section position with distance from the centre of the Al-3Mg-0.2Sc discs after processing by HPT at 300 K and subsequent annealing.

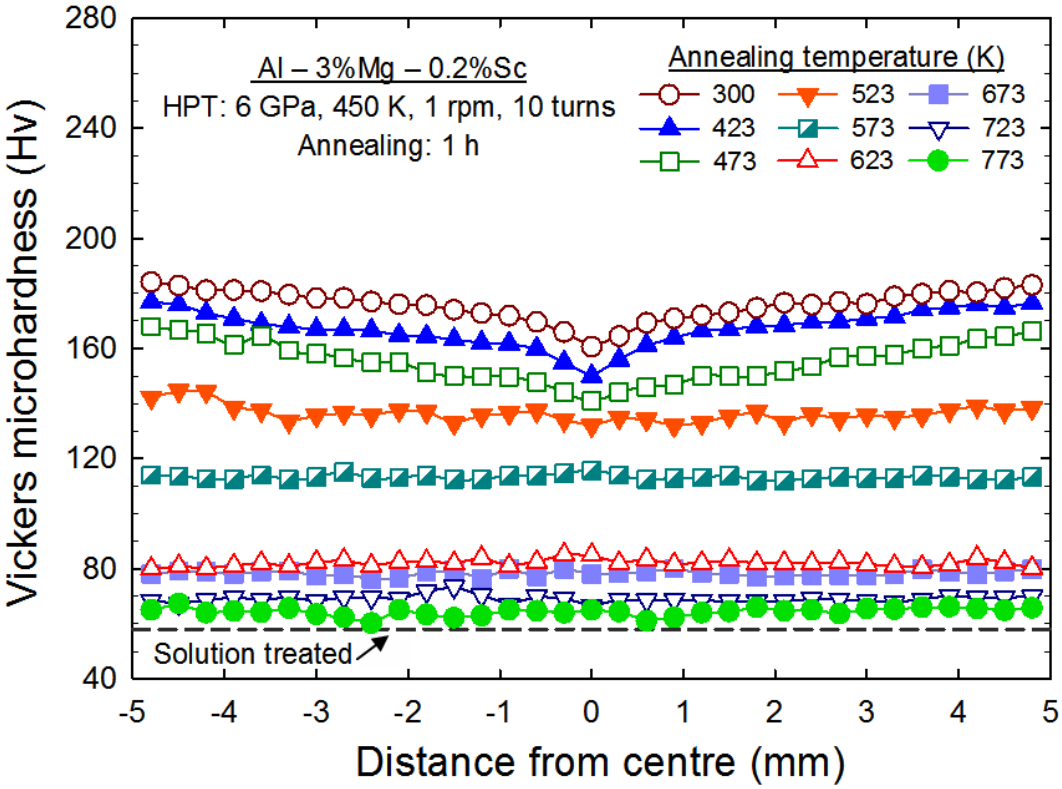

Figure 6.6 - Variation of the Vickers microhardness recorded at the middle-section position with distance from the centre of the Al-3Mg-0.2Sc discs after processing by HPT at 300 K and subsequent annealing.

originally processed by 10 turns of HPT at 450 K, but nevertheless the overall shape of the microhardness distribution remains essentially unchanged. In addition, the microhardness distribution in the HPT-HT metal becomes reasonably homogeneous after annealing at $T > 473$ K, although the hardness values continue decreasing with increasing temperatures.

In order to provide information about the softening kinetics in Al-Mg-Sc alloys processed by HPT when exposed to elevated temperatures, Figure 6.7 shows the variation of the area-weighted average microhardness with the annealing temperature for Al-3Mg-0.2Sc discs processed by HPT at different temperatures and subsequently annealed for 1 h. The results reveal that the Al alloy exhibits an average microhardness of ~190 Hv after 10 turns of HPT at 300 K and further annealing at $T \leq 423$ K. By contrast, annealing in the temperature range from 473 to 623 K leads to a sharp reduction in the hardness values of the HPT-RT material and these values continue to decrease but at lower rates for annealing temperatures superior to 673 K.

It is demonstrated in Figure 6.7 that the average microhardness of the HPT-HT metal is ~180 Hv and this marginally decreases after heat treatment at temperatures up to 473 K

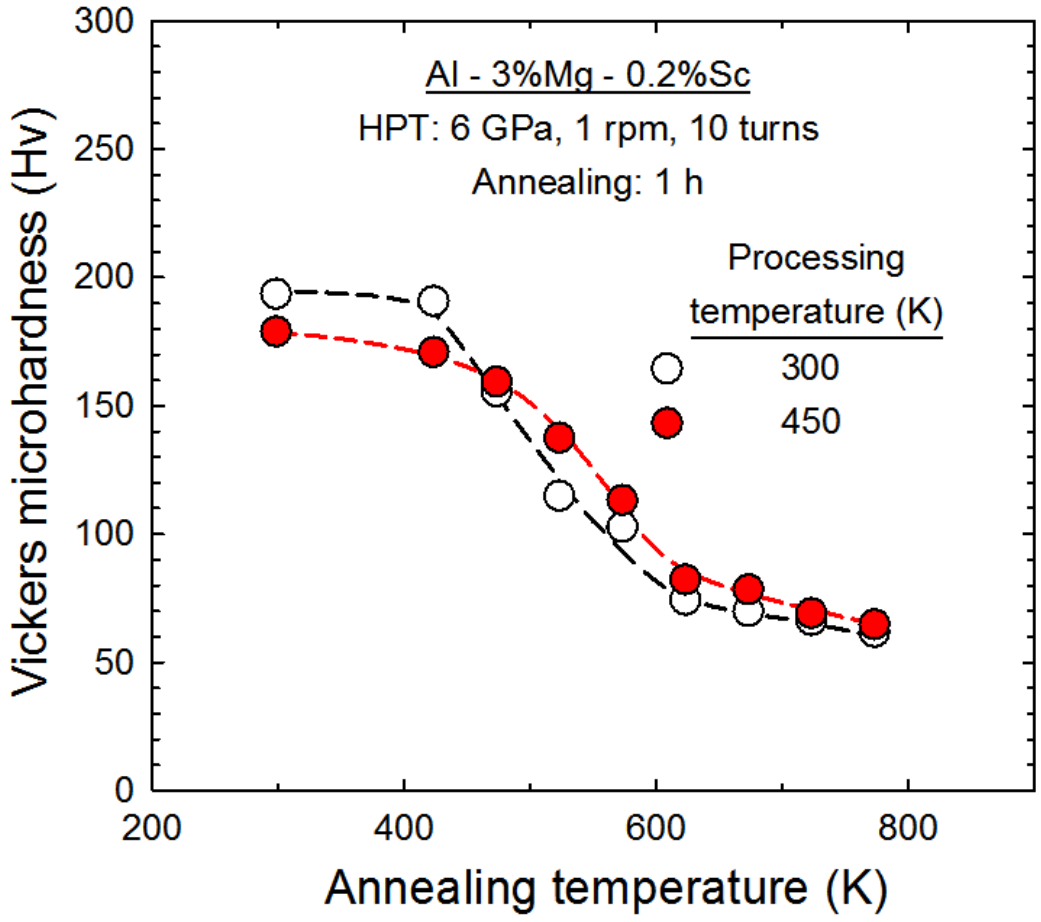

Figure 6.7 - Average microhardness as a function of annealing temperature for the Al-3Mg-0.2Sc discs processed through 10 turns of HPT at either 300 or 450 K and further annealed for 1 h at temperatures from 423 to 773 K.

wherein the Vickers microhardness is ~160 Hv. Conversely, it is clearly evident that annealing at temperatures within the interval from 523 to 623 K leads to a more significant reduction in the hardness values which continue to decline but at rates comparable to the HPT-RT samples annealed at $T \geq 673$ K.

It is also apparent in Figure 6.7 that the Al-3Mg-0.2Sc alloy processed through 10 turns of HPT at 300 K exhibits higher hardness values immediately after processing and after heat treatment for 1 h at $T \leq 423$ K by comparing with the metal originally processed by HPT at a high temperature. Nevertheless, these plots clearly show that the material processed by HPT at $\sim 0.5T_m$ displays superior microhardness after annealing at $T \geq 473$ K as a consequence of the faster softening kinetics of the HPT-RT metal.

6.2.1.2 Microstructural Evolution

Figures 6.8 and 6.9 show typical STEM images taken at positions located at distances of ~3-4 mm from the centre of the Al-3Mg-0.2Sc discs processed through 10 turns of HPT at either 300 or 450 K, respectively. It is evident in these figures that the microstructures of the HPT-processed samples are constituted by UFG structures with similar sizes even though they were deformed at markedly distinct temperatures. Furthermore, the grains developed after 10 turns of HPT processing are homogeneously distributed throughout the areas of the discs examined in these STEM images.

The linear intercept method was used to estimate the average grain boundary spacing in Figures 6.8 (a) and 6.9 (a). As a result, grain sizes of ~140 and ~150 nm were calculated for the Al-3Mg-0.2Sc alloy subjected to 10 revolutions of HPT processing at either 300 or 450 K, respectively. Although similar grain sizes were obtained after processing, it is apparent that high-pressure torsion at $\sim 0.5T_m$ leads to the formation of fairly equiaxed grains, whilst the grain structures formed during processing at room temperature are somewhat elongated.

Inspection of Figures 6.8 and 6.9 also reveals the presence of dislocations within some of the UFG structures formed after severe plastic deformation, as more evidently seen in Figures 6.8 (c) and 6.9 (c). The dislocations lines are mainly isolated and few of these crystalline defects apparently pile up at grain boundaries. Nevertheless, a more detailed examination of Figures 6.9 (b) and (c) shows that some dislocations in the HPT-HT metal are arranged in the form of cell structures and this could be a result of the increasing participation of recovery during deformation at higher temperatures.

In this investigation, there was no experimental evidence of precipitation of nano-sized Al_3Sc dispersoids in the solution treated Al-3Mg-0.2Sc alloy during HPT processing at either 300 or 450 K. The Al_3Sc phases were not detected either by STEM examinations as indicated in Figures 6.8 and 6.9 or through extensive SEM, TEM and HRTEM analyses, with the exception of few dispersoids with sizes comparable to the undissolved precipitates shown in Figure 4.4 (b).

Samples of the HPT-processed metal were final polished using 0.06 μm silica colloidal and then etched using an aqueous solution having 5 % of HBF_4. Afterwards, EBSD scans with a step size of 30 nm were performed at positions located at distances of ~3 mm from the centres of the discs and the OIM images obtained for the Al-3Mg-0.2Sc alloy immediately after 10 turns of HPT processing at either 300 or 450 K are shown in Figure 6.10.

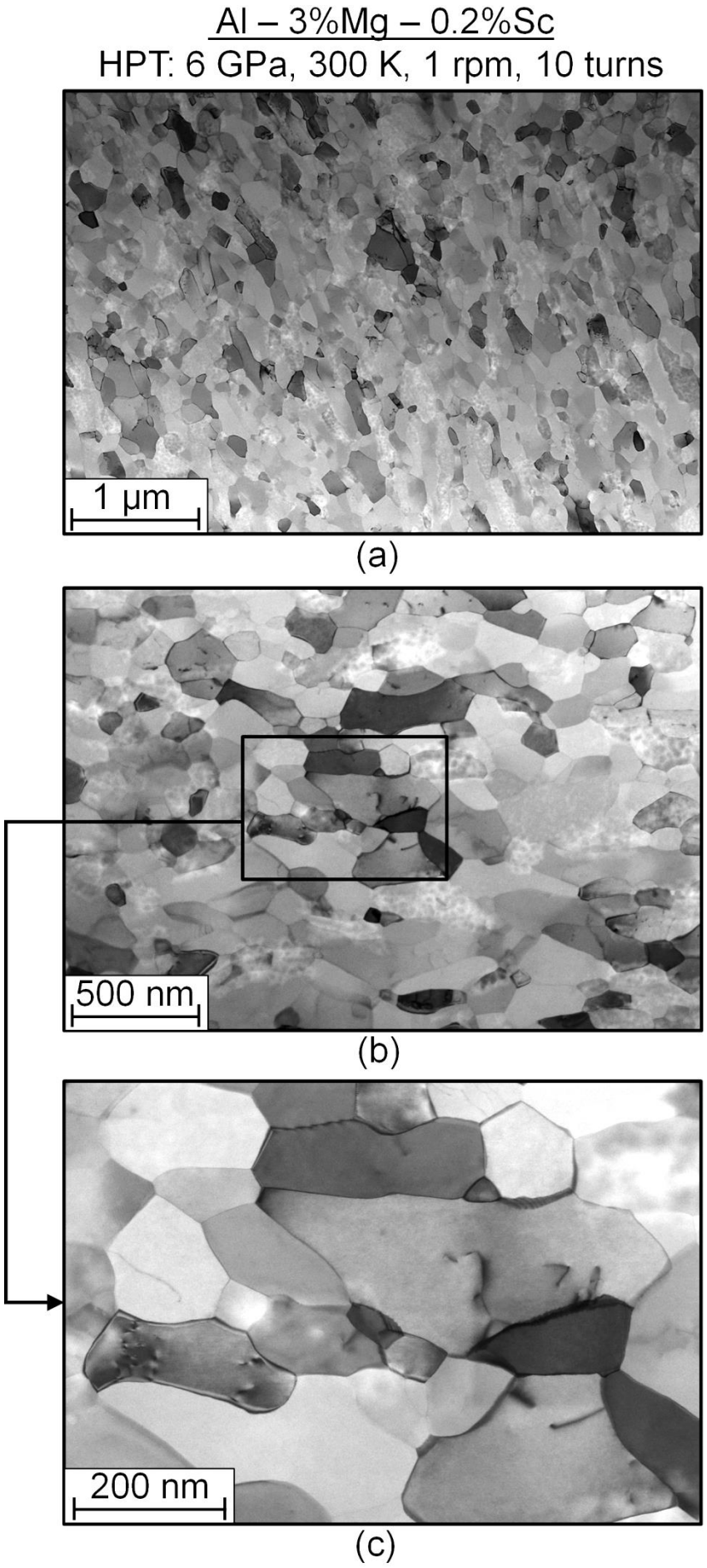

Figure 6.8 - STEM images of the Al-3Mg-0.2Sc alloy processed by 10 turns of HPT at 300 K.

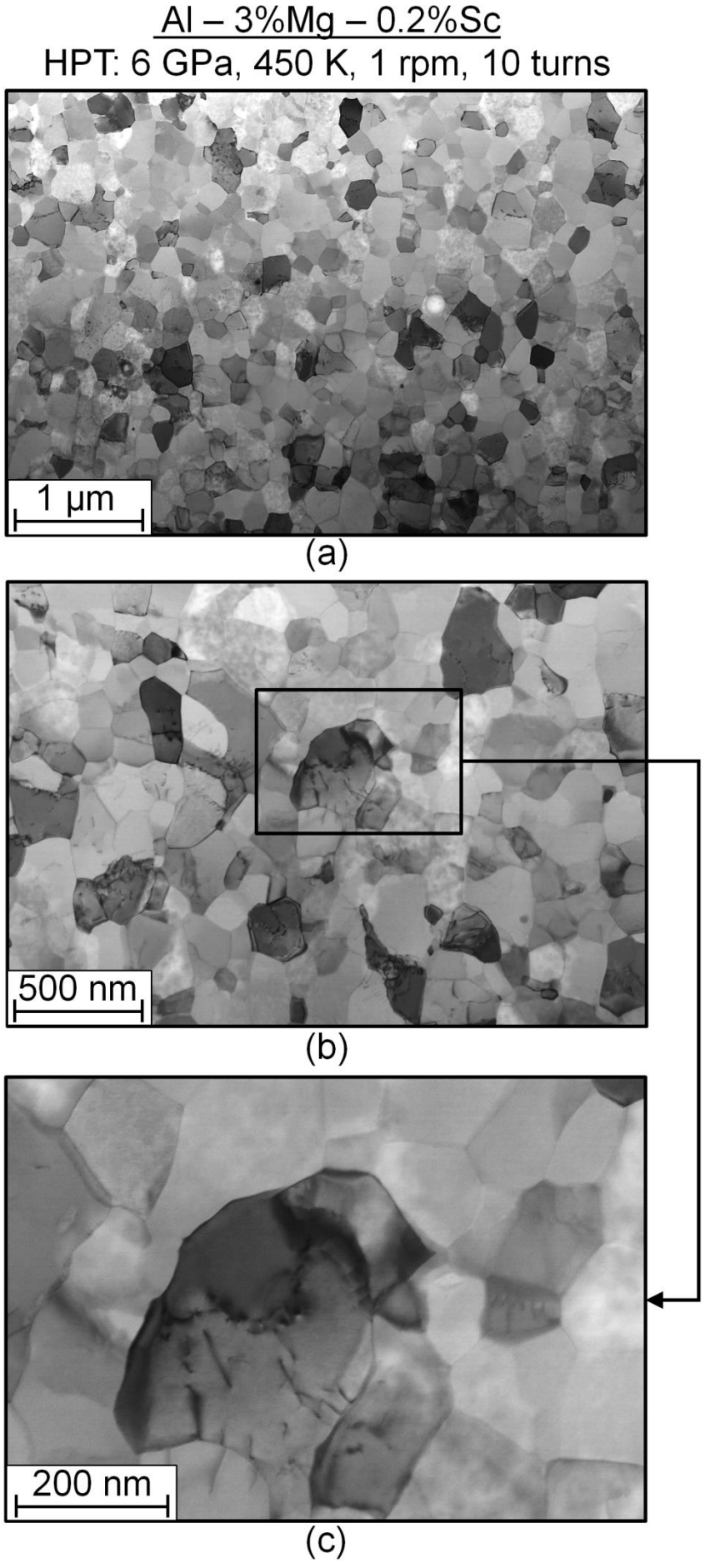

Figure 6.9 - STEM images of the Al-3Mg-0.2Sc alloy processed by 10 turns of HPT at 450 K.

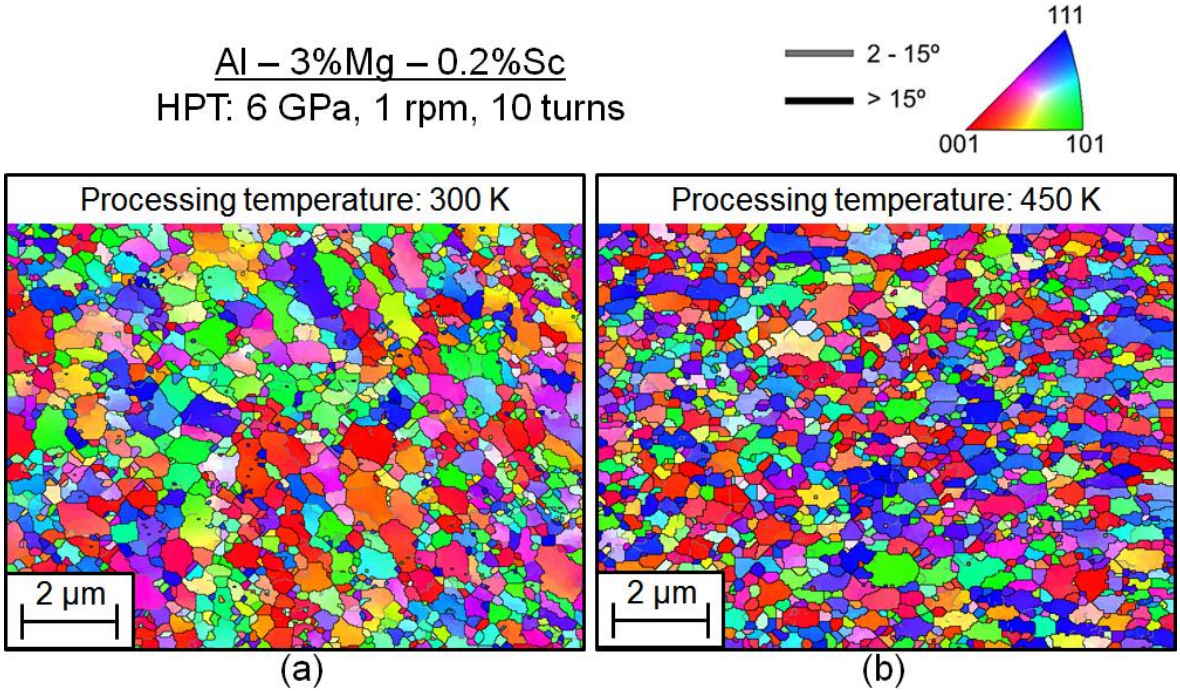

Figure 6.10 - OIM images of the Al-3Mg-0.2Sc alloy processed through 10 turns of HPT at either (a) 300 or (b) 450 K.

The results displayed in Figure 6.10 are consistent with the STEM images in Figures 6.8 and 6.9. It is clearly seen in the OIM images that the grain structures of the HPT-processed material have comparable sizes and are more elongated in the case of the alloy processed at a lower homologous temperature. It is also apparent that the microstructures after 10 turns of HPT are mostly formed by UFG structures with HAGBs and very few LAGBs are observed in the form of subgrains within grains having relatively large sizes.

Similarly to the STEM images, the linear intercept method was also used to measure the grain sizes in Figures 6.10 (a) and (b), but only considering boundaries with misorientation angles higher than 15º as intercepts. Accordingly, average grain boundary spacings of ~0.17 μm were estimated for both the HPT-RT and the HPT-HT alloy, showing good agreement with the values previously calculated in Figures 6.8 (a) and 6.9 (a) together with the average grain size of ~ 0.15 μm obtained using the same alloy after processing through 5 turns of HPT at RT [48].

Figure 6.11 displays histograms of (a) the area fraction of grain diameters and (b) the misorientation angles based on the OIM images in Figure 6.10 for the Al-3Mg-0.2Sc alloy subjected to 10 turns of HPT processing. It follows from Figure 6.11 (a) that samples processed by HPT at either 300 or 450 K have the same average grain diameter of ~ 0.32 μm, although the distribution of grain diameters is more disperse for the HPT-RT metal which has not achieved its saturation after 10 HPT revolutions.

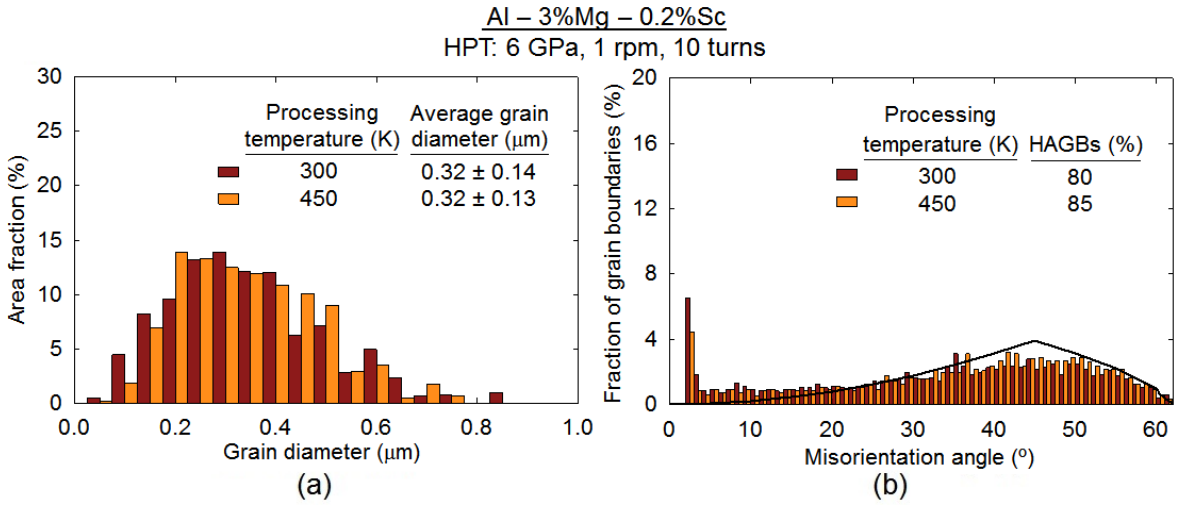

Figure 6.11 - Histograms of (a) the area fraction of grain diameters and (b) the misorientation angles for the Al-3Mg-0.2Sc alloy processed through 10 turns of HPT at either 300 or 450 K.

It is readily seen in Figure 6.11 (b) that the Al-Mg-Sc alloy has a notably high fraction of HAGBs after 10 turns of HPT processing. The material processed at room temperature exhibits a slightly lower fraction of HAGBs (~80 %) compared with the metal processed at $\sim 0.5T_m$ for which less than 15 % of the boundaries have misorientations below 15°. It is also noted in Figure 6.11 (b) that both histograms have the same overall shape, although the histogram of the HPT-HT metal conform more closely with the Mackenzie distribution [205].

In this study, the microstructural changes in Al-3Mg-0.2Sc samples processed by 10 turns of HPT and subsequently annealed were also examined through systematic EBSD scans at positions located at ~3 mm from the centres of the discs. Figures 6.12 and 6.13 show typical OIM images of the material processed by HPT at 300 and 450 K, respectively, after heat treatment for 1 h at temperatures ranging from 523 to 773 K.

It is clearly demonstrated in Figures 6.12 (a) and (b) that the HPT-RT metal has a uniform distribution of submicrometre grains with $\bar{L} \leq 0.5$ μm after heat treatment for 1 h at temperatures up to 573 K. Furthermore, substructures with LAGBs are seldom observed within the grains with HAGBs. Conversely, inspection of Figures 6.12 (c) and (d) reveals that there is an abnormal grain growth in the microstructure of the Al alloy annealed at 623 and 673 K. The average size of grains not abruptly coarsened is ~1 μm after annealing at 673 K, however more than 70 % of the area fraction of the analysed image corresponds to large grains with $\bar{L} > 10$ μm containing a notable fraction of LAGBs in their interior. After annealing at $T \geq 723$ K, the fraction of coarse grains further increases together with the average grain boundary spacing and the microstructural homogeneity as evident in Figures 6.12 (e) and (f).

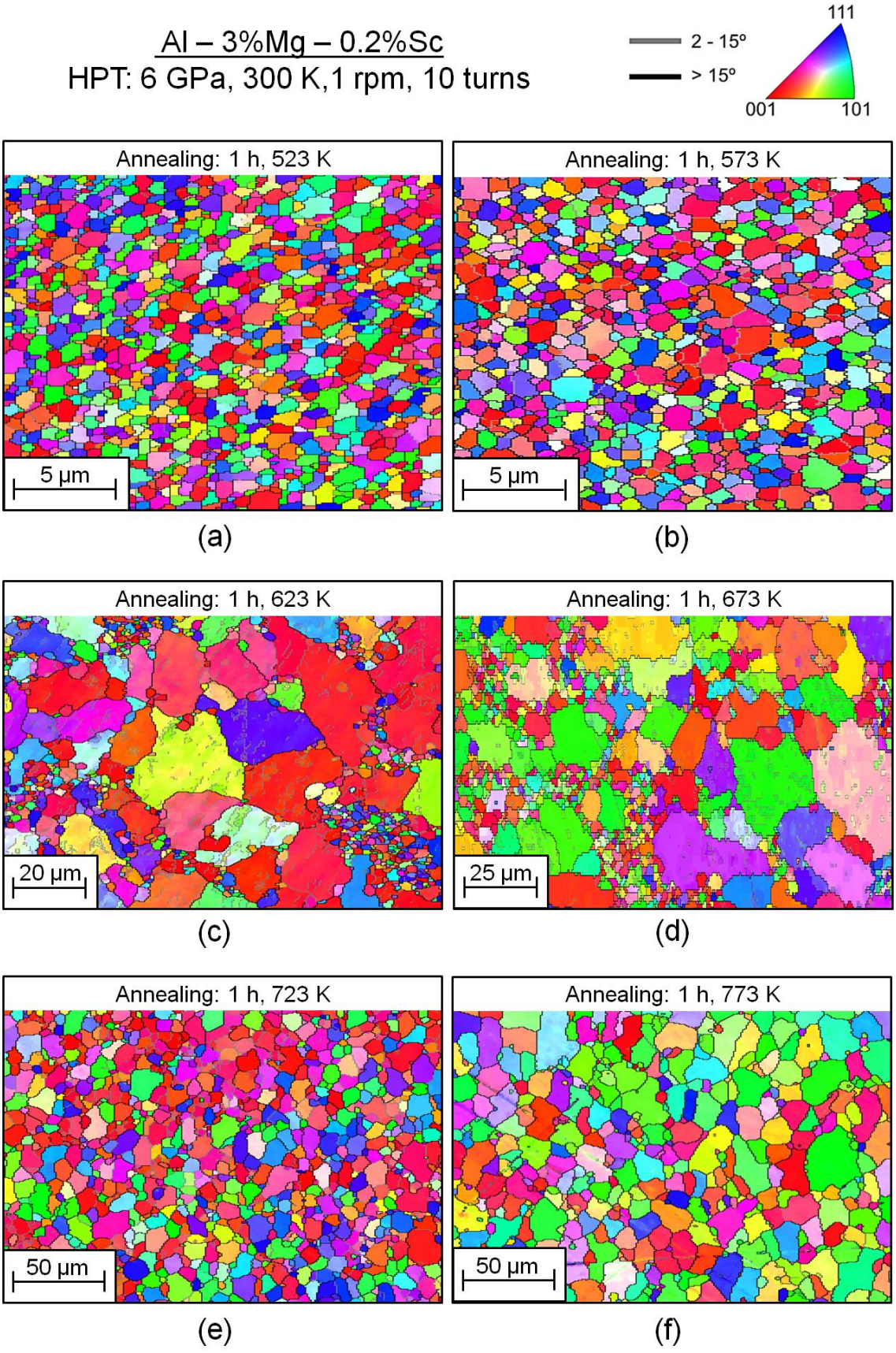

Figure 6.12 - OIM images of the Al-3Mg-0.2Sc alloy processed through 10 turns of HPT at 300 K and subsequently annealed at (a) 523, (b) 573, (c) 623, (d) 673, (e) 723 and (f) 773 K for 1 h.

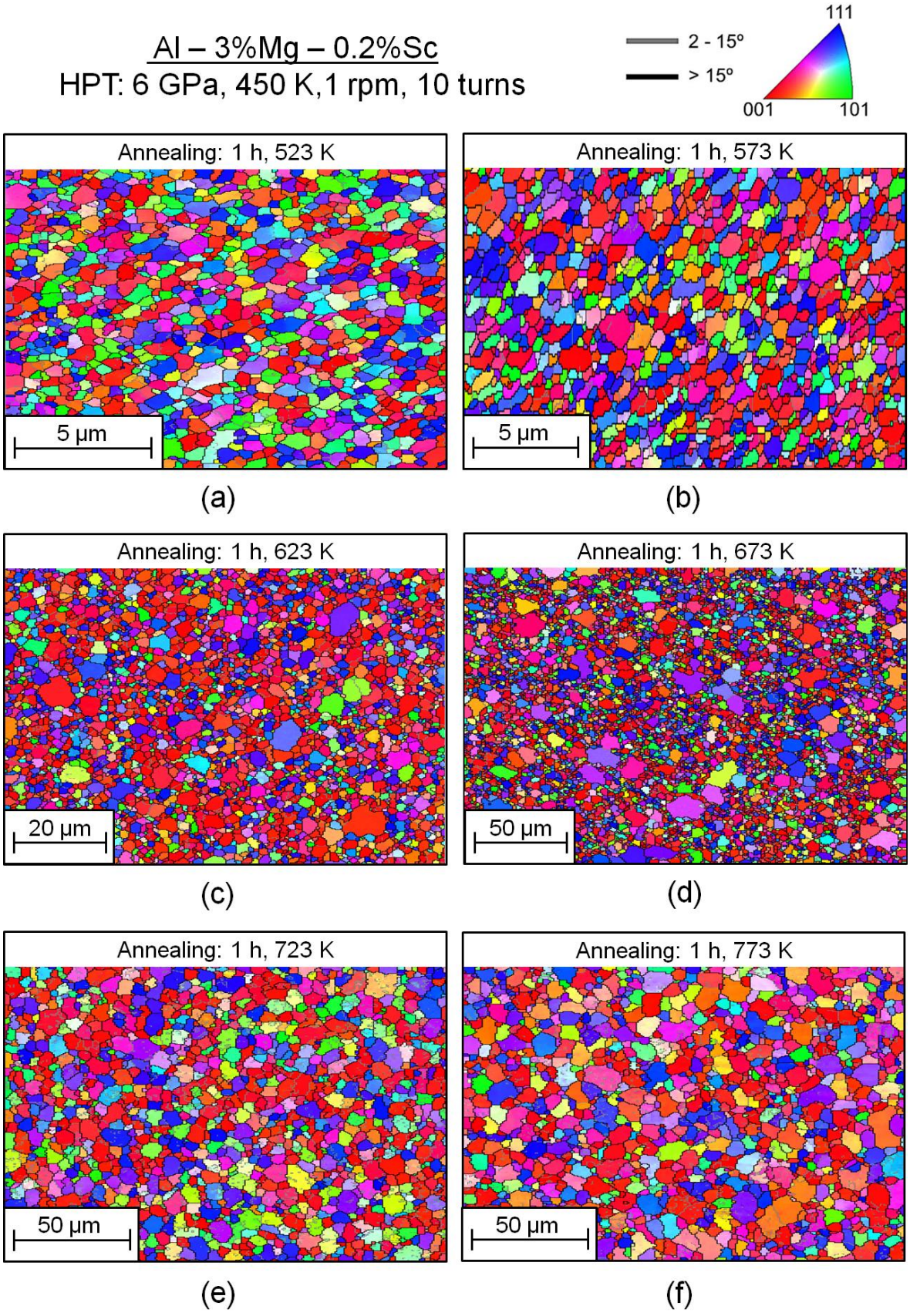

Figure 6.13 – OIM images of the Al-3Mg-0.2Sc alloy processed through 10 turns of HPT at 450 K and subsequently annealed at (a) 523, (b) 573, (c) 623, (d) 673, (e) 723 and (f) 773 K for 1 h.

It follows from Figures 6.13 (a) and (b) that the Al alloy processed by HPT at $\sim 0.5T_m$ exhibits a homogeneous distribution of UFG structures after annealing at $T \leq 573$ K for 1 h. Similarly to the HPT-RT metal, most of these structures are formed by HAGBs and subgrains are rarely visible in these OIM images. Additionally, it is readily observed in Figures 6.13 (c) and (d) the onset of a bimodal distribution of grains in the HPT-HT alloy annealed at 623 and 673 K for 1 h, but nevertheless the coarsening kinetics are comparatively slower in relation to the metal originally processed by HPT at 300 K as the UFG structures represent more than 70 % of the area fraction of the microstructure examined after heating at 673 K.

A more detailed inspection of Figures 6.13 (c) and (d) revealed the grain structures were reasonably equiaxed and substructures developed within some of the larger grains during annealing at 623 and 673 K. In addition, the average grain size and the amount of LAGBs in the HPT-HT alloy further increased after heat treatment at $T \geq 773$ K for 1 h as seen in Figures 6.13 (e) and (f).

The average grain sizes of the Al-3Mg-0.2Sc alloy immediately after processing through 10 turns of HPT and subsequent annealing were estimated in the OIM images depicted in Figures 6.12 and 6.13 using the linear intercept method. Accordingly, aiming to permit a clear comparison of the effect of processing temperature on the microstructural stability after HPT, Figure 6.14 shows the variation of the average grain boundary spacing as a function of annealing temperature for the metal subjected to HPT processing at either 300 or 450 K and further heat treated for 1 h at temperatures ranging from 423 to 773 K. For comparison purposes, the average grain boundary spacings calculated in Figures 6.8 (a) and 6.9 (a) were also added to these plots together with the average grain sizes calculated using the same procedure in representative SEM images taken in samples processed by HPT and further annealed at 423 and 473 K.

As depicted in Figure 6.14, there is no relevant increase in the size of the grain structures of the HPT-RT alloy after annealing at $T \leq 473$ K and this behaviour extends to temperatures up to 523 K for samples originally processed by HPT at 450 K. However, the grain sizes in the HPT-processed material grow at extremely fast rates when exposed to $T > 523$ K and this is particularly more substantial for the material processed by HPT at 300 K which achieves an average grain size of ~ 6.2 μm after heat treatment at 773 K for 1 h.

It should be noted that although the grain sizes rapidly increase after annealing at temperatures within the interval of ~573-673K, the grain coarsening rate decreases to almost negligible values for the HPT-HT metal annealed at $T > 673$ K such that $\bar{L} < 2$ μm after annealing at 773 K for 1 h. Furthermore, the average grain size in the Al-3Mg-0.2Sc alloy

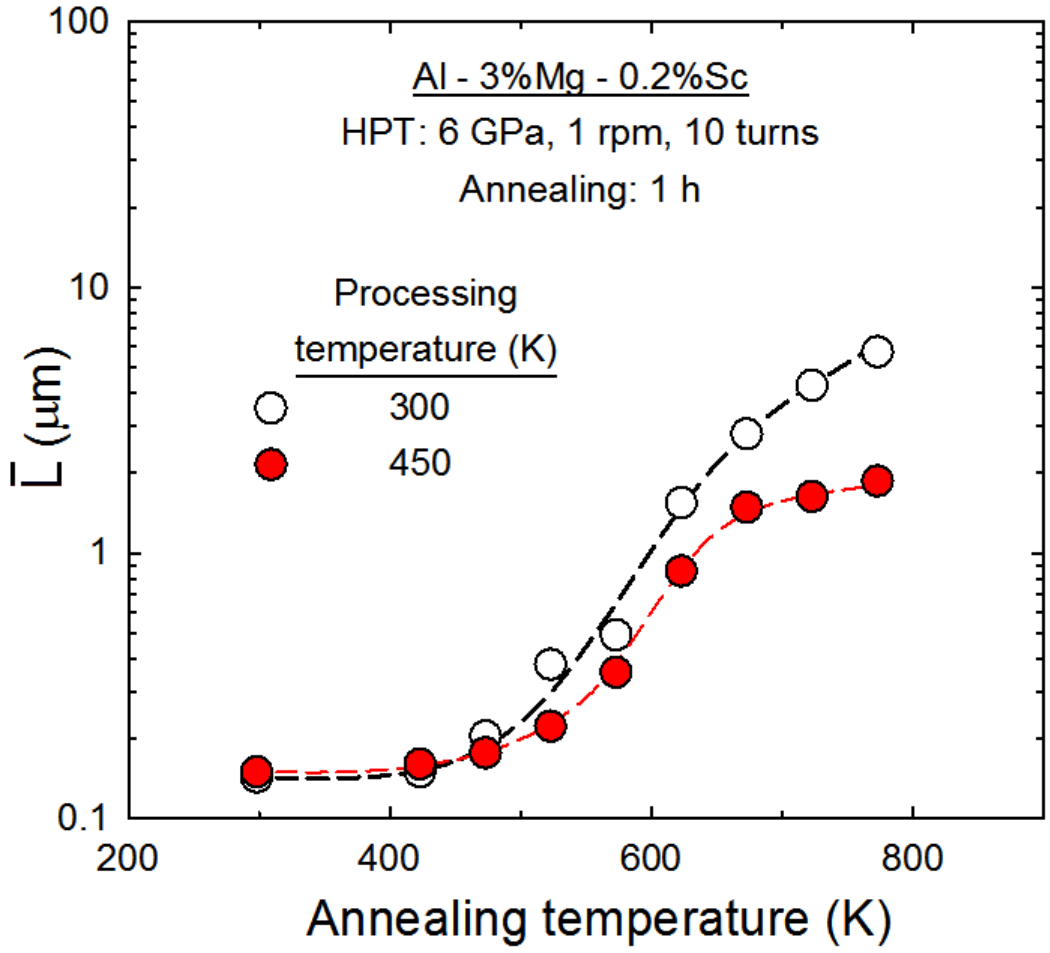

Figure 6.14 – Average grain boundary spacing, $\bar{L}$, as a function of annealing temperature for the Al-3Mg-0.2Sc alloy processed through 10 turns of HPT at either 300 or 450 K and further annealed for 1 h at temperatures ranging from 423 to 773 K.

subjected to HPT at ambient temperature was only slightly inferior to the values measured in the same metal immediately after HPT at 450 K. Nevertheless, the experimental data displayed in Figure 6.14 demonstrate that the grain structures developed during HPT processing at 300 K are less stable and become noticeably coarser than in the HPT-HT metal after annealing at equivalent conditions for $T \geq 473$ K.

As discussed in detail in Chapter 5, although the linear intercept method is extensively used to calculate the grain sizes of UFG metals, this procedure may underestimate the grain size in duplex structures and if used solely does not provide sufficient information about the grain size distributions. Therefore, in order to statistically describe the different grain sizes observed in the OIM images taken after systematic heat treatment, Figure 6.15 shows histograms of the area fraction of grain diameters for the HPT-processed alloy further annealed at temperatures ranging from 523 to 773 K.

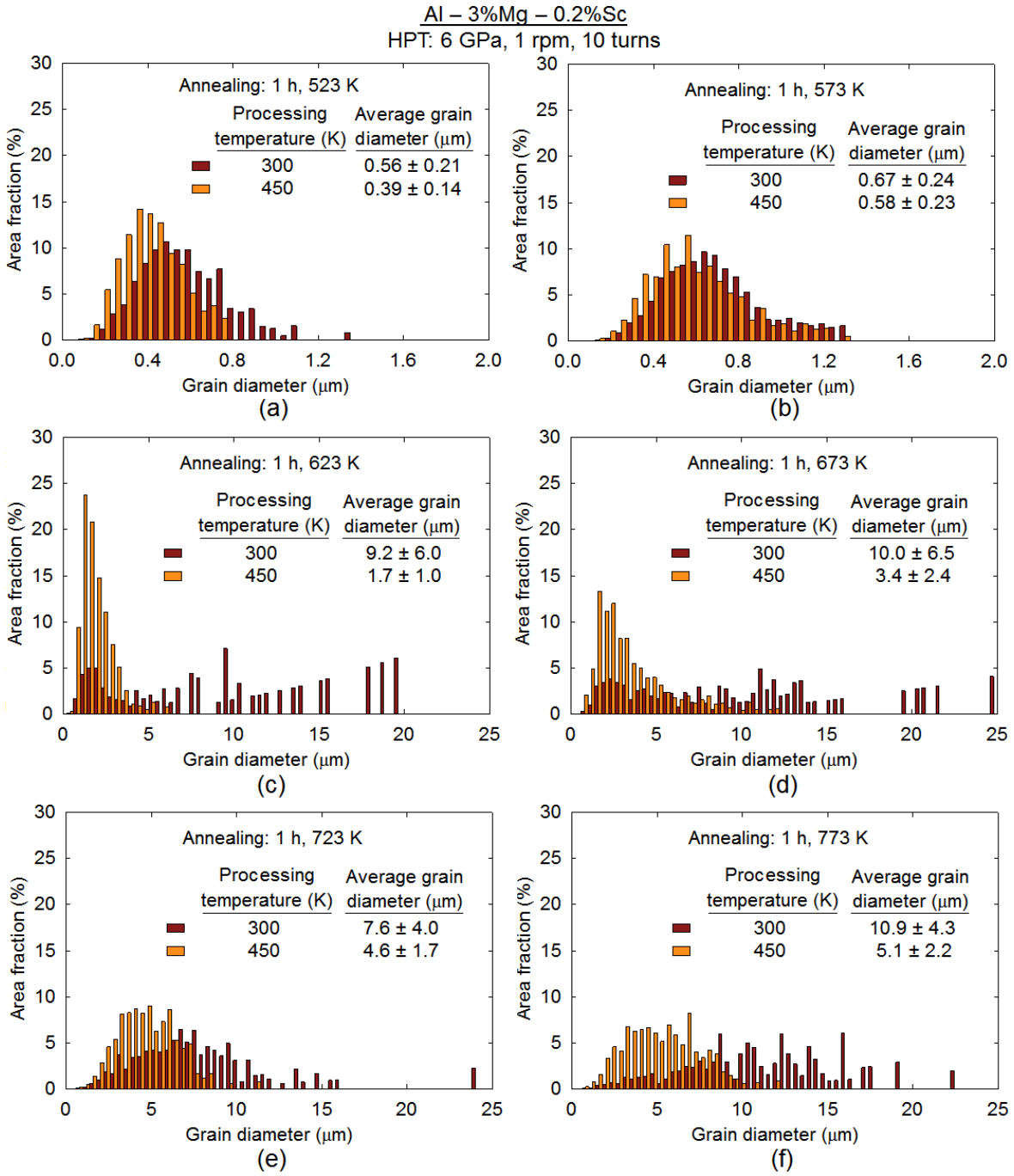

Figure 6.15 - Histograms of the area fraction of grain diameters for the Al-3Mg-0.2Sc alloy processed through 10 turns of HPT at different temperatures and further annealed for 1 h at (a) 523, (b) 573, (c) 623, (d) 673, (e) 723 and (f) 773 K.

It is readily observed in Figures 6.15 (a) and (b) that the Al-3Mg-0.2Sc alloy displays similar distributions of grain diameters after post-HPT heat treatment for 1 h at $T \leq 573$ K, regardless of the processing temperatures. Nevertheless, the HPT-HT metal consistently exhibits smaller grain sizes and has average grain diameters of ~0.39 and 0.58 μm after annealing at 523 and 573 K, respectively.

The onset of abnormal coarsening after HPT processing and subsequent heat treatment at 623 and 673 K is clearly characterized by the distributions of grain diameters depicted in Figures 6.15 (c) and (d). The histograms become significantly more disperse at these annealing conditions and this is particularly more evident for the Al alloy originally processed by HPT at 300 K which has grains with diameters ranging from ~0.6 to 25 μm for T = 673 K. By contrast, examination of these plots together with Figures 6.13 (c) ad (d) demonstrates that grain growth occurs more uniformly throughout the microstructures of the HPT-HT metal annealed at either 623 or 673 K and their abnormally coarsened grains have smaller sizes compared with the structures formed in the HPT-RT metal at equivalent temperatures.

The results displayed in Figures 6.15 (e) and (f) reveal that the distributions of grain diameters after annealing at 723 and 773 K are less disperse by comparing with the histograms obtained for HPT-processed discs heat treated at 623 and 673 K. Furthermore, it is surprisingly shown that the average grain diameters for the HPT-RT alloy annealed at $T \geq 723$ K are lower or marginally higher than after annealing at 673 K. It is also worth mentioning that the individual grain diameters in the material processed by HPT at ~0.5T_m continue virtually smaller than 10 μm even after annealing for 1 h at 773 K.

Figure 6.16 shows the variation of the average grain diameters with the annealing temperature for the Al-3Mg-0.2Sc alloy processed through 10 turns of HPT and further annealed for 1 h at temperatures from 523 to 773 K. A comparison of the plots in Figures 6.14 and 6.16 confirms that the linear intercept method gives lower values of grain size compared with the calculations of the area-weighted average grain diameter. Also, these differences are more prominent for samples having a bimodal distribution of grains as $\bar{L} \approx 1.5$ μm whereas $d_{eq} \approx 10$ μm after HPT at RT and subsequent annealing at 673 K.

It should be noted n Figure 6.16 that increasing the annealing temperature from 573 to 623 K for samples of the HPT-RT metal results in an abrupt increase of the average grain diameter from ~0.67 to 9.2 μm. Nevertheless, the average grain diameter increases only marginally with further temperature rises and apparently achieves an upper limit of ~ 10 μm. Although there is a sudden increase in the coarsening rate for discs of the HPT-HT alloy annealed at 623 K, this rate is not as high as in samples processed by HPT at 300 K. As a result, $d_{eq} \approx 1.7$ μm after annealing at 623 K and an average grain diameter of ~5.1 μm was achieved for T = 773 K.

Figure 6.17 shows plots of the fractions of grain boundaries as a function of the misorientation angles for samples of the Al-3Mg-0.2Sc alloy processed by 10 turns of HPT and further annealed at the same conditions as in Figure 6.16. Inspection of Figures 6.11 (b) and 6.17 (a) reveals that there is an increase in the fraction of HAGBs for the HPT-processed discs

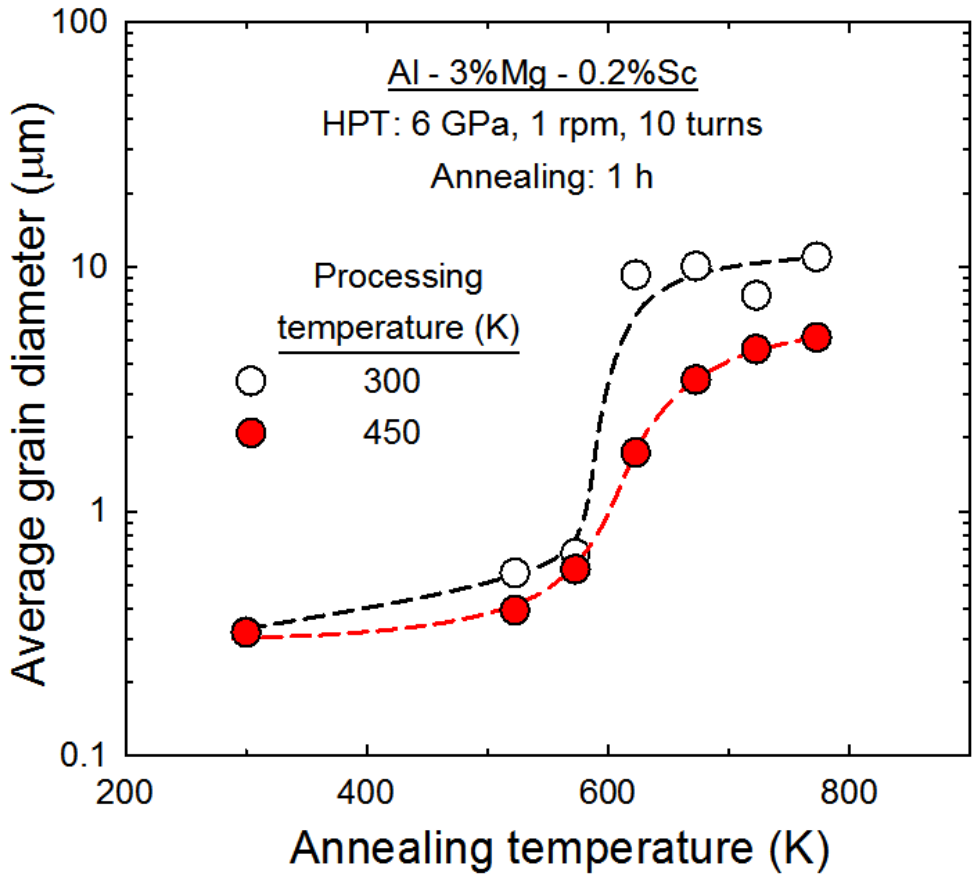

Figure 6.16 – Area-weighted average grain diameter as a function of annealing temperature for the Al-3Mg-0.2Sc alloy processed through 10 turns of HPT at either 300 or 450 K and further annealed for 1 h at temperatures ranging from 523 to 773 K.

after heat treatment at 523 K and the correlated pixel-to-pixel misorientation distributions [204] display close resemblance with the Mackenzie distribution [205] at this annealing condition.

The fraction of LAGBs increases after heat treatment at 623 K and this is more pronounced for Al-Mg-Sc discs originally processed by HPT at ambient temperature as evident in Figure 6.17 (c). It is noteworthy that after annealing at $T \geq 623$ K the histograms of the misorientation angles diverge significantly from the Mackenzie distribution, although the proportion of HAGBs remains superior to 80 % for samples of the HPT-HT metal annealed at 623 and 673 K. Furthermore, increasing the annealing temperature from 673 to 723 K leads to a relevant reduction of the fraction of HAGBs in samples processed by HPT at 450 K, whereas this fraction increases from ~58 to 76 % for the HPT-RT alloy.

In order to provide important information about the distribution of Al_3Sc dispersoids, samples of the Al-3Mg-0.2Sc alloy processed through 10 turns of HPT and annealed at 673 K for 1 h were prepared by Ar-ion milling and subsequently examined by SEM. A photo-diode backscattered electron (PDBSE) detector operating in composition mode was used in these

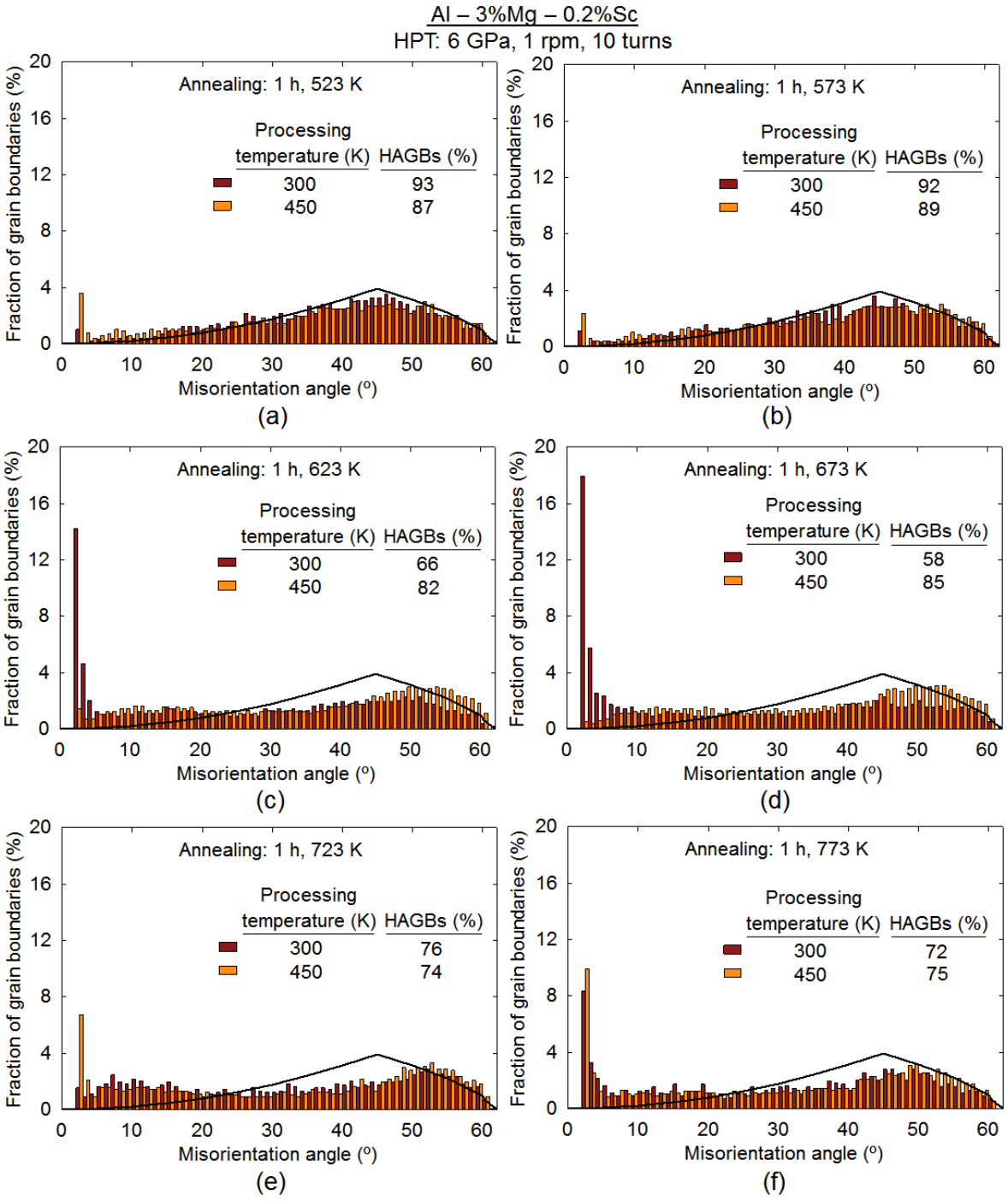

Figure 6.17 - Histograms of the misorientation angles for the Al-3Mg-0.2Sc alloy processed through 10 turns of HPT at different temperatures and further annealed for 1 h at (a) 523, (b) 573, (c) 623, (d) 673, (e) 723 and (f) 773 K.

analyses which allowed a clear distinction of the precipitates formed during heat treatment as apparent in Figure 6.18.

It follows from Figure 6.18 that there is profuse precipitation in the microstructure of the HPT-processed metal during annealing at 673 K. These precipitates were identified as Al_3Sc dispersoids through EDX measurements and they correspond to the white particles in

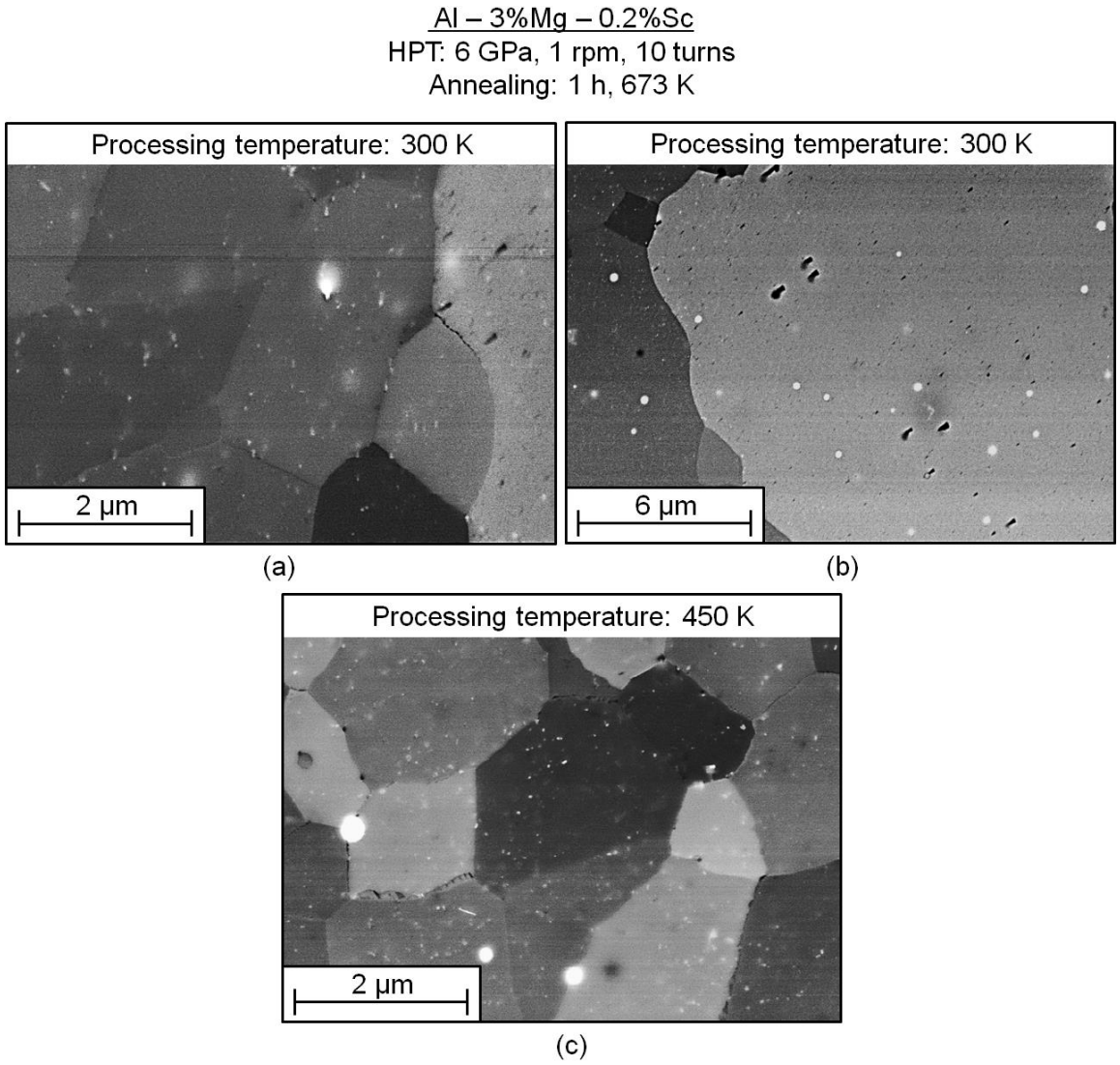

Figure 6.18 – SEM images of the Al-3Mg-0.2Sc alloy processed through 10 turns of HPT at either (a,b) 300 or (c) 450 K and subsequently annealed at 673 K for 1 h.

Figure 6.18. It is also evident in these SEM images the existence of two distinct groups of Al_3Sc particles based on the mean precipitate size. As noted in Figure 6.18, there is a group of coarse dispersoids with diameters exceeding 100 nm. They are sparsely distributed throughout the entire microstructure of both the HPT-RT and the HPT-HT metal and apparently correspond to Al_3Sc precipitates not fully dissolved in solid solution during heat treatment prior to HPT processing.

By contrast, there is also a group of extremely fine precipitates dispersedly distributed throughout the entire microstructure of the annealed discs. Although these phases are not fully resolved in Figure 6.18 due to the relatively low magnification of the SEM images, it is apparent that they have diameters smaller than 40 nm. Further inspection of Figure 6.18 (b) reveals that this group of fine Al_3Sc precipitates is almost absent within areas of the HPT-RT metal which underwent extensive coarsening during annealing, apart from regions in the vicinity of the grain boundaries.

The precipitates and grain structures of the Al-3Mg-0.2Sc alloy processed by HPT and subsequently annealed at 673 K were also examined by TEM as displayed in Figures 6.19. The images on the left-hand side in Figure 6.19 were taken using diffraction contrast in the TEM facility, whereas phase contrast was used for their counterparts on the right-hand side.

The results in Figure 6.19 demonstrate that Al_3Sc particles are extensively precipitated during annealing at 673 K for samples processed by 10 turns of HPT at either 300 or 450 K. Examination of the morphology of the dispersoids in the TEM images with

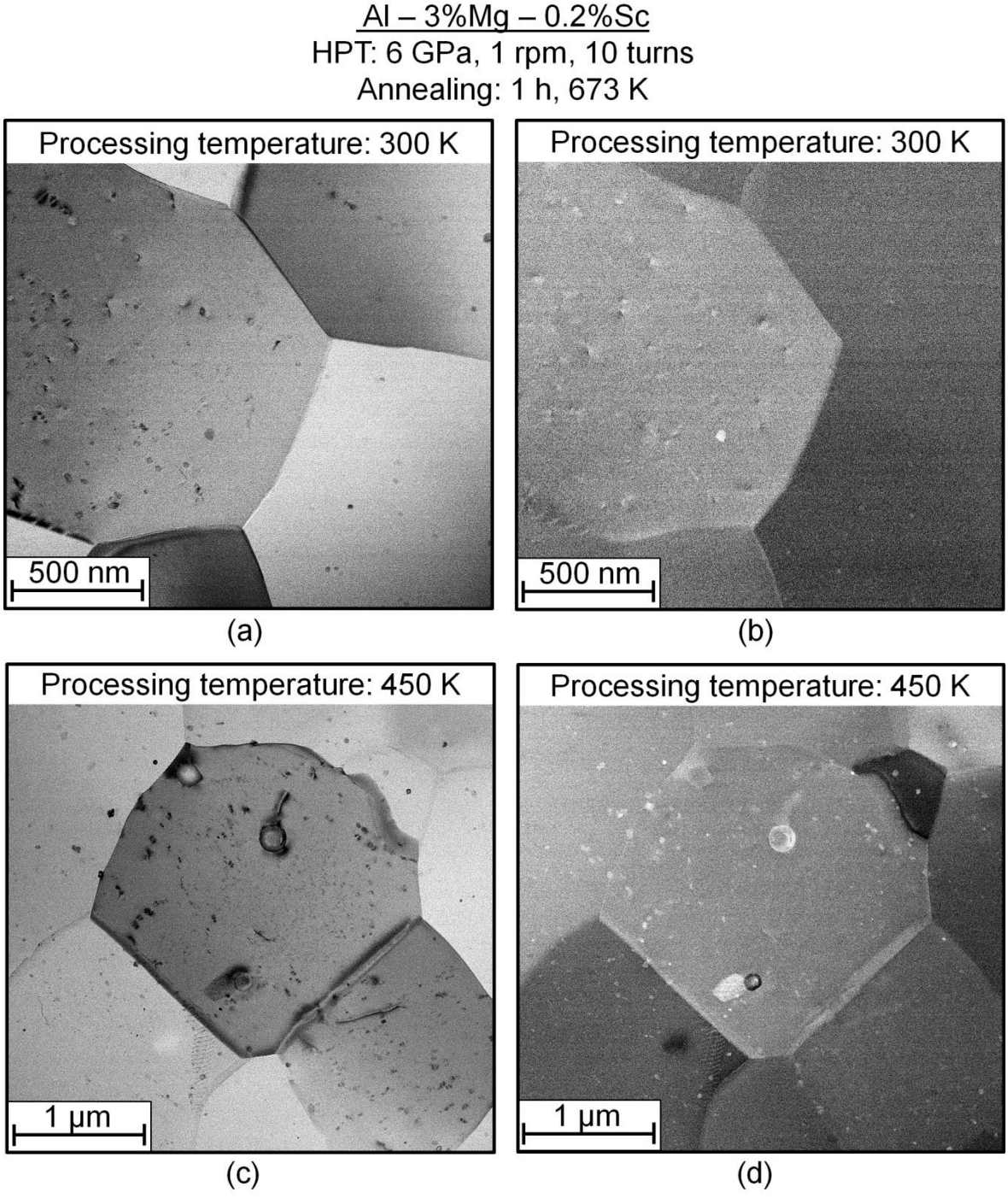

Figure 6.19 – TEM images of the Al-3Mg-0.2Sc alloy processed through 10 turns of HPT at either (a,b) 300 or (c,d) 450 K and subsequently annealed at 673 K for 1 h.

diffraction contrast also reveals that most of these phases display a coffee-bean-like contrast indicating that they continue coherent with the Al matrix even after heat treatment for 1 h.

The distribution, size and relative coherency of the Al_3Sc precipitates formed during annealing at 673 K are detailed shown in Figures 6.20 and 6.21 for disc-shaped samples of the Al-3Mg-0.2Sc alloy previously processed by HPT at 300 and 450 K, respectively. It is readily observed in the bottom area of Figure 6.20 (a) that the nano-sized dispersoids of the HPT-RT metal with a radius inferior to ~5 nm are closely spaced and coherent with the Al-Mg-Sc

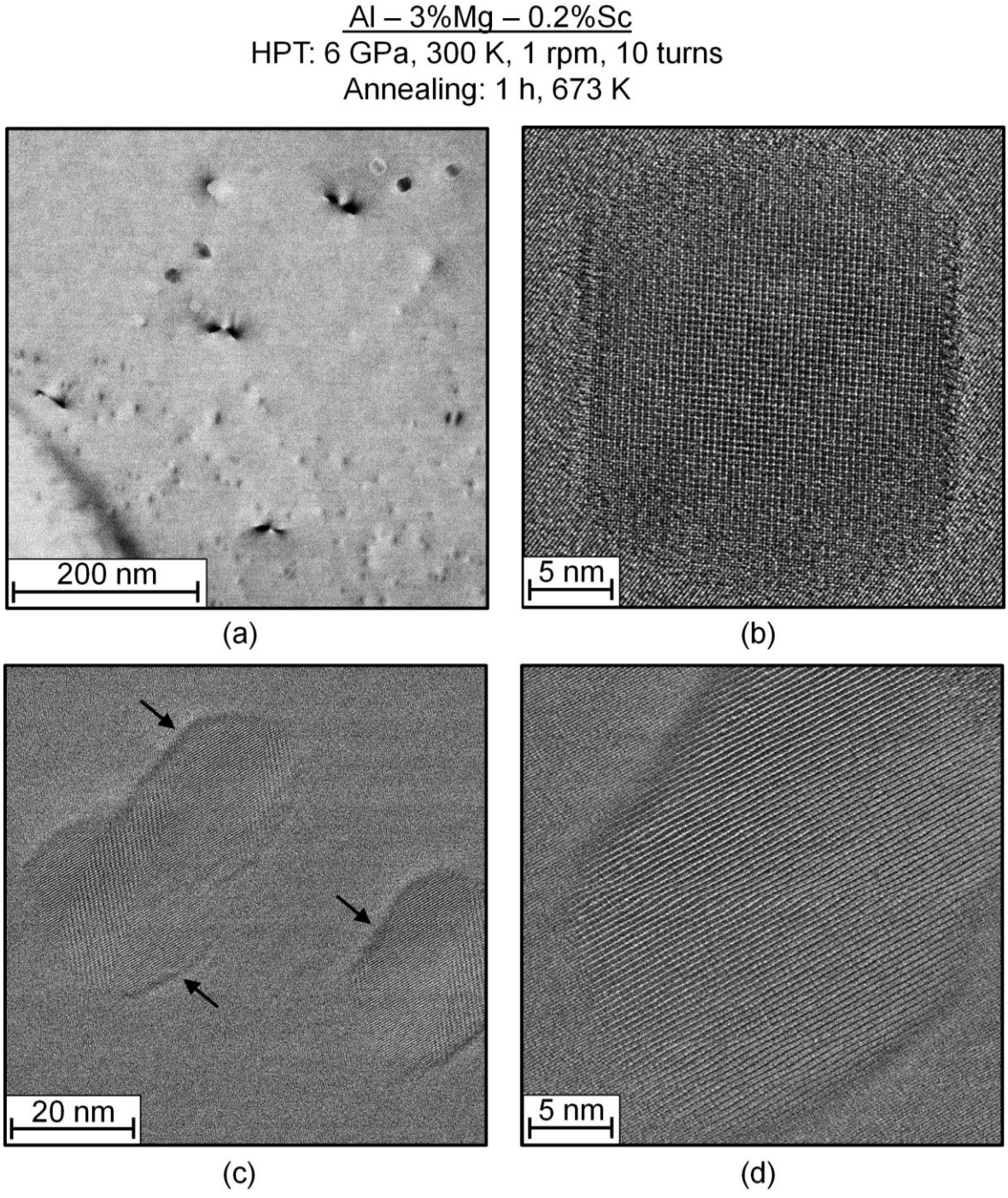

Figure 6.20 –TEM and HRTEM images showing Al_3Sc precipitates in an Al-3Mg-0.2Sc alloy processed through 10 turns of HPT at 300 K and further annealed at 673 K for 1 h.

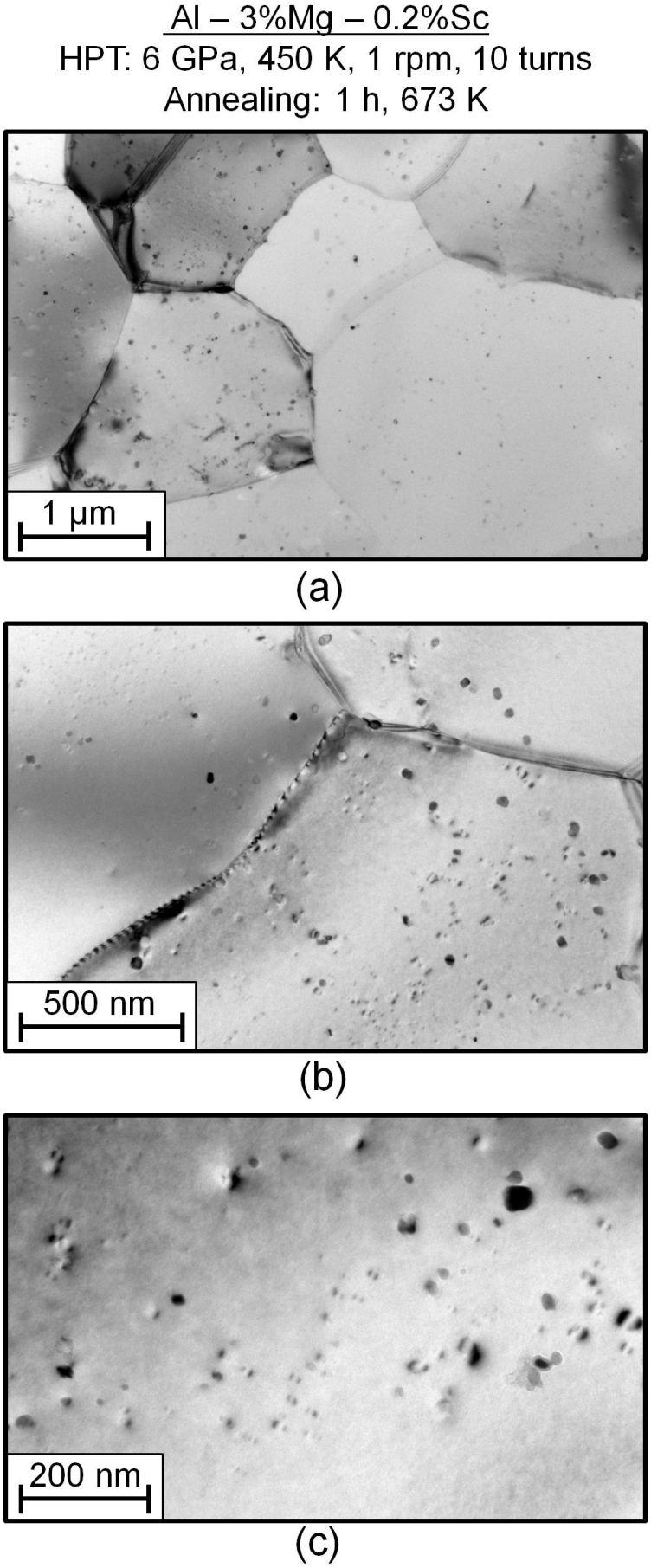

Figure 6.21 –TEM images showing Al_3Sc precipitates in an Al-3Mg-0.2Sc alloy processed through 10 turns of HPT at 450 K and further annealed at 673 K for 1 h.

matrix as inferred from their typical coffee-bean-like contrast.

Conversely, some Al_3Sc precipitates with diameters higher than ~25 nm lost their coherency with the matrix as clearly visible in the HRTEM image depicted in Figure 6.20 (b). In addition, the interspacing distance between dispersoids is substantially larger at the vicinity of these coarse phases and this is apparent in all TEM images shown in Figures 6.20 and 6.21. It is also worth mentioning that the structures observed through TEM represent a two-dimensional projection of a three-dimensional volume. As a result, Al_3Sc precipitates may deceptively overlap given a false impression of a large second-phase particle and this is consistently verified in Figures 6.20 (c) and (d) for the alloy originally processed by HPT at ~$0.3T_m$.

Figure 6.22 shows the precipitate size distribution for samples of the Al-3Mg-0.2Sc alloy processed through 10 turns of HPT at different temperatures and subsequently annealed for 1 h at 673 K. These histograms were generated after measurement of the radii of precipitates using representative TEM images with high magnifications as in Figures 6.20 (a) and 6.21 (c). In these calculations, a total of 153 and 192 dispersoids were identified for discs originally processed by HPT at either 300 or 450 K, respectively.

The results displayed in Figure 6.22 reveal that the HPT-processed discs have very similar distributions of precipitate radius after annealing at 673 K, although the histograms

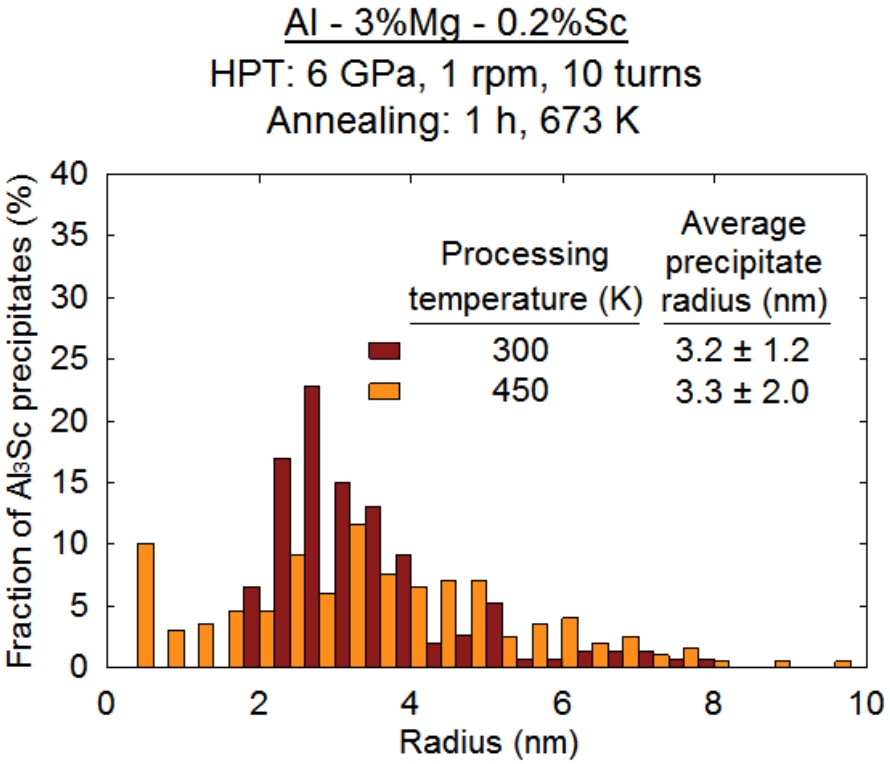

Figure 6.22 – Histograms showing the distribution of precipitate radius for the Al-3Mg-0.2Sc alloy processed through 10 turns of HPT and further annealed at 673 K for 1 h.

are somewhat more disperse for the HPT-HT metal. The Al_3Sc particles of the alloy processed by HPT at different temperatures have, in practice, the same average size as r_p values of ~3.2 and 3.3 nm were calculated for the HPT-RT and HPT-HT material, respectively. It should be further noted that the values estimated in this investigation for the average radius of dispersoids display excellent consistency with the earlier analysis performed with an Al-0.25Sc alloy as $r_p \approx 3.5$ nm for the Al_3Sc precipitates developed after heat treatment at comparable conditions [256].

XRD patterns were recorded along the complete surface of the Al-3Mg-0.2Sc discs immediately after 10 turns of HPT at 300 and 450 K. Afterwards, the lattice microstrain, the average crystallite size and the dislocation density were calculated using these patterns as displayed in Table 6.1.

It follows from Table 6.1 that the microstrain estimated for the HPT-RT metal is four times higher compared with the material processed at 450 K. Additionally, average crystallite sizes of ~160 and 190 nm were calculated for samples processed by HPT at either 300 or 450 K, respectively. As a result, the Al alloy processed by HPT at ambient temperature exhibits a dislocation density of $\sim 3.6 \times 10^{13}$ m^{-2}, whereas $\rho \approx 7 \times 10^{12}$ m^{-2} for the HPT-HT metal.

Table 6.1 - Lattice microstrain, $\langle \varepsilon^2 \rangle^{1/2}$, average crystallite size, D_c, and dislocation density, ρ, for the Al-3Mg-0.2Sc alloy processed by HPT at different temperatures.

Metal-working procedure	Microstrain (%)	Crystallite size (nm)	Dislocation density ($m^{-2} \times 10^{13}$)
HPT: 300 K, 6 GPa, 1 rpm, 10 turns	0.048 ± 0.004	160 ± 2	3.6 ± 0.4
HPT: 450 K, 6 GPa, 1 rpm, 10 turns	0.012 ± 0.002	190 ± 2	0.7 ± 0.1

6.2.2 Tensile Properties and Microstructure of the HPT-Processed Al-Mg-Sc Alloy

Samples of an Al-3Mg-0.2Sc alloy were processed through 10 turns of HPT under a processing temperature of either 300 or 450 K. Afterwards, miniature tensile specimens with the same dimensions depicted in Figure 3.3 (b) were machined from these discs and then tested in tension using different strain rates and temperatures. Figure 6.23 shows plots of true stress vs true strain for the Al alloy processed by HPT at (a,b) 300 or (c,d) 450 K and further pulled to failure at 523 and 723 K using strain rates ranging from 3.3×10^{-4} to 1.4 s^{-1}.

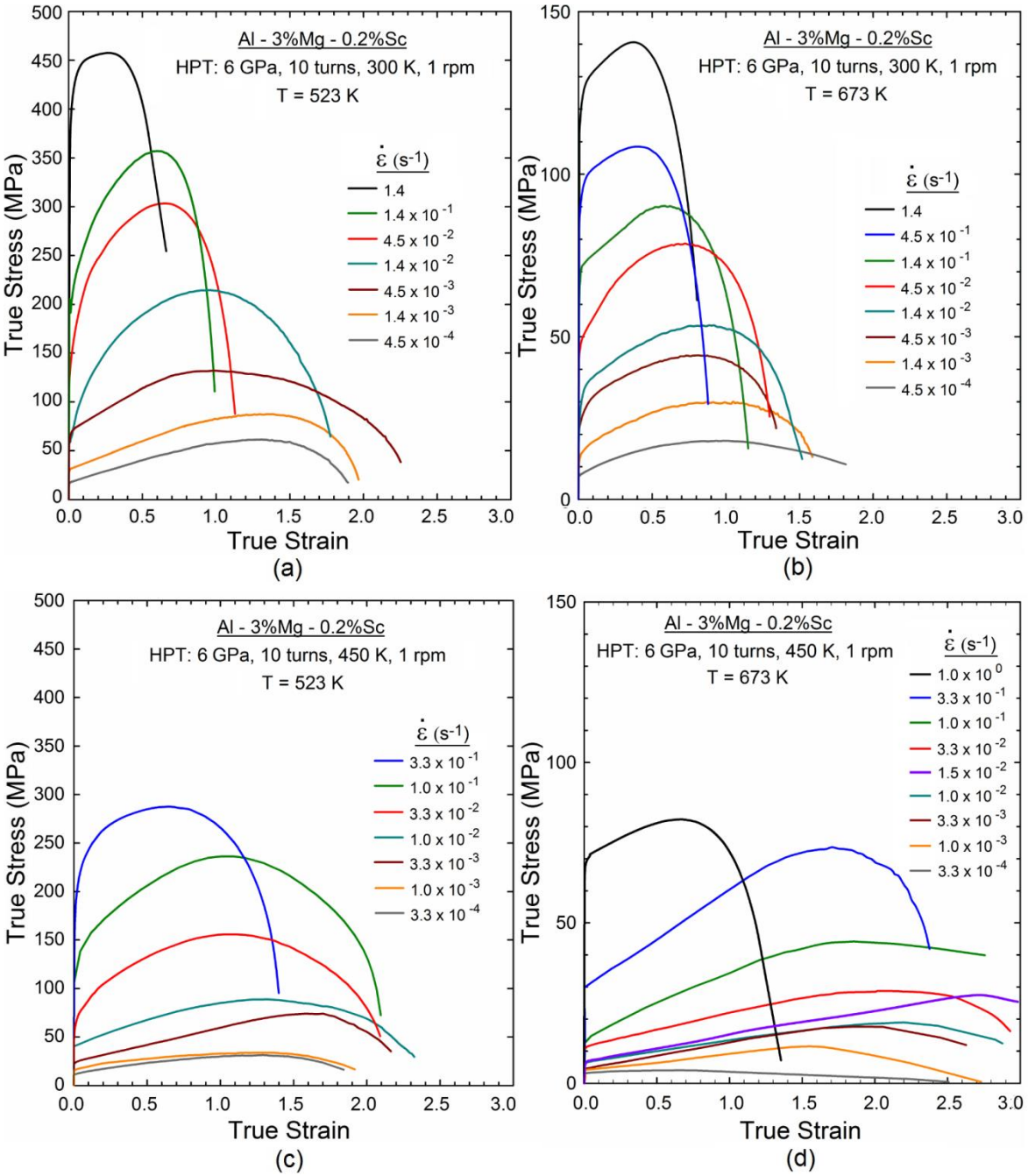

Figure 6.23 - True stress vs true strain curves of the Al-3Mg-0.2Sc alloy processed through 10 turns of HPT at either 300 K and pulled to failure at (a) 523 and (b) 673 K or 450 K and tested in tension at (c) 523 and (d) 673 K.

Figure 6.23 demonstrates that the mechanical strength and ductility of the HPT-processed alloy strongly depends on the processing temperature used during severe plastic deformation. The HPT-HT metal exhibits lower flow stresses and higher maximum strains compared with the material processed by HPT at RT for tests performed at 523 K using $\dot{\varepsilon} \geq 1.0 \times 10^{-2}$ s^{-1}. Nevertheless, specimens tested at 523 K using strain rates lower than 1.0×10^{-2} s^{-1} display very similar ductilities, even though higher flow stresses are needed to deform the HPT-RT alloy during testing at comparable conditions.

It is readily observed in Figures 6.23 (b) and (d) that increasing the testing temperature from 523 to 673 K leads to a significant reduction of the flow stresses achieved during plastic straining for samples processed by HPT at either 300 or 450 K. There is an extraordinary increase in the ductility of the HPT-HT samples as true strains superior to 2.5 are now attained for tests performed using initial strain rates ranging from 3.3×10^{-4} to 1.0×10^{-1} s^{-1}. By contrast, it is surprisingly revealed that the specimens of the HPT-RT alloy fracture at similar or even lower strains after increasing the deformation temperature from 523 to 673 K. It should also be noted that the material processed by HPT at $\sim 0.5 T_m$ achieves a maximum strain of ~2.4 when tested at 673 K with $\dot{\varepsilon} = 3.3 \times 10^{-1}$ s^{-1} and this strain was not reached for the HPT-RT alloy at any testing conditions shown in Figures 6.23 (a) and (b).

Figures 6.24 and 6.25 show the shapes of Al-3Mg-0.2Sc specimens after tensile testing for the material originally subjected to 10 turns of HPT processing at either 300 or 450 K, respectively. The values of the elongation to failure are displayed on the right-hand side of the deformed specimens for each testing condition.

Inspection of Figure 6.24 (a) demonstrates that HPT-RT samples pulled to failure at 523 K consistently achieved elongations superior to 400 % for tests performed at the strain rate interval of 4.5×10^{-4} to 1.4×10^{-2} s^{-1}, indicating the occurrence of high strain rate superplasticity. Furthermore, a comparison of Figures 5.16 (a), 5.17 (a), 6.24 (a) and 6.25 (a) shows that the miniature specimens processed by HPT generally exhibit superior ductility at 523 K compared with the ECAP-processed alloy as elongations as high as ~850 and 1020 % were attained at this temperature using HPT-RT and HPT-HT samples, respectively.

The results in Figure 6.24 (b) reveal that the HPT-RT metal tested at 673 K only displays a superplastic elongation when deformed using an initial strain rate of 4.5×10^{-4} s^{-1}. In addition, this elongation is even lower than after plastic straining at the same strain rate for T = 523 K. A more detailed examination of the deformed samples in Figure 6.24 shows that the HPT-RT metal develops a diffuse neck during testing at 673 K with $\dot{\varepsilon} \leq 4.5 \times 10^{-3}$ s^{-1} as the width of the tensile specimens is reasonably uniform along their entire gauge lengths. On the other hand, the Al alloy processed by HPT at 300 K and further deformed at 523 K exhibits a sharper width gradient after testing at similar strain rates, although the HPT-RT samples attained comparatively higher superplastic elongations.

It follows from Figure 6.25 (a) that the Al-3Mg-0.2Sc alloy processed by HPT at a high homologous temperature displays significantly enhanced low temperature superplasticity by comparing with the same metal after processing by ECAP either 300 or 600 K and HPT at RT. High strain rate superplasticity is consistently observed in samples tested at 523 K and the HPT-HT metal displays an elongation to failure of ~700 % after plastic straining with

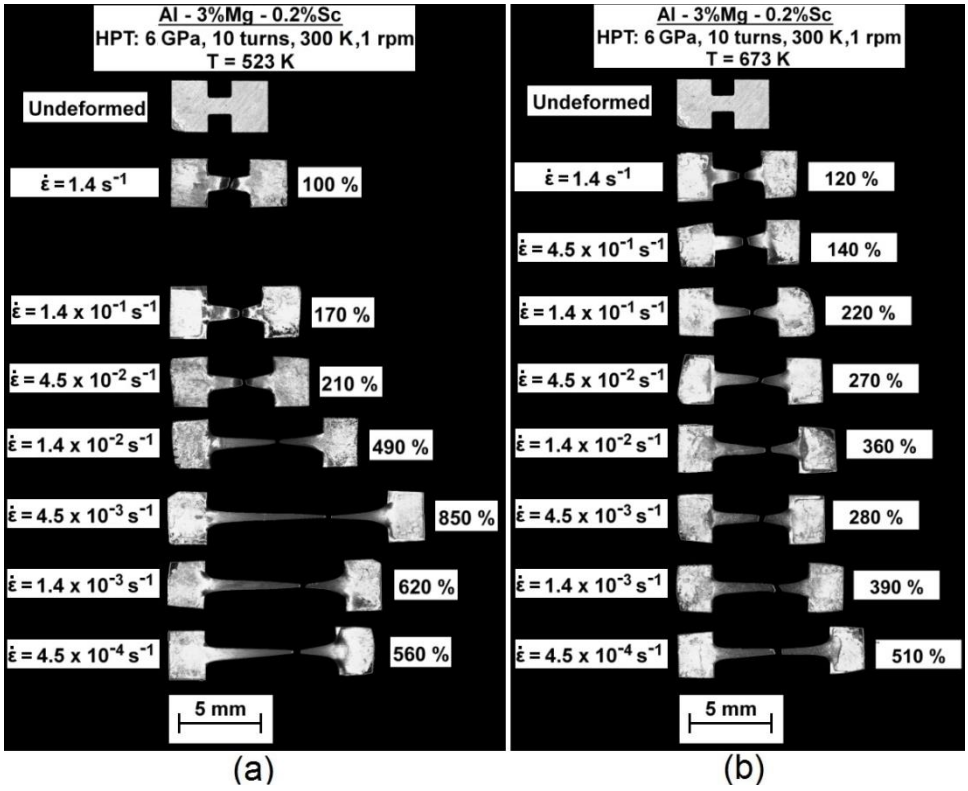

Figure 6.24 - Samples of the Al-3Mg-0.2Sc alloy processed through 10 turns of HPT at 300 K and further pulled to failure at (a) 523 and (b) 673 K.

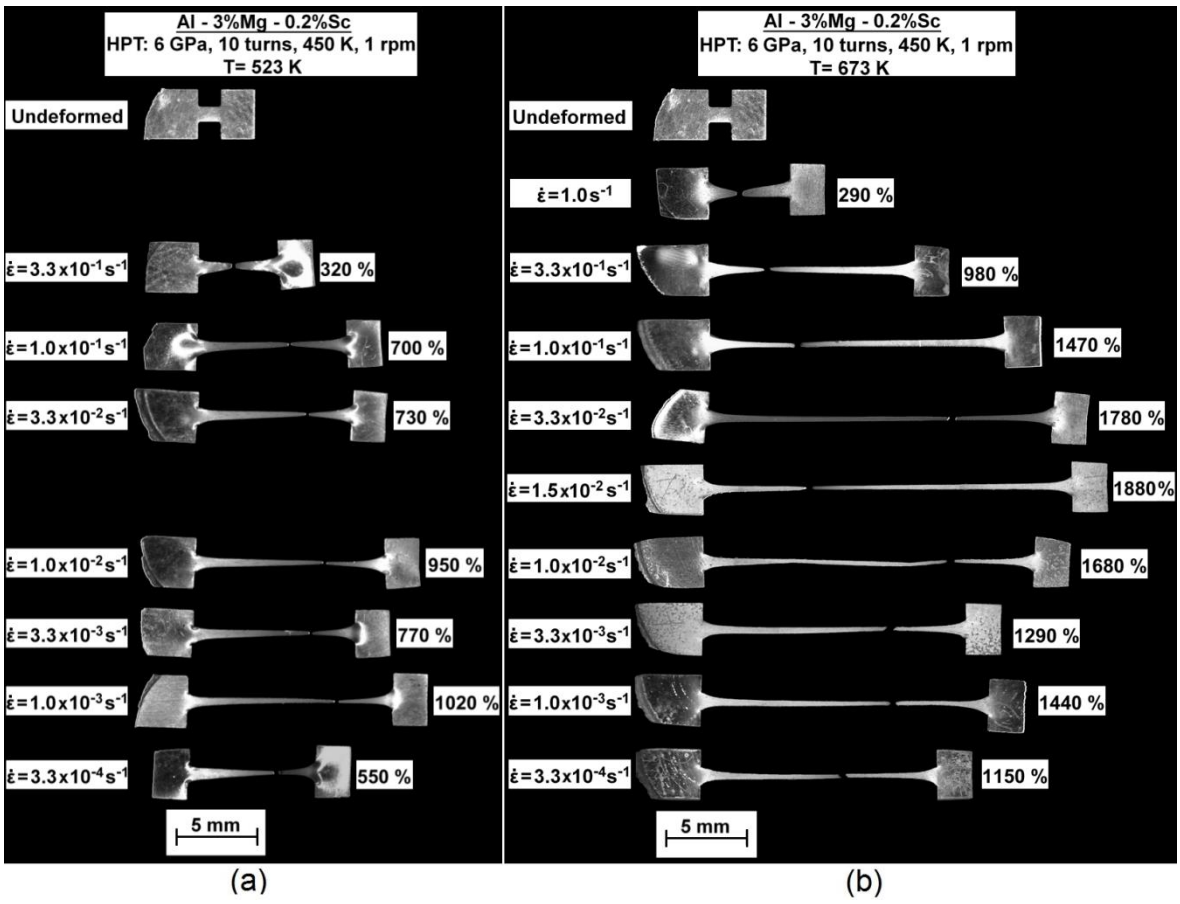

Figure 6.25 - Samples of the Al-3Mg-0.2Sc alloy processed through 10 turns of HPT at 450 K and further pulled to failure at (a) 523 and (b) 673 K.

$\dot{\varepsilon} = 1.0 \times 10^{-1}$ s^{-1}, noting that tensile testing was performed using miniature specimens with a thickness of ~ 0.6 mm. Similarly to the HPT-RT samples, it is also apparent in Figure 6.25 (a) that the width of the HPT-HT specimens gradually reduces with decreasing distance from the fracture tip and this demonstrates the existence of a stage of non-uniform deformation during testing at 523 K.

Figure 6.25 (b) shows the HPT-HT alloy achieves extraordinarily high superplastic elongations during tensile testing at 673 K. It is consistently revealed that a maximum elongation of 1880 % was attained during plastic straining using an initial strain rate of 1.5×10^{-2} s^{-1} and this represents the highest elongation achieved to date in any material subjected to conventional HPT processing [139,141]. It should be further noted that the maximum elongation obtained in miniature specimens of the ECAP-processed alloy was recorded as ~1490 %. Therefore, although higher elongations were already documented for the ECAP-processed metal using standard tensile specimens [43,45], this investigation reliably demonstrates that the Al-3Mg-0.2Sc alloy processed by HPT at $\sim 0.5T_m$ displays superior superplastic properties compared with the material processed by ECAP at either 300 or 600 K.

The range of strain rates in which the HPT-HT metal attains elongations superior to the minimum threshold of 400 % increases by increasing the testing temperature from 523 to 673 K. The material processed by HPT at 450 K achieved elongations higher than 900 % after testing using strain rates within the interval from 3.3×10^{-4} to 3.3×10^{-1} s^{-1} and there is no visible necking in the fractured specimens, except for the metal tested at 3.3×10^{-1} s^{-1}. Additionally, it is apparent that the HPT-HT alloy has optimum ductility at strain rates ranging from 1.0×10^{-2} to 1.0×10^{-1} s^{-1} and the elongations to failure noticeably diminish beyond this interval.

Figure 6.26 shows plots of the elongation to failure vs strain rate for samples of the HPT-processed material after tensile testing at temperatures ranging from 473 to 723 K using strain rates from 3.3×10^{-4} to 1.4 s^{-1}. Inspection of Figure 6.26 reveals that the material processed by HPT at 300 K exhibits a superplastic elongation of ~560 % when tested at 473 K with $\dot{\varepsilon} = 1.4 \times 10^{-3}$ s^{-1}. Increasing the temperature from 473 up to 573 K leads to a general improvement in the ductility of the HPT-RT samples which attained an elongation of ~800 % after testing at 573 K using an initial strain rate of 1.4×10^{-2} s^{-1}. By contrast, the elongations to failure drastically decrease with increasing testing temperatures for $T \geq 623$ K. As a result, there is only one experimental condition wherein the HPT-RT metal exhibits elongations higher than 400 % for tests performed at 673 K.

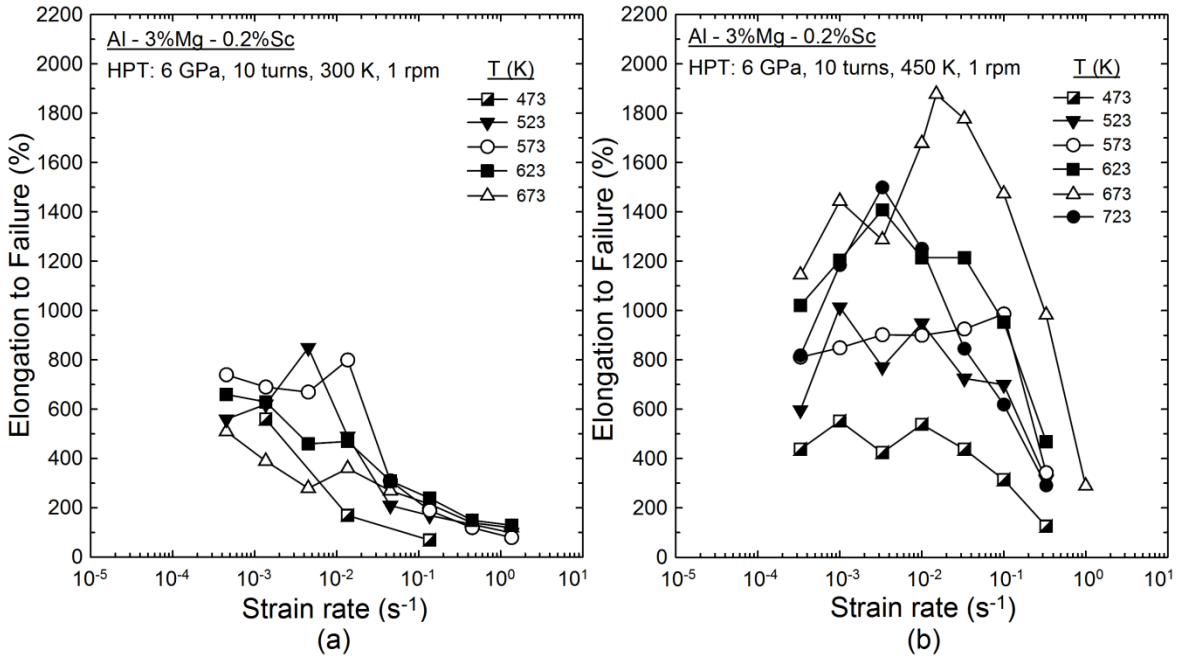

Figure 6.26 - Elongation to failure vs strain rate for the Al-3Mg-0.2Sc alloy processed through 10 turns of HPT at either (a) 300 or (b) 450 K and further tested in tension at temperatures from 473 to 723 K.

The results in Figure 6.26 (b) consistently demonstrate that, in practice, the Al-3Mg-0.2Sc alloy processed through 10 turns of HPT at $\sim 0.5T_m$ exhibits superior superplastic properties than the same metal after processing by HPT at $\sim 0.3T_m$. Elongations to failure > 400 % were attained in miniature specimens of the HPT-HT material after testing at 473 K using $\dot{\varepsilon} \leq 3.3 \times 10^{-2}$ s^{-1}. It is also clearly noted in these plots that the elongations increase with increasing testing temperatures and achieve optimum values at T = 673 K. Conversely, there is a general decrease in the ductility after increasing the deformation temperature from 673 to 723 K, although superplastic elongations were still obtained in tests performed with initial strain rates within the interval from 3.3×10^{-4} to 1.0×10^{-1} s^{-1}.

Figure 6.27 displays the variation of the flow stress at ε = 0.3 with the strain rate for samples of the Al-Mg-Sc alloy processed by HPT at either (a) 300 or (b) 450 K and tensile tested at temperature ranging from 473 to 723 K. Similarly to Figures 4.3 and 5.19, the experimental datum points were plotted using logarithmic scales for both the true stress and the strain rate such that the slope of these curves represents the strain rate sensitivity, *m*, at a given testing temperature.

It is readily observed in Figure 6.27 (a) that the curves corresponding to the HPT-RT material have two distinguishable slopes depending upon the testing temperature and strain rate. For tests performed at 473 K, $m \approx 0.5$ in samples deformed using strain rates lower than $\sim 10^{-2}$ s^{-1} and a slope of ~ 0.22 is measured at faster strain rates. It is also noted that the range

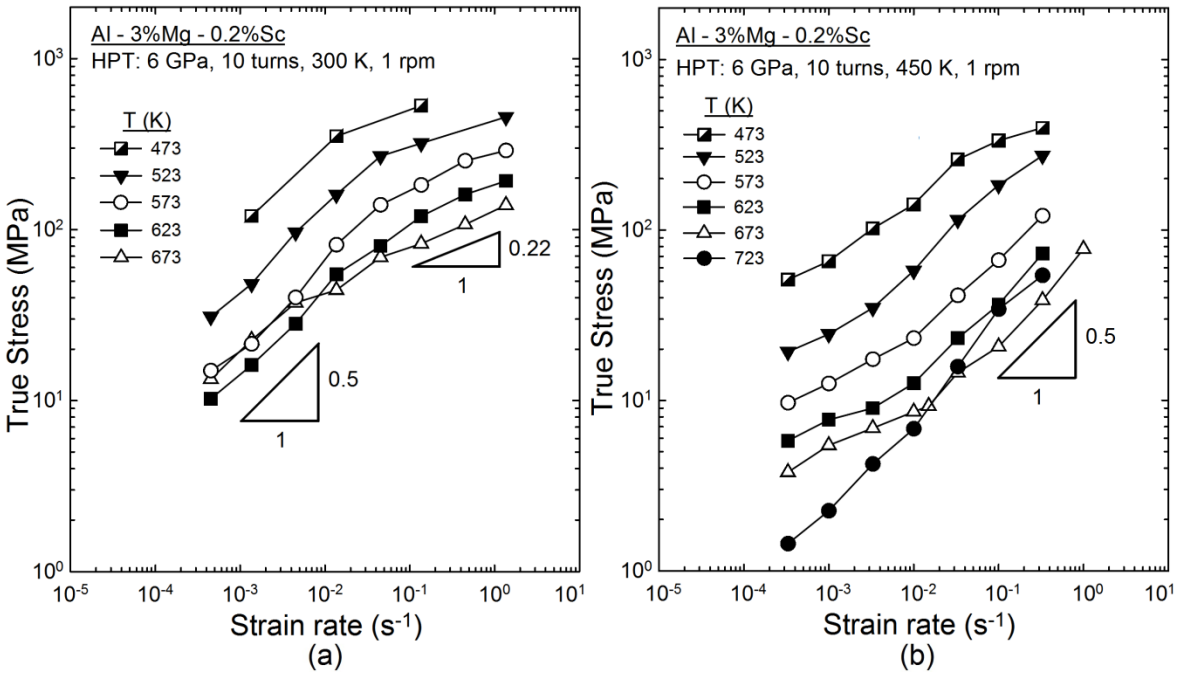

Figure 6.27 - Variation of the true stress at a true strain of 0.3 with the strain rate for the Al-3Mg-0.2Sc alloy processed through 10 turns of HPT at either (a) 300 or (b) 450 K and further tested in tension at temperatures from 473 to 723 K.

of strain rates with *m* values of ~0.5 expands to faster strain rates (~4.5×10^{-2} s^{-1}) at the testing temperatures of 523 and 573 K and this is concomitant with a decrease in the flow stresses at $\varepsilon = 0.3$. Nevertheless, further increases in the temperature result in reduction of the interval of strain rates having a slope of ~0.5 and this extends up to $\dot{\varepsilon} \approx 4.5 \times 10^{-3}$ s^{-1} for the Al alloy processed by HPT at RT and tested in tension at 673 K.

A comparison of Figures 6.27 (a) and (b) reveals that the HPT-HT material exhibits significantly lower true stresses at $\varepsilon = 0.3$ compared with the metal processed at 300 K, for all testing conditions used in this study. The curves corresponding to the HPT-HT alloy tested at 473 and 523 K have a sigmoidal shape and display a slope of ~0.5 at intermediate strain rates. On the other hand, the shape of the true stress vs strain rate plots noticeably changes and they appear to have only two distinguishable slopes for tests performed at temperatures from 573 to 673 K.

The Al alloy processed by HPT at 450 K clearly shows $m \geq 0.5$ when tested at $T \geq 573$ K using strain rates higher than 1.0×10^{-2} s^{-1}. However, the slope of the plots in Figure 6.27 (b) decrease with decreasing initial strain rates and the HPT-HT metal exhibits *m* values within the interval of ~0.2-0.3 at temperatures from 573 to 673 K and $\dot{\varepsilon} < 1.0 \times 10^{-2}$ s^{-1}. It is also worth noting that samples tested at 723 K achieved lower flow stresses at $\varepsilon = 0.3$ by comparing with the metal deformed at 673 K for strain rates higher than 1.0×10^{-2} s^{-1}.

The same procedure used in Chapter 5 to examine the surface topography of fractured tensile specimens was repeated in the HPT-processed samples after tensile testing at high temperatures. Accordingly, Figure 6.28 shows SEM images taken along the gauge area of Al-3Mg-0.2Sc specimens originally processed by HPT at different temperatures and subsequently pulled to failure at 673 K using comparable strain rates.

Similarly to the ECAP-processed samples, the grain structures of the material processed by HPT stand out on the surface of the tensile specimens after extensive plastic deformation and this is clearly apparent in Figures 6.28 (a) and (b). After testing at 673 K using an initial strain rate of 4.5×10^{-2} s^{-1}, the HPT-RT metal exhibits an inhomogeneous microstructure constituted by two distinguishable groups of grain structures. Part of these grains is nearly equiaxed and has diameters in the order of few micrometres. These structures are intermixed with larger grains which are noticeably elongated along the tensile direction. It is also apparent in Figure 6.28 (a) the existence of numerous cavities at the grain boundaries and triple junctions. These cavities are visible at the boundaries of both groups of grains, but appear to have larger sizes when formed in elongated grain structures.

By contrast, the Al alloy processed by HPT at $\sim 0.5T_m$ has a uniform distribution of grains after plastic straining at 673 K using a strain rate of 3.3×10^{-2} s^{-1}. These grains are slightly larger compared with the population of fine structures observed in the SEM image of the HPT-RT metal and have an average size of ~2.4 μm as estimated using the linear intercept

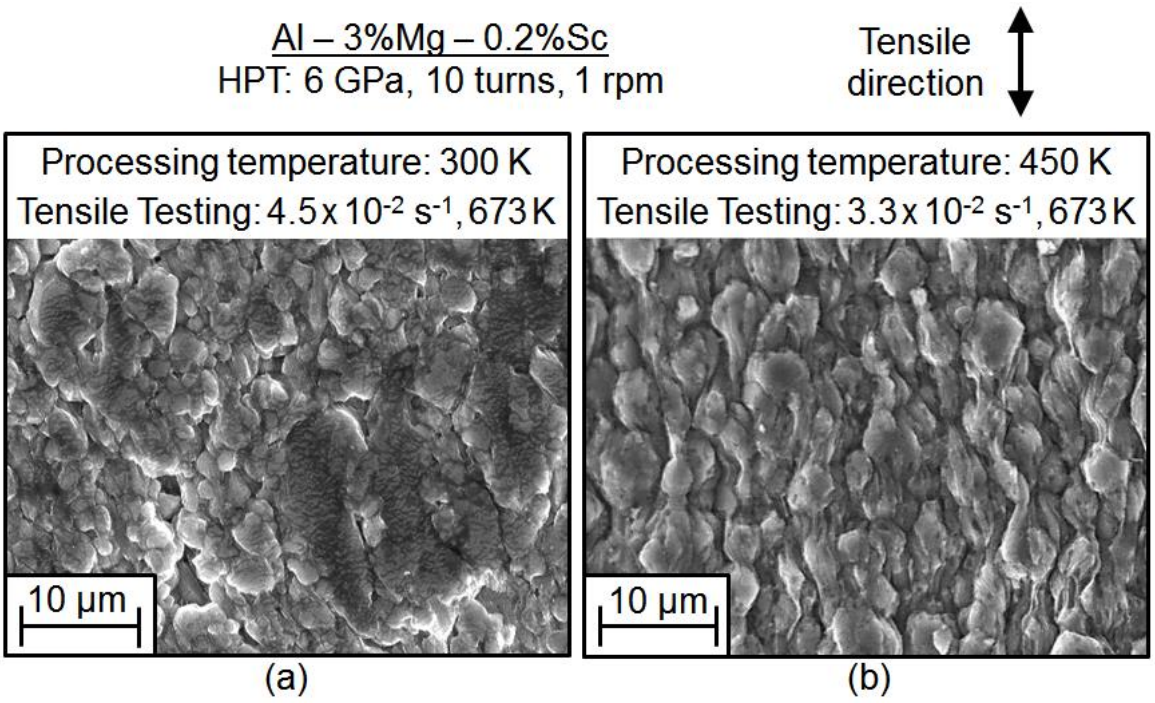

Figure 6.28 – SEM images taken along the gauge area of Al-3Mg-0.2Sc samples processed through 10 turns of HPT at either (a) 300 or (b) 450 K and further pulled to failure at 673 K using strain rates of (a) 4.5×10^{-2} or (b) 3.3×10^{-2} s^{-1}.

method. It should be further noted that intergranular creep cavities are rarely seen along the area analysed in Figure 6.28 (b) and extensive fibre structures develop nearly parallel to the tensile direction during testing at superplastic conditions.

The linear intercept method was also used to measure the average grain boundary spacing in Figure 6.28 (a). These calculations revealed that $\bar{L} \approx 2.4$ μm for the HPT-RT metal tested at 673 K with $\dot{\varepsilon} = 4.5 \times 10^{-2}$ s^{-1} and this grain size is virtually identical to the value estimated for the HPT-HT metal in Figure 6.28 (b). It is relevant to note the HPT-RT sample achieved an elongation of only ~270 % and thereby was kept at the furnace of the testing facility for a total time of ~660 s. Conversely, the metal processed by HPT at 450 K displayed a superplastic elongation of ~1780 % and remained at the testing temperature of 673 K for additional ~8 min.

The grain structures of the Al-3Mg-0.2Sc alloy processed by HPT at ambient temperature and further tested at 673 K were also examined through EBSD scans using a step size of 200 nm. Figure 6.29 shows representative OIM images and corresponding {111} pole figures taken along both the head and the gauge area of a fractured specimen of the HPT-RT metal after tensile testing at 673 K with $\dot{\varepsilon} = 4.5 \times 10^{-2}$ s^{-1}. For comparison purposes, the intensity index of the pole figures was normalised to values ranging from 0 to 5 and the average grain boundary spacing was calculated for each OIM image as depicted in the heading of Figures 6.29 (a) and (b).

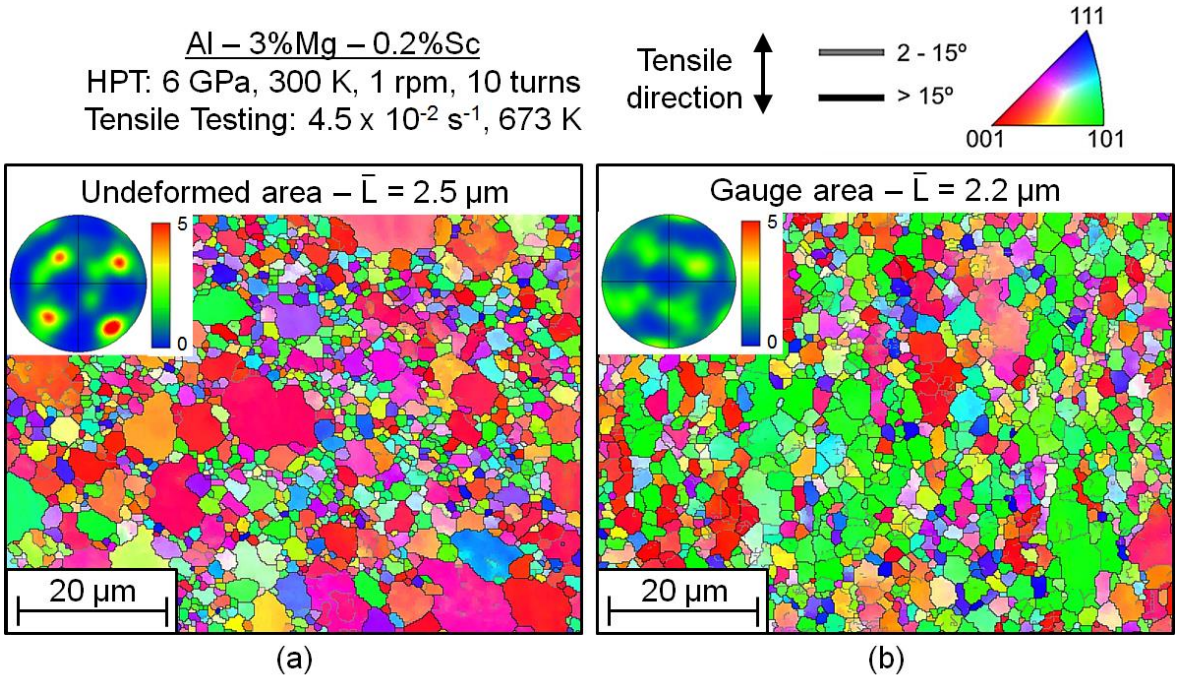

Figure 6.29 – OIM images and corresponding {111} pole figures taken along (a) the undeformed and (b) the gauge area of an Al-3Mg-0.2Sc specimen processed through 10 turns of HPT at 300 K and further tested in tension at 4.5×10^{-2} s^{-1} at 673 K.

Inspection of Figures 6.28 (a) and 6.29 (b) demonstrates that the features observed at the surface of the fractured specimens of the HPT-RT metal are fairly consistent with the grain structures revealed in the EBSD analysis. It is apparent that the large structures identified in Figure 6.28 (a) correspond to grains having a preferential texture with the {110} planes oriented mainly perpendicular to the thickness direction. Also, these grain structures are elongated in a direction parallel to the tensile axis and contain a substantial fraction of substructures with LAGBs, frequently organized in the form of subgrains.

It follows from Figure 6.29 (a) that the alloy processed by HPT at 300 K develops a bimodal distribution of grains during static heating at 673 K for ~660 s and this is consistent with the results obtained after annealing for 1 h at the same temperature as displayed in Figure 6.12 (d). A comparison of Figures 6.29 (a) and (b) also reveals that the grain structures in the undeformed area of the fractured tensile specimen are slightly coarser compared with its gauge section as $\bar{L}$ values of ~2.5 and ~2.2 μm, respectively, were measured in each OIM image. In addition, there appear to exist fewer substructures in the undeformed area of the HPT-RT specimens, although fine subgrains are often encountered in regions having grains not yet coarsened.

Figure 6.30 shows histograms of both (a) the area fraction of grain diameters and (b) the misorientation angles for the HPT-RT alloy after tensile testing at 4.5×10^{-2} s^{-1} at 673 K. The results in Figures 6.30 (a) and (b) demonstrate that the deformed area of tensile specimens has a narrower distribution of grain sizes than the head of the sample, but nevertheless both distributions display evidence of the presence of duplex structures. The undeformed area of the fractured specimen has grains with diameters as high as ~15 μm and

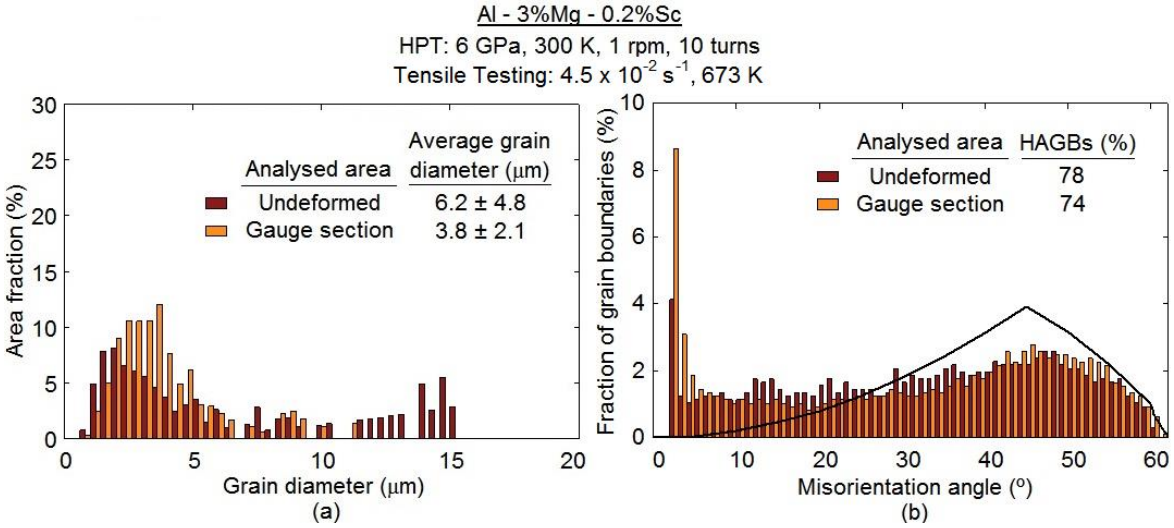

Figure 6.30 – Histograms of (a) the area fraction of grain diameters and (b) the misorientation angles for the Al-3Mg-0.2Sc alloy processed through 10 turns of HPT at 300 K and further tested in tension at 4.5×10^{-2} s^{-1} at 673 K.

an average diameter of ~6.2 μm. By contrast, the average grain diameter in the gauge section is ~3.8 μm and ~90 % of these HAGBs structures have diameters smaller than 6 μm.

Examination of Figure 6.30 (b) reveals that the histograms of the misorientation angles for the tested specimens of the material originally processed by HPT at ~0.3T_m are noticeably different than the Mackenzie distribution [205] and this may be associated with the presence of a significant fraction of LAGBs together with the development of a microstructure having a preferential texture during tensile testing at 4.5×10^{-2} s^{-1} at 673 K. Furthermore, the undeformed and the gauge area of the sample exhibit fractions of LAGBs of ~22 and 26 %, respectively, and these values are higher than the fraction measured immediately after HPT processing at ambient temperature as follows from Figure 6.11 (b).

The fractured specimens of the Al-3Mg-0.2Sc alloy processed by HPT at ~0.5T_m and subsequently pulled to failure at 673 K using strain rates of 1.0, 3.3×10^{-2} and 3.3×10^{-4} s^{-1} were polished and afterwards analysed through EBSD scans with step sizes within the interval of 90-400 nm. Figure 6.31 shows typical OIM images and corresponding {111} pole figures taken at both the head and the gauge area of tested specimens of the HPT-HT alloy after tensile testing at 673 K using various strain rates. The lines coloured in white represent boundaries with a misorientation angle of 60º and they were added to these images to verify whether Σ3 60º <111> twin boundaries are formed during either static annealing or deformation at 673 K.

The results in Figure 6.31 demonstrate that a bimodal distribution of grains gradually evolves in the undeformed area of the HPT-HT samples during heating at 673 K. It is clearly visible that the Al specimens tested at faster strain-rates and thereby exposed to the testing temperature for shorter periods of time exhibit smaller grain sizes and this is apparent for both the head and the gauge area. It is also noted that larger grain sizes are measured at the gauge section of the samples by comparing with their undeformed counterparts and all the microstructures in Figure 6.31 are mostly constituted by structures having HAGBs.

Inspection of Figures 6.31 (a) and (b) shows that the gauge section of the specimen tested using a strain rate of 1.0 s^{-1} has a weaker texture than the undeformed regions. There is also an increase in the population of grains having a texture component around {110}. Additionally, plastic straining at this fast strain rate results in the development of few LAGBs structures within elongated grains lying parallel to the tensile direction.

It is verified in Figures 6.28 (b) and 6.31 (d) that the structures observed through SEM analyses performed on the surface of a specimen processed by HPT and further tensile tested at 3.3×10^{-2} s^{-1} at 673 K truly correspond to grains which stood out during plastic straining. An average grain size of ~2.6 μm was estimated using the OIM image in Figure 6.31 (d) and

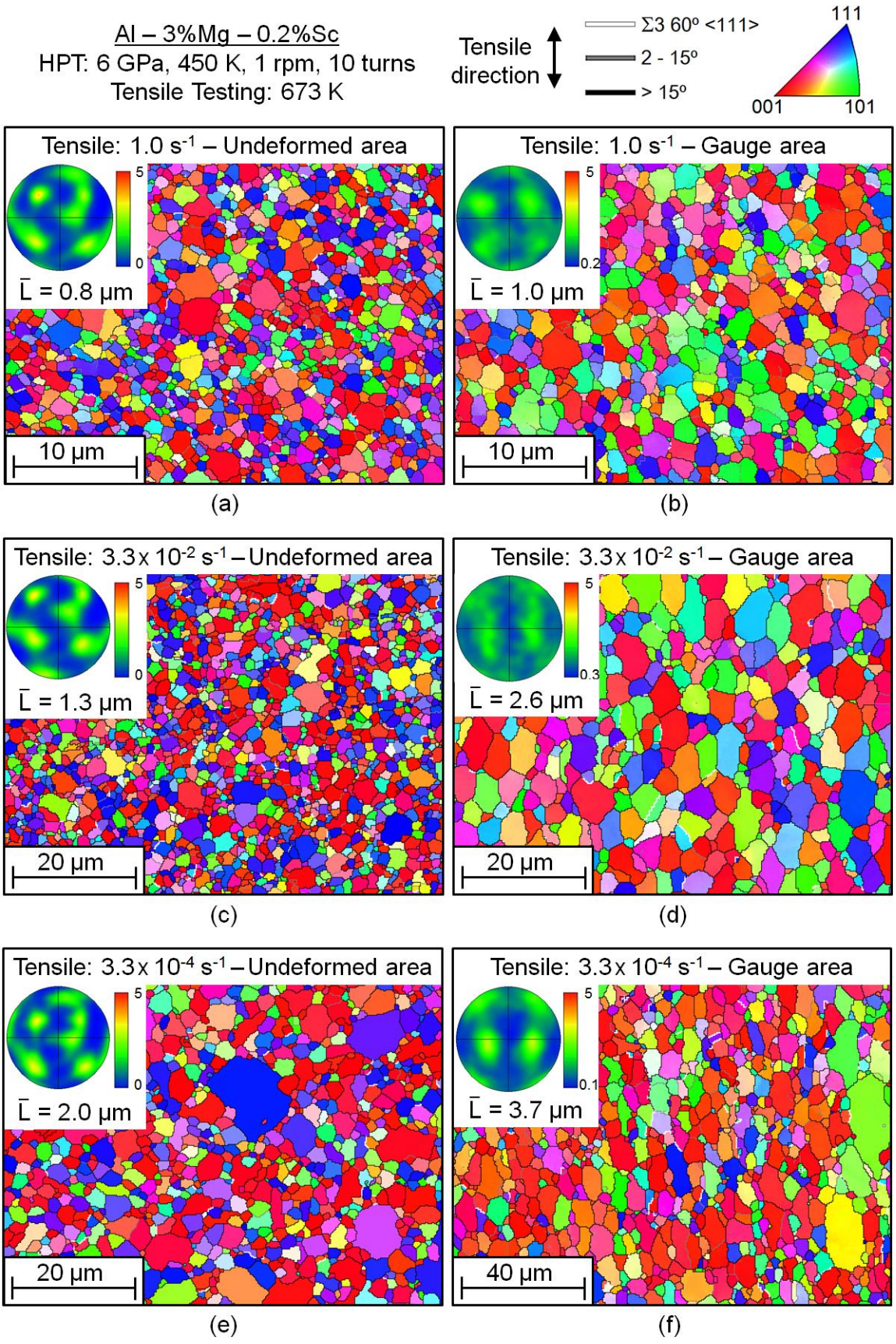

Figure 6.31 - OIM images and corresponding {111} pole figures of both (a,c,e) the undeformed and (b,d,f) the gauge area of Al-3Mg-0.2Sc specimens processed by 10 turns of HPT at 450 K and subsequently pulled to failure at 673 K using strain rates of (a,b) 1.0, (c,d) 3.3×10^{-2} and (e,f) 3.3×10^{-4} s^{-1}.

this value is consistent with the measurements from the SEM micrograph which gave $\bar{L} \approx 2.4$ μm. The results also reveal that the HPT-HT metal develops an essentially random texture during superplastic deformation at 3.3×10^{-2} s^{-1} and displays a microstructure almost entirely constituted by grains with HAGBs.

It follows from Figure 6.31 (f) that the grain structures of the metal deformed at 673 K using a strain rate of 3.3×10^{-4} s^{-1} have higher aspect ratios compared with the same material tested at faster strain rates. An average grain size of ~3.7 μm was calculated at this testing condition and there are few abnormally large grains lying parallel to the tensile direction. Furthermore, there appears to exist some twinning activity during tensile testing using strain rates of 3.3×10^{-2} and 3.3×10^{-4} s^{-1} as boundaries having a misorientation angle of 60^{o} are noticed in Figures 6.31 (d) and (f).

Figure 6.32 shows histograms of both (a) the area fraction of grain diameters and (b) the misorientation angles for the Al-3Mg-0.2Sc alloy processed through 10 turns of HPT at 450 K and further tested in tension at 673 K using strain rates ranging from 3.3×10^{-4} to 1.0 s^{-1}. It is readily seen in the histograms on the left-hand side of Figure 6.32 that the grain structures in the gauge section of the fractured specimens exhibit larger average diameters and broader distributions compared with the undeformed areas, except for tests performed with $\dot{\varepsilon} = 1.0$ s^{-1}. Nevertheless, it is evident from the histograms obtained at the head of the specimens the development of a bimodal distribution of grain sizes during static annealing which is more distinguishable in samples tested using slower strain rates.

It is worth noting that the values of area-weighted diameters calculated based on the histograms in Figure 6.32 are consistently higher than the average grain boundary spacings and this difference is obviously more prominent in samples displaying higher fractions of abnormally large grains. In addition, the histograms in Figure 6.32 (e) show evidence of abnormal coarsening not only in the head of the specimens, but also in the deformed area of the HPT-HT alloy tested at 3.3×10^{-4} s^{-1}.

Inspection of the histograms on the right-hand side of Figure 6.32 reveals that the undeformed areas of the HPT-HT samples have very similar misorientation distributions and a fraction of LAGBs of only ~11 % after tensile testing at 673 K using different initial strain rates. However, these histograms do not conform closely with Mackenzie distribution as their corresponding microstructures clearly display a preferential texture as seen in Figure 6.31.

It follows from Figure 6.32 (b) that the fraction of boundaries with $\theta_{mis} < 5^{o}$ noticeably increases during plastic straining at 1.0 s^{-1}, although both the undeformed and the gauge area of the tensile specimens have the same fraction of HAGBs. There is an increase in the fraction

of HAGBs in the HPT-HT samples deformed using a strain rate of 3.3×10^{-2} s^{-1} as apparent in Figure 6.32 (c). In addition, the misorientation distribution at this testing condition shows close similarity with the Mackenzie predictions thereby indicating the formation of a random texture during superplastic flow.

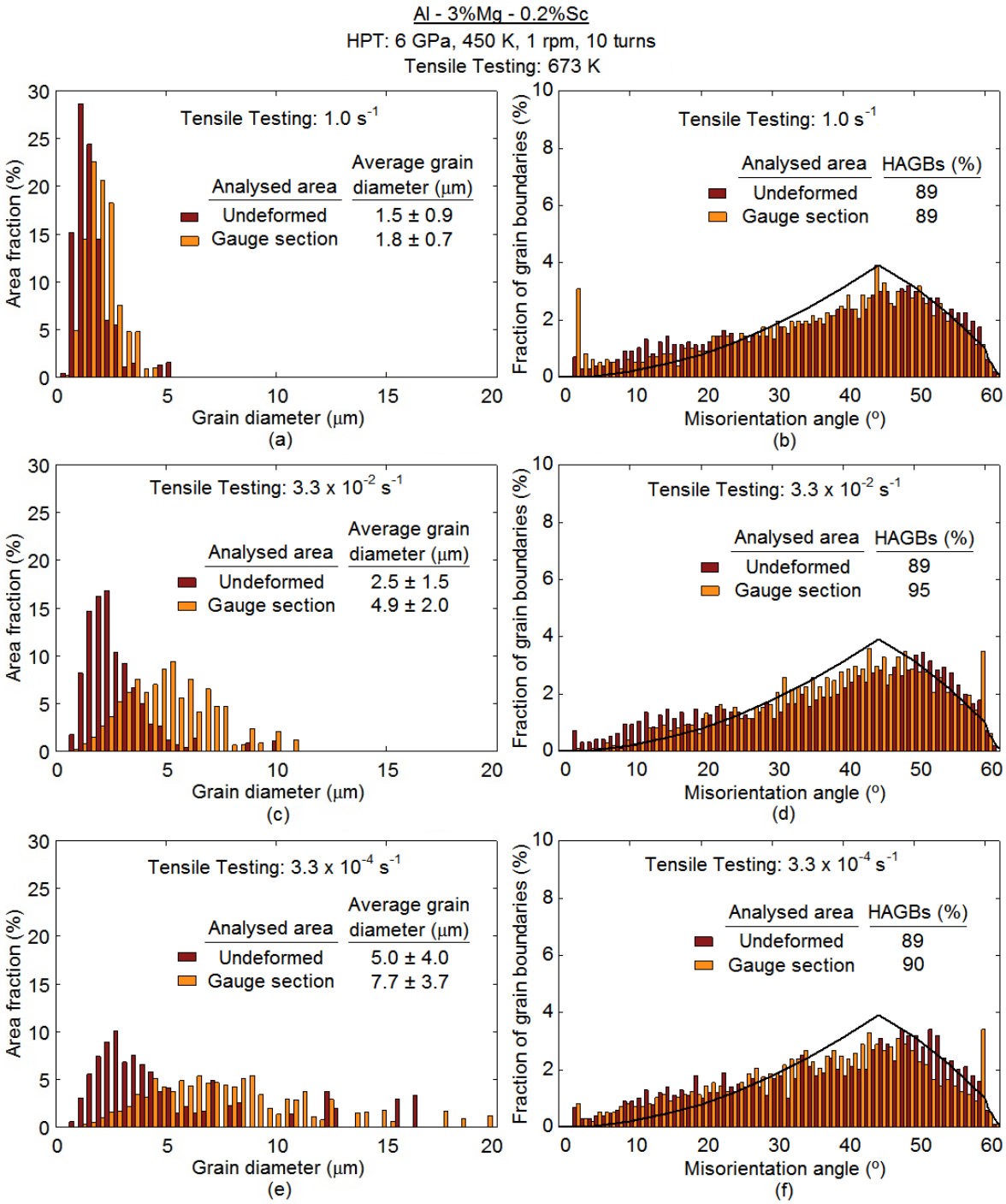

Figure 6.32 – Histograms of (a,c,e) the area fraction of grain diameters and (b,d,f) the misorientation angles for the Al-3Mg-0.2Sc alloy processed by 10 turns of HPT at 450 K and deformed at 673 K using strain rates of (a,b) 1.0, (c,d) 3.3×10^{-2} and (e,f) 3.3×10^{-4} s^{-1}.

The results in Figure 6.32 (f) demonstrate that, in practice, the material originally processed by HPT at 450 K and further pulled to failure at 3.3×10^{-4} s^{-1} has the same fraction of HAGBs at both the head and the gauge section. Also, the histograms of the misorientation angles are still unlike the Mackenzie distribution, even though a superplastic elongation of ~1150 % was attained at this testing condition. It should be further noted that the misorientation distributions of the HPT-HT specimens display unusually high fractions of boundaries with $\theta_{mis} \approx 60^{o}$ after deformation with initial strain rates of 3.3×10^{-2} and 3.3×10^{-4} s^{-1}. Accordingly, this confirms the development of coherent twins at these testing conditions as already indicated in the OIM images in Figures 6.31 (d) and (f).

Several SEM micrographs were taken along the gauge section of specimens of the Al-3Mg-0.2Sc alloy deformed at different temperatures and strain rates. These images were used to estimate the grain sizes after tensile testing at selected conditions and examine the grain coarsening kinetics in samples originally processed through 10 turns of HPT at either 300 or 450 K. These results are presented in Figure 6.33 as plots of average grain boundary spacing vs time at testing temperature for the HPT-processed metal pulled to failure at temperatures from 473 to 723 K.

It follows from Figure 6.33 that the HPT-RT material exhibits faster kinetics of grain growth by comparison with the same alloy processed by HPT at ~0.5T_m. After tensile testing at 473 K, all samples continue having UFG structures even after heating times of ~4 h. There is a significant increase in the $\bar{L}$ values after increasing the temperature from 473 to 523 K, although the HPT-HT metal displays slightly smaller grain sizes after testing at

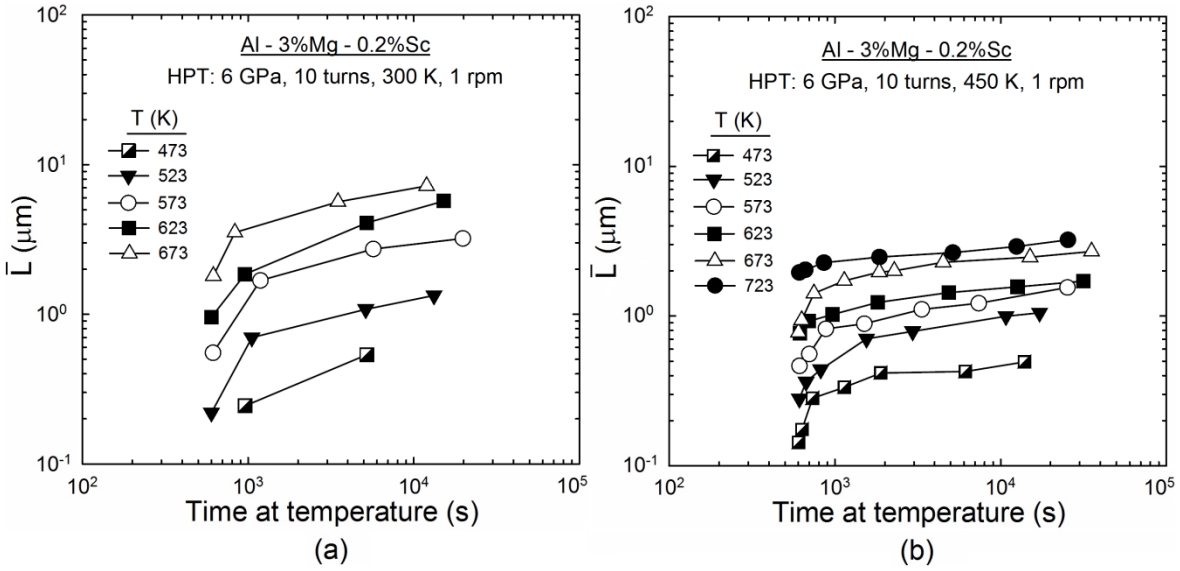

Figure 6.33 - Average grain boundary spacing, $\bar{L}$, as a function of time at temperature for samples of the Al-Mg-Sc alloy processed through 10 turns of HPT at either (a) 300 or (b) 450 K and further tested in tension at temperatures from 473 to 723 K.

comparable conditions. Further increases in the testing temperature result in only moderate coarsening for the Al-Mg-Sc alloy originally processed at 450 K, whereas the average grain sizes substantially increase for tests performed with HPT-RT samples at $T \geq 573$ K.

The results in Figure 6.33 also demonstrate that faster coarsening rates are evident in samples strained at extremely high strain rates and therefore for very short periods of time. On the other hand, it is apparent in Figure 6.33 (b) that the total time at temperature has limited influence on the average grain boundary spacing attained in HPT-HT specimens deformed using $\dot{\varepsilon} \leq 1.0 \times 10^{-2}$ s^{-1} as there appears to exist only minor grain growth with decreasing strain rates.

A comparison of Figures 5.24 and 6.33 reveals that the Al-3Mg-0.2Sc alloy processed by HPT at $\sim 0.5T_m$ consistently displays smaller grain sizes than the ECAP-processed metal after tensile testing at equivalent temperatures and strain rates, except for test performed at 723 K using very high strain rates. By contrast, the same metal processed by HPT at room temperature exhibits noticeably higher grain sizes compared with the ECAP-processed samples after deformation at $T \geq 573$ K for total heating times superior to ~15 min.

6.3 Discussion

6.3.1 Effect of Processing Temperature on the Hardening Kinetics and Microstructural Evolution of an Al-Mg-Sc Alloy Processed by HPT

This investigation demonstrates that processing through 10 turns of HPT at 450 K leads to a lower average microhardness (~180 Hv) and slightly larger grain sizes (~150 nm) in the Al-3Mg-0.2Sc alloy compared with HPT at RT. These results are consistent with earlier studies that examined the influence of the processing temperature on the restoration mechanisms during high-pressure torsion [56,136]. Accordingly, lower hardness values and larger grain sizes are achieved after HPT processing at increasing homologous temperatures and this is attributed to a more significant contribution of dynamic softening mechanisms such as recovery and recrystallization during severe plastic deformation, as observed in pure nickel [56], palladium and copper [136]. Nevertheless, the difference in the average grain sizes for the Al alloy processed by HPT at either ~0.3 or $\sim 0.5T_m$ is almost negligible by comparing with pure metals processed at comparable conditions [136] and this may be associated to a more difficult recovery in solid solutions with large amounts of Mg [15].

The Vickers microhardness measurements depicted in Figures 6.1 and 6.2 showed that there is a gradual evolution towards homogeneity with increasing numbers of turns in HPT processing. Nonetheless, after 10 turns of HPT at 450 K, it is clearly noted that there is no

further increase in the hardness values along the diameter of the discs. Conversely, it appears from Figure 6.1 that the metal processed by HPT at ~0.3T_m only attains its maximum hardness after 60 turns and additional torsional straining results in an overall reduction in the microhardness.

The hardness values in Figures 6.1 and 6.2 were used to construct plots of the Vickers microhardness against the equivalent strain imposed in the discs during processing by HPT. The equivalent strain, ε_{HPT}, was calculated using Eq. 2.5 [114] considering a thickness of ~0.7 mm and the microhardness values after processing by a given number of turns were calculated based on the average of the values recorded at the same individual radial position, as shown in Figures 6.34 and 6.35 for the Al-Mg-Sc alloy processed by HPT at either 300 or 450 K, respectively.

The results in Figure 6.34 demonstrate that, in the initial stages of HPT processing at room temperature, the Vickers microhardness increases at fast rates and achieves values higher than 200 Hv at an imposed strain of ~250. Thereafter, there is a noticeable reduction in the hardening kinetics; however, the hardness values continue increasing with the equivalent strain up to $\varepsilon_{HPT} \approx 1500$. From this point, the microhardness slightly decreases and appears to saturate at a value of ~190 Hv.

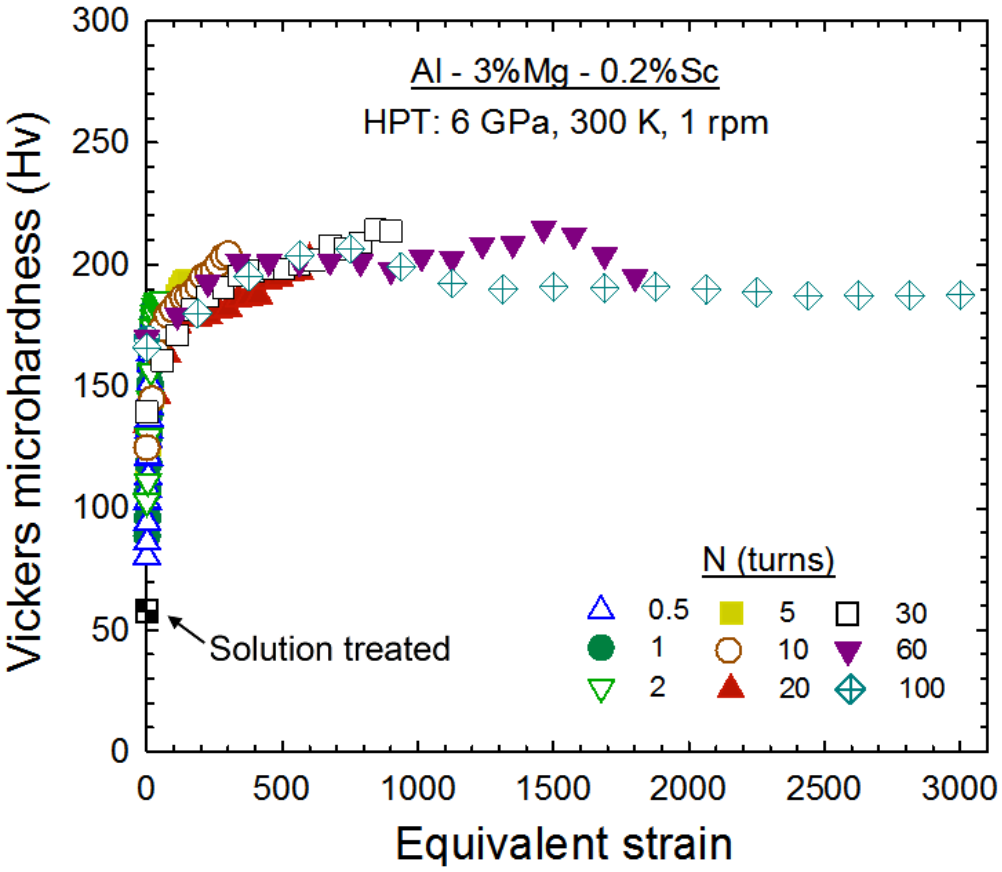

Figure 6.34 - The Vickers microhardness values plotted against the equivalent strain for samples of the Al-3Mg-0.2Sc alloy processed by HPT at 300 K.

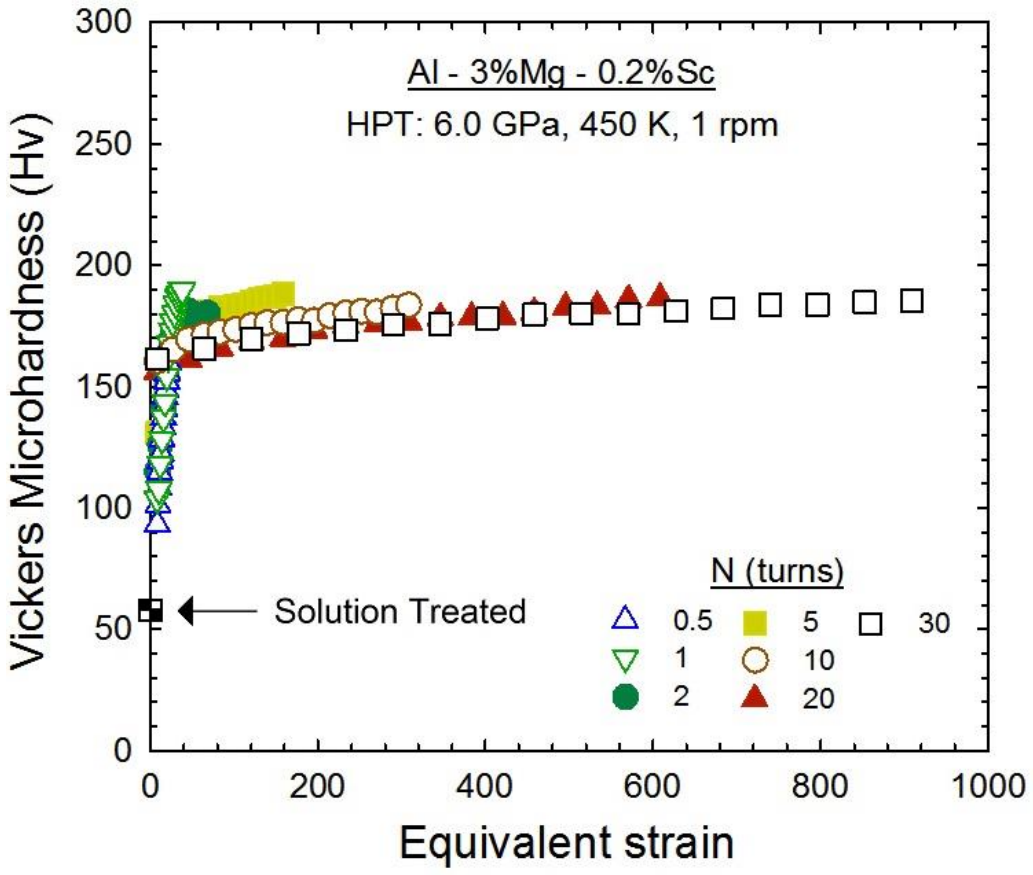

Figure 6.35 - The Vickers microhardness values plotted against the equivalent strain for samples of the Al-3Mg-0.2Sc alloy processed by HPT at 450 K.

Inspection of Figures 6.34 and 6.35 reveals that the material processed by HPT at 450 K exhibits faster kinetics of hardening than during HPT processing at an initial temperature of ~300 K. The microhardness rapidly increases after 1 HPT turn and achieves a peak value of ~190 Hv at $\varepsilon_{HPT} \approx 40$. Afterwards, there is a very minor decrease in the Vickers microhardness with increasing strains and a saturation value of ~185 Hv is already attained after 5 revolutions.

The hardening behaviour observed in this study for the Al-3Mg-0.2Sc alloy is designated softening with recovery [134] and is commonly encountered in pure metals processed by HPT at homologous temperatures ranging from ~0.3 to 0.5 [134,136]. It is worth noting that there are several investigations showing that Al-Mg alloys with more than 0.6 wt. % of Mg do not display softening during HPT at RT [15,132,137,219,274]. Nevertheless, in these studies, HPT processing was conducted to a maximum of 20 turns and a reduction in the microhardness values of the Al-3Mg-0.2Sc alloy was only noticed after 60 revolutions at ~$0.3T_m$. Therefore, there appears to exist a critical amount of accumulated strain energy from which dynamic softening mechanisms are triggered during HPT. Furthermore, this critical value is shifted to lower strains during processing at higher homologous temperatures due to an increase in the rate of recovery.

Samples of a high-purity Al were subjected to HPT processing at ~298 K using a nominal pressure of 1 GPa and a rotation rate of 0.5 rpm [136]. Similarly to the current investigation, the microhardness in this metal reaches a peak after sufficient torsional straining and thereafter decreases down to an equilibrium value. However, this hardness peak was attained at $\varepsilon_{HPT} \approx 5$, whereas softening was only observed in the Al-3Mg-0.2Sc alloy at an equivalent strain of ~1500. These results thereby indicate that materials with higher strain hardening capacities require larger amounts of torsional straining to undergo softening during HPT processing.

The temperature rise of the Al-3Mg-0.2Sc alloy after 60 and 100 turns of HPT processing was calculated as ~37 K using Eq. 2.7 [121]. By considering this increase in the temperature of the sample, the homologous temperature increases from ~0.32 to 0.37. Therefore, although there is only a minor increment in the temperature of the discs during high pressure torsion, this slightly increases the rate of diffusion during plastic deformation and may partially contribute to the decrease of the hardness values after a sufficiently high number of revolutions.

It follows from careful examination of the STEM images in Figures 6.8 and 6.9 together with the EBSD results in Figures 6.10 and 6.11 that the Al-3Mg-0.2Sc alloy displays grain structures with virtually the same average size after 10 turns of HPT at either 300 or 450 K. However, the HPT-RT metal was not completely refined after processing as additional torsional straining leads to an overall increase in the average microhardness up to 60 turns of HPT processing. For this reason, the material processed through 10 turns of HPT at RT exhibits larger amounts of LAGBs and a broader distribution of grain sizes compared with the HPT-HT alloy.

This investigation also demonstrates that the UFG structures developed in the Al-Mg-Sc alloy during HPT processing at $\sim 0.3T_m$ are visibly elongated along the shear direction as previously documented for armco iron [275], nickel [56] and tantalum [276] after processing by HPT at comparable homologous temperatures. Nevertheless, an increase in the processing temperature from 300 to 450 K led to the formation of fairly equiaxed microstructures after 10 HPT revolutions. The reduction in the aspect ratios with increasing temperatures was already noticed in several metals after SPD processing [56,275–278] and is mainly attributed to the faster recovery rates during high temperature deformation. It should be further noted that the Al alloy processed by HPT at $\sim 0.5T_m$ exhibits a dislocation density of $\sim 7 \times 10^{12}$ m^{-2}, whilst $\rho \approx 3.6 \times 10^{13}$ m^{-2} for the same metal processed by HPT at RT. These results are consistent with the lower average microhardness of the HPT-HT metal and are also associated with the increasing participation of dynamic recovery at elevated temperatures.

6.3.2 Effect of Processing Temperature on the Stored-Strain Energy and Thermal Stability of an Al-Mg-Sc Alloy Processed by HPT

The experimental results displayed in Figures 6.12 to 6.16 consistently confirm that the microstructural stability of Al-Mg-Sc alloys processed by HPT is notably enhanced by conducting this procedure at an elevated temperature. The Al-3Mg-0.2Sc alloy subjected to 10 turns of HPT at 300 K and annealed at either 623 or 673 K exhibits an inhomogeneous microstructure formed by few UFG structures and a large fraction of coarse grains with an average size of >10 μm, which is similar to the duplex structures reported for pure nickel processed by HPT at 300 K and further annealed at 448 K for 1 h [56]. By contrast, the HPT-HT alloy displays a more uniform distribution of grains and significantly smaller grain sizes after annealing at comparable conditions.

Similarly to the ECAP-processed alloy, the reasons for the superior thermal stability in Al-Mg-Sc alloys processed by HPT at high homologous temperatures may be initially assessed by estimating the driving and restraining pressures for grain boundary migration. The driving pressures due to stored dislocations, P_d, and release of the boundary energy, P_b, for the material processed by 10 turns of HPT at different temperatures were calculated using Eqs. 5.1 and 5.2, respectively, with γ = 0.324 Jm^{-2} [253], **b** = 2.86 × 10^{-10} m and G = 25.42 GPa [237]. The values of P_d and P_b are displayed in Table 6.2 and were determined based on the average grain diameters in Figure 6.11 (a) and the dislocation densities in Table 6.1.

It is readily observed in Table 6.2 that the Al-3Mg-0.2Sc alloy processed by HPT at either 300 or 450 K displays $P_b \approx 3.04$ MPa and this value is nearly three times higher than after 8 passes of ECAP at RT. It is also noted the values of P_d are almost negligible compared with the driving pressures due to release of the grain boundary energy as the HPT-RT material exhibits a driving pressure due to stored dislocations of ~0.04 MPa, whereas $P_d \approx 0.01$ MPa for samples processed at $\sim 0.5T_m$.

Table 6.2 -Driving pressure for grain boundary migration due to stored dislocations, P_d, and boundary energy, P_b, for the Al-3Mg-0.2Sc alloy processed by HPT at different temperatures.

Metal-working procedure	P_d (MPa)	P_b (MPa)
HPT: 300 K, 6 GPa, 1 rpm, 10 turns	0.04	3.04
HPT: 450 K, 6 GPa, 1 rpm, 10 turns	0.01	3.04

The presence of nanoprecipitates significantly improves the microstructural stability at high temperatures as they exert a restraining pressure, P_Z, on the moving boundaries during grain growth [161,252]. Additionally, both the size and the spatial distribution of these particles strongly influence the grain structures developed during heat treatment as, in practice, regions with fewer and larger precipitates permit the formation of coarser grain structures [158]. In this investigation, the Al-3Mg-0.2Sc alloy was processed by HPT in the solution treated condition and there was no experimental evidence of precipitation of Al_3Sc phases during severe plastic deformation. This is consistent with the TTT diagram depicted in Figure 2.24 [158] which shows that Al_3Sc dispersoids are absent in a supersaturated Al-0.23Sc alloy after heat treatment at ~500 K for total times below 100 min.

Nevertheless, Al_3Sc precipitates were profusely formed in the microstructure of the HPT-processed material during post-HPT annealing at 673 K for 1 h, as evident in Figures 6.18 to 6.21. These dispersoids are classified into two distinct categories based on their size and distribution. There is a group of nano-sized precipitates finely dispersed within regions having fine-grained structures. These particles have average radii within the range of ~3.2-3.3 nm in good agreement with the r_p value of ~3.5 nm previously reported for an Al-0.25Sc alloy [256]. Conversely, there is also a group of coarse precipitates with diameters of hundreds of nanometres. They are scarcer compared with the nano-sized precipitates and probably correspond to particles not dissolved during the solution treatment prior to high-pressure torsion.

The values of ΔP and ψ_b were calculated for the Al-3Mg-0.2Sc alloy processed by HPT and further annealed at different temperatures using the same procedure described for the ECAP-processed samples in Chapter 5. The susceptibility for grain boundary migration was evaluated by summing the contributions of the driving and Zener drag pressures ($\Delta P = P_d + P_b - P_Z$) shown in Tables 6.2 and 5.3, except for discs annealed for 1 h at 673 K wherein the r_p values were taken from Figure 6.22 to give restraining pressures of ~0.70 and 0.68 MPa for the material originally processed by HPT at either 300 or 450 K, respectively.

The dimensionless parameter for boundary stability, ψ_b, was also estimated for the HPT-processed discs using Eq. 5.3 [161,257] with k_p = 1.5. The average grain diameters were taken from Figure 6.16 and the values of r_p and f were obtained from Table 5.3, apart from the average precipitate radii after annealing at 673 K which were estimated based on the TEM analyses performed in the current study. The values of ψ_b and ΔP are displayed in Table 6.3 for samples of the Al-3Mg-0.2Sc alloy processed through 10 revolutions of HPT at either 300 or 450 K and subsequently heat treated for 1 h at temperatures ranging from 573 to 773 K.

Table 6.3 -Sum of the driving and restraining pressures for grain boundary migration, ΔP, and dimensionless parameter for boundary stability, ψ_b, for the Al-3Mg-0.2Sc alloy processed by HPT at either 300 or 450 K and further annealed at different temperatures.

Metal-working procedure	T (K)	$\Delta P = P_d + P_b - P_Z$ (MPa)	ψ_b
HPT: 300 K, 6 GPa, 1 rpm, 10 turns	573	0.65	1.20
	623	1.79	0.64
	673	2.37	0.35
	723	2.86	0.11
	773	3.00	0.04
HPT: 450 K, 6 GPa, 1 rpm, 10 turns	573	0.62	1.20
	623	1.76	0.64
	673	2.36	0.34
	723	2.83	0.11
	773	2.97	0.04

The results shown in Table 6.3 demonstrate that $\Delta P > 0$ for the HPT-processed alloy further annealed at all conditions considered in these calculations. The values of ΔP increase with increasing temperatures mainly due to coarsening of precipitates and achieve a maximum value of ~3 MPa for the HPT-RT metal annealed at 773 K. Also, the HPT-HT alloy exhibits lower values of ΔP compared with the material processed by HPT at 300 K. Nevertheless, the differences in the values of ΔP are almost negligible and appear to underestimate the significantly enhanced thermal stability obtained after HPT processing at an elevated temperature.

It follows from the hardness measurements together with the TEM and EBSD examinations that the microstructure of the HPT-RT metal is more inhomogeneous than after processing at $\sim 0.5T_m$. In addition, the metal processed at RT displays a significantly higher density of dislocations which are mainly isolated and heterogeneously distributed throughout the deformed discs. These highly strained areas are likely to exhibit higher driving pressures for grain boundary migration by comparing with the average values predicted in Table 6.2 and this may partially contribute to accelerate the coarsening kinetics in the Al alloy processed by HPT at RT during post-SPD annealing.

Table 6.3 also reveals that $\psi_b \approx 1.2$ for the HPT-processed samples annealed at 573 K. However, according to the mathematical model used to derive Eq. 5.3, no grain growth should occur when $\psi_b > 1.0$ [161,257] and this is apparently inconsistent with the experimental evidence obtained in this study. Nonetheless, it is important to note that the values of ψ_b correspond to the distribution of Al_3Sc dispersoids after annealing for 1 h and the precipitation of these particles is a time-dependent phenomenon. As a result, it is conceivable that grain boundary migration may have initiated prior to formation of the Al_3Sc phases and the advancing boundaries were efficiently restrained only after precipitation of a large amount of dispersoids.

It has been demonstrated that, for a sufficiently disperse distribution of grain diameters, abnormal grain growth occurs when $0.25 < \psi_b < 1$ [161,257]. In this investigation, the grain structures of the Al-3Mg-0.2Sc alloy processed by HPT at different temperatures underwent abnormal coarsening during heat treatment at either 623 or 673 K and this is consistent with the ψ_b values of 0.64 and 0.35 depicted in Table 6.3. Furthermore, particularly at these temperatures, the HPT-RT alloy exhibits notably faster kinetics of grain growth compared with the material processed by HPT at 450 K. The origin of these very distinct coarsening rates may also be associated with the different arrangements and density of dislocations measured in this Al alloy after HPT processing.

An early study on the precipitation kinetics of an Al-0.2%Sc alloy revealed that the nano-sized Al_3Sc particles are uniformly distributed within the microstructure of the Al-Sc alloy after heat treatment at temperatures below 623 K, whereas ageing at $T \geq 643$ K leads to an inhomogeneous distribution of dispersoids due to the occurrence of discontinuous precipitation [158]. It is worth mentioning that this material was aged immediately after solution treatment and thus it likely displayed a relatively low dislocation density. In addition, it is well-recognised that dislocation lines are preferential sites for nucleation of precipitates [255] and therefore an increase in the dislocation density reduces the minimum ageing temperatures from which discontinuous precipitation becomes dominant [259].

Based on these observations, it is possible to presume that abnormal grain coarsening occurred at faster rates in the HPT-RT metal primarily due to its higher density of dislocations that enabled the occurrence of incipient discontinuous precipitation during heat treatment at high temperatures. This hypothesis is also supported by the microstructural analyses performed in the HPT-processed alloy after annealing at 673 K as they clearly demonstrated the existence of a large amount of nano-sized dispersoids in regions having fine-grained structures, whist only few and mostly large Al_3Sc particles were identified within abnormally coarse grains.

It is readily apparent in Table 6.3 that that ψ_b varies from 0.11 to 0.04 for the HPT-processed discs annealed for 1 h at $T \geq 723$ K. It should be further noted that, although these samples exhibited some broadening in their distributions of grain diameters, there is no evidence of formation of duplex structures after heat treatment. These results are reasonably consistent with the theoretical model associated with Eq. 5.3 which predicts the occurrence of limited broadening but not abnormal coarsening for ψ_b values of less than ~0.1 [161,257].

Aiming to summarize the experimental findings obtained in this study and more clearly distinguish the microstructural features observed in the HPT-processed samples after heat treatment, Figures 6.36 and 6.37 display schematic representations of the microstructural changes in supersaturated Al alloys containing dispersoid elements after HPT processing at a homologous temperature of either ~0.3 or ~0.5, respectively, and further annealing.

Figures 6.36 illustrates that the microstructure of solid solution alloys after HPT processing at RT is constituted by a uniform array of elongated UFG structures. These grains are mostly limited by HAGBs, although this metal comprises high fractions of LAGBs in the form of mobile dislocations as represented using lines coloured in red. After annealing at $T_1 \approx 0.55T_m$, there is a slight increase in the overall size of the grains and a more significant reduction in the density of dislocations as indicated in Figure 6.7 by the sharp decrease in the Vickers microhardness after annealing for 1 h at 473 K.

Abnormal grain growth occurs concomitantly with discontinuous precipitation of second-phase particles during heat treatment at moderate temperatures ($T_2 \approx 0.7T_m$). Nano-sized particles rapidly precipitate in highly strained areas of the HPT-processed metal and this permits the preservation of fine-grained structures due to the Zener pinning effect [161,252]. However, this inhomogeneous nucleation of dispersoids has the deleterious effect of allowing the existence of areas with fewer particles whereby grain boundaries can easily advance during annealing treatment. For this reason, the highly deformed microstructure of the HPT-RT alloy evolves into duplex structures during heat treatment at 623 and 673 K as represented in Figure 6.36 (c). By contrast, fairly homogeneous grain structures with larger average sizes are developed after annealing at higher temperatures ($T_3 > 0.75T_m$). This may be associated with the faster kinetics of particle coarsening at these temperatures together with the completion of recrystallization prior to the occurrence of significant precipitation as experimentally verified in a deformed Al-0.12Sc alloy after annealing at 748 K [163].

After 10 turns of HPT processing at $\sim 0.5T_m$, the Al-3Mg-0.2Sc alloy developed a homogeneous microstructure formed by equiaxed grains with nearly the same average size achieved after HPT at room temperature. The HPT-HT metal also displayed a substantially lower density of dislocations compared with the HPT-RT alloy and these features are

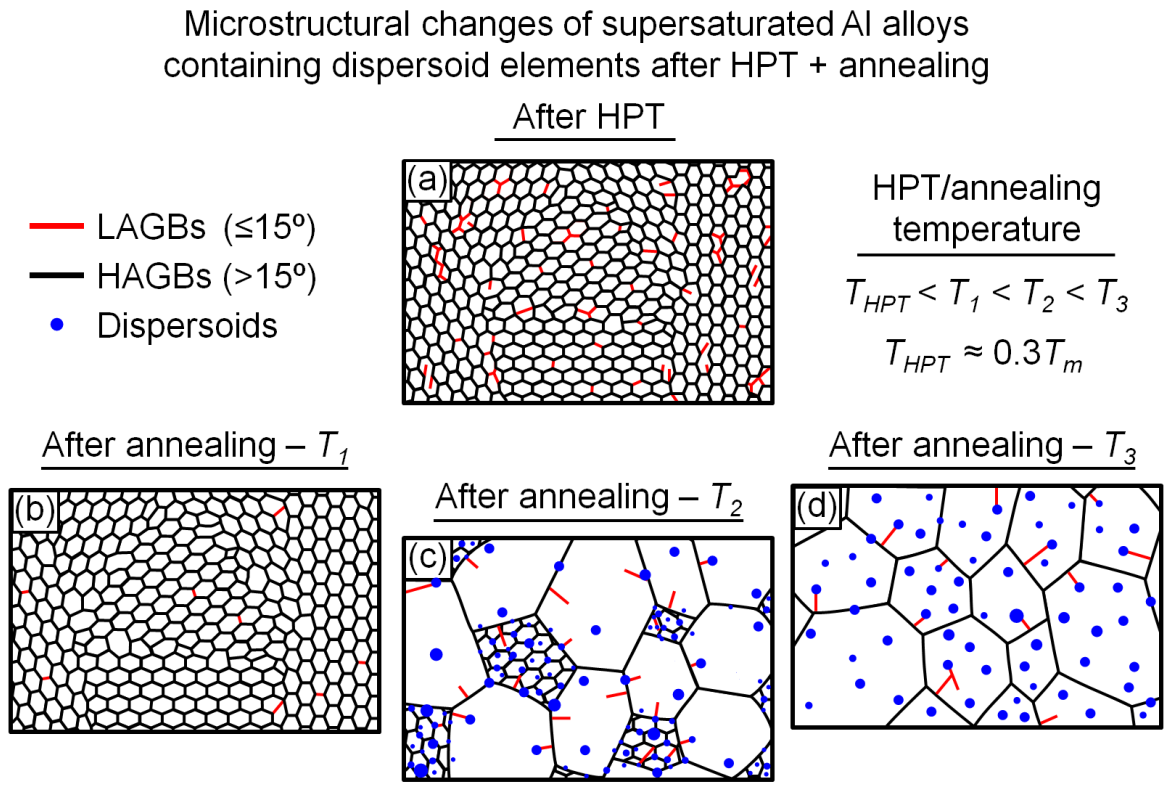

Figure 6.36 - Schematic representation of the microstructural changes of supersaturated Al alloys containing dispersoid elements after HPT processing at ambient temperature and subsequent annealing.

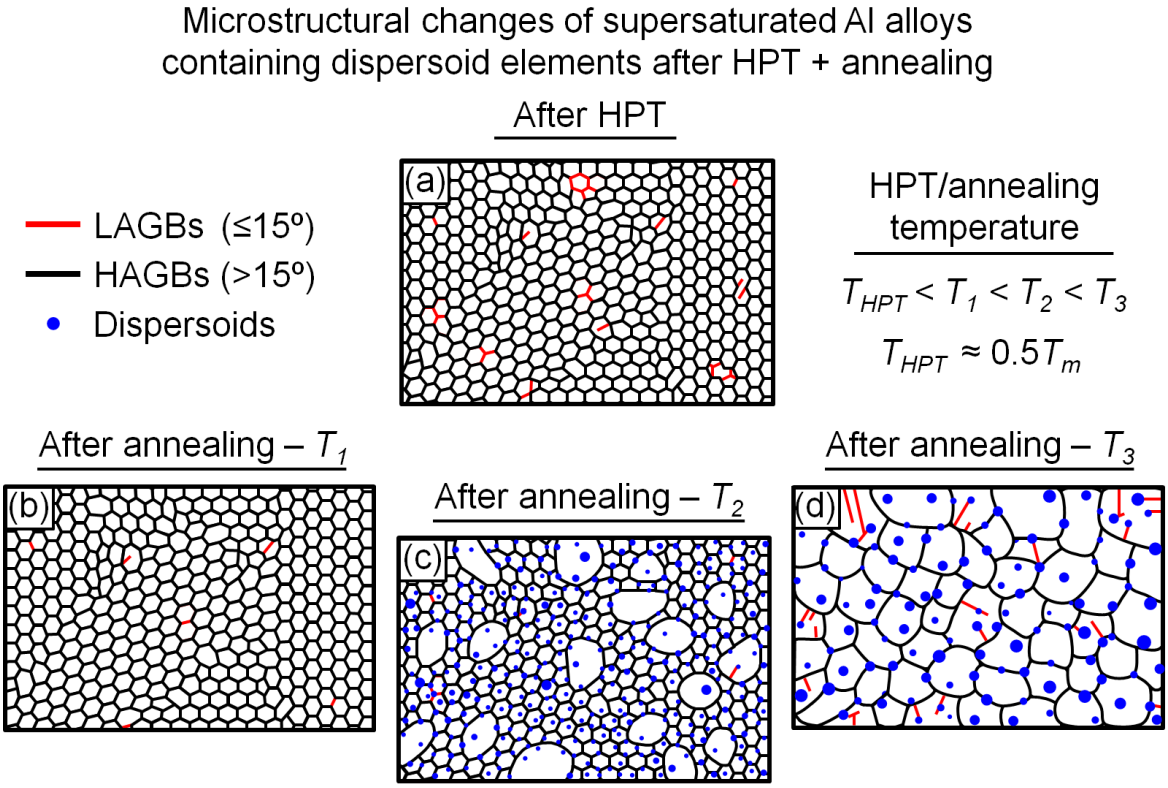

Figure 6.37 - Schematic representation of the microstructural changes of supersaturated Al alloys containing dispersoid elements after HPT processing at a moderate homologous temperature and subsequent annealing.

pictorially represented in Figure 6.37 (a). After heat treatment at temperatures up to $\sim 0.55T_m$, the average grain size remains practically unchanged, whereas there is a decrease in the hardness values probably due to annihilation and rearrangement of dislocations into low energy configurations during recovery.

Annealing at homologous temperatures within the interval of ~0.65-0.75 promotes the development of duplex structures in the solid solution alloy originally processed by HPT at $\sim 0.5T_m$. Nevertheless, this metal exhibits slower coarsening kinetics compared with the HPT-RT alloy and this leads to a less heterogeneous distribution of grains, as illustrated in Figure 6.37 (c). The reasons for the enhanced microstructural stability of the HPT-HT material at this temperature range directly follow from both the lower density of dislocations and the more homogeneous microstructure developed during HPT. The HPT-HT alloy has much fewer sites for heterogeneous nucleation of dispersoids and this permits the predominance of continuous precipitation during annealing at T_2. As a result, the nano-sized particles uniformly precipitated throughout the microstructure act as effective barriers to the advancing boundaries and delay the coarsening rate of growing crystallites.

Inspection of Figures 6.13 (c) and (d) demonstrates that the HPT-HT alloy develops a reasonably homogeneous microstructure after annealing at 723 and 773 K, respectively. This is indicated in Figure 6.37 (d) that also displays a disperse distribution of second-phase particles after heat treatment at T_3. As both the HPT-RT and the HPT-HT metal exhibit similar driving pressures for boundary migration but distinct dislocation densities, it is believed that the smaller grain sizes observed in the HPT-HT alloy are associated with an extension in the range of temperatures in which precipitation occurs homogeneously during heat treatment.

Dynamic recovery becomes more important and the rate of annihilation of dislocations increases during plastic straining at higher homologous temperatures. Accordingly, the strain energy stored in the form of microstructural defects is diminished in Al-Mg-Sc alloys processed by HPT at elevated temperatures as indicated by both the XRD analyses performed in this investigation and the DSC examinations conducted on an Al-5Mg-0.3Sc-0.08Zr alloy processed by HPT at different temperatures [50]. It is concluded therefore that the microstructural stability in Al-Mg-Sc alloys is significantly improved by conducting HPT processing at 450 K due to the occurrence of dynamic recovery and this permits the retention of the benefits obtained through grain refinement in applications at high temperatures.

6.3.3 Superplastic Characteristics of Al-Mg-Sc Alloys Processed by HPT

The individual values of elongation to failure in Figure 6.26 were used to construct colour-coded maps delineating the range of temperatures and strain rates wherein the HPT-processed Al-3Mg-0.2Sc alloy exhibits true superplastic ductilities [105]. These maps are depicted in Figure 6.38 for the material subjected to 10 turns of HPT processing at either (a) 300 or (b) 450 K and thereafter tensile tested using a wide variety of strain rates and temperatures.

The results in Figure 6.38 consistently demonstrate that the HPT-HT alloy exhibits remarkably improved superplasticity compared with the material processed at ambient temperature. In practice, the HPT-HT metal achieved superior elongations for all testing conditions assessed in this study and displayed true superplastic ductilities in an extended range of strain rates and temperatures. The overall elongation values increase with increasing temperatures up to $T \approx 673$ K in which they are higher than 1400 % for tests performed using initial strain rates within the interval of $\sim 10^{-2}$-10^{-1} s^{-1}. By contrast, the superplastic properties for samples of the HPT-RT alloy appear to deteriorate at $T \geq 623$ K, although the elongations attained at 523 and 573 K are similar to those obtained after processing through 10 HPT revolutions at $\sim 0.5 T_m$.

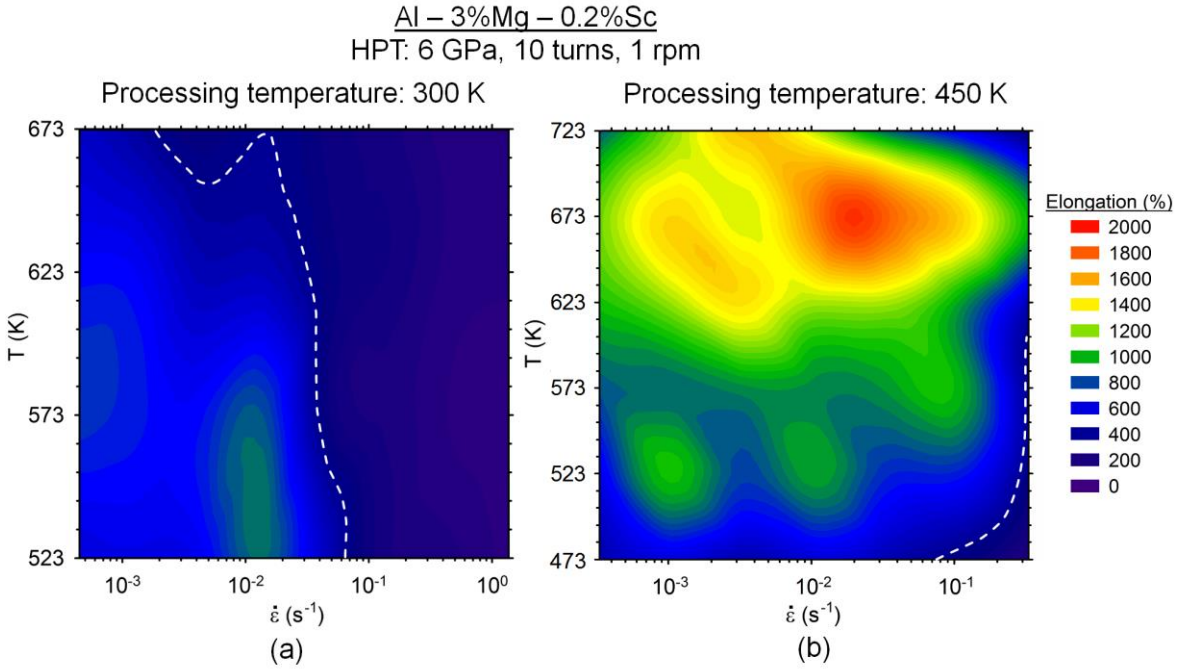

Figure 6.38 - Colour-coded contour maps showing the elongations to failure for the Al-3Mg-0.2Sc alloy processed through 10 turns of HPT at either (a) 300 or (b) 450 K: the broken lines delineate the minimum elongation normally observed after true superplastic flow [105].

The superior superplastic behaviour observed in samples of the Al-3Mg-0.2Sc alloy processed by HPT at an elevated temperature is intrinsically associated with its enhanced microstructural stability by comparing with the HPT-RT material. It follows from Figures 6.12 to 6.16 that the HPT-HT alloy displays smaller grain sizes after annealing for 1 h at $T \geq 473$ K. This trend is also consistent with the measurements of the average grain boundary spacing conducted on the HPT-processed specimens after tensile testing. As a result, superplastic flow is likely to occur at faster rates in the HPT-HT metal as it preserves smaller grains and thereby exhibits a higher density of HAGBs available to undergo grain boundary sliding during deformation at high temperatures [38,105,139].

It should be further noted that the Al alloy processed by HPT at $\sim 0.3T_m$ has a large fraction of grains with $\bar{L} > 10$ μm after static heating at 623 and 673 K. These coarse structures comprise a notable fraction of LAGBs as evident from the EBSD scans conducted on both the annealed discs and the undeformed area of the tensile specimens tested at 673 K with $\dot{\varepsilon} = 4.5 \times 10^{-2}$ s^{-1}. Also, although the HPT-RT alloy still possesses remaining fine-grained structures capable to deform by GBS, this mechanism may not be operative in the abnormally coarse grains which are more likely to deform by dislocation climb when tested using increasingly faster strain rates. Therefore, the reduction in the superplastic elongations in samples processed by HPT at 300 K and tested at $T \geq 623$ K may be attributed to the decreasing contribution of GBS in the total deformation.

This hypothesis is strongly supported by the EBSD results corresponding to the deformed area of the HPT-RT specimen tested at 673 K. Figure 6.29 (b) reveals the existence of grain structures displaying the {110} planes mainly parallel to thickness direction. This preferential texture is characteristic of fcc metals deformed in either compression or tension under non-superplastic conditions [203] and is not notable along the undeformed area of the same sample. In addition, these grains are elongated in a direction parallel to the tensile axis and this is inconsistent with the occurrence of straining entirely by Rachinger GBS whereby equiaxed grains should preserve their original shape [279]. It also follows from the plots depicted in Figure 6.27 (a) that the interval of strain rates having $m \approx 0.22$ increases for $T \geq 623$ K. This indicates that dislocation climb becomes predominant at these testing conditions in good agreement with the results shown in Chapter 4 for the unprocessed alloy.

It is evident from the plots of the true stress vs strain rate in Figure 6.27 that the material processed by HPT at 450 K exhibits lower flow stresses compared with the HPT-RT metal tested at comparable conditions. Nevertheless, in various testing conditions, $m < 0.5$ although these samples achieved superplastic elongations [105]. This apparent dichotomy is likely associated with a more significant grain growth in specimens tested using slower deformation rates which may lead to an overestimation of the true stress at $\varepsilon = 0.3$ [264,265].

Therefore, in order to reliably identify the rate controlling flow process in the Al-3Mg-0.2Sc alloy processed by HPT and further tested in tension, Figure 6.39 shows the variation of the temperature and grain size compensated strain rate, $(\dot{\varepsilon}kT/D_{gb}G\mathbf{b})(d/\mathbf{b})^2$, with the normalized stress, (σ/G). These plots were constructed exclusively for samples which displayed elongations higher than 400 % using σ as the maximum flow stress and *d* as the spatial grain size after tensile testing. Similarly to the ECAP-processed alloy, these calculations considered Q_{gb} = 86 kJ mol^{-1}, $D_{o,gb}$ = 1.86×10^{-4} m^2 s^{-1}, **b** = 2.86×10^{-10} m and G (MPa) = (3.022×10^4) - $16T$ [237]. In addition, the theoretical prediction of the rate of superplasticity in conventional metals was calculated using Eq. 2.2 with A = 10 [38] and plotted in Figure 6.39 using a solid line labelled $\dot{\varepsilon}_{sp}$.

The results displayed in Figure 6.39 reveal that the experimental values of the temperature and grain size compensated strain rate calculated for the HPT-processed alloy are consistent with the predictions from the theoretical model for grain boundary sliding accommodated by dislocation climb. Similarly to the ECAP-processed material, most of the experimental datum points lie slightly above the theoretical line and they appear to be more consistent with these predictions at lower testing temperatures. Nevertheless, it is apparent in Figure 6.39 (a) that the slope of the experimental points originated from the HPT-RT specimens tested at 623 K tend to deviate from the predicted stress exponent of n = 2, especially at lower strain rates. This may indicate that superplastic flow is accommodated by viscous glide at these testing conditions as observed in other fine-grained solid solution alloys which displayed *n* values of ~1 [280].

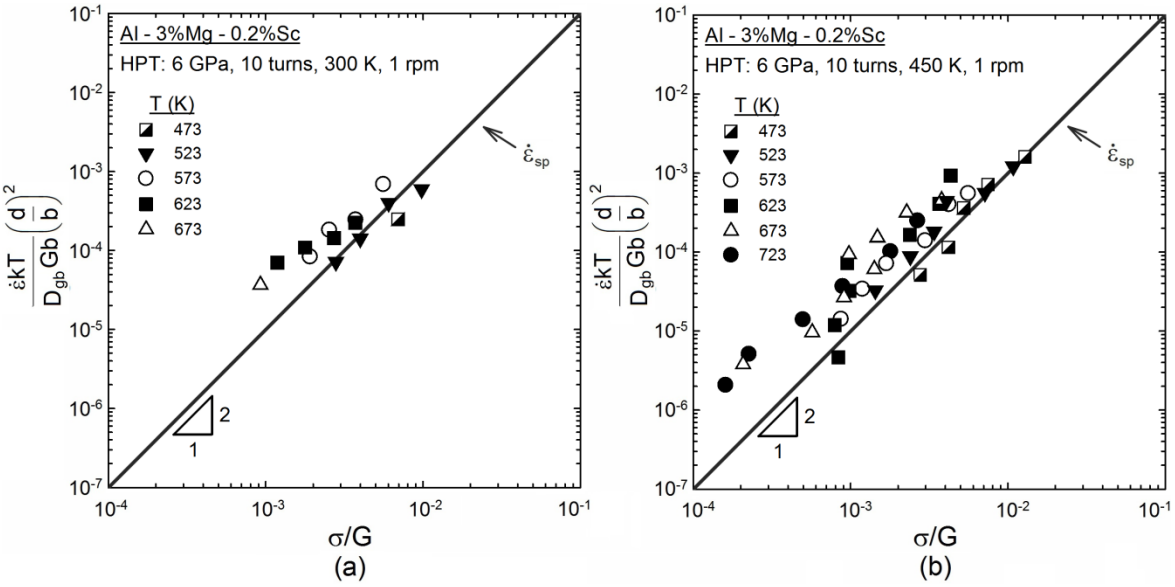

Figure 6.39 - Temperature and grain size compensated strain rate plotted as a function of normalized stress for the Al-3Mg-0.2Sc alloy processed through 10 turns of HPT at either (a) 300 or (b) 450 K.

The activation energy for superplasticity where accommodation by dislocation climb is rate controlling was calculated for the Al-3Mg-0.2Sc alloy processed by HPT at either 300 or 450 K as shown in Figure 6.40. It follows from the measurements of the slopes of the fitted lines that the activation energies of the HPT-processed metal vary from ~100 to 118 kJ mol^{-1}. These values are consistent with the activation energies calculated for the ECAP-processed alloy in Chapter 5 which are also comprised within the range for grain boundary diffusion in pure aluminium (~86 kJ mol^{-1}) [237] and interdiffusion in Al-Mg alloys (~130.5 kJ mol^{-1}) [268]. Furthermore, inspection of Figures 6.40 (a) and (b) demonstrates that the metal processed by HPT at ~0.5T_m exhibits lower values of Q_{gb} than the HPT-RT alloy when tested using $\dot{\varepsilon} \geq 3.3 \times 10^{-3}$ s^{-1}.

It is readily apparent from the histograms of the misorientation angles depicted in Figures 6.17 and 6.30 (b) that there is a substantial increase in fraction of LAGBs in the HPT-RT alloy annealed at 623 and 673 K. These LAGBs are predominantly organised in the form of subgrains which are visible within areas having fine and coarse-grained structures. Accordingly, the reduction in the ductility observed in HPT-RT samples tested at $T \geq 623$ K may also be associated with lower accommodation rates during GBS due to hindrance of mobile dislocations by subgrain boundaries [241]. For this reason, in order to assess whether there is any correlation between the presence of subgrain structures and the elongations achieved in this study, Figure 6.41 displays the variation of the average grain boundary spacing, $\overline{L}$, with the modulus-compensated stress, σ/G, for the Al-3Mg-0.2Sc alloy processed by HPT at different temperatures and further tested in tension: The solid line represents the theoretical prediction for λ in Al-Mg alloys using Eq. 4.1 with ζ = 20, **b** = 2.86 × 10^{-10} m and G (MPa) = (3.022 × 10^4) – 16T [237].

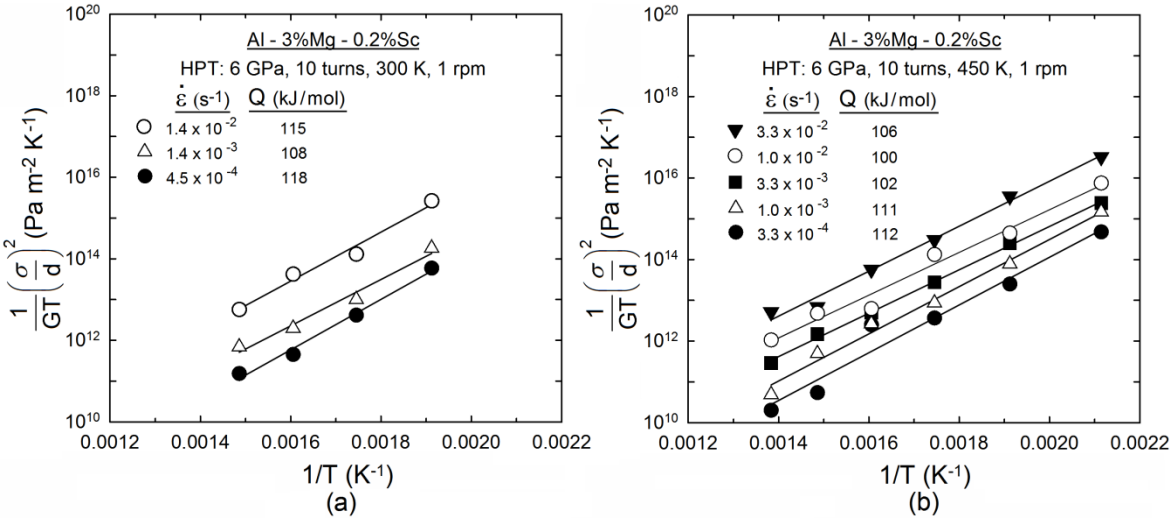

Figure 6.40 - Estimation of the activation energy for superplastic flow using an analysis based on Eq. (2.2) for the Al-3Mg-0.2Sc alloy processed through 10 turns of HPT at either (a) 300 or (b) 450 K.

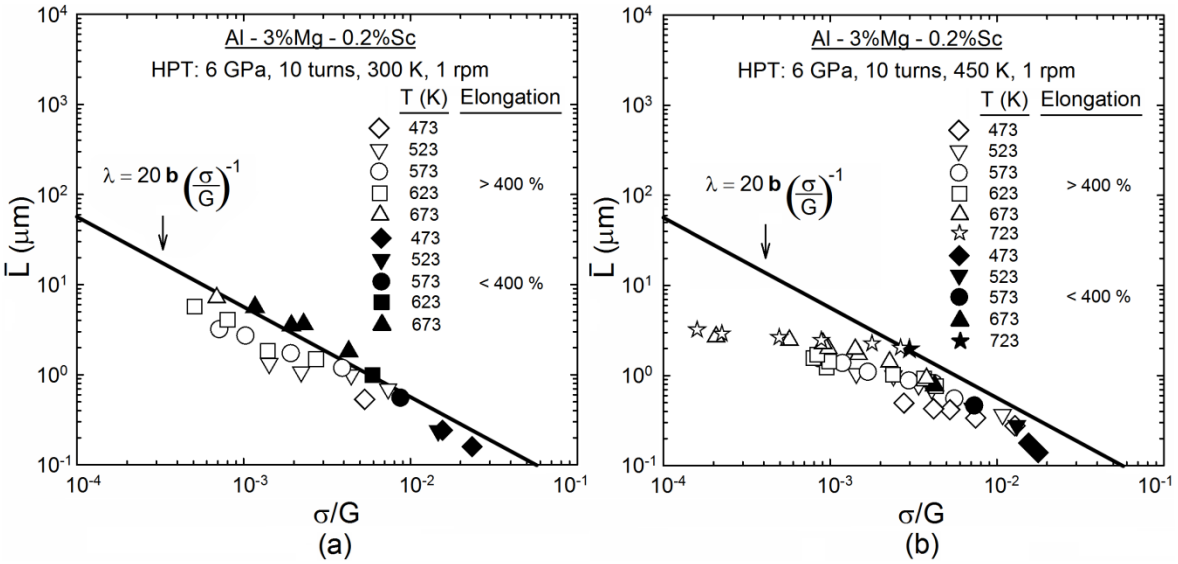

Figure 6.41 - Average grain boundary spacing, $\bar{L}$, vs modulus-compensated stress, σ/G, for the Al-3Mg-0.2Sc alloy processed through 10 turns of HPT at either (a) 300 or (b) 450 K after tensile testing at various temperatures and strain rates: the solid line represents the theoretical prediction for λ using Eq. 4.1.

Inspection of Figure 6.41 reveals that all samples exhibiting superplastic elongations after tensile testing have average grain sizes inferior to the theoretical predictions for the steady state subgrain size in Al-Mg alloys. This is consistent with the OIM images in Figures 6.31 (d) and (f) as they clearly demonstrate that the microstructure of the HPT-HT alloy is essentially composed by HAGBs and subgrains are nearly absent after plastic deformation at 673 K using $\dot{\varepsilon} \leq 3.3 \times 10^{-2}$ s^{-1}. As a result, GBS is more easily accommodated at these testing conditions and this permits the achievement of extensive superplastic ductilities.

By contrast, $\bar{L} > \lambda$ for samples of the HPT-RT alloy tested in tension at 673 K using initial strain rates higher than 4.5×10^{-4} s^{-1}. This suggests that the significant grain coarsening at these temperatures resulted in the development of subgrain structures as experimentally verified in the EBSD results in Figure 6.29 (b) for the HPT-RT specimen tested at 673 K using $\dot{\varepsilon} = 4.5 \times 10^{-2}$ s^{-1}. Accordingly, intragranular slip occurs at slower rates due to the hindrance of dislocations and this promotes premature failure during superplastic flow due to the increased rates of formation and coalescence of cavities [241]. This mode of failure is more likely to occur during tensile testing at lower strain rates and it is consistent with the shape of the fractured specimens in Figure 6.24 (b) as they display diffuse necking when deformed using $\dot{\varepsilon} \leq 4.5 \times 10^{-3}$ s^{-1}.

It also follows from Figures 6.38 and 6.41 that superplastic elongations were not always achieved in samples of the HPT-processed alloy having grain sizes smaller than the steady-state subgrain size. Grain boundary sliding is a thermally activated process and thus the sliding rate of adjacent grains increases with increasing temperatures. Therefore,

although the absence of subgrains facilitates the accommodation during superplastic flow, GBS requires extremely small grains to efficiently operate during deformation at low temperatures and fast strain rates. This explains why the HPT-HT metal displayed an elongation of ~540 % after tensile testing at 473 K using $\dot{\varepsilon} = 1.0 \times 10^{-2}$ s^{-1}, whereas the HPT-RT alloy attained an elongation of ~170 % when deformed at a comparable condition.

Careful examination of Figure 6.41 (b) demonstrates that the Al alloy processed by HPT at $\sim 0.5T_m$ and deformed at 673 K exhibits $\bar{L}$ values smaller than the theoretical predictions for λ, regardless of the testing strain rate. This is consistent with the OIM images in Figure 6.31 wherein substructures with LAGBs are rarely visible along the gauge area of the fractured specimens. Nevertheless, an increase in the temperature from 673 to 723 K results in a more prominent grain growth in samples tested using strain rates higher than 1.0×10^{-2} s^{-1} as $\bar{L} \approx \lambda$. Accordingly, the substantial decrease in the elongations to failure at these testing conditions may be partially attributed to a more difficult accommodation process during GBS due to the presence of subgrain structures.

A comparison of the results presented in Chapters 5 and 6 consistently demonstrates that the Al-3Mg-0.2Sc alloy processed by HPT at 450 K displays improved superplastic properties compared with the same material processed by ECAP at either 300 or 600 K. In this investigation, tensile tests were conducted on miniature specimens with the same dimensions for both the ECAP and the HPT-processed material. Superplastic elongations higher than 900 % were achieved in HPT-HT samples deformed at 573 K using strain rates within the interval of 3.3×10^{-3} to 1.0×10^{-1} s^{-1}. By contrast, the values for the elongation to failure did not exceed 620 % for the ECAP-processed metal tested at comparable conditions.

It should be further noted that the HPT-HT alloy achieves extraordinarily high elongations during tensile testing at 673 K. A record elongation of ~1880 % for HPT-processed materials was attained at this temperature using an initial strain rate of 1.5×10^{-2} s^{-1}. These values are notably higher than the elongations obtained in miniature specimens of the ECAP-processed alloy and true superplastic ductilities are obtained for tests performed at strain rates as high as 3.3×10^{-1} s^{-1}. This excellent superplastic behaviour is a direct consequence of the extremely small grain sizes together with the larger proportion of grains with HAGBs in the HPT-HT metal and will be discussed in more detail in Chapter 7.

It is therefore concluded that the Al-3Mg-0.2Sc alloy subjected to 10 turns of HPT at 450 K exhibits significantly enhanced superplasticity compared with the same material processed either by ECAP or HPT at 300 K. Accordingly, HPT processing at high temperatures has emerged as an efficient strategy to produce UFG metals suitable for applications demanding products with high strength to density ratio fabricated by superplastic forming.

6.4 Summary and Conclusions

1. An Al-3% Mg-0.2% Sc alloy with an initial grain size of ~300 μm was processed through 10 turns of HPT at either 300 or 450 K to produce grain sizes of ~140 and 150 nm, respectively. Microhardness measurements and EBSD examinations were performed immediately after HPT processing and after annealing for 1 h at temperatures up to 773 K. Tensile testing was conducted in specimens of the HPT-processed alloy at high temperatures using strain rates from 3.3×10^{-4} to 1 s^{-1}.
2. The Al alloy processed by 10 turns of HPT at 450 K displays a lower average microhardness (~180 Hv), but faster hardening kinetics than after HPT at 300 K. This follows from a more significant contribution of recovery during HPT processing at high temperatures which permits the achievement of uniform microstructures and hardness distributions at lower levels of torsional straining.
3. The microstructure is more homogeneous and the grain coarsening kinetics are delayed in the metal processed by HPT at 450 K compared with the alloy processed by HPT at 300 K. The grain structures were mostly formed by HAGBs and the average grain sizes were inferior to 2 μm after annealing for 1 h at 773 K.
4. The HPT-processed alloy undergoes abnormal grain coarsening leading to the formation of a bimodal distribution of grains after annealing at 623 and 673 K. Nevertheless, the metal processed by HPT at RT displays faster coarsening kinetics as a consequence of its higher density of dislocations by comparing with the material processed by HPT at ~0.5T_m.
5. High superplastic elongations were consistently observed in the metal processed by HPT at 300 K after testing at temperatures up to 573 K. A maximum elongation of ~850 % was obtained at 523 K using an initial strain rate of 4.5×10^{-3} s^{-1}. However, the overall elongation values decreased for tests performed at $T \geq 623$ K due to the occurrence of significant grain growth at these conditions.
6. The Al alloy processed by HPT at 450 K exhibits enhanced low temperature superplasticity than after HPT at RT. Elongations higher than 900 % were attained after testing at 573 K using strain rates from 3.3×10^{-3} to 1.0×10^{-1} s^{-1}. High strain rate superplasticity was also achieved for an extended range of strain rates at temperatures down to 473 K. This follows from the extremely small grain sizes and the low proportion of substructures with LAGBs in the metal originally processed at 450 K during plastic straining at low homologous temperatures.

7. The metal processed by HPT at ~0.5T_m displays optimum superplastic ductilities when tested at 673 K. A record elongation of ~1880 % for HPT-processed materials was attained at 673 K using a strain rate of 1.5×10^{-2} s^{-1}. At this testing temperature, superplastic elongations were achieved for samples tested using strain rates as high as 3.3×10^{-1} s^{-1} with elongation values of ≥ 980 %. This improved superplasticity originates from both the high diffusion rates at 673 K and the retention of grains with average sizes < 4 μm even after heating for ~10 h.
8. Analysis of the data confirms a stress exponent of n = 2 for the HPT-processed alloy during superplastic flow, except for samples originally processed at 300 K and tested at 623 K which displayed n values of ~1. This suggests that grain boundary sliding is mainly accommodated by dislocation climb and viscous glide may become the rate controlling mechanism in the metal processed by HPT at RT when tested using slow strain rates after sufficient grain growth. The activation energies for grain boundary sliding lie within the range of ~100-118 kJ mol^{-1} and are consistent with the values obtained for the Al-Mg-Sc alloy processed by ECAP.
9. For tests performed at temperatures up to 673 K, the Al-3Mg-0.2Sc alloy processed by HPT at 450 K exhibits notably improved superplastic properties compared with the same metal processed by ECAP. This is demonstrated using miniature specimens with similar dimensions during tensile testing as the material processed by HPT at ~0.5T_m consistently achieved higher elongations to failure and it displayed true superplastic flow in an extended range of strain rates.

Chapter 7 General Discussion on the Mechanical Properties, Thermal Stability and Superplastic Characteristics of Al-Mg-Sc Alloys

This investigation demonstrates that severe plastic deformation through HPT processing promotes further grain refinement in the Al-3Mg-0.2Sc alloy by comparison with ECAP processing. These results follow from the larger strains imposed on the samples during high-pressure torsion and they display good agreement with the grain sizes obtained in earlier studies for various Al-Mg-Sc alloys processed either by HPT [34,48,51–53] or ECAP [20,86,167,182,183,245,277,281–284] using different processing temperatures.

There have been several exploratory studies showing that the saturation grain size achieved through SPD processing increases with increasing deformation temperatures [56,86,136,169,245]. This is consistent with the results obtained for the ECAP-processed alloy; however, almost identical average grain sizes are produced after 10 turns of HPT processing at 300 and 450 K. Nevertheless, it should be noted that, the Al alloy processed by either ECAP or HPT at high temperatures exhibits reasonably uniform arrays of equiaxed grains, whereas the same metal developed more heterogeneous microstructures having ultrafine grains somewhat elongated along the shear direction after processing at 300 K.

It is well established that the microstructural evolution during plastic deformation at high temperatures depends also upon the instantaneous strain rate and these variables are often represented using the Zener-Hollomon parameter, Z, as follows [161]:

$$Z = \dot{\varepsilon} e^{\left(\frac{Q}{RT}\right)} \tag{7.1}$$

where Q is the activation energy and R is the universal gas constant. Accordingly, in order to assess the influence of the nature of the SPD procedure and the processing temperature on the grain sizes obtained through severe plastic deformation, Figure 7.1 shows plots of the steady-state grain size as a function of the Zener-Hollomon parameter, Z, for various Al-Mg alloys processed by either ECAP [20,86,167,182,183,245,277,281–284] or HPT [34,48,51–53] at different deformation conditions.

Similarly to an earlier investigation [56], these calculations were performed using R = 8.314 $J mol^{-1} K^{-1}$ and considering Q as the activation energy for grain boundary diffusion (Q_{gb} = 86 $kJ mol^{-1}$ [237]). The average strain rate during ECAP was estimated for each experimental conditions using an analytical equation [250]. The strain rate during HPT

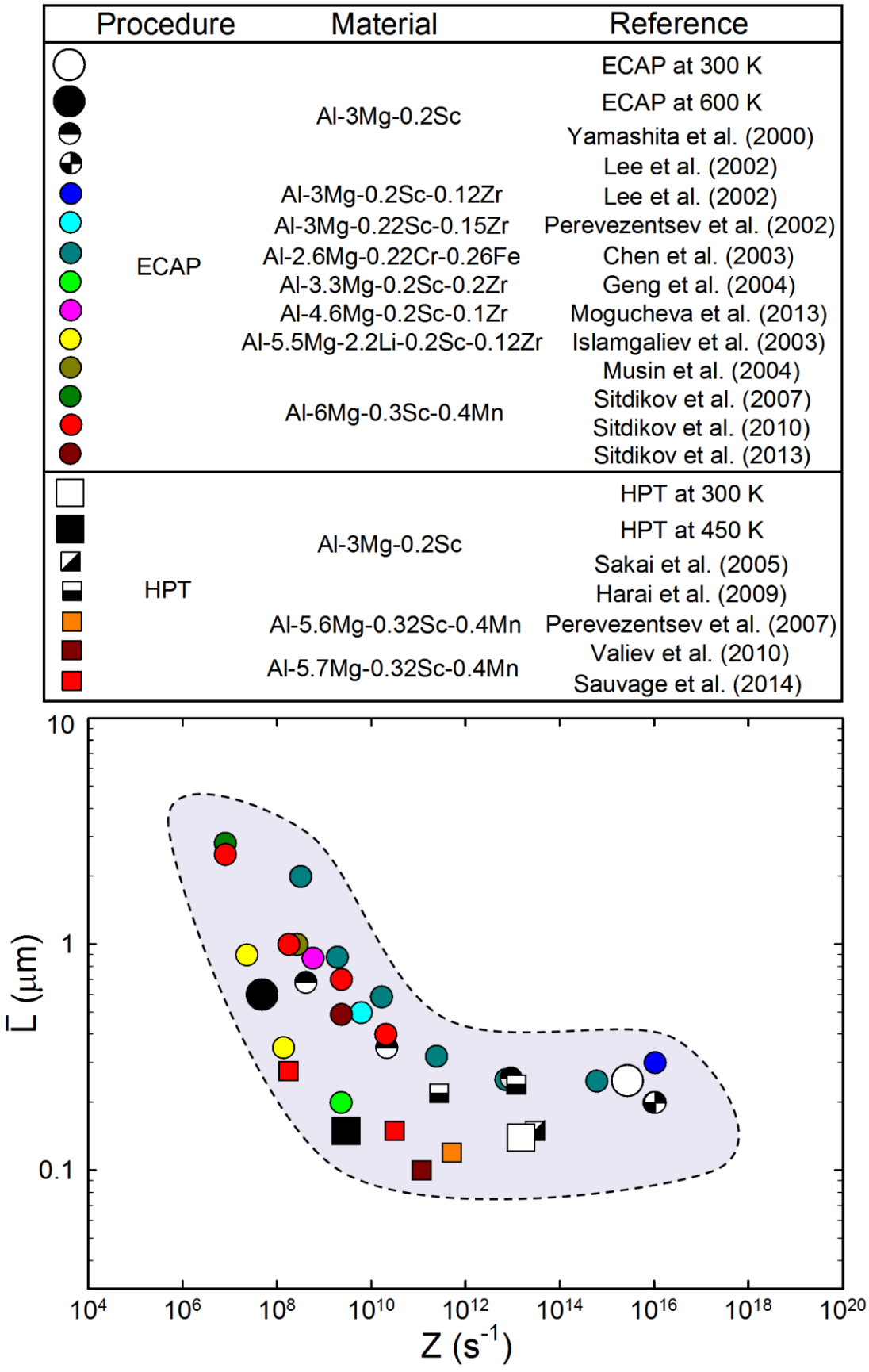

Figure 7.1 – Steady-state grain size after SPD processing as a function of the Zener-Hollomon parameter, *Z*, for the Al-3Mg-0.2Sc alloy processed by either ECAP or HPT at different temperatures: Additional datum points are included for similar Al alloys processed by ECAP [20,86,167,182,183,245,277,281–284] and HPT [34,48,51–53].

processing, $\dot{\varepsilon}_{\mathrm{HPT}}$, was estimated at the radial position from which the grain size measurements were performed using $\dot{\varepsilon}_{\mathrm{HPT}} = \frac{2\pi \dot{N} r}{h\sqrt{3}}$ where $\dot{N}$ is the number of revolutions per second. Also, the temperature rise for discs processed by HPT at RT was estimated using an empirical equation [121] and these values were considered in the calculations of *Z*.

It is clearly observed in Figure 7.1 that the minimum grain size attained in Al-Mg-Sc alloys processed by SPD techniques is strongly influenced by the deformation temperature and strain rates for $Z < \sim 10^{10}$ s^{-1}. At these processing conditions, the restoration mechanisms during SPD processing are thermally activated [56,276] and thereby smaller grains are obtained by decreasing the processing temperature or increasing the deformation rates.

By contrast, the steady-state grain sizes achieved in Al-Mg-Sc alloys after SPD processing appear to be practically independent of the Zener-Hollomon parameter for $Z > \sim 10^{10}$ s^{-1}. These results are fairly consistent with the earlier analyses performed using different Al-Mg alloys [167,285] and it shows that any attempts to decrease the temperature and increase the strain rates during severe plastic deformation are pointless concerning the production of finer grain structures. Also, the restoration mechanism during SPD processing at low homologous temperatures is basically athermal and this ultimately gives rise to grains with high aspect ratios as demonstrated in recent studies [56,276].

Further inspection of Figure 7.1 reveals that, in general, Al-Mg-Sc alloys processed by HPT exhibit notably smaller grain sizes than after ECAP considering equivalent values of *Z*. Nevertheless, the Al-3Mg-0.2Sc alloy processed by HPT using ring samples displays grain sizes ranging from ~0.22 to 0.24 μm which are close to the values obtained after ECAP [53]. This apparently anomalous behaviour is likely associated with a more significant temperature rise in the annular samples that could not be well predicted using the relationship derived for disc-shaped samples [121] and further studies are needed to fully substantiate this effect.

It also important to note that $Z \approx 3 \times 10^9$ s^{-1} for the Al-3Mg-0.2Sc alloy processed by HPT at 450 K and this value appears to be at the transition separating the different restoration mechanisms identified during severe plastic deformation [56]. This is perfectly consistent with the relatively low density of dislocations together with the equiaxed grain structures observed in the HPT-HT alloy which support the occurrence of a thermally driven restoration process at these processing conditions. Therefore, it readily follows from Figure 7.1 that processing Al-Mg-Sc alloys by HPT at $\sim 0.5T_m$ using a rotation rate of ~1 rpm appears to constitute an optimum deformation condition which permits the development of grain structures having the minimum grain size achievable through grain refinement processes assisted by dynamic recovery.

The grain boundary strengthening during plastic deformation at low temperatures may be expressed in terms of the Hall-Petch relationship [61,62] considering the Vickers microhardness, H, and the average grain size, d, as follows [221]:

$$H = H_0 + k_H d^{\left(-\frac{1}{2}\right)} \tag{7.2}$$

where H_0 and k_H are material constants.

In order to examine the range of grain sizes in which this relationship remains accurate and evaluate the effect of the Mg content on the mechanical properties of Al-Mg-Sc alloys, the Vickers microhardness was plotted as a function of the inverse square root of the grain boundary spacing for the Al-3Mg-0.2Sc alloy after either ECAP or HPT at different temperatures and after subsequent annealing. For comparison purposes, additional datum points are included for similar Al-Mg-Sc alloys processed by ECAP [19,47,167,284] or HPT [48,50], as depicted in Figure 7.2.

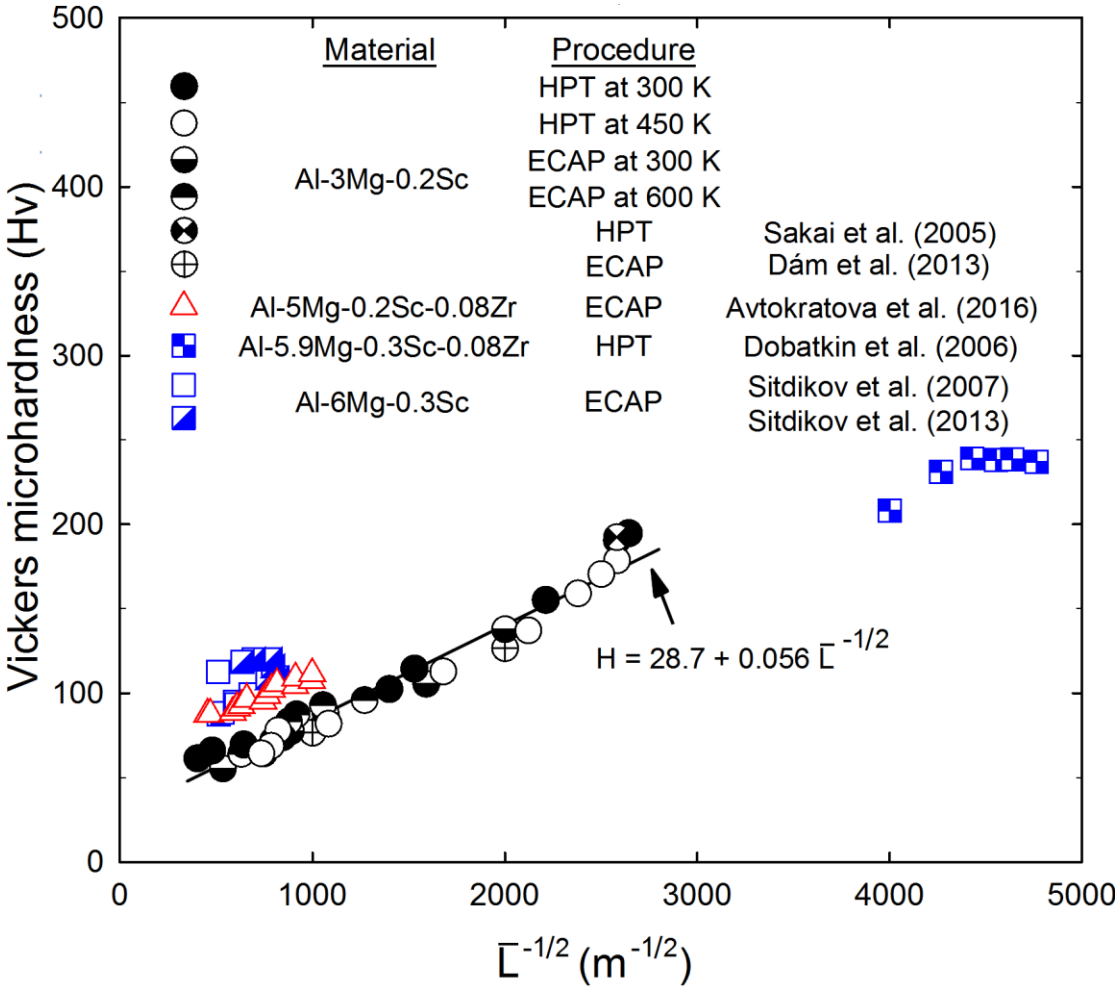

Figure 7.2 - Plot of Vickers microhardness as a function of $\bar{L}^{-1/2}$ for the Al-3Mg-0.2Sc alloy processed by either ECAP or HPT at different temperatures: Additional datum points are included for similar Al-Mg-Sc alloys processed by HPT [48,50] and ECAP [19,47,167,284].

It is apparent from Figure 7.2 that there is a linear relationship between H and $\bar{L}^{-1/2}$ for the Al-3Mg-0.2Sc alloy processed by different SPD conditions in this investigation. In addition, all the experimental datum points referring to Al-Mg-Sc alloys with ~3 % Mg in weight lie close to a single line with $H_0 \approx 28.7$ Hv and $k_H \approx 0.056$ Hv $m^{-1/2}$. However, the Vickers microhardness of the Al alloy immediately after HPT processing at RT is underestimated by the fitted line as a consequence of its higher density of dislocations.

It is clearly noted in Figure 7.2 that the Al-Mg-Sc-Zr alloys with ~5 and 6 % of Mg display increased hardness values compared with the Al-3Mg-0.2Sc alloy having the same average grain sizes. This additional hardening is a direct consequence of solid solution strengthening caused by the addition of Mg in solid solution. Nevertheless, the Hall-Petch relationship remains reasonably accurate for the ECAP-processed material with $\bar{L}^{-1/2} < 1000$ $m^{-1/2}$ and $k_H \approx 0.056$ Hv $m^{-1/2}$ for Al-Mg-Sc alloys with higher Mg contents. Figure 7.2 also reveals an apparent breakdown in the Hall-Petch relationship in Al-Mg-Sc alloys with $\bar{L} <$ ~50 nm. This is consistent with the results presented in Chapter 4 which demonstrated that grain boundary strengthening is accurately predicted using this relationship for Al-Mg-Sc alloys having grain sizes down to ~100 nm.

The breakdown in the Hall-Petch relationship in nanostructured metals is normally attributed to the action of different deformation mechanisms such as dislocation emission at grain boundaries and the increasing contribution of GBS [65]. It is worth noting that Mg segregation is observed in the Al-5.7Mg-0.32Sc alloy processed by HPT [51] at similar conditions as in the experimental datum points displaying no further increase in the hardness values with decreasing grain sizes [50]. In practice, however, these segregations may reduce the boundary energy and ultimately increase the local stress needed for the emission of extrinsic dislocations [224,225]. Therefore, a more comprehensive study is needed to determine whether the breakdown occurs because GBS becomes active at low deformation temperatures or the applied stress is sufficiently high to promote the emission and annihilation of dislocations at grain boundaries in the Al-Mg-Sc alloy with grain sizes <50 nm.

A series of tabulations was prepared to record all results published to date showing true superplastic elongations in Al-Mg-Sc alloys after processing through ECAP, HPT or conventional metal forming techniques. First, it should be noted that there have been numerous studies dedicated to examine the superplasticity in Al-Mg-Sc alloys even without processing using SPD techniques. These results cover several metal-working procedures based primarily on cold or hot rolling and they are summarised in Table 7.1 [46,181,186,187,286–298]. For processing by SPD, results from ECAP [20,42,43,45,48,73,156,159,180,182–184,189,244,281,299–312] and HPT [48,49,52,53] are given in Tables 7.2 and 7.3, respectively.

Table 7.1 - Reports of superplasticity in Al-Mg-Sc alloys without SPD processing.

Alloy or composition (wt.%)	Metal-working procedure	Grain size (μm)	Superplasticity			Reference
			Testing temperature (K)	Strain rate (s^{-1})	Maximum elongation (%)	
Al-4Mg-0.5Sc	Cold-rolling+annealing at 672 K for 1h	~1–2	672	1.0×10^{-2}	>1020[a]	Sawtell *et al.* (1990) [286]
Al-5.76Mg-0.32Sc-0.3Mn	Cold-rolling+annealing at 748 K for 45 min	~1	748	1.4×10^{-2}	1130	Nieh *et al.* (1998) [181]
Al-5Mg-0.2Sc-0.18Mn-0.08Zr	Cold-rolling	~5-15[b]	793	5.6×10^{-2}	2300	Kaibyshev *et al.* (2006) [46]
Al-6.2Mg-0.4Mn-0.25Sc-0.12Zr	Cold-rolling	—	813	1.7×10^{-3}	690	Peng *et al.* (2007) [287]
Al-6.3Zn-2.3Mg-1.5Cu-0.23Sc-0.14Zr	Hot-rolling at 673 K	~10[b]	748	1.9×10^{-2}	650	Kumar *et al.* (2010) [288]
Al-4.5Mg-0.46Mn-0.44Sc	Cold-rolling+annealing at 773 K for 2 h	~11	823	5.0×10^{-3}	1960	Smolej *et al.* (2010) [289]
Al-6.3Zn-2.3Mg-1.5Cu-0.23Sc-0.14Zr	Hot-rolling at 673 K	~2.4	698	$(10^{-1}+10^{-2})$[c]	916	Mukhopadhyay *et al.* (2011) [290]
Al-6.1Mg-0.3Mn-0.25Sc-0.1Zr	Cold-rolling+annealing at 573 K for 1 h	~2.5	798	5.0×10^{-3}	3250	Cao *et al.* (2015) [186]
Al-5.4Zn-1.9Mg-0.32Mn-0.25Cu-0.1Sc-0.1Zr	Cold-rolling + solution treatment at 743 K for 1 h + Ageing at 393 K for 12 h	~3.1	773	5.0×10^{-3}	1050	Duan *et al.* (2015) [292]
Al-6.1Mg-0.3Mn-0.25Sc-0.1Zr	Free Forging	~3.7	748	1.0×10^{-3}	1590	Duan *et al.* (2015) [187]
Al-5.4Zn-1.9Mg-0.33Mn-0.32Cu-0.25Sc-0.1Zr	Cold-rolling + solution treatment at 743 K for 1 h + ageing at 393 K for 12 h	~2.8	773	1.0×10^{-2}	1520	Duan *et al.* (2015) [291]
Al-4.2Mg-3.7Zn-0.7Cu-0.2Zr-0.15Sc	Cold-rolling+annealing at 693 K	~2	693	2.0×10^{-3}	800	Kotov *et al.* (2016) [293]
Al-Zn-Mg-0.2Zr-0.1Sc-Fe-Ni[d]	Cold-rolling+annealing at 753 K for 20 min	~2.5	753	1.0×10^{-2}	915	Mikhaylovskaya *et al.* (2016) [294]
Al-5.8Mg-0.40Mn-0.25Sc-0.10Zr	Cold-rolling+annealing at 672 K for 1h	~5[b]	773	1.67×10^{-3}	740	Sun *et al.* (2016) [295]
Al-6.1Mg-0.3Mn-0.25Sc-0.1Zr	Asymmetrical rolling + annealing at 573 K for 1 h	~1.5	773	5.0×10^{-2}	3200	Xu *et al.* (2016) [296]
Al-5.4Zn-2Mg-0.35Cu-0.3Mn-0.25Sc-0.1Zr	Cold-rolling	~3	773	1.0×10^{-2}	540	Xiang *et al.* (2016) [297]
Al-5.8Mg-0.4Mn-0.2Sc-0.1Zr (Al1570c)	Cold-rolling	~3.8[b]	773	6.7×10^{-3}	740	Li *et al.* (2017) [298]

[a] Maximum possible elongation detected by the tensile testing facility used in the referred study.
[b] Grain size in the gauge area after tensile testing.
[c] Tensile testing conducted at 1.0×10^{-1} s^{-1} up to a true strain of 0.73 and at 1.0×10^{-2} s^{-1} afterwards.
[d] The Mg, Zn, Ni and Fe contents in this alloy were not reported.

Table 7.2 - Reports of superplasticity in Al-Mg-Sc alloys after ECAP.

Alloy or composition (wt.%)	ECAP processing				Procedure after ECAP	Grain size (μm)	Superplasticity			Reference
	ϕ (°)	*T* (K)	ECAP route	Nº of passes			Testing temperature (K)	Strain rate (s^{-1})	Maximum elongation (%)	
Al-3Mg-0.2Sc	90	RT	B_c	8	—	~0.2	673	3.3×10^{-2}	1030	Komura *et al.* (1998) [180][a]
Al-3Mg-0.2Sc	90	RT	B_c	8	—	~0.2	673	3.3×10^{-2}	2280	Horita *et al.* (2000) [73]
Al-3Mg-0.2Sc	90	RT	B_c	8	—	~0.2	673	3.3×10^{-2}	950	Komura *et al.* (2000) [159][b]
Al-3Mg-0.2Sc	90	RT	B_c	8	Cold-rolling	~0.2[c]	673	3.3×10^{-2}	1860	Akamatsu *et al.* (2001) [299]
Al-1Mg-0.2Sc	90	RT	B_c	8	—	~0.36	673	1.0×10^{-3}	580	Furukawa *et al.* (2001) [244]
Al-3Mg-0.2Sc	90	RT	B_c	8	—	~0.2	723	3.3×10^{-3}	2580	Komura *et al.* (2001) [43]
Al-3Mg-0.2Sc	90	RT	A	8	—	—	673	3.3×10^{-2}	1170	Komura *et al.* (2001) [156]
Al-3Mg-0.2Sc	90	RT	C	8	—	—	673	3.3×10^{-2}	1370	Komura *et al.* (2001) [156]
Al-3Mg-0.2Sc-0.12Zr	90	RT	B_c	6	—	~0.3	773	1.0×10^{-2}	1680	Lee *et al.* (2002) [20]
Al-4.5Mg-0.22Sc-0.15Zr	90	448	B_c	6	—	~0.1	723	3.3×10^{-2}	2250	Perevezentsev *et al.* (2002) [281]
Al-3Mg-0.2Sc	90	RT	B_c	8	—	~0.2	523	3.3×10^{-4}	640	Ota *et al.* (2002) [305]
Al-1.5Mg-0.22Sc-0.15Zr	90	448	B_c	6–8[d]	—	~0.1	723	1.0×10^{-1}	1590	Perevezentsev *et al.* (2002) [300]
Al-5.5Mg-2.2Li-0.2Sc-0.12Zr (Al1421)	90	643	B_c	12	—	~0.3-0.4	673	1.0×10^{-1}	1500	Islamgaliev *et al.* (2003) [182]
Al-5.8Mg-0.3Mn-0.32Sc-0.2Si-0.1Fe	90	598	B_c	16	—	~1[e]	723	5.6×10^{-2}	2000	Musin *et al.* (2004) [183]
Al-4.5Mg-0.22Sc-0.15Zr	90	473	B_c	6	—	~0.5	723	1	880	Perevezentsev *et al.* (2004) [301]
Al-1Mg-0.2Sc	90	RT	B_{cz}[f]	4	—	~0.5	673	1.0×10^{-3}	440	Kamachi *et al.* (2004) [302]
Al-3.2Mg-0.13Sc	90	473	B_c	4	Cold-rolling	~0.2-0.4[c]	723	5.0×10^{-3}	810	Park *et al.* (2004) [303]
Al-3Mg-0.2Sc	90	RT	B_c	8	—	~0.2	673	3.3×10^{-2}	580	Sakai *et al.* (2004) [304] (2005) [48][g]
Al-4.1Mg-2Li-0.16Sc-0.08Zr (Al1421)	90	673	B_{cz}[f]	16	—	~2.6	723	1.4×10^{-2}	3000	Kaibyshev *et al.* (2005) [306]
Al-1.5Mg-0.2Sc-0.18Zr	90	423	B_c	6	—	~1.4-1.6[h]	710	1.0×10^{-2}	>900[i]	Málek *et al.* (2007) [307]
Al-4.5Mg-0.2Sc-0.2Zr	90	523	B_c	6	—	~0.3-1	773	4.5×10^{-2}	2130	Turba *et al.* (2007) [308]
Al-5Mg-0.18Mn-0.2Sc-0.08Zr (Al1570c)	90	598	B_{cz}[f]	10	—	~1	723	5.6×10^{-2}	4100	Avtokratova *et al.* (2012) [45]

Table 7.2 - Reports of superplasticity in Al-Mg-Sc alloys after ECAP. (continued)

Alloy or composition (wt.%)	ECAP processing				Procedure after ECAP	Grain size (μm)	Superplasticity			Reference
	ϕ (°)	*T* (K)	ECAP route	Nº of passes			Testing temperature (K)	Strain rate (s^{-1})	Maximum elongation (%)	
Al-5Mg-0.18Mn-0.2Sc-0.08Zr (Al1570c)	90	598	B_{cz} [f]	8	—	~1	748	5.6×10^{-2}	3300	Avtokratova *et al.* (2012) [184]
Al-5.4Mg-0.2Sc-0.07Zr (Al1570c)	90	573	B_{cz} [f]	12	—	~0.6	723	1.4×10^{-1}	2400	Kaibyshev *et al.* (2013) [309]
Al-5.8Mg-0.4Mn-0.32Sc-0.1Zr (Al1570c)	90	598	B_{cz} [f]	8	Warm-rolling at 598 K	~1	723	1.4×10^{-1}	2330	Avtokratova *et al.* (2015) [189]
Al-6Mg-0.5Mn-0.2Sc-0.07Zr (Al1570)	90	573	B_{cz} [f]	12	Warm-rolling at 573 K	~0.3-0.6	723	1.4×10^{-1}	1970	Dubyna *et al.* (2016) [310]
Al-4.6Mg-0.35Mn-0.2Sc-0.09Zr (Al5024)	90	573	B_{cz} [f]	12	Cold-rolling	~0.3-1.8	723	1.4×10^{-1}	1440	Mogucheva *et al.* (2016) [311]
Al-4.6Mg-0.35Mn-0.2Sc-0.09Zr (Al5024)	90	573	B_{cz} [f]	12	—	~0.7	548	5.6×10^{-3}	1200	Yuzbekova *et al.* (2016) [312]
Al-4.6Mg-0.35Mn-0.2Sc-0.09Zr (Al5024)	90	573	B_{cz} [f]	12	—	~0.7	723	5.6×10^{-1}	3300	Yuzbekova *et al.* (2016) [42]

[a] First report of superplasticity in Al-Mg-Sc alloys after SPD.
[b] Elongation after solution treatment at 873 K and further ECAP processing. At higher solution treatment temperatures, more particles are precipitated and the tensile elongations are superior.
[c] Grain size measured after ECAP.
[d] The number of passes in which the maximum elongation was attained was not specified. Nevertheless, it was reported that ECAP processing was conducted for the total of 6 to 8 passes.
[e] Grain size measured after annealing at 443 K for 4 h.
[f] ECAP was conducted using plate samples.
[g] Tensile testing conducted in miniature tensile specimens.
[h] Grain size measured after annealing at 710 K for 1 h.
[i] Maximum possible elongation detected by the tensile testing facility used in the referred study.

Table 7.3 - Reports of superplasticity in Al-Mg-Sc alloys after HPT.

Alloy or composition (wt.%)	HPT processing				Grain size (μm)	Superplasticity				Reference
	Geometry of the HPT sample	P_{nom} (GPa)	*T* (K)	Nº of turns		Testing temperature (K)	Strain rate (s^{-1})	Maximum elongation (%)	Sample size (mm)	
Al-3Mg-0.2Sc	Disc (10 × 0.8)	6	RT	5	~0.15	673	3.3×10^{-2}	500	1×1×0.6	Sakai *et al.* (2005) [48]
Al-5.6Mg-0.4Mn-0.32Sc	Disc (20 × 1.5)	6	RT	5	~0.12	673	1.0×10^{-2}	1460	2.8	Perevezentsev *et al.* (2007) [52]
Al-3Mg-0.2Sc	Bulk sample (10 × 8.6)	1	RT	2	~0.13	573	3.3×10^{-3}	1600	1×1×1	Horita and Langdon (2008) [49]
Al-3Mg-0.2Sc	Ring sample (40×3×0.8)	1.25	RT	1	~0.22	573	3.3×10^{-3}	1510	1×1×0.6	Harai *et al.* (2009) [53]

[a] Diameter × thickness for the discs, diameter × height for the bulk samples and outer diameter × width × thickness for the rings.
[b] Gauge length or gauge length × gauge width × thickness of the tensile specimens.
[c] Grain size in the gauge area after tensile testing.

It is apparent in Table 7.1 that grain sizes within the range of ~1-10 μm were produced after processing through conventional metal-working procedures. The Al-Mg-Sc alloys display maximum elongations as high as ~3250 % after tensile testing using specimens with regular dimensions and they were usually achieved after deformation at $T \geq 748$ K using strain rates of ~10^{-3}-10^{-2} s^{-1}.

In Table 7.2, the materials were mostly processed either at RT or at ~500-600 K, all ECAP dies had channel angles of 90° so that an equivalent strain of ~1 was introduced on each pass [81], and the billets were basically processed using route B_c or its variation for plate samples (route B_{cz}). After ECAP processing, the grains sizes are generally in the submicrometer range, all samples exhibit excellent superplasticity with elongations up to and exceeding 2000 % and tests performed at ~650-750 K with $10^{-2} \leq \dot{\varepsilon} \leq 10^{-1}$ s^{-1} appear to be the optimum deformation conditions for superplastic flow.

Table 7.3 shows that there are only few and limited reports investigating the superplastic behaviour of Al-Mg-Sc alloys processed by HPT. All samples were processed at room temperature using nominal pressures ranging from ~1-6 GPa and they had very distinct geometries due to the use of variations of the HPT technique. Typically, the grain sizes in the HPT-processed metals are in the range of ~0.12-0.22 μm and tensile testing was performed using miniature specimens with small thicknesses due to the inherent limitations on the size of the HPT sample. Nevertheless, HPT processing produces good superplastic elongations up to >1000 %.

To check the applicability of Eq. 2.2 to the many superplastic results now available for the various Al-Mg-Sc alloys, similar analyses were conducted using the experimental data presented in Tables 7.1 to 7.3. The temperature and grain size compensated strain rate was plotted against the normalized stress using the same procedure described in Chapters 5 and 6. These plots are shown in Figure 7.3 for results obtained after (a) conventional metal-working procedures [46,181,186,187,286–289,291–298], (b) ECAP [20,37,42,43,48,73,182,183,244,299–304,306,308–310] or (c) HPT [48,49,52,53]. These analyses were performed using basic parameters for pure Al where $D_{o,gb} = 1.86 \times 10^{-4}$ m^2 s^{-1}, $Q_{gb} = 86$ kJ mol^{-1}, $\mathbf{b} = 2.86 \times 10^{-10}$ m and G (MPa) = $(3.022 \times 10^4) - 16T$ [237]. In each plot, the line labelled $\dot{\varepsilon}_{sp}$ corresponds to the theoretical prediction of the rate of superplasticity in conventional materials as calculated using Eq. 2.2 with $A = 10$ [38]. For comparison purposes, the experimental data obtained in this investigation for the Al-3Mg-0.2Sc alloy processed by either ECAP or HPT is also included in these plots as denoted using circles coloured in either black or white for samples originally processed at 300 K or at a high homologous temperature, respectively.

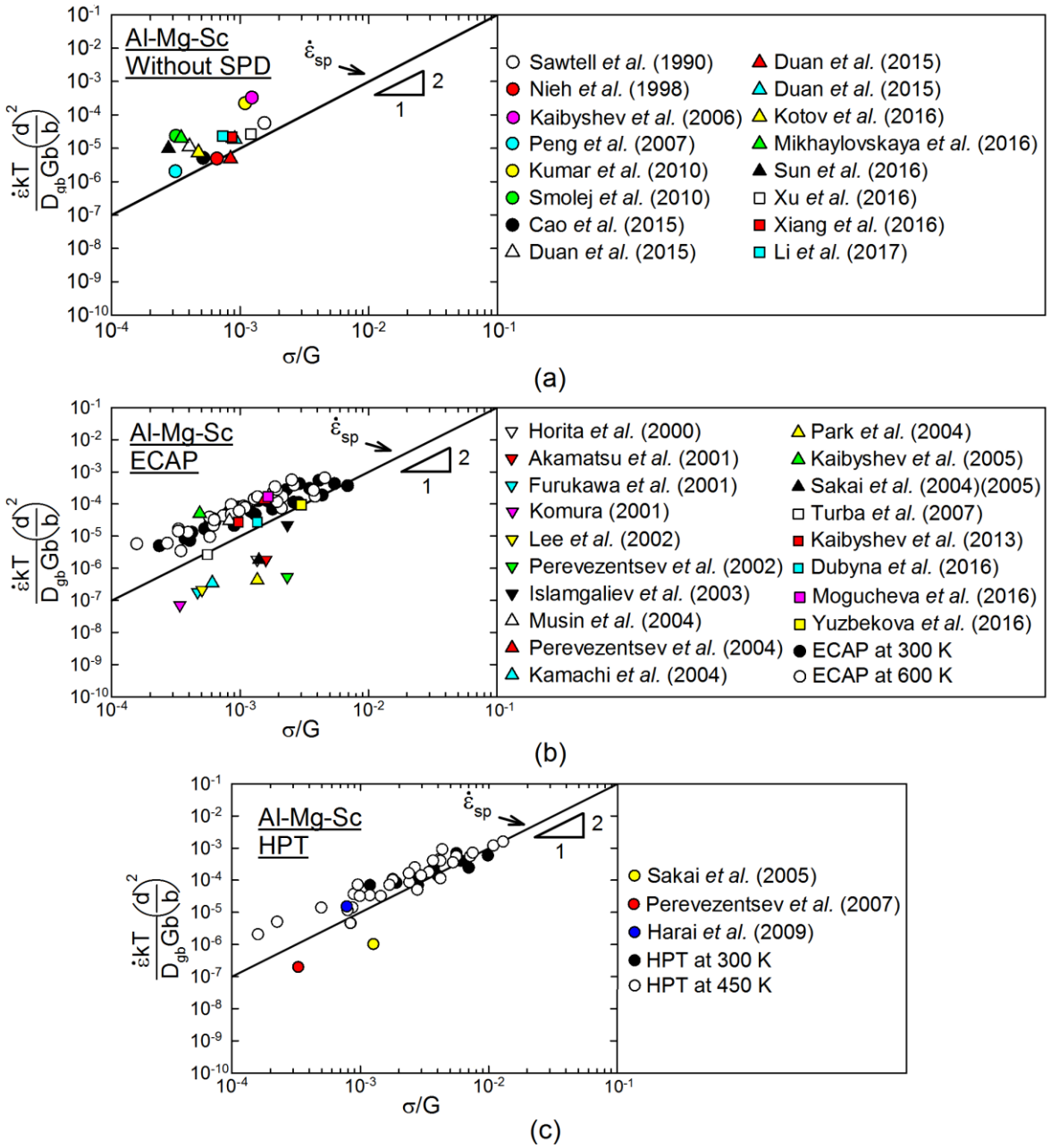

Figure 7.3 - Temperature and grain size compensated strain rate as a function of normalized stress for various superplastic Al-Mg-Sc alloys processed by (a) conventional metal-working procedures [46,181,186,187,286–289,291–298], (b) ECAP [20,37,42,43,48,73,182,183,244,299–304,306,308–310] or (c) HPT [48,49,52,53]: the solid line shows the theoretical prediction for superplastic flow in conventional metals not processed by SPD.

Inspection of Figure 7.3 reveals that there is a general consistency with the predicted stress exponent of $n = 2$. Although these examinations are based on more than forty different publications reporting data obtained in laboratories in many different countries, all results tend to lie close to the predicted line for conventional superplasticity and this suggests that dislocation climb is the rate controlling mechanism during GBS at these testing conditions.

It follows from Figure 7.3 that the experimental datum points corresponding to samples processed by either ECAP or HPT at RT generally lie below the predicted line for superplastic flow. This may be explained by the unstable grain structures developed in the Al-Mg-Sc alloys during SPD processing at ~300 K. For samples processed at RT, the grain sizes were taken from measurements performed immediately after SPD due to limited availability of experimental data. Nevertheless, the submicrometre grains exhibit significant coarsening during deformation at high temperatures and this leads to an underestimation of the values of the strain rate in Figure 7.3. By contrast, the results obtained after SPD at high temperatures or after conventional thermo-mechanical processing are more consistent with the theoretical predictions as these materials display less pronounced grain growth during deformation at superplastic conditions.

In this study however, the temperature and grain size compensated strain rates were calculated using both the maximum true stress and the spatial grain size measured along the gauge section of the fractured specimens. As a result, even though grain coarsening always occurs during tensile testing at elevated temperatures, this procedure permits a more accurate assessment of the rate controlling mechanism during superplasticity, as clearly visible from the experimental data depicted in Figures 7.3 (b) and (c).

The data summarised in Tables 7.1 to 7.3 represent three different processing methods. To compare the superplastic behaviour in Al-Mg-Sc alloys after processing using these different fabrication procedures, Figure 7.4 shows plots of elongation to failure vs temperature for the results corresponding to the highest reported elongations for each separate processing technique. Additional datum points are included for the maximum superplastic elongations attained in this investigation for samples of the Al-3Mg-0.2Sc alloy processed either by ECAP or HPT at different temperatures.

It is readily apparent in Figure 7.4 that the elongations tend to increase with increasing temperatures. Furthermore, the Al alloys with larger grain sizes immediately after processing appear to display optimum superplastic elongations at higher temperatures. This behaviour is consistent with the results documented in this study and it directly follows the faster coarsening kinetics observed in microstructures having smaller grains and thereby higher driving pressures for grain boundary migration.

Figure 7.4 reveals that the highest elongation reported to date for Al-Mg-Sc alloys was achieved after ECAP processing at 723 K [45]. In this investigation, the Al-3Mg-0.2Sc alloy was processed by ECAP using identical conditions as documented for the material displaying a record elongation of ~4100 %. Nevertheless, tensile testing was conducted using miniature tensile specimens with thicknesses of ~0.6 mm and a maximum elongation of only

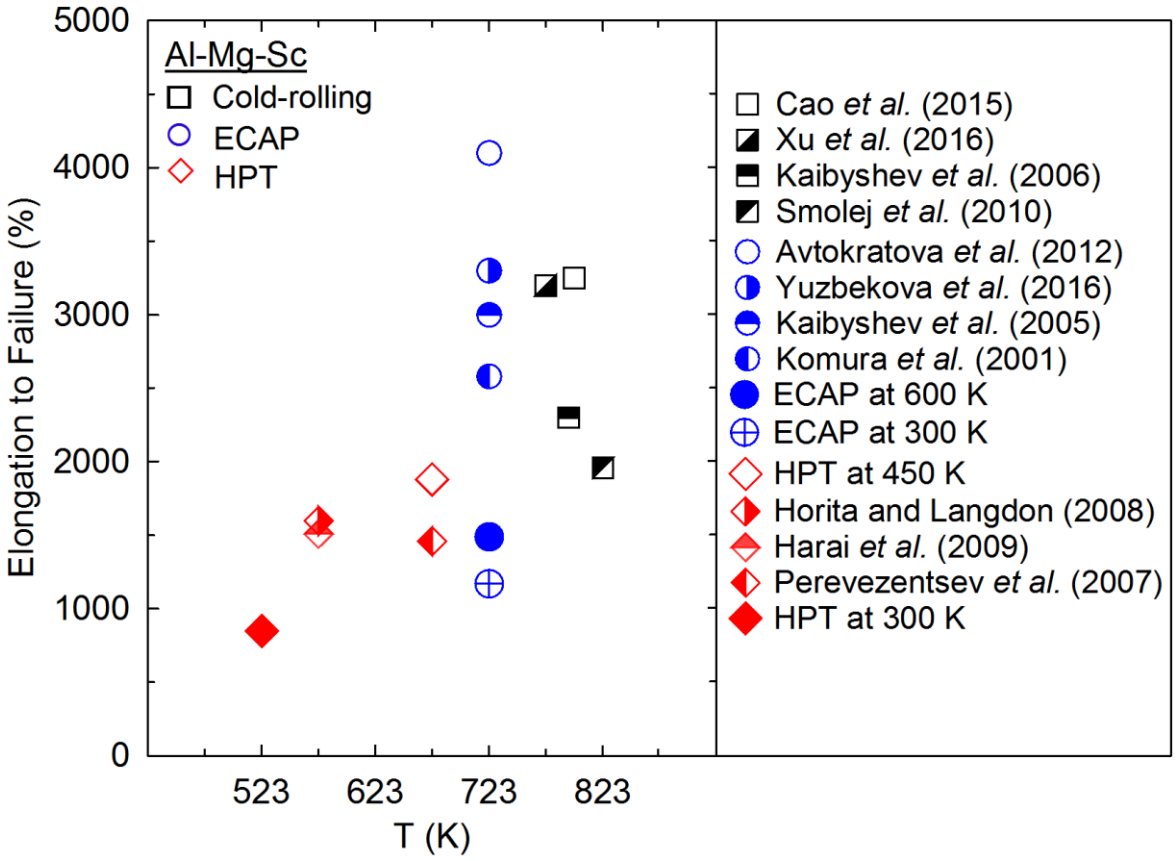

Figure 7.4 – Maximum elongation to failure vs temperature for various superplastic Al-Mg-Sc alloys from different processing routes: Cold-rolling [46,186,289,296], ECAP [42,43,45,306] and HPT [48,49,52,53].

~1490 % was achieved after testing at 723 K. Although the measured elongations in tensile testing tend to increase with decreasing gauge length [142], the exceptionally reduced thicknesses in miniature specimens lead to easy and premature failure. For this reason, the higher elongations achieved when processing by cold rolling or ECAP in Figure 7.4 shall not be taken as evidence of superior superplasticity by comparison with the HPT-processed samples.

In order to permit a more reliable comparison of the superplastic properties after severe plastic deformation, Figure 7.5 shows plots of (a) maximum elongation and (b) maximum strain rates displaying true superplastic flow vs temperature for the Al-3Mg-0.2Sc alloy processed through either ECAP or HPT at different temperatures and further tested in tension using miniature specimens having the same dimensions.

The results in Figure 7.5 (a) demonstrate that the elongations tend to increase with increasing temperatures, except for the HPT-RT metal which displayed a maximum elongation of ~850 % when tested at 523 K. Higher maximum elongations are attained in the HPT-processed samples for tests performed at temperatures up to 573 K. For $T \geq 623$ K, there is a notable increase in the elongations to failure for the ECAP-processed samples, but

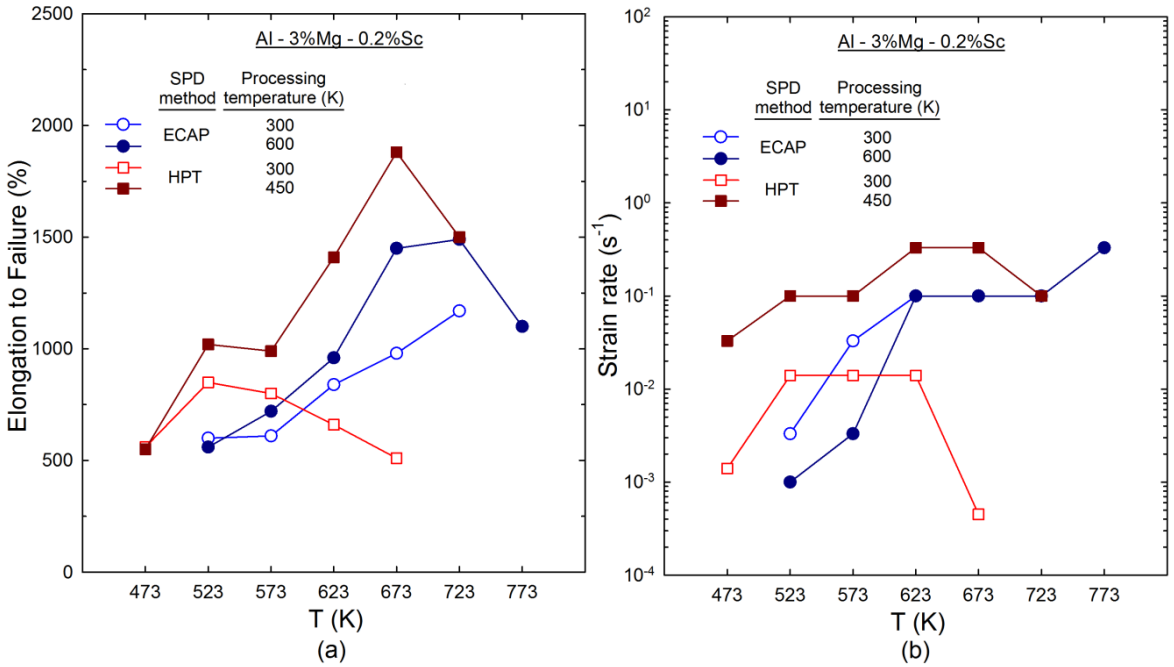

Figure 7.5 – Plots of (a) maximum superplastic elongation and (b) maximum strain rates displaying true superplastic flow as a function of testing temperature for the Al-3Mg-0.2Sc alloy processed through either HPT or ECAP at different temperatures and further pulled to failure using miniature tensile specimens.

nevertheless, the HPT-HT alloy continues exhibiting superior superplastic ductilities and achieves a maximum elongation of 1880 % after testing at 673 K.

Figure 7.5 (b) shows that the Al-3Mg-0.2Sc alloy processed by HPT at ~0.5T_m displays true superplastic elongations at faster deformation rates compared with the same metal processed by HPT at 300 K or ECAP for equivalent testing temperatures. In general, the superplastic regime extends to faster strain rates with increasing temperatures but there appears to exist an optimum temperature from which the maximum strain rates attained under superplastic conditions start to decrease. This transition temperature and the strain rate magnitude clearly depend on the nature of the SPD technique and the processing temperature as evident from the narrower range of temperatures displaying HSRS for the HPT-RT alloy.

This investigation consistently reveals that the Al-3Mg-0.2Sc alloy processed through 10 revolutions of HPT at 450 K exhibits remarkably superior elongations among all SPD processing conditions. To summarise the main microstructural aspects which justify this enhanced superplastic behaviour, Figure 7.6 shows plots of (a) average grain boundary spacing and (b) fraction of LAGBs as a function of annealing temperature for the metal processed by either HPT or ECAP at high temperatures and subsequently annealed for 1 h at temperatures up to 773 K.

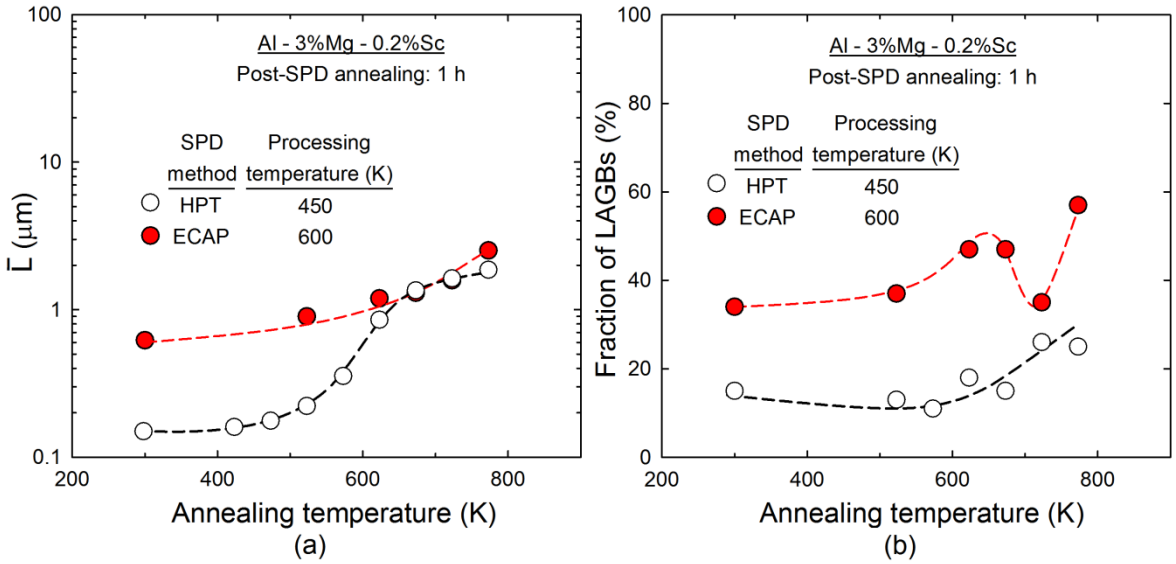

Figure 7.6 – Plots of (a) average grain boundary spacing and (b) fraction of LAGBs as a function of annealing temperature for the Al-3Mg-0.2Sc alloy processed through either HPT at 450 K or ECAP at 600 K and annealed for 1 h at temperatures up to 773 K.

First, it is important to note that the results in Figure 7.6 correspond to the processing conditions which ultimately displayed the highest elongations after either ECAP or HPT. These plots demonstrate that the HPT-HT alloy exhibits extremely small grain sizes and a low fraction of LAGBs immediately after processing. By contrast, although the ECAP-HT metal also displays an UFG microstructure after processing, both the average grain boundary spacing and the fraction of substructures with LAGBS are notably higher than after HPT at 450 K.

After annealing for 1 h at temperatures up to 573 K, the grain structures of the HPT-HT alloy have an average size of < 0.4 μm and the proportion of HAGBs achieves a maximum of ~90 %. Conversely, there is an apparent increase in the fraction of LAGBs for the ECAP-processed metal and it displays grain sizes at least twice higher the HPT-HT metal. These results are consistent with the superior low temperature superplasticity observed in the Al-3Mg-0.2Sc alloy after HPT at $\sim 0.5T_m$ as this material exhibits an exceptionally high density of HAGBs available for undergoing GBS.

It is apparent in Figure 7.6 (a) that the HPT-HT material displays substantial grain coarsening at $T \geq 623$ K. As result, this alloy has virtually the same grain sizes as the ECAP-HT samples after annealing for 1 h at 673 K. Nevertheless, the fraction of LAGBs in the HPT-HT alloy does not exceed 15 %, whereas it is > 50 % for the ECAP-processed alloy. For this reason, the accommodation of GBS occurs at faster rates for the material originally processed by HPT at 450 K which thereby exhibits higher superplastic ductilities compared with the ECAP-HT samples when tested at 673 K. It should be further noted that these materials achieve comparable elongations for test performed at 723 K and this is consistent with their similar grain sizes and proportions of LAGBs after annealing.

From an economic perspective, the current findings raise the possibility of fabricating complex products in the superplastic forming industry at faster production rates using Al-Mg-Sc alloys processed by either ECAP or HPT. Furthermore, as superplastic elongations are consistently observed after deformation at lower temperatures than for alloys processed through conventional metal-working procedures, this may permit a significant reduction in energy consumption and thereby decrease the manufacturing costs.

It is worth noting that the HPT-processed alloy exhibits high superplastic ductilities when tested at 473 K and the fractured samples continue having average grain sizes below ~0.5 μm. This demonstrates that by combining HPT processing with superplastic forming it is possible to overcome the difficulties associated with the low ductility of UFG metals at low deformation temperatures and fabricate high value products which preserve the refinement benefits attained through severe plastic deformation.

From this comprehensive analysis, it is therefore reasonable to conclude that the microstructural stability in Al-Mg-Sc alloys is consistently improved by conducting SPD processing at elevated temperatures. This effect is more prominent for the material processed through 10 turns of HPT at 450 K which, as a result, achieved superior superplastic elongations among all processing conditions.

Chapter 8 Conclusions and Future Work

8.1 Conclusions

An Al-3% Mg-0.2% Sc alloy with an average grain size of ~300 μm was processed through 10 turns of HPT at 300 and 450 K, 8 passes of ECAP at 300 K and 10 passes of ECAP at 600 K to produce grain sizes in the range of ~140-600 nm. Thereafter, samples were annealed for 1 h at temperatures up to 773 K or mechanically tested at different temperatures over a very wide range of strain rates from 3.3×10^{-4} to 4.0×10^{3} s^{-1}.

Dynamic strain ageing occurred in the Al alloy with and without processing by ECAP when tested at ~300 K using strain rates lower than ~10^{-1} s^{-1}. The results suggest that grain refinement promotes a change in the flow mechanism from dislocation climb to grain boundary sliding (GBS) for samples deformed at 673 K. For tests performed at dynamic conditions, both the coarse and UFG alloy exhibit microstructures with strong fibre-type textures and grain boundary strengthening is consistent with the Hall-Petch predictions. This indicates that intragranular dislocation slip remains active even at extremely high strain rates.

Excellent mechanical strength was attained after SPD processing. The metal processed by ECAP at RT displayed flow stresses of > 450 MPa when tested in tension at ~300 K under quasi-static conditions. After 10 turns of HPT processing, the same metal exhibited average hardness values within the interval of ~180-200 Hv. These results are consistent with the Hall-Petch relationship and confirm that deformation at ambient temperature is primarily controlled by intragranular slip for Al-Mg-Sc alloys down to grain sizes of ~100 nm.

The material processed by ECAP at RT exhibited higher microhardness values and smaller grain sizes (~0.25 μm) than after ECAP at 600 K (~0.60 μm). This processing condition also led to the development of elongated grain structures, whereas equiaxed grains were obtained after ECAP at a high temperature. This follows from the increasing contribution of dynamic recovery for samples processed by ECAP at 600 K which promotes annihilation and rearrangement of dislocations into low energy configuration and increases the steady-state grain size achieved after processing.

Both the driving and restraining pressures for grain boundary migration were calculated after ECAP at different temperatures and subsequent annealing. The results revealed that the Al alloy processed by ECAP at 600 K exhibited lower driving pressures which led to superior thermal stability compared with the material processed at 300 K. For this reason, after annealing at $T \geq 623$ K, it exhibited smaller grain sizes and higher hardness values than the metal processed by ECAP at 300 K and heat treated at comparable conditions.

True superplastic elongations were achieved in specimens of the ECAP-processed metal pulled to failure at temperatures from 523 to 773 K. The alloy processed by ECAP at 600 K showed higher elongations at $T \geq 673$ K due to its superior microstructural stability compared with the metal processed by ECAP at RT. A maximum elongation of ~1490 % was attained after testing at 723 K using a strain rate of 3.3×10^{-3} s^{-1}. Nevertheless, for tests performed at 523 and 573 K, superplasticity was attained at faster strain rates after ECAP at 300 K as follows from the less pronounced grain growth at these conditions.

The HPT-processed discs exhibited grain sizes of ~0.15 μm and average hardness values as high as ~190 Hv. By contrast, the material processed by ECAP displayed lower Vickers microhardness and exhibited areas not fully refined. Also, the fraction of LAGBs do not exceed 80 % for samples processed by 10 turns of HPT, whilst it is ~50 % after ECAP at RT. These results are associated with the larger strains imposed on HPT-processed samples which promotes further hardening and grain refinement in the Al-3Mg-0.2Sc alloy than ECAP.

The Al alloy processed through 10 turns of HPT at 450 K exhibited a lower average microhardness (~180 Hv), but faster hardening kinetics than after HPT at 300 K. This processing condition generated more uniform microstructures with lower density of dislocations. These characteristics are attributed to a more significant contribution of dynamic recovery during HPT processing at high temperatures. As a result, this alloy exhibited a remarkably improved thermal stability and it retained grain structures with an average size below 2 μm after annealing for 1 h at 773 K.

The Al-3Mg-0.2Sc alloy processed by ECAP at 300 K and HPT at either 300 or 450 K undergoes abnormal grain coarsening leading to the formation of duplex structures after annealing at selected conditions. This phenomenon occurs at lower temperatures for the HPT-processed samples (623 and 673 K) due to their finer grain structures compared with the ECAP-processed alloy. Nevertheless, the metal processed by HPT at 450 K displays slower coarsening kinetics than after HPT at 300 K because of its more homogeneous microstructure and lower dislocation density.

High strain rate superplasticity was achieved in samples processed by HPT at 300 K when tested at temperatures up to 623 K. A maximum elongation of ~850 % was obtained at 523 K using a strain rate of 4.5×10^{-3} s^{-1}. However, the overall superplastic elongations decreased at $T \geq 623$ K due to the occurrence of sizable grain growth at these conditions. After processing through 10 turns of HPT at 450 K, the Al-3Mg-0.2Sc alloy displayed improved low temperature superplasticity than after HPT at 300 K and it achieved elongations as high as ~1020 % after testing at 523 K with an initial strain rate of 3.3×10^{-3} s^{-1}.

The Al alloy processed by HPT at 450 K achieved optimum superplastic properties when tested at 673 K. Elongations to failure of > 1100 % were attained after testing at 673 K within the strain rate range from 3.3×10^{-4} to 1.0×10^{-1} s^{-1}. A record elongation of ~1880 % for HPT-processed metals was obtained at this temperature using a strain rate of 1.5×10^{-2} s^{-1}. These results follow from the enhancement of the thermal stability in the Al-Mg-Sc alloys after high-pressure torsion at 450 K which permitted the retention of grains with average sizes below 4 μm even after tensile testing at 673 K for ~10 h.

This investigation confirmed that the use of miniature specimens leads to significantly lower elongations than in conventional ECAP samples for tensile tests performed at superplastic conditions. After testing at $T \geq 623$ K, elongations of > 2000 % were reported for regular specimens of Al-Mg-Sc alloys processed by ECAP using the same conditions as in this study. By contrast, the elongation values did not exceed 1500 % for tests conducted on miniature specimens of the ECAP-processed alloy. This originates from the exceptionally reduced thicknesses of ~0.6 mm in miniature samples which leads to easy and premature failure during tensile testing.

The Al-3Mg-0.2Sc alloy processed through 10 turns of HPT at 450 K exhibits remarkably superior superplastic ductilities among all SPD processing conditions. This alloy consistently achieved higher elongations to failure and it displayed true superplastic flow in a larger range of strain rates and temperatures. This excellent superplastic behaviour is attributed to the presence of extremely small grains having a low fraction of substructures in the material processed by HPT at 450 K during deformation at high temperatures.

Analysis of the data confirms a stress exponent of $n = 2$ for samples of the SPD-processed metal having superplastic elongations, as predicted using the theoretical model for superplastic flow in conventional alloys, and all experimental results are reasonably consistent with this model within one order of magnitude of strain rate. This indicates that grain boundary sliding is mainly accommodated by dislocation climb in Al-Mg-Sc alloys. The calculated activation energies for superplasticity lie within the range of ~99-125 kJ mol^{-1} for all processing temperatures.

8.2 Recommendations for Future Work

This doctoral thesis revealed that the microstructural stability in an Al-3Mg-0.2Sc alloy is significantly enhanced by conducting HPT processing at 450 K. It has been demonstrated in earlier studies that the sample temperature increases with increasing torsional straining during HPT processing. This is more significant for tests conducted using faster rotation rates and discs with larger diameters. Thus, it is conceivable that the same benefits attained in this study could be reproduced by altering the processing conditions to permit a temperature rise comparable to ~150 K without using heating elements.

It is also revealed that the solution-treated alloy processed by HPT at 300 K displays significant grain coarsening during annealing at $T \geq 623$ K and this may be associated with recrystallization preceding precipitation of Al_3Sc dispersoids. Accordingly, both the thermal stability and the superplastic behaviour of this alloy could be improved by ageing the samples prior to HPT processing to promote an effective boundary pinning in the early stages of annealing. Furthermore, ageing treatment at low temperatures for extended periods of time could also be performed in the metal immediately after processing by HPT.

There is a breakdown in the Hall-Petch relationship in Al-Mg-Sc alloys with average grain sizes below ~50 nm. Nevertheless, it is still unknown whether this originated from the increasing participation of GBS or other deformation mechanisms. Accordingly, a more comprehensive study is needed to identify the flow mechanism in Al-Mg-Sc alloys after the Hall-Petch breakdown. For this purpose, HPT processing could be conducted at RT using Al-Mg-Sc alloys with high Mg contents (> 5 wt. %) to produce grain sizes below ~50 nm. The flow mechanisms at RT could be identified through tensile testing using different strain rates and careful inspection of the microstructures of the fractured specimens.

The UFG alloy undergoes abnormal grain coarsening after annealing at selected conditions. Although this phenomenon had a negative effect for the superplastic properties, the ductility of UFG metals may be considerably improved by developing bimodal grain structures which preserve most of the strengthening benefits attained during SPD processing. For this reason, annealing for shorter times could be systematically conducted in SPD-processed Al-Mg-Sc alloys to generate duplex microstructures with an optimum combination between strength and ductility at ambient temperature.

The dimensions of the specimens significantly influence the elongations to failure achieved after tensile testing. As a result, this parameter shall not be used to directly compare the superplastic ductilities in materials tested using samples with notably different sizes. This motivates the development of systematic investigations dedicated to quantitatively measure

the influence of the sample size on the elongations achieved during superplastic flow. Finite element analyses could be used to simulate tensile testing at superplastic conditions using samples with different thicknesses, widths and gauge lengths. The simulation results may be validated by experiments and then used to derive a mathematical relationship between the sample dimensions and the elongations attained after testing.

The Al-Mg-Sc alloy exhibits excellent mechanical strength and superplastic properties after processing through SPD procedures. However, there are few isolated studies examining the flow behaviour of this UFG metal at strain rates below $\sim 10^{-4}$ s^{-1}. Creep testing at different temperatures could be conducted on ECAP-processed samples to assess the influence of grain refinement on the flow properties and deformation mechanisms of an Al-3Mg-0.2Sc alloy processed by ECAP at creep conditions.

Bibliography

[1] R.Z. Valiev, R.K. Islamgaliev, I. V. Alexandrov, Bulk nanostructured materials from severe plastic deformation, Prog. Mater. Sci. 45 (2000) 103–189.

[2] T.G. Langdon, Twenty-five years of ultrafine-grained materials: Achieving exceptional properties through grain refinement, Acta Mater. 61 (2013) 7035–7059.

[3] Y. Estrin, A. Vinogradov, Extreme grain refinement by severe plastic deformation: A wealth of challenging science, Acta Mater. 61 (2013) 782–817.

[4] R.Z. Valiev, T.G. Langdon, Principles of equal-channel angular pressing as a processing tool for grain refinement, Prog. Mater. Sci. 51 (2006) 881–981.

[5] A.P. Zhilyaev, T.G. Langdon, Using high-pressure torsion for metal processing: Fundamentals and applications, Prog. Mater. Sci. 53 (2008) 893–979.

[6] K. Edalati, Z. Horita, A review on high-pressure torsion (HPT) from 1935 to 1988, Mater. Sci. Eng. A. 652 (2016) 325–352.

[7] R.B. Figueiredo, P.R. Cetlin, T.G. Langdon, The processing of difficult-to-work alloys by ECAP with an emphasis on magnesium alloys, Acta Mater. 55 (2007) 4769–4779.

[8] M. Kleiner, M. Geiger, A. Klaus, Manufacturing of Lightweight Components by Metal Forming, CIRP Ann. - Manuf. Technol. 52 (2003) 521–542.

[9] W.S. Miller, L. Zhuang, J. Bottema, A.J. Wittebrood, P. De Smet, A. Haszler, A. Vieregge, Recent development in aluminium alloys for the automotive industry, Mater. Sci. Eng. A. 280 (2000) 37–49.

[10] J. May, H.W. Höppel, M. Göken, Strain rate sensitivity of ultrafine-grained aluminium processed by severe plastic deformation, Scr. Mater. 53 (2005) 189–194.

[11] Y.J. Chen, Y.C. Chai, H.J. Roven, S.S. Gireesh, Y.D. Yu, J. Hjelen, Microstructure and mechanical properties of Al-xMg alloys processed by room temperature ECAP, Mater. Sci. Eng. A. 545 (2012) 139–147.

[12] G. Horváth, N.Q. Chinh, J. Gubicza, J. Lendvai, Plastic instabilities and dislocation densities during plastic deformation in Al-Mg alloys, Mater. Sci. Eng. A. 445–446 (2007) 186–192.

[13] C. Xu, Z. Horita, T.G. Langdon, Microstructural evolution in an aluminum solid solution alloy processed by ECAP, Mater. Sci. Eng. A. 528 (2011) 6059–6065.

[14] T. Morishige, T. Hirata, T. Uesugi, Y. Takigawa, M. Tsujikawa, K. Higashi, Effect of Mg content on the minimum grain size of Al-Mg alloys obtained by friction stir processing, Scr. Mater. 64 (2011) 355–358.

[15] K. Edalati, D. Akama, A. Nishio, S. Lee, Y. Yonenaga, J.M. Cubero-Sesin, Z. Horita, Influence of dislocation-solute atom interactions and stacking fault energy on grain size of single-phase alloys after severe plastic deformation using high-pressure torsion, Acta Mater. 69 (2014) 68–77.

[16] J. Wang, Y. Iwahashi, Z. Horita, M. Furukawa, M. Nemoto, R.Z. Valiev, T.G. Langdon, An investigation of microstructural stability in an Al-Mg alloy with submicrometer grain size, Acta Mater. 44 (1996) 2973–2982.

[17] D.G. Morris, M.A. Muñoz-Morris, Microstructure of severely deformed Al-3Mg and its evolution during annealing, Acta Mater. 50 (2002) 4047–4060.

[18] P.B. Prangnell, J.S. Hayes, J.R. Bowen, P.J. Apps, P.S. Bate, Continuous recrystallisation of lamellar deformation structures produced by severe deformation, Acta Mater. 52 (2004) 3193–3206.

[19] K. Dám, P. Lejček, A. Michalcová, In situ TEM investigation of microstructural behavior of superplastic Al-Mg-Sc alloy, Mater. Charact. 76 (2013) 69–75.

[20] S. Lee, A. Utsunomiya, H. Akamatsu, K. Neishi, M. Furukawa, Z. Horita, T.G. Langdon, Influence of scandium and zirconium on grain stability and superplastic ductilities in ultrafine-grained Al-Mg alloys, Acta Mater. 50 (2002) 553–564.

[21] U. Andrade, M.A. Meyers, K.S. Vecchio, A.H. Chokshi, Dynamic recrystallization in high-strain, high-strain-rate plastic deformation of copper, Acta Metall. Mater. 42 (1994) 3183–3195.

[22] J.A. Hines, K.S. Vecchio, Recrystallization kinetics within adiabatic shear bands, Acta Mater. 45 (1997) 635–649.

[23] L. Zhen, G.A. Li, J.S. Zhou, D.Z. Yang, Micro-damage behaviors of Al-6Mg alloy impacted by projectiles with velocities of 1-3.2 km/s, Mater. Sci. Eng. A. 391 (2005) 354–366.

[24] R. Kapoor, J.B. Singh, J.K. Chakravartty, High strain rate behavior of ultrafine-grained Al-1.5 Mg, Mater. Sci. Eng. A. 496 (2008) 308–315.

[25] B. Mishra, C. Mondal, R. Goyal, P. Ghosal, K.S. Kumar, V. Madhu, Plastic flow behavior of 7017 and 7055 aluminum alloys under different high strain rate test methods, Mater. Sci. Eng. A. 612 (2014) 343–353.

[26] L. Wang, Y. Wang, A.P. Zhilyaev, A. V. Korznikov, S. Li, E. Korznikova, T.G. Langdon, Dynamic compressive behavior of ultrafine-grained pure Ti at elevated temperatures after processing by ECAP, J. Mater. Sci. 49 (2014) 6640–6647.

[27] L. Wang, Y.C. Wang, A.P. Zhilyaev, A. V. Korznikov, S.K. Li, E. Korznikova, T.G. Langdon, Microstructure and texture evolution in ultrafine-grained pure Ti processed by equal-channel angular pressing with subsequent dynamic compression, Scr. Mater. 77 (2014) 33–36.

[28] J. Yu, Z. Liu, Y. Dong, Z. Wang, Dynamic compressive property and failure behavior of extruded Mg-Gd-Y alloy under high temperatures and high strain rates, J. Magnes. Alloy. 3 (2015) 134–141.

[29] S. Zhang, Y.C. Wang, A.P. Zhilyaev, D. V. Gunderov, S. Li, G.I. Raab, E. Korznikova, T.G. Langdon, Effect of temperature on microstructural stabilization and mechanical properties in the dynamic testing of nanocrystalline pure Ti, Mater. Sci. Eng. A. 634 (2015) 64–70.

[30] S. Zhang, Y.C. Wang, A.P. Zhilyaev, E. Korznikova, S. Li, G.I. Raab, T.G. Langdon, Effect of grain size on compressive behaviour of titanium at different strain rates, Mater. Sci. Eng. A. 645 (2015) 311–317.

[31] P.H.R. Pereira, Y.C. Wang, Y. Huang, T.G. Langdon, Influence of grain size on the flow properties of an Al-Mg-Sc alloy over seven orders of magnitude of strain rate, Mater. Sci. Eng. A. 685 (2017) 367–376.

[32] Y. Ye, P. Li, L.S. Novikov, V.S. Avilkina, L. He, Comparison of residual microstructures associated with impact craters in Al-Sc and Al-Ti alloys, Acta Mater. 58 (2010) 2520–2526.

[33] W.G. Zhang, Y.C. Ye, L.J. He, P.J. Li, X. Feng, L.S. Novikov, Dynamic response and microstructure control of Al-Sc binary alloy under high-speed impact, Mater. Sci. Eng. A. 578 (2013) 35–45.

[34] R.Z. Valiev, N.A. Enikeev, M.Y. Murashkin, V.U. Kazykhanov, X. Sauvage, On the origin of the extremely high strength of ultrafine-grained Al alloys produced by severe plastic deformation, Scr. Mater. 63 (2010) 949–952.

[35] N. Kumar, R.S. Mishra, Additivity of strengthening mechanisms in ultrafine grained Al-Mg-Sc alloy, Mater. Sci. Eng. A. 580 (2013) 175–183.

[36] D. Zhemchuzhnikova, R. Kaibyshev, Mechanical Behavior of an Al-Mg-Mn-Sc Alloy with an Ultrafine Grain Structure at Cryogenic Temperatures, Adv. Eng. Mater. 17 (2015) 1804–1811.

[37] A. Mogucheva, D. Yuzbekova, R. Kaibyshev, T. Lebedkina, M. Lebyodkin, Effect of Grain Refinement on Jerky Flow in an Al-Mg-Sc Alloy, Metall. Mater. Trans. A Phys. Metall. Mater. Sci. 47 (2016) 2093–2106.

[38] T.G. Langdon, A unified approach to grain boundary sliding in creep and superplasticity, Acta Metall. Mater. 42 (1994) 2437–2443.

[39] R.Z. Valiev, D.A. Salimonenko, N.K. Tsenev, P.B. Berbon, T.G. Langdon, Observations of high strain rate superplasticity in commercial aluminum alloys with ultrafine grain sizes, Scr. Mater. 37 (1997) 1945–1950.

[40] J. Røyset, N. Ryum, Scandium in aluminium alloys, Int. Mater. Rev. 50 (2005) 19–44.

[41] Y.A. Filatov, V.I. Yelagin, V. V Zakharov, New Al–Mg–Sc alloys, Mater. Sci. Eng. A. 280 (2000) 97–101.

[42] D. Yuzbekova, A. Mogucheva, R. Kaibyshev, Superplasticity of ultrafine-grained Al–Mg–Sc–Zr alloy, Mater. Sci. Eng. A. 675 (2016) 228–242.

[43] S. Komura, Z. Horita, M. Furukawa, M. Nemoto, T.G. Langdon, An evaluation of the flow behavior during high strain rate superplasticity in an Al-Mg-Sc alloy, Metall. Mater. Trans. A Phys. Metall. Mater. Sci. 32 (2001) 707–716.

[44] F. Musin, R. Kaibyshev, Y. Motohashi, G. Itoh, Superplastic behavior and microstructure evolution in a commercial Al-Mg-Sc alloy subjected to intense plastic straining, Metall. Mater. Trans. A. 35 (2004) 2383–2392.

[45] E. Avtokratova, O. Sitdikov, M. Markushev, R. Mulyukov, Extraordinary high-strain rate superplasticity of severely deformed Al–Mg–Sc–Zr alloy, Mater. Sci. Eng. A. 538 (2012) 386–390.

[46] R. Kaibyshev, E. Avtokratova, A. Apollonov, R. Davies, High strain rate superplasticity in an Al-Mg-Sc-Zr alloy subjected to simple thermomechanical processing, Scr. Mater. 54 (2006) 2119–2124.

[47] E. Avtokratova, O. Sitdikov, O. Mukhametdinova, M. Markushev, S.V.S.N. Murty, M.J.N.V. Prasad, B.P. Kashyap, Microstructural evolution in Al–Mg–Sc–Zr alloy during severe plastic deformation and annealing, J. Alloys Compd. 673 (2016) 182–194.

[48] G. Sakai, Z. Horita, T.G. Langdon, Grain refinement and superplasticity in an aluminum alloy processed by high-pressure torsion, Mater. Sci. Eng. A. 393 (2005) 344–351.

[49] Z. Horita, T.G. Langdon, Achieving exceptional superplasticity in a bulk aluminum alloy processed by high-pressure torsion, Scr. Mater. 58 (2008) 1029–1032.

[50] S. V. Dobatkin, V. V. Zakharov, a. Y. Vinogradov, K. Kitagawa, N. a. Krasil'nikov, T.D. Rostova, E.N. Bastarash, Nanocrystalline structure formation in Al-Mg-Sc alloys during severe plastic deformation, Russ. Metall. 2006 (2006) 533–540.

[51] X. Sauvage, N. Enikeev, R. Valiev, Y. Nasedkina, M. Murashkin, Atomic-scale analysis of the segregation and precipitation mechanisms in a severely deformed Al-Mg alloy, Acta Mater. 72 (2014) 125–136.

[52] V.N. Perevezentsev, M.Y. Shcherban', M.Y. Murashkin, R.Z. Valiev, High-strain-rate superplasticity of nanocrystalline aluminum alloy 1570, Tech. Phys. Lett. 33 (2007) 648–650.

[53] Y. Harai, K. Edalati, Z. Horita, T.G. Langdon, Using ring samples to evaluate the processing characteristics in high-pressure torsion, Acta Mater. 57 (2009) 1147–1153.

[54] H. Shahmir, T.G. Langdon, Using heat treatments, high-pressure torsion and post-deformation annealing to optimize the properties of Ti-6Al-4V alloys, Acta Mater. 141 (2017) 419–426.

[55] M. El-Tahawy, P.H.R. Pereira, Y. Huang, H. Park, H. Choe, T.G. Langdon, J. Gubicza, Exceptionally high strength and good ductility in an ultrafine-grained 316L steel processed by severe plastic deformation and subsequent annealing, Mater. Lett. 214 (2018) 240–242.

[56] P. Ghosh, O. Renk, R. Pippan, Microtexture analysis of restoration mechanisms during high pressure torsion of pure nickel, Mater. Sci. Eng. A. 684 (2017) 101–109.

[57] M.M. Abramova, N.A. Enikeev, X. Sauvage, A. Etienne, B. Radiguet, E. Ubyivovk, R.Z. Valiev, Thermal stability and extra-strength of an ultrafine grained stainless steel produced by high pressure torsion, Rev. Adv. Mater. Sci. 43 (2015) 83–88.

[58] S. V. Dobatkin, O. V. Rybalchenko, N.A. Enikeev, A.A. Tokar, M.M. Abramova, Formation of fully austenitic ultrafine-grained high strength state in metastable Cr-Ni-Ti stainless steel by severe plastic deformation, Mater. Lett. 166 (2016) 276–279.

[59] Y. Harai, M. Kai, K. Kaneko, Z. Horita, T.G. Langdon, Microstructural and Mechanical Characteristics of AZ61 Magnesium Alloy Processed by High-Pressure Torsion, Mater. Trans. 49 (2008) 76–83.

[60] M. Kai, Z. Horita, T.G. Langdon, Developing grain refinement and superplasticity in a magnesium alloy processed by high-pressure torsion, Mater. Sci. Eng. A. 488 (2008) 117–124.

[61] E.O. Hall, The Deformation and Ageing of Mild Steel: III Discussion of Results, Proc. Phys. Soc. Sect. B. 64 (1951) 747–753.

[62] N.J. Petch, The cleavage strength of polycrystals, J. Iron Steel Inst. 174 (1953) 25–28.

[63] A.H. Chokshi, A. Rosen, J. Karch, H. Gleiter, On the validity of the hall-petch relationship in nanocrystalline materials, Scr. Metall. 23 (1989) 1679–1683.

[64] K.S. Kumar, H. Van Swygenhoven, S. Suresh, Mechanical behavior of nanocrystalline metals and alloys, Acta Mater. 51 (2003) 5743–5774.

[65] M.A. Meyers, A. Mishra, D.J. Benson, Mechanical properties of nanocrystalline materials, Prog. Mater. Sci. 51 (2006) 427–556.

[66] J.R. Trelewicz, C.A. Schuh, The Hall-Petch breakdown in nanocrystalline metals: A crossover to glass-like deformation, Acta Mater. 55 (2007) 5948–5958.

[67] E.N. Hahn, M.A. Meyers, Grain-size dependent mechanical behavior of nanocrystalline metals, Mater. Sci. Eng. A. 646 (2015) 101–134.

[68] K.S. Kumar, S. Suresh, M.F. Chisholm, J.A. Horton, P. Wang, Deformation of electrodeposited nanocrystalline nickel, Acta Mater. 51 (2003) 387–405.

[69] S. Cheng, J.A. Spencer, W.W. Milligan, Strength and tension/compression asymmetry in nanostructured and ultrafine-grain metals, Acta Mater. 51 (2003) 4505–4518.

[70] D. Farkas, Atomistic simulations of metallic microstructures, Curr. Opin. Solid State Mater. Sci. 17 (2013) 284–297.

[71] G.J. Tucker, M.A. Tschopp, D.L. McDowell, Evolution of structure and free volume in symmetric tilt grain boundaries during dislocation nucleation, Acta Mater. 58 (2010) 6464–6473.

[72] K. Kinoshita, T. Shimokawa, T. Kinari, Grain Boundary Structure Dependence of Extrinsic Grain Boundary Dislocation Emission Phenomena: A Molecular Dynamics Study, Mater. Trans. 53 (2012) 147–155.

[73] Z. Horita, M. Furukawa, M. Nemoto, A.. Barnes, T.. Langdon, Superplastic forming at high strain rates after severe plastic deformation, Acta Mater. 48 (2000) 3633–3640.

[74] R.Z. Valiev, O.A. Kaibyshev, R.I. Kuznetsov, R.S. Musalimov, N.K. Tsenev, Low-temperature superplasticity of metallic materials, Sov. Phys. Dokl. 33 (1988) 626–628.

[75] R.Z. Valiev, T.G. Langdon, The 7th International Conference on Nanomaterials by Severe Plastic Deformation: a report of the International NanoSPD Steering Committee, IOP Conf. Ser. Mater. Sci. Eng. 194 (2017) 12001.

[76] Y. Saito, H. Utsunomiya, N. Tsuji, T. Sakai, Novel ultra-high straining process for bulk materials—development of the accumulative roll-bonding (ARB) process, Acta Mater. 47 (1999) 579–583.

[77] T. Sakai, A. Belyakov, R. Kaibyshev, H. Miura, J.J. Jonas, Dynamic and post-dynamic recrystallization under hot, cold and severe plastic deformation conditions, Prog. Mater. Sci. 60 (2014) 130–207.

[78] G. Sakai, K. Nakamura, Z. Horita, T.G. Langdon, Developing high-pressure torsion for use with bulk samples, Mater. Sci. Eng. A. 406 (2005) 268–273.

[79] Y.G. Jin, H.M. Baek, Y.T. Im, B.C. Jeon, Continuous ECAP process design for manufacturing a microstructure-refined bolt, Mater. Sci. Eng. A. 530 (2011) 462–468.

[80] Y. Huang, T.G. Langdon, Advances in ultrafine-grained materials, Mater. Today. 16 (2013) 85–93.

[81] Y. Iwahashi, J. Wang, Z. Horita, M. Nemoto, T.G. Langdon, Principle of equal-channel angular pressing for the processing of ultra-fine grained materials, Scr. Mater. 35 (1996) 143–146.

[82] Y. Wu, I. Baker, An experimental study of equal channel angular extrusion, Scr. Mater. 37 (1997) 437–442.

[83] W. Wei, A. V. Nagasekhar, G. Chen, Y. Tick-Hon, K.X. Wei, Origin of inhomogenous behavior during equal channel angular pressing, Scr. Mater. 54 (2006) 1865–1869.

[84] R.B. Figueiredo, I.P. Pinheiro, M.T.P. Aguilar, P.J. Modenesi, P.R. Cetlin, The finite element analysis of equal channel angular pressing (ECAP) considering the strain path dependence of the work hardening of metals, J. Mater. Process. Technol. 180 (2006) 30–36.

[85] P.B. Berbon, M. Furukawa, Z. Horita, M. Nemoto, T.G. Langdon, Influence of pressing speed on microstructural development in equal-channel angular pressing, Metall. Mater. Trans. A. 30A (1999) 1989–1997.

[86] A. Yamashita, D. Yamaguchi, Z. Horita, T.G. Langdon, Influence of pressing temperature on microstructural development in equal-channel angular pressing, Mater. Sci. Eng. A. 287 (2000) 100–106.

[87] C.F. Gu, L.S. Tóth, D.P. Field, J.J. Fundenberger, Y.D. Zhang, Room temperature equal-channel angular pressing of a magnesium alloy, Acta Mater. 61 (2013) 3027–3036.

[88] M. Furukawa, Y. Iwahashi, Z. Horita, M. Nemoto, T.G. Langdon, The shearing characteristics associated with equal-channel angular pressing, Mater. Sci. Eng. A. 257 (1998) 328–332.

[89] K. Nakashima, Z. Horita, M. Nemoto, T.G. Langdon, Development of a multi-pass facility for equal-channel angular processing to high total strains, Mater. Sci. Eng. A. 281 (2000) 82–87.

[90] F.S.J. Poggiali, C.L.P. Silva, P.H.R. Pereira, R.B. Figueiredo, P.R. Cetlin, Determination of mechanical anisotropy of magnesium processed by ECAP, J. Mater. Res. Technol. 3 (2014) 331–337.

[91] S. Biswas, S. Singh Dhinwal, S. Suwas, Room-temperature equal channel angular extrusion of pure magnesium, Acta Mater. 58 (2010) 3247–3261.

[92] Y. Iwahashi, Z. Horita, M. Nemoto, T.G. Langdon, The process of grain refinement in equal-channel angular pressing, Acta Mater. 46 (1998) 3317–3331.

[93] M.A. Muñoz-Morris, C. Garcia Oca, G. Gonzalez-Doncel, D.G. Morris, Microstructural evolution of dilute Al-Mg alloys during processing by equal channel angular pressing and during subsequent annealing, Mater. Sci. Eng. A. 375–377 (2004) 853–856.

[94] M. Kawasaki, Z. Horita, T.G. Langdon, Microstructural evolution in high purity aluminum processed by ECAP, Mater. Sci. Eng. A. 524 (2009) 143–150.

[95] S.C. Baik, Y. Estrin, H.S. Kim, R.J. Hellmig, Dislocation density-based modeling of deformation behavior of aluminium under equal channel angular pressing, Mater. Sci. Eng. A. 351 (2003) 86–97.

[96] M.J. Starink, X.G. Qiao, J. Zhang, N. Gao, Predicting grain refinement by cold severe plastic deformation in alloys using volume average dislocation generation, Acta Mater. 57 (2009) 5796–5811.

[97] R.B. Figueiredo, T.G. Langdon, Principles of grain refinement in magnesium alloys processed by equal-channel angular pressing, J. Mater. Sci. 44 (2009) 4758–4762.

[98] F. Dalla Torre, R. Lapovok, J. Sandlin, P.F. Thomson, C.H.J. Davies, E. V. Pereloma, Microstructures and properties of copper processed by equal channel angular extrusion for 1-16 passes, Acta Mater. 52 (2004) 4819–4832.

[99] Y.T. Zhu, T.G. Langdon, The fundamentals of nanostructured materials processed by severe plastic deformation, JOM 56 (2004) 58–63.

[100] H. Shahmir, P.H.R. Pereira, Y. Huang, T.G. Langdon, Mechanical properties and microstructural evolution of nanocrystalline titanium at elevated temperatures, Mater. Sci. Eng. A. 669 (2016) 358–366.

[101] R.Z. Valiev, I. V Alexandrov, Y.T. Zhu, T.C. Lowe, Paradox of strength and ductility in metals processed by severe plastic deformation, J. Mater. Res. 17 (2002) 5–8.

[102] I. Semenova, G. Salimgareeva, G. Da Costa, W. Lefebvre, R. Valiev, Enhanced strength and ductility of ultrafine-grained Ti processed by severe plastic deformation, Adv. Eng. Mater. 12 (2010) 803–807.

[103] T. Mungole, P. Kumar, M. Kawasaki, T.G. Langdon, A critical examination of the paradox of strength and ductility in ultrafine-grained metals, J. Mater. Res. 29 (2014) 2534–2546.

[104] T.G. Langdon, Seventy-five years of superplasticity: Historic developments and new opportunities, J. Mater. Sci. 44 (2009) 5998–6010.

[105] M. Kawasaki, T.G. Langdon, Principles of superplasticity in ultrafine-grained materials, J. Mater. Sci. 42 (2007) 1782–1796.

[106] R.B. Figueiredo, T.G. Langdon, Record superplastic ductility in a magnesium alloy processed by equal-channel angular pressing, Adv. Eng. Mater. 10 (2008) 37–40.

[107] P.W. Bridgman, Effects of high shearing stress combined with high hydrostatic pressure, Phys. Rev. 48 (1935) 825–847.

[108] A. Hohenwarter, A. Bachmaier, B. Gludovatz, S. Scheriau, R. Pippan, Technical parameters affecting grain refinement by high pressure torsion, Int. J. Mater. Res. 100 (2009) 1653–1661.

[109] P.H.R. Pereira, R.B. Figueiredo, P.R. Cetlin, T.G. Langdon, Using finite element modelling to examine the flow process and temperature evolution in HPT under different constraining conditions, IOP Conf. Ser. Mater. Sci. Eng. 63 (2014) 12041.

[110] P.H.R. Pereira, R.B. Figueiredo, P.R. Cetlin, T.G. Langdon, An examination of the elastic distortions of anvils in high-pressure torsion, Mater. Sci. Eng. A. 631 (2015) 201–208.

[111] P.H.R. Pereira, T.H.P. Costa, R.B. Figueiredo, P.R. Cetlin, T.G. Langdon, Analysis of Plastic Deformation and Sample Geometry during the Compression Stage in High-Pressure Torsion, Adv. Mater. Res. 922 (2014) 592–597.

[112] R.B. Figueiredo, P.R. Cetlin, T.G. Langdon, Using finite element modeling to examine the flow processes in quasi-constrained high-pressure torsion, Mater. Sci. Eng. A. 528 (2011) 8198–8204.

[113] D.J. Lee, E.Y. Yoon, L.J. Park, H.S. Kim, The dead metal zone in high-pressure torsion, Scr. Mater. 67 (2012) 384–387.

[114] R.Z. Valiev, Y. V. Ivanisenko, E.F. Rauch, B. Baudelet, Structure and deformaton behaviour of Armco iron subjected to severe plastic deformation, Acta Mater. 44 (1996) 4705–4712.

[115] J.J. Jonas, C. Ghosh, L.S. Toth, The equivalent strain in high pressure torsion, Mater. Sci. Eng. A. 607 (2014) 530–535.

[116] R.B. Figueiredo, M.T.P. Aguilar, P.R. Cetlin, T.G. Langdon, Analysis of plastic flow during high-pressure torsion, J. Mater. Sci. 47 (2012) 7807–7814.

[117] R.B. Figueiredo, G.C. V De Faria, P.R. Cetlin, T.G. Langdon, Three-dimensional analysis of plastic flow during high-pressure torsion, J. Mater. Sci. 48 (2013) 4524–4532.

[118] D.J. Lee, H.S. Kim, Finite element analysis for the geometry effect on strain inhomogeneity during high-pressure torsion, J. Mater. Sci. 49 (2014) 6620–6628.

[119] A.. Zhilyaev, G.. Nurislamova, B.-K. Kim, M.. Baró, J.. Szpunar, T.. Langdon, Experimental parameters influencing grain refinement and microstructural evolution during high-pressure torsion, Acta Mater. 51 (2003) 753–765.

[120] M.J. Zehetbauer, H.P. Stüwe, A. Vorhauer, E. Schafler, J. Kohout, The Role of Hydrostatic Pressure in Severe Plastic Deformation, Adv. Eng. Mater. 5 (2003) 330–337.

[121] P.H.R. Pereira, R.B. Figueiredo, Y. Huang, P.R. Cetlin, T.G. Langdon, Modeling the temperature rise in high-pressure torsion, Mater. Sci. Eng. A. 593 (2014) 185–188.

[122] K. Edalati, R. Miresmaeili, Z. Horita, H. Kanayama, R. Pippan, Significance of temperature increase in processing by high-pressure torsion, Mater. Sci. Eng. A. 528 (2011) 7301–7305.

[123] R.B. Figueiredo, P.H.R. Pereira, M.T.P. Aguilar, P.R. Cetlin, T.G. Langdon, Using finite element modeling to examine the temperature distribution in quasi-constrained high-pressure torsion, Acta Mater. 60 (2012) 3190–3198.

[124] G.B. Rathmayr, R. Pippan, Influence of impurities and deformation temperature on the saturation microstructure and ductility of HPT-deformed nickel, Acta Mater. 59 (2011) 7228–7240.

[125] K. Edalati, Y. Hashiguchi, P.H.R. Pereira, Z. Horita, T.G. Langdon, Effect of temperature rise on microstructural evolution during high-pressure torsion, Mater. Sci. Eng. A. 714 (2018) 167–171.

[126] M. Kawasaki, T.G. Langdon, The significance of strain reversals during processing by high-pressure torsion, Mater. Sci. Eng. A. 498 (2008) 341–348.

[127] Y. Huang, M. Kawasaki, T.G. Langdon, Influence of anvil alignment on shearing patterns in high-pressure torsion, Adv. Eng. Mater. 15 (2013) 747–755.

[128] P. Serre, R.B. Figueiredo, N. Gao, T.G. Langdon, Influence of strain rate on the characteristics of a magnesium alloy processed by high-pressure torsion, Mater. Sci. Eng. A. 528 (2011) 3601–3608.

[129] K. Edalati, Z. Horita, T.G. Langdon, The significance of slippage in processing by high-pressure torsion, Scr. Mater. 60 (2009) 9–12.

[130] W.F. Hosford, R. Caddell, Metal Forming: Mechanics and Metallurgy, third ed., Cambridge University Press, New York, 2007.

[131] N. Gao, M.J. Starink, T.G. Langdon, Using differential scanning calorimetry as an analytical tool for ultrafine grained metals processed by severe plastic deformation, Mater. Sci. Technol. 25 (2009) 687–698.

[132] P. Bazarnik, Y. Huang, M. Lewandowska, T.G. Langdon, Structural impact on the Hall-Petch relationship in an Al-5Mg alloy processed by high-pressure torsion, Mater. Sci. Eng. A. 626 (2015) 9–15.

[133] S. Sabbaghianrad, J. Wongsa-Ngam, M. Kawasaki, T.G. Langdon, An examination of the saturation microstructures achieved in ultrafine-grained metals processed by high-pressure torsion, J. Mater. Res. Technol. 3 (2014) 319–326.

[134] M. Kawasaki, Different models of hardness evolution in ultrafine-grained materials processed by high-pressure torsion, J. Mater. Sci. 49 (2014) 18–34.

[135] M. Kawasaki, S.N. Alhajeri, C. Xu, T.G. Langdon, The development of hardness homogeneity in pure aluminum and aluminum alloy disks processed by high-pressure torsion, Mater. Sci. Eng. A. 529 (2011) 345–351.

[136] K. Edalati, Z. Horita, Significance of homologous temperature in softening behavior and grain size of pure metals processed by high-pressure torsion, Mater. Sci. Eng. A. 528 (2011) 7514–7523.

[137] O. Andreau, J. Gubicza, N. Xian Zhang, Y. Huang, P. Jenei, T.G. Langdon, Effect of short-term annealing on the microstructures and flow properties of an Al-1% Mg alloy processed by high-pressure torsion, Mater. Sci. Eng. A. 615 (2014) 231–239.

[138] Y. Huang, M. Lemang, N.X. Zhang, P.H.R. Pereira, T.G. Langdon, Achieving superior grain refinement and mechanical properties in vanadium through high-pressure torsion and subsequent short-term annealing, Mater. Sci. Eng. A. 655 (2016) 60–69.

[139] M. Kawasaki, T.G. Langdon, Review: achieving superplasticity in metals processed by high-pressure torsion, J. Mater. Sci. 49 (2014) 6487–6496.

[140] M. Kawasaki, T.G. Langdon, Grain boundary sliding in a superplastic zinc-aluminum alloy processed using severe plastic deformation, Mater. Trans. 49 (2008) 84–89.

[141] M. Kawasaki, T.G. Langdon, Developing superplasticity and a deformation mechanism map for the Zn-Al eutectoid alloy processed by high-pressure torsion, Mater. Sci. Eng. A. 528 (2011) 6140–6145.

[142] Y.H. Zhao, Y.Z. Guo, Q. Wei, A.M. Dangelewicz, C. Xu, Y.T. Zhu, T.G. Langdon, Y.Z. Zhou, E.J. Lavernia, Influence of specimen dimensions on the tensile behavior of ultrafine-grained Cu, Scr. Mater. 59 (2008) 627–630.

[143] J.E. Field, S.M. Walley, W.G. Proud, H.T. Goldrein, C.R. Siviour, Review of experimental techniques for high rate deformation and shock studies, Int. J. Impact Eng. 30 (2004) 725–775.

[144] B. Hopkinson, A method of measuring the pressure produced in the detonation of high, explosives or by the impact of bullets, Philos. Trans. R. Soc. London. Ser. A. 213 (1914) 437–456.

[145] G.I. Taylor, The testing of materials at high rates of loading., J. Inst. Civ. Eng. 26 (1946) 486–519.

[146] E. Volterra, Alcuni risultati di prove dinamichi sui materiali, Riv. Nuovo Cim. 4 (1948) 1–28.

[147] H. Kolsky, An investigation of the mechanical properties of materials at very high rates of loading, Proc. Phys. Soc. Sect. B. 62 (1949) 676–700.

[148] G.T. Gray, Classic Split-Hopkinson Pressure Bar Testing, in: ASM Metals Handbook: Mechanical Testing and Evaluation, vol. 8, ASM International, Metals Park (OH), 2000: 462-476.

[149] R.W. Armstrong, S.M. Walley, High strain rate properties of metals and alloys, Int. Mater. Rev. 53 (2008) 105–128.

[150] W.S. Lee, W.C. Sue, C.F. Lin, C.J. Wu, The strain rate and temperature dependence of the dynamic impact properties of 7075 aluminum alloy, J. Mater. Process. Technol. 100 (2000) 116–122.

[151] Y.B. Xu, W.L. Zhong, Y.J. Chen, L.T. Shen, Q. Liu, Y.L. Bai, M.A. Meyers, Shear localization and recrystallization in dynamic deformation of 8090 Al-Li alloy, Mater. Sci. Eng. A. 299 (2001) 287–295.

[152] W.S. Lee, T.H. Chen, Rate-dependent deformation and dislocation substructure of Al-Sc alloy, Scr. Mater. 54 (2006) 1463–1468.

[153] L.E. Murr, E. V. Esquivel, Observations of common microstructural issues associated with dynamic deformation phenomena: Twins, microbands, grain size effects, shear bands, and dynamic recrystallization, J. Mater. Sci. 39 (2004) 1153–1168.

[154] J.C. Sanchez, L.E. Murr, K.P. Staudhammer, Effect of grain size and pressure on twinning and microbanding in oblique shock loading of copper rods, Acta Mater. 45 (1997) 3223–3235.

[155] I. Sabirov, M.Y. Murashkin, R.Z. Valiev, Nanostructured aluminium alloys produced by severe plastic deformation: New horizons in development, Mater. Sci. Eng. A. 560 (2013) 1–24.

[156] S. Komura, M. Furukawa, Z. Horita, M. Nemoto, T.G. Langdon, Optimizing the procedure of equal-channel angular pressing for maximum superplasticity, Mater. Sci. Eng. A. 297 (2001) 111–118.

[157] S.I. Fujikawa, M. Sugaya, H. Takei, K.I. Hirano, Solid solubility and residual resistivity of scandium in aluminum, J. Less-Common Met. 63 (1979) 87–97.

[158] J. Røyset, N. Ryum, Kinetics and mechanisms of precipitation in an Al-0.2wt.% Sc alloy, Mater. Sci. Eng. A. 396 (2005) 409–422.

[159] S. Komura, Z. Horita, M. Furukawa, M. Nemoto, T.G. Langdon, Influence of scandium on superplastic ductilities in an Al-Mg-Sc alloy, J. Mater. Res. 15 (2000) 2571–2576.

[160] J. Taendl, A. Orthacker, H. Amenitsch, G. Kothleitner, C. Poletti, Influence of the degree of scandium supersaturation on the precipitation kinetics of rapidly solidified Al-Mg-Sc-Zr alloys, Acta Mater. 117 (2016) 43–50.

[161] F.J. Humphreys, M. Hatherly, Recrystallization and Related Annealing Phenomena, Second edition, Pergamon Press, Oxford, 2004.

[162] G. Couturier, R. Doherty, C. Maurice, R. Fortunier, 3D finite element simulation of the inhibition of normal grain growth by particles, Acta Mater. 53 (2005) 977–989.

[163] M.J. Jones, F.J. Humphreys, Interaction of recrystallization and precipitation: The effect of Al3Sc on the recrystallization behaviour of deformed aluminium, Acta Mater. 51 (2003) 2149–2159.

[164] S. Iwamura, Y. Miura, Loss in coherency and coarsening behavior of Al_3Sc precipitates, Acta Mater. 52 (2004) 591–600.

[165] E.A. Marquis, D.N. Seidman, Coarsening kinetics of nanoscale Al3Sc precipitates in an Al–Mg–Sc alloy, Acta Mater. 53 (2005) 4259–4268.

[166] Y. Buranova, V. Kulitskiy, M. Peterlechner, A. Mogucheva, R. Kaibyshev, S.V. Divinski, G. Wilde, Al_3(Sc,Zr)-based precipitates in Al–Mg alloy: Effect of severe deformation, Acta Mater. 124 (2017) 210–224.

[167] O. Sitdikov, T. Sakai, E. Avtokratova, R. Kaibyshev, Y. Kimura, K. Tsuzaki, Grain refinement in a commercial Al-Mg-Sc alloy under hot ECAP conditions, Mater. Sci. Eng. A. 444 (2007) 18–30.

[168] O. Sitdikov, E. Avtokratova, T. Sakai, K. Tsuzaki, R. Kaibyshev, Y. Watanabe, Effect of Processing Temperature on Microstructure Development during ECAP of Al-Mg-Sc Alloy, Mater. Sci. Forum. 584–586 (2008) 481–486.

[169] O. Sitdikov, T. Sakai, E. Avtokratova, R. Kaibyshev, K. Tsuzaki, Y. Watanabe, Microstructure behavior of Al-Mg-Sc alloy processed by ECAP at elevated temperature, Acta Mater. 56 (2008) 821–834.

[170] G. Sha, L. Yao, X. Liao, S.P. Ringer, Z.C. Duan, T.G. Langdon, Segregation of solute elements at grain boundaries in an ultrafine grained Al-Zn-Mg-Cu alloy, Ultramicroscopy. 111 (2011) 500–505.

[171] X. Sauvage, A. Ganeev, Y. Ivanisenko, N. Enikeev, M. Murashkin, R. Valiev, Grain boundary segregation in UFG alloys processed by severe plastic deformation, Adv. Eng. Mater. 14 (2012) 968–974.

[172] X. Sauvage, G. Wilde, S. V. Divinski, Z. Horita, R.Z. Valiev, Grain boundaries in ultrafine grained materials processed by severe plastic deformation and related phenomena, Mater. Sci. Eng. A. 540 (2012) 1–12.

[173] M. Cabibbo, Microstructure strengthening mechanisms in an Al-Mg-Si-Sc-Zr equal channel angular pressed aluminium alloy, Appl. Surf. Sci. 281 (2013) 38–43.

[174] F. Fazeli, W.J. Poole, C.W. Sinclair, Modeling the effect of Al3Sc precipitates on the yield stress and work hardening of an Al-Mg-Sc alloy, Acta Mater. 56 (2008) 1909–1918.

[175] S. Malopheyev, V. Kulitskiy, R. Kaibyshev, Deformation structures and strengthening mechanisms in an AlMgScZr alloy, J. Alloys Compd. 698 (2017) 957–966.

[176] E.V. Avtokratova, R.O. Kaibyshev, O.Sh. Sitdikov, Fatigue of a fine-grained high-strength Al-6Mg-Sc alloy produced by equal-channel angular pressing, Phys. Met. Metallogr. 105 (2008) 500–508.

[177] A. Vinogradov, A. Washikita, K. Kitagawa, V.I. Kopylov, Fatigue life of fine-grain Al-Mg-Sc alloys produced by equal-channel angular pressing, Mater. Sci. Eng. A. 349 (2003) 318–326.

[178] M. Furukawa, Z. Horita, M. Nemoto, R.Z. Valiev, T.G. Langdon, Factors influencing the flow and hardness of materials with ultrafine grain sizes, Philos. Mag. A. 78 (1998) 203–215.

[179] M. V. Markushev, M.Y. Murashkin, Structure and mechanical properties of commercial Al-Mg 1560 alloy after equal-channel angular extrusion and annealing, Mater. Sci. Eng. A. 367 (2004) 234–242.

[180] S. Komura, P.B. Berbon, M. Furukawa, Z. Horita, M. Nemoto, T.G. Langdon, High strain rate superplasticity in an Al-Mg alloy containing scandium, Scr. Mater. 38 (1998) 1851–1856.

[181] T.G. Nieh, L.M. Hsiung, J. Wadsworth, R. Kaibyshev, High strain rate superplasticity in a continuously recrystallized Al–6%Mg–0.3%Sc alloy, Acta Mater. 46 (1998) 2789–2800.

[182] R.K. Islamgaliev, N.F. Yunusova, R.Z. Valiev, N.K. Tsenev, V.N. Perevezentsev, T.G. Langdon, Characteristics of superplasticity in an ultrafine-grained aluminum alloy processed by ECA pressing, Scr. Mater. 49 (2003) 467–472.

[183] F. Musin, R. Kaibyshev, Y. Motohashi, G. Itoh, High strain rate superplasticity in a commercial Al-Mg-Sc alloy, Scr. Mater. 50 (2004) 511–516.

[184] E. Avtokratova, O. Sitdikov, O. Mukhametdinova, M. Markushev, High strain rate superplasticity in an Al-Mg-Sc-Zr alloy produced by equal channel angular pressing and subsequent cold and warm rolling, Mater. Sci. Forum. 710 (2012) 223–228.

[185] F.C. Liu, Z.Y. Ma, F.C. Zhang, High Strain Rate Superplasticity in a Micro-grained Al-Mg-Sc Alloy with Predominant High Angle Grain Boundaries, J. Mater. Sci. Technol. 28 (2012) 1025–1030.

[186] X. Cao, G. Xu, Y. Duan, Z. Yin, L. Lu, Y. Wang, Achieving high superplasticity of a new Al–Mg–Sc–Zr alloy sheet prepared by a simple thermal–mechanical process, Mater. Sci. Eng. A. 647 (2015) 333–343.

[187] Y.L. Duan, G.F. Xu, D. Xiao, L.Q. Zhou, Y. Deng, Z.M. Yin, Excellent superplasticity and deformation mechanism of Al–Mg–Sc–Zr alloy processed via simple free forging, Mater. Sci. Eng. A. 624 (2015) 124–131.

[188] K. Higashi, M. Mabuchi, T.G. Langdon, High-Strain-Rate Superplasticity in Metallic Materials and the Potential for Ceramic Materials, ISIJ Int. 36 (1996) 1423–1438.

[189] E.V. Avtokratova, O.S. Sitdikov, M.V. Markushev, Effect of cold/warm rolling following warm ECAP on superplastic properties of an Al 5.8%Mg-0.32%Sc alloy, Lett. Mater. 5 (2015) 319–323.

[190] R.B. Figueiredo, T.G. Langdon, Development of structural heterogeneities in a magnesium alloy processed by high-pressure torsion, Mater. Sci. Eng. A. 528 (2011) 4500–4506.

[191] A.S.M. Metals, Handbook: Properties and Selection on Nonferrous Alloys and Special-Purpose Materials 2, ASM International, Metals Park (OH), 1990.

[192] J. Wongsa-Ngam, M. Kawasaki, T.G. Langdon, The development of hardness homogeneity in a Cu-Zr alloy processed by equal-channel angular pressing, Mater. Sci. Eng. A. 556 (2012) 526–532.

[193] F.A. Mohamed, T.G. Langdon, Creep at low stress levels in the superplastic Zn-22% Al eutectoid, Acta Metall. 23 (1975) 117–124.

[194] H.M. Rietveld, A profile refinement method for nuclear and magnetic structures, J. Appl. Crystallogr. 2 (1969) 65–71.

[195] G.K. Williamson, R.E. Smallman, Dislocation densities in some annealed and cold-worked metals from measurements on the X-ray Debye-Scherrer spectrum, Philos. Mag. 1 (1956) 34–46.

[196] R.E. Smallman, K.H. Westmacott, Stacking faults in face-centred cubic metals and alloys, Philos. Mag. 2 (1957) 669–683.

[197] T.A. Lebedkina, M.A. Lebyodkin, T.T. Lamark, M. Janeček, Y. Estrin, Effect of equal channel angular pressing on the Portevin–Le Chatelier effect in an Al3Mg alloy, Mater. Sci. Eng. A. 615 (2014) 7–13.

[198] G.J. Fan, G.Y. Wang, H. Choo, P.K. Liaw, Y.S. Park, B.Q. Han, E.J. Lavernia, Deformation behavior of an ultrafine-grained Al-Mg alloy at different strain rates, Scr. Mater. 52 (2005) 929–933.

[199] L. Ziani, S. Boudrahem, H. Ait-Amokhtar, M. Mehenni, B. Kedjar, Unstable plastic flow in the Al-2%Mg alloy, effect of annealing process, Mater. Sci. Eng. A. 536 (2012) 239–243.

[200] D.A. Zhemchuzhnikova, M.A. Lebyodkin, T.A. Lebedkina, R.O. Kaibyshev, Unusual behavior of the Portevin-Le Chatelier effect in an AlMg alloy containing precipitates, Mater. Sci. Eng. A. 639 (2015) 37–41.

[201] H. Ishikawa, F.A. Mohamed, T.G. Langdon, The influence of strain rate on ductility in the superplastic Zn–22% Al eutectoid, Philos. Mag. 32 (1975) 1269–1271.

[202] H. Hu, Texture of Metals, Texture. 1 (1974) 233–258.

[203] C.A. Bronkhorst, S.R. Kalidindi, L. Anand, Polycrystalline plasticity and the evolution of crystallographic texture in FCC metals, Philos. Trans. R. Soc. A. 341 (1992) 443–477.

[204] L.S. Tóth, B. Beausir, C.F. Gu, Y. Estrin, N. Scheerbaum, C.H.J. Davies, Effect of grain refinement by severe plastic deformation on the next-neighbor misorientation distribution, Acta Mater. 58 (2010) 6706–6716.

[205] J.K. Mackenzie, Second paper on statistics associated with the random disorientation of cubes, Biometrika. 45 (1958) 229–240.

[206] S. Li, I.J. Beyerlein, M.A.M. Bourke, Texture formation during equal channel angular extrusion of fcc and bcc materials: Comparison with simple shear, Mater. Sci. Eng. A. 394 (2005) 66–77.

[207] I.J. Beyerlein, L.S. Tóth, Texture evolution in equal-channel angular extrusion, Prog. Mater. Sci. 54 (2009) 427–510.

[208] C.F. Gu, L.S. Tóth, C.H.J. Davies, Effect of strain reversal on texture and grain refinement in route C equal channel angular pressed copper, Scr. Mater. 65 (2011) 167–170.

[209] C.F. Gu, L.S. Tóth, The origin of strain reversal texture in equal channel angular pressing, Acta Mater. 59 (2011) 5749–5757.

[210] K. Furuno, H. Akamatsu, K. Oh-Ishi, M. Furukawa, Z. Horita, T.G. Langdon, Microstructural development in equal-channel angular pressing using a 60° die, Acta Mater. 52 (2004) 2497–2507.

[211] E.A. Marquis, D.N. Seidman, D.C. Dunand, Effect of Mg addition on the creep and yield behavior of an Al-Sc alloy, Acta Mater. 51 (2003) 4751–4760.

[212] H. Hasegawa, S. Komura, A. Utsunomiya, Z. Horita, M. Furukawa, M. Nemoto, T.G. Langdon, Thermal stability of ultrafine-grained aluminum in the presence of Mg and Zr additions, Mater. Sci. Eng. A. 265 (1999) 188–196.

[213] J.R. Trelewicz, C.A. Schuh, The Hall-Petch breakdown at high strain rates: Optimizing nanocrystalline grain size for impact applications, Appl. Phys. Lett. 93 (2008) 171916.

[214] M.J. Starink, Dislocation versus grain boundary strengthening in SPD processed metals: Non-causal relation between grain size and strength of deformed polycrystals, Mater. Sci. Eng. A. 705 (2017) 42–45.

[215] Z. Horita, T. Fujinami, M. Nemoto, T.G. Langdon, Equal-channel angular pressing of commercial aluminum alloys: Grain refinement, thermal stability and tensile properties, Metall. Mater. Trans. A 31 (2000) 691–701.

[216] N. Tsuji, in: Y.T. Zhu, V. Varyukhin (Eds.), Nanostructured Materials by High-pressure Severe Plastic Deformation, Springer Netherlands, 2006: 227.

[217] C. Kwan, Z. Wang, S.B. Kang, Mechanical behavior and microstructural evolution upon annealing of the accumulative roll-bonding (ARB) processed Al alloy 1100, Mater. Sci. Eng. A. 480 (2008) 148–159.

[218] A. Azimi, S. Tutunchilar, G. Faraji, M.K. Besharati Givi, Mechanical properties and microstructural evolution during multi-pass ECAR of Al 1100-O alloy, Mater. Des. 42 (2012) 388–394.

[219] H.-J. Lee, J.-K. Han, S. Janakiraman, B. Ahn, M. Kawasaki, T.G. Langdon, Significance of grain refinement on microstructure and mechanical properties of an Al-3% Mg alloy processed by high-pressure torsion, J. Alloys Compd. 686 (2016).

[220] R. Kapoor, J.K. Chakravartty, Deformation behavior of an ultrafine-grained Al-Mg alloy produced by equal-channel angular pressing, Acta Mater. 55 (2007) 5408–5418.

[221] M. Furukawa, Z. Horita, M. Nemoto, R.Z. Valiev, T.G. Langdon, Microhardness measurements and the hall-petch relationship in an Al-Mg alloy with submicrometer grain size, Acta Mater. 44 (1996) 4619–4629.

[222] J.S. Hayes, R. Keyte, P.B. Prangnell, Effect of grain size on tensile behaviour of a submicron grained Al–3 wt-%Mg alloy produced by severe deformation, Mater. Sci. Technol. 16 (2000) 1259–1263.

[223] N. Kumar, R.S. Mishra, C.S. Huskamp, K.K. Sankaran, Critical grain size for change in deformation behavior in ultrafine grained Al-Mg-Sc alloy, Scr. Mater. 64 (2011) 576–579.

[224] F. Abdeljawad, S.M. Foiles, Stabilization of nanocrystalline alloys via grain boundary segregation: A diffuse interface model, Acta Mater. 101 (2015) 159–171.

[225] L.E. Karkina, I.N. Karkin, A.R. Kuznetsov, I.K. Razumov, P.A. Korzhavyi, Y.N. Gornostyrev, Solute-grain boundary interaction and segregation formation in Al: First principles calculations and molecular dynamics modeling, Comput. Mater. Sci. 112 (2016) 18–26.

[226] A. Van Den Beukel, U.F. Kocks, The strain dependence of static and dynamic strain-aging, Acta Metall. 30 (1982) 1027–1034.

[227] W.A. Curtin, D.L. Olmsted, L.G. Hector, A predictive mechanism for dynamic strain ageing in aluminium–magnesium alloys, Nat. Mater. 5 (2006) 875–880.

[228] H. Aboulfadl, J. Deges, P. Choi, D. Raabe, Dynamic strain aging studied at the atomic scale, Acta Mater. 86 (2015) 34–42.

[229] P.R. Cetlin, A.Ş. Güleç, R.E. Reed-Hill, Serrated flow in aluminum 6061 alloy, Metall. Trans. 4 (1973) 513–517.

[230] A.M. Giarola, P.H.R. Pereira, P.A. Stemler, A.E.M. Pertence, H.B. Campos, M.T.P. Aguilar, P.R. Cetlin, Strain heterogeneities in the rolling direction of steel sheets submitted to the skin pass: A finite element analysis, J. Mater. Process. Technol. 216 (2015) 234–247.

[231] P. Yavari, T.G. Langdon, An examination of the breakdown in creep by viscous glide in solid solution alloys at high stress levels, Acta Metall. 30 (1982) 2181–2196.

[232] I. Sabirov, M.R. Barnett, Y. Estrin, P.D. Hodgson, The effect of strain rate on the deformation mechanisms and the strain rate sensitivity of an ultra-fine-grained Al alloy, Scr. Mater. 61 (2009) 181–184.

[233] M.T. Pérez-Prado, G. González-Doncel, O.A. Ruano, T.R. McNelley, Texture analysis of the transition from slip to grain boundary sliding in a discontinuously recrystallized superplastic aluminum alloy, Acta Mater. 49 (2001) 2259–2268.

[234] W.A. Rachinger, Relative grain translations in the plastic flow of aluminium, Journal Inst. Met. 81 (1952) 33–41.

[235] J.E. Bird, A.K. Mukherjee, J.E. Dorn, in: D.G. Brandon, A. Rosen (Eds.), Quantitative Relation between Properties and Microstructure, Israel Universities Press, Jerusalem, Israel, 1969: 255-342.

[236] W.R. Cannon, T.G. Langdon, Creep of ceramics - Part 2 An examination of flow mechanisms, J. Mater. Sci. 23 (1988) 1–20.

[237] F.A. Mohamed, T.G. Langdon, Deformation mechanism maps based on grain size, Metall. Trans. 5 (1974) 2339–2345.

[238] Y. Xun, F.A. Mohamed, Slip-accommodated superplastic flow in Zn-22 wt%Al, Philos. Mag. 83 (2003) 2247–2266.

[239] R.Z. Valiev, T.G. Langdon, An investigation of the role of intragranular dislocation strain in the superplastic Pb-62% Sn eutectic alloy, Acta Metall. Mater. 41 (1993) 949–954.

[240] L.K.L. Falk, P.R. Howell, G.L. Dunlop, T.G. Langdon, The role of matrix dislocations in the superplastic deformation of a copper alloy, Acta Metall. 34 (1986) 1203–1214.

[241] R.B. Figueiredo, S. Terzi, T.G. Langdon, Using X-ray microtomography to evaluate cavity formation in a superplastic magnesium alloy processed by equal-channel angular pressing, Acta Mater. 58 (2010) 5737–5748.

[242] T. Ungár, E. Schafler, J. Gubicza, Microstructure of Bulk Nanomaterials Determined by X-Ray Line-Profile Analysis, in: Bulk Nanostructured Materials, Wiley-VCH Verlag GmbH & Co. KGaA, Weinheim, 2009: 361-386.

[243] T.G. Langdon, An evaluation of the strain contributed by grain boundary sliding in superplasticity, Mater. Sci. Eng. A. 174 (1994) 225–230.

[244] M. Furukawa, A. Utsunomiya, K. Matsubara, Z. Horita, T.G. Langdon, Influence of magnesium on grain refinement and ductility in a dilute Al-Sc alloy, Acta Mater. 49 (2001) 3829–3838.

[245] O.S. Sitdikov, E.V. Avtokratova, R.I. Babicheva, Effect of temperature on the formation of a microstructure upon equal-channel angular pressing of the Al-Mg-Sc 1570 alloy, Phys. Met. Metallogr. 110 (2010) 153–161.

[246] P.J. Apps, M. Berta, P.B. Prangnell, The effect of dispersoids on the grain refinement mechanisms during deformation of aluminium alloys to ultra-high strains, Acta Mater. 53 (2005) 499–511.

[247] Y. Iwahashi, Z. Horita, M. Nemoto, Terence G. Langdon, Factors influencing the equilibrium grain size in equal-channel angular pressing: Role of Mg additions to aluminum, Metall. Mater. Trans. A. 29 (1998) 2503–2510.

[248] R.B. Figueiredo, M.T.P. Aguilar, P.R. Cetlin, Finite element modelling of plastic instability during ECAP processing of flow-softening materials, Mater. Sci. Eng. A. 430 (2006) 179–184.

[249] T.G. Langdon, The principles of grain refinement in equal-channel angular pressing, Mater. Sci. Eng. A. 462 (2007) 3–11.

[250] H.S. Kim, Evaluation of strain rate during equal-channel angular pressing, J. Mater. Res. 17 (2002) 172–179.

[251] V. Kulitskiy, S. Malopheyev, S. Mironov, R. Kaibyshev, Grain refinement in an Al-Mg-Sc alloy: Equal channel angular pressing versus friction-stir processing, Mater. Sci. Eng. A. 674 (2016) 480–490.

[252] K. Huang, K. Marthinsen, Q. Zhao, R.E. Logé, The double-edge effect of second-phase particles on the recrystallization behaviour and associated mechanical properties of metallic materials, Prog. Mater. Sci. 92 (2018) 284–359.

[253] L.E. Murr, Interfacial Phenomena in Metals and Alloys, Addison-Wesley Pub. Co., Advanced Book Program, Reading (MA), 1975.

[254] P.B. Prangnell, J.R. Bowen, M. Berta, P.J. Apps, P.S. Bate, Stability of ultra-fine “grain structures” produced by severe deformation, Mater. Sci. Forum. 467–470 (2004) 1261–1270.

[255] E.A. Marquis, D.N. Seidman, Nanoscale structural evolution of Al_3Sc precipitates in Al(Sc) alloys, Acta Mater. 49 (2001) 1909–1919.

[256] M. Ferry, N.E. Hamilton, F.J. Humphreys, Continuous and discontinuous grain coarsening in a fine-grained particle-containing Al–Sc alloy, Acta Mater. 53 (2005) 1097–1109.

[257] F.J. Humphreys, A unified theory of recovery, recrystallization and grain growth, based on the stability and growth of cellular microstructures - II. The effect of second-phase particles, Acta Mater. 45 (1997) 5031–5039.

[258] M. Ferry, N. Burhan, Microstructural evolution in a fine-grained Al-0.3 wt.% Sc alloy produced by severe plastic deformation, Scr. Mater. 56 (2007) 525–528.

[259] J.D. Robson, M.J. Jones, P.B. Prangnell, Extension of the N-model to predict competing homogeneous and heterogeneous precipitation in Al-Sc alloys, Acta Mater. 51 (2003) 1453–1468.

[260] H.Y. Wang, Z.P. Yu, L. Zhang, C.G. Liu, M. Zha, C. Wang, Q.C. Jiang, Achieving high strength and high ductility in magnesium alloy using hard-plate rolling (HPR) process, Sci. Rep. 5 (2015).

[261] K. Edalati, S. Toh, H. Iwaoka, M. Watanabe, Z. Horita, D. Kashioka, K. Kishida, H. Inui, Ultrahigh strength and high plasticity in TiAl intermetallics with bimodal grain structure and nanotwins, Scr. Mater. 67 (2012) 814–817.

[262] M. Zha, Y. Li, R.H. Mathiesen, R. Bjørge, H.J. Roven, Microstructure evolution and mechanical behavior of a binary Al-7Mg alloy processed by equal-channel angular pressing, Acta Mater. 84 (2015) 42–54.

[263] Y. Wang, M. Chen, F. Zhou, E. Ma, High tensile ductility in a nanostructured metal, Nature. 419 (2002) 912–915.

[264] G. Rai, N.J. Grant, On the measurements of superplasticity in an Al-Cu alloy, Metall. Trans. A. 6 (1975) 385–390.

[265] T.G. Langdon, The mechanical properties of superplastic materials, Metall. Trans. A. 13 (1982) 689–701.

[266] M. Kawasaki, N. Balasubramanian, T.G. Langdon, Flow mechanisms in ultrafine-grained metals with an emphasis on superplasticity, Mater. Sci. Eng. A. 528 (2011) 6624–6629.

[267] M. Kawasaki, T.G. Langdon, Review: achieving superplastic properties in ultrafine-grained materials at high temperatures, J. Mater. Sci. 51 (2016) 19–32.

[268] S.J. Rothman, N.L. Peterson, L.J. Nowicki, L.C. Robinson, Tracer diffusion of magnesium in aluminum single crystals, Phys. Status Solidi. 63 (1974) K29–K33.

[269] S. V. Divinski, V. Kulitcki, B.T. Kavakbasi, A. Gupta, Y. Buranova, T. Hickel, J. Neugebauer, G. Wilde, Grain boundary diffusion in severely deformed Al-based alloy, (2017).

[270] F.A. Mohamed, T.G. Langdon, Deformation mechanism maps for superplastic materials, Scr. Metall. 10 (1976) 759–762.

[271] R.B. Figueiredo, S. Sabbaghianrad, A. Giwa, J.R. Greer, T.G. Langdon, Evidence for exceptional low temperature ductility in polycrystalline magnesium processed by severe plastic deformation, Acta Mater. 122 (2017) 322–331.

[272] H. Matsunoshita, K. Edalati, M. Furui, Z. Horita, Ultrafine-grained magnesium–lithium alloy processed by high-pressure torsion: Low-temperature superplasticity and potential for hydroforming, Mater. Sci. Eng. A 640 (2015) 443–448.

[273] Y. Song, E.Y. Yoon, D.J. Lee, J.H. Lee, H.S. Kim, Mechanical properties of copper after compression stage of high-pressure torsion, Mater. Sci. Eng. A. 528 (2011) 4840–4844.

[274] A. Loucif, R.B. Figueiredo, T. Baudin, F. Brisset, R. Chemam, T.G. Langdon, Ultrafine grains and the Hall-Petch relationship in an Al-Mg-Si alloy processed by high-pressure torsion, Mater. Sci. Eng. A 532 (2012) 139–145.

[275] A. Vorhauer, R. Pippan, On the onset of a steady state in body-centered cubic iron during severe plastic deformation at low homologous temperatures, Metall. Mater. Trans. A Phys. Metall. Mater. Sci. 39 (2008) 417–429.

[276] O. Renk, P. Ghosh, R. Pippan, Generation of extreme grain aspect ratios in severely deformed tantalum at elevated temperatures, Scr. Mater. 137 (2017) 60–63.

[277] Y.C. Chen, Y.Y. Huang, C.P. Chang, P.W. Kao, The effect of extrusion temperature on the development of deformation microstructures in 5052 aluminium alloy processed by equal channel angular extrusion, Acta Mater. 51 (2003) 2005–2015.

[278] Y.Y. Wang, P.L. Sun, P.W. Kao, C.P. Chang, Effect of deformation temperature on the microstructure developed in commercial purity aluminum processed by equal channel angular extrusion, Scr. Mater. 50 (2004) 613–617.

[279] T.G. Langdon, Identifying creep mechanisms in plastic flow, Int. J. Mater. Res. 96 (2005) 522–531.

[280] H. Fukuyo, H.C. Tsai, T. Oyama, O.D. Sherby, Superplasticity and Newtonian-viscous flow in fine-grained class I solid solution alloys, ISIJ Int. 31 (1991) 76–85.

[281] V. Perevezentsev, Developing high strain rate superplasticity in Al–Mg–Sc–Zr alloys using equal-channel angular pressing, Ann. Chim. Sci. Des Matériaux. 27 (2002) 99–109.

[282] H.B. Geng, S.B. Kang, B.K. Min, High temperature tensile behavior of ultra-fine grained Al-3.3Mg-0.2Sc-0.2Zr alloy by equal channel angular pressing, Mater. Sci. Eng. A. 373 (2004) 229–238.

[283] A. Mogucheva, E. Babich, B. Ovsyannikov, R. Kaibyshev, Microstructural evolution in a 5024 aluminum alloy processed by ECAP with and without back pressure, Mater. Sci. Eng. A. 560 (2013) 178–192.

[284] O. Sitdikov, E. Avtokratova, T. Sakai, K. Tsuzaki, Ultrafine-grain structure formation in an Al-Mg-Sc alloy during warm ECAP, Metall. Mater. Trans. A. 44 (2013) 1087–1100.

[285] S.L. Semiatin, P.B. Berbon, T.G. Langdon, Deformation heating and its effect on grain size evolution during equal channel angular extrusion, Scr. Mater. 44 (2001) 135–140.

[286] R.R. Sawtell, C.L. Jensen, Mechanical properties and microstructures of Al-Mg-Sc alloys, Metall. Trans. A. 21 (1990) 421–430.

[287] Y. Peng, Z. Yin, B. Nie, L. Zhong, Effect of minor Sc and Zr on superplasticity of Al-Mg-Mn alloys, Trans. Nonferrous Met. Soc. China. 17 (2007) 744–750.

[288] A. Kumar, A.K. Mukhopadhyay, K.S. Prasad, Superplastic behaviour of Al–Zn–Mg–Cu–Zr alloy AA7010 containing Sc, Mater. Sci. Eng. A. 527 (2010) 854–857.

[289] A. Smolej, B. Skaza, V. Dragojević, Superplastic Behavior of Al-4.5Mg-0.46Mn-0.44Sc Alloy Sheet Produced by a Conventional Rolling Process, J. Mater. Eng. Perform. 19 (2010) 221–230.

[290] A.K. Mukhopadhyay, A. Kumar, S. Raveendra, I. Samajdar, Development of grain structure during superplastic deformation of an Al–Zn–Mg–Cu–Zr alloy containing Sc, Scr. Mater. 64 (2011) 386–389.

[291] Y.L. Duan, G.F. Xu, X.Y. Peng, Y. Deng, Z. Li, Z.M. Yin, Effect of Sc and Zr additions on grain stability and superplasticity of the simple thermal–mechanical processed Al–Zn–Mg alloy sheet, Mater. Sci. Eng. A. 648 (2015) 80–91.

[292] Y. Duan, G. Xu, L. Zhou, D. Xiao, Y. Deng, Z. Yin, B. Peng, Q. Pan, Y. Wang, L. Lu, Achieving high superplasticity of a traditional thermal-mechanical processed non-superplastic Al-Zn-Mg alloy sheet by low Sc additions, J. Alloys Compd. 638 (2015) 364–373.

[293] A.D. Kotov, A. V. Mikhaylovskaya, M.S. Kishchik, A.A. Tsarkov, S.A. Aksenov, V.K. Portnoy, Superplasticity of high-strength Al-based alloys produced by thermomechanical treatment, J. Alloys Compd. 688 (2016) 336–344.

[294] A.V. Mikhaylovskaya, O.A. Yakovtseva, V.V. Cheverikin, A.D. Kotov, V.K. Portnoy, Superplastic behaviour of Al-Mg-Zn-Zr-Sc-based alloys at high strain rates, Mater. Sci. Eng. A. 659 (2016) 225–233.

[295] X. Sun, Q. Pan, M. Li, Y. Shi, J. Yan, Superplastic deformation behavior of cold-rolled Al-Mg-Sc-Zr alloy, Chinese J. Nonferr. Met. 26 (2016) 280.

[296] G. Xu, X. Cao, T. Zhang, Y. Duan, X. Peng, Y. Deng, Z. Yin, Achieving high strain rate superplasticity of an Al-Mg-Sc-Zr alloy by a new asymmetrical rolling technology, Mater. Sci. Eng. A. 672 (2016) 98–107.

[297] H. Xiang, Q.L. Pan, X.H. Yu, X. Huang, X. Sun, X.D. Wang, M.J. Li, Z.M. Yin, Superplasticity behaviors of Al-Zn-Mg-Zr cold-rolled alloy sheet with minor Sc addition, Mater. Sci. Eng. A. 676 (2016) 128–137.

[298] M. Li, Q. Pan, Y. Shi, X. Sun, H. Xiang, High strain rate superplasticity in an Al–Mg–Sc–Zr alloy processed via simple rolling, Mater. Sci. Eng. A. 687 (2017) 298–305.

[299] H. Akamatsu, T. Fujinami, Z. Horita, T.G. Langdon, Influence of rolling on the superplastic behavior of an Al-Mg-Sc alloy after ECAP, Scr. Mater. 44 (2001) 759–764.

[300] V.N. Perevezentsev, V.N. Chuvil'deev, A.N. Sysoev, V.I. Kopylov, T.G. Langdon, Achieving high-strain-rate superplasticity in Al-Mg-Sc-Zr alloys after severe plastic deformation, Phys. Met. Metallogr. 94 (2002) S45–S53.

[301] V.N. Perevezentsev, V.N. Chuvil'deev, V.I. Kopylov, A.N. Sysoev, T.G. Langdon, High-strain-rate superplasticity of Al-Mg-Sc-Zr alloys, Russ. Metall. 2004 (2004) 28–35.

[302] M. Kamachi, M. Furukawa, Z. Horita, T.G. Langdon, Achieving superplasticity of Al-1%Mg-0.2%Sc alloy in plate samples processed by equal-channel angular pressing, Mater. Trans. 45 (2004) 2521–2524.

[303] K.-T. Park, H.-J. Lee, C.S. Lee, W.J. Nam, D.H. Shin, Enhancement of high strain rate superplastic elongation of a modified 5154 Al by subsequent rolling after equal channel angular pressing, Scr. Mater. 51 (2004) 479–483.

[304] G. Sakai, Z. Horita, T.G. Langdon, An evaluation of superplastic anisotropy after processing by equal-channel angular pressing, Mater. Trans. 45 (2004) 3079–3081.

[305] A. Ota, H. Akamatsu, K. Neishi, M. Furukawa, Z. Horita, T.G. Langdon, Low-temperature superplasticity in aluminium alloys processed by equal-channel angular pressing, Mater. Trans. 43 (2002) 2364–2369.

[306] R. Kaibyshev, K. Shipilova, F. Musin, Y. Motohashi, Achieving high strain rate superplasticity in an Al–Li–Mg alloy through equal channel angular extrusion, Mater. Sci. Technol. 21 (2005) 408–418.

[307] P. Málek, K. Turba, M. Cieslar, I. Drbohlav, T. Kruml, Structure development during superplastic deformation of an Al-Mg-Sc-Zr alloy, Mater. Sci. Eng. A. 462 (2007) 95–99.

[308] K. Turba, P. Málek, M. Cieslar, Superplasticity in an Al–Mg–Zr–Sc alloy produced by equal-channel angular pressing, Mater. Sci. Eng. A. 462 (2007) 91–94.

[309] R. Kaibyshev, D. Zhemchuzhnikova, A. Mogucheva, Effect of Mg content on high strain rate superplasticity of Al-Mg-Sc-Zr alloys subjected to equal-channel angular pressing, Mater. Sci. Forum. 735 (2013) 265–270.

[310] A. Dubynaa, S. Malopheyev, R. Kaibyshev, Effect of rolling on superplastic behavior of an Al-Mg-Sc alloy with ultrafine-grained structure, Mater. Sci. Forum. 838–839 (2016) 416–421.

[311] A. Mogucheva, D. Yuzbekova, R. Kaibyshev, Superplasticity in a 5024 aluminium alloy subjected to ECAP and subsequent cold rolling, Mater. Sci. Forum. 838–839 (2016) 428–433.

[312] D. Yuzbekova, A. Mogucheva, R. Kaibyshev, Low-temperature superplasticity in an Al-Mg-Sc alloy processed by ECAP, Mater. Sci. Forum. 838–839 (2016) 422–427.